GEORGIA DOT RESEARCH PROJECT 22-17

Final Report

NONDESTRUCTIVE/NONCONTACT INSPECTION PROTOCOLS AND TECHNOLOGIES FOR AGING MECHANICALLY STABILIZED EARTH AND MODULAR BLOCK RETAINING WALLS

VOLUME I

Office of Performance-based Management and Research
600 West Peachtree Street NW | Atlanta, GA 30308

October 2025

TECHNICAL REPORT DOCUMENTATION PAGE

1. Report No.: FHWA-GA-25-227	2. Government Accession No.: N/A	3. Recipient's Catalog No.: N/A
4. Title and Subtitle: Nondestructive/Noncontact Inspection Protocols and Technologies for Aging Mechanically Stabilized Earth and Modular Block Retaining Walls, Volume I		5. Report Date: October 2025 6. Performing Organization Code: N/A
7. Author(s): Marcel Maghiar, Ph.D. Gustavo O. Maldonado, Ph.D. PE Soonkie Nam, Ph.D. Shakil Ahmed Md. Mehrab Hossain & Charles Lawal		8. Performing Organization Report No.: 22-17
9. Performing Organization Name and Address: Georgia Southern University Department of Civil Engineering & Construction 201 COBA Drive, BLDG 232, Statesboro, GA 30458 Phone: 912-478-1894 Email: mmaghiar@georgiasouthern.edu		10. Work Unit No.: N/A 11. Contract or Grant No.: PI#0019323
12. Sponsoring Agency Name and Address: Georgia Department of Transportation (SPR) Office of Performance-based Management and Research 600 West Peachtree St. NW Atlanta, GA 30308		13. Type of Report and Period Covered: Final; April 2023 – October 2025 14. Sponsoring Agency Code: N/A
15. Supplementary Notes: Prepared in cooperation with the U.S. Department of Transportation, Federal Highway Administration.		

16. Abstract: This volume is the first in a series. The other volume in the series is FHWA-GA-25-2217 Volume II.

As Mechanically Stabilized Earth and Modular Block retaining walls age within Georgia's highway infrastructure, their stability and safety are critical concerns. Currently, unlike bridges, these retaining walls lack standardized inspection protocols, and studies show that, nationwide, a significant number of them exhibit signs of distress such as cracking or bulging. GDOT's Research Project RP 22-17 addresses this by exploring nondestructive, noncontact inspection using advanced sensing technologies. The project specifically evaluates terrestrial LiDAR, Close-Range Photogrammetry (CRP), and Infrared Thermography (IRT), using a robotic total station (RTS) for reference. Key findings indicate that terrestrial LiDAR, particularly Target-Based LiDAR, with field-acquired targets at high-resolution, is soundly effective in detecting small, near-centimeter displacements. Visual-Alignment LiDAR also showed comparable accuracy with less field work, but requiring highly overlapped scans and more post-processing. The goal is to proactively detect issues like structural movement and deterioration, which can extend the service life of those walls, enhance safety, and reduce costly repairs. The research aims to equip GDOT with a data-informed strategy for monitoring critical displacements in these essential infrastructure components.

17. Keywords: MSE and MB walls, Inspection Protocol, Terrestrial LiDAR, Close-Range Photogrammetry, Infrared Thermography	18. Distribution Statement: No Restriction

19. Security Classification (of this report): Unclassified	20. Security Classification (of this page): Unclassified	21. No. of Pages: 379	22. Price: Free

From DOT 1700.7 (8-72) Reproduction of completed page authorized

GDOT Research Project 22-17

Final Report

NONDESTRUCTIVE/NONCONTACT INSPECTION PROTOCOLS AND TECHNOLOGIES FOR AGING MECHANICALLY STABILIZED EARTH AND MODULAR BLOCK RETAINING

VOLUME I

By

Marcel Maghiar
Professor, Department of Civil Engineering & Construction

Gustavo O. Maldonado
Professor, Department of Civil Engineering & Construction

Soonkie Nam
Associate Professor, Department of Civil Engineering & Construction

Shakil Ahmed,
Mehrab Hossain and Charles Lawal
Graduate Research Assistants, Department of Civil Engineering & Construction

Georgia Southern University Research and Services Foundation

Contract with
Georgia Department of Transportation

In cooperation with
U.S. Department of Transportation,
Federal Highway Administration

October 2025

The contents of this report reflect the views of the authors, who are responsible for the facts and accuracy of the data presented herein. The contents do not necessarily reflect the official views or policies of the Georgia Department of Transportation or the Federal Highway Administration. This report does not constitute a standard, specification, or regulation.

SI* (MODERN METRIC) CONVERSION FACTORS

APPROXIMATE CONVERSIONS TO SI UNITS

Symbol	When You Know	Multiply By	To Find	Symbol
		LENGTH		
in	inches	25.4	millimeters	mm
ft	feet	0.305	meters	m
yd	yards	0.914	meters	m
mi	miles	1.61	kilometers	km
		AREA		
in^2	square inches	645.2	square millimeters	mm^2
ft^2	square feet	0.093	square meters	m^2
yd^2	square yard	0.836	square meters	m^2
ac	acres	0.405	hectares	ha
mi^2	square miles	2.59	square kilometers	km^2
		VOLUME		
fl oz	fluid ounces	29.57	milliliters	mL
gal	gallons	3.785	liters	L
ft^3	cubic feet	0.028	cubic meters	m^3
yd^3	cubic yards	0.765	cubic meters	m^3
		NOTE: volumes greater than 1000 L shall be shown in m^3		
		MASS		
oz	ounces	28.35	grams	g
lb	pounds	0.454	kilograms	kg
T	short tons (2000 lb)	0.907	megagrams (or "metric ton")	Mg (or "t")
		TEMPERATURE (exact degrees)		
°F	Fahrenheit	5 (F-32)/9 or (F-32)/1.8	Celsius	°C
		ILLUMINATION		
fc	foot-candles	10.76	lux	lx
fl	foot-Lamberts	3.426	$candela/m^2$	cd/m^2
		FORCE and PRESSURE or STRESS		
lbf	poundforce	4.45	newtons	N
lbf/in^2	poundforce per square inch	6.89	kilopascals	kPa

APPROXIMATE CONVERSIONS FROM SI UNITS

Symbol	When You Know	Multiply By	To Find	Symbol
		LENGTH		
mm	millimeters	0.039	inches	in
m	meters	3.28	feet	ft
m	meters	1.09	yards	yd
km	kilometers	0.621	miles	mi
		AREA		
mm^2	square millimeters	0.0016	square inches	in^2
m^2	square meters	10.764	square feet	ft^2
m^2	square meters	1.195	square yards	yd^2
ha	hectares	2.47	acres	ac
km^2	square kilometers	0.386	square miles	mi^2
		VOLUME		
mL	milliliters	0.034	fluid ounces	fl oz
L	liters	0.264	gallons	gal
m^3	cubic meters	35.314	cubic feet	ft^3
m^3	cubic meters	1.307	cubic yards	yd^3
		MASS		
g	grams	0.035	ounces	oz
kg	kilograms	2.202	pounds	lb
Mg (or "t")	megagrams (or "metric ton")	1.103	short tons (2000 lb)	T
		TEMPERATURE (exact degrees)		
°C	Celsius	1.8C+32	Fahrenheit	°F
		ILLUMINATION		
lx	lux	0.0929	foot-candles	fc
cd/m^2	$candela/m^2$	0.2919	foot-Lamberts	fl
		FORCE and PRESSURE or STRESS		
N	newtons	0.225	poundforce	lbf
kPa	kilopascals	0.145	poundforce per square inch	lbf/in^2

* SI is the symbol for the International System of Units. Appropriate rounding should be made to comply with Section 4 of ASTM E380. (Revised March 2003)

TABLE OF CONTENTS

LIST OF FIGURES

LIST OF TABLES

LIST OF ABBREVIATIONS & SYMBOLS

ACP	Auxiliary control points
NAD83	North American Datum 1983
AEC	Architecture, Engineering, and Construction
AF	Alignment Factor
AG	Aggregate
AI	Artificial Intelligence
ASCE	American Society of Civil Engineers
B1	Bridge Site 1 at Crossgate
B2	Bridge Site 2 at Old River
B3	Bridge Site 3 at Sandersville
B4	Bridge Site 4 at King George
BEaM	Built Environment and Modeling Lab
^{O}C	Degree Celsius
C2C	Cloud to Cloud
C2M	Cloud to Mesh
CAD	Computer-Aided Design
CC	CloudCompare
CDFs	Cumulative Distribution Functions
CPs	Checkpoints
CRP	Close-Range Photogrammetry
CSV	Comma-Separated Values

CW	Control Wall
DB	Database
DD	Distance Discrepancy
DE	DroneDeploy with EACPs
DE	DroneDeploy with Elevated GCPs
DE1	DroneDeploy with Elevated GCPs at epoch 1
DE2	DroneDeploy with Elevated GCPs at epoch 2
DelDOT	Delaware Department of Transportation
DG	DroneDeploy – Ground-level GCPs
DG1	DroneDeploy – Ground-level GCPs at epoch 1
DG2	DroneDeploy – Ground-level GCPs at epoch 2
DOT	Department of Transportation
DS	Drone Survey
DS1	DroneDeploy with Elevated GCPs at epoch 1
DSLR	Digital Single-Lens Reflex
DSM	Digital Surface Model
EACP	Elevated Auxiliary Control Point
EDM	Electronic Distance Measurement
EGM	Earth Gravitational Model
EPS	Expanded polystyrene
ERS	Earth Retaining Structure
ET	Electronic Theodolites
EXIF	Exchangeable Image File Format

FCC	Federal Communications Commission
FHWA	Federal Highway Administration
FIG	Figure
FLIR	Forward Looking Infrared
FM	Frequency Modulation
FPA	Focal Plane Array
FRP	Fiber-Reinforced Polymer
FTL	The Field target-based terrestrial LiDAR
GA	Georgia
GAEC	Georgia Architecture, Engineering, and Construction
GAEC	Global Angular Error of Closure
GAM	Geo-technical Asset Management
GB	Gigabyte
GCP	Ground Control Point
GDOT	Georgia Department of Transportation
GLONASS	Global Navigation Satellite System
GNSS	Global Navigation Satellite System
GPR	Ground Penetrating Radar
GPS	Global Positioning System
GRS	Geodetic Reference System
GRS	Geodetic Reference System
GSU	Georgia Southern University
HD	High Definition

HDPE	High-Density Polyethylene
Hz	Hertz
IATS	Image-Assisted Total Station
ID	Identifier
IMU	Inertial Measurement Unit
IP55	Ingress Protection 55
IR	Infrared Radiation
IRT	Infrared Thermography
ISO	International Organization for Standardization
JPG	Joint Photographic Experts Group
kg	Kilogram
Km	Kilometer
LAEC	Local Angular Error of Closure
LAEC	Local Angular Error of Closure
LCD	Liquid Crystal Display
LD	Left-Lower
LEC	Longitudinal Error of Closure
LEC	Longitudinal Error of Closure
LiDAR	Light Detection and Ranging
LT	Left-Top
LT	LiDAR model using target-based alignment
LT1	LiDAR model using target-based alignment at epoch 1
LT2	LiDAR model using target-based alignment at epoch 2

LTE	Long-Term Evolution
LU	Left-Upper
LV	Left-Vertical
LV	LiDAR model using visual alignment
LV1	LiDAR model using visual alignment at epoch 1
LV2	LiDAR model using visual alignment at epoch 2
LVL	Loop Visual-Alignment LiDAR
LWIR	Long-Wave Infrared
M30	DJI Matrice 30
M3C2	Multiscale Model-to-Model Cloud Comparison
MAE	Mean Absolute Error
MAP-21	Moving Ahead for Progress in the 21st Century Act
MAX	Maximum
MB	Modular Block
MD	Mean Deviation
MD	Metashape model generated from UAV images
MD1	Metashape model generated from UAV images at epoch 1
MD2	Metashape model generated from UAV images at epoch 2
MDOT	Michigan Department of Transportation
MDP	Metashape processed Drone Picture Model
MED	Median
MHP	Metashape Handheld Pictures
MIN	Minimum

ML	Metashape with Large Image Set
ML1	Metashape with Large Image Set at epoch 1
ML2	Metashape with Large Image Set at epoch 2
MM	Millimeter
MM	Metashape with Medium Image Set
MM1	Metashape with Medium Image Set at epoch 1
MM2	Metashape with Medium Image Set at epoch 2
MP	Megapixel
MP	Million pixels
MS	Metashape with Small Image Set
MS1	Metashape with Small Image Set at epoch 1
MS2	Metashape with Small Image Set at epoch 2
MSE	Mechanically Stabilized Earth
MSL	Mean Sea Level
MSL	Mean Sea Level
MSX	Multi-Spectral Dynamic Imaging
MTP	Manual Tie Point
MTP	Manual Tie Point
MU	Middle-Upper
N	North
NAD	North American Datum
NBI	National Bridge Inventory
NBIS	National Bridge Inspection Standards

NCDOT	North Carolina Department of Transportation
NCHRP	National Cooperative Highway Research Program
NDE	Non-Destructive Evaluation
NDT	Non-Destructive Testing
NED	Northeast Down
NETD	Noise Equivalent Temperature Difference
NEU	Northeast Upper
N-FTL	North Wall – Fixed-Target LiDAR
NHP	North-side Handheld Photogrammetry
NMD	North Middle Down
N-MHP	North Wall – Metashape Handheld Photogrammetry
NMU	North Middle Upper
N-TBL1	North Wall Target Based LiDAR – Epoch 1
N-TBL2	North Wall Target Based LiDAR – Epoch 2
N-VAL1	North Wall Visual-Alignment LiDAR – Epoch 1
N-VAL2	North Wall Visual-Alignment LiDAR – Epoch 2
NW	Northwest
NW1 D	Northwest Wall – Segment 1 – Down
NW1 U	Northwest Wall – Segment 1 – Upper
NW2 D	Northwest Wall – Segment 2 – Down
NW2 U	Northwest Wall – Segment 2 – Upper
NW3 D	Northwest Wall – Segment 3 – Down
NW3 U	Northwest Wall – Segment 3 – Upper

NW4 D	Northwest Wall – Segment 4 – Down
NW4 U	Northwest Wall – Segment 4 – Upper
NWD	Northwest Down
NWU	Northwest Upper
PCF	Per cubic feet
PD	Position Discrepancy
PennDOT	Pennsylvania Department of Transportation
PL1	Pix4D Mapper model with a large number of DSLR images
PPK	Post-Processed Kinematic
QZSS	Quasi-Zenith Satellite System
RAM	Random Access Memory
RD	Right-Down
RDM	Remote Distance Measurement
RMS	Root Mean Square
RMSE	Root Mean Square Error
RMSV	Root Mean Square Value
RoI	Region of Interest
RTK	Real-Time Kinematic
RTS	Robotic Total Station
RTS1	Robotic Total Station Data from Epoch 1
RTS2	Robotic Total Station Data from Epoch 2
RTS21	Robotic Total Station Data from Epoch 2 Attempt 1
RTS22	Robotic Total Station Data from Epoch 2 Attempt 2

RU	Upper Right
RVL	Random Visual-Alignment LiDAR
S	South
SBAS	Satellite-Based Augmentation System
SE	Southeast
SE5 D	Southeast Wall – Segment 5 – Down
SE5 U	Southeast Wall – Segment 5 – Upper
SE6 D	Southeast Wall – Segment 6 – Down
SE6 U	Southeast Wall – Segment 6 – Upper
SE7 D	Southeast Wall – Segment 7 – Down
SE7 U	Southeast Wall – Segment 7 – Upper
SE8 D	Southeast Wall – Segment 8 – Down
SE8 U	Southeast Wall – Segment 8 – Upper
SED	Southeast Down
SEU	Southeast Upper
S-FTL	South Wall – Fixed-Target LiDAR
SHM	Structural Health Monitoring
SI	International System of Units
SLS	Structured Light Scanning
SMD	South Middle Down
S-MHP	South Wall – Metashape Handheld Photogrammetry
SMU	South Middle Upper
SNBI	Specifications for the National Bridge Inventory

SR	State Route
ST	Scan Station
S-TBL1	South wall Target Based LiDAR – Epoch 1
S-TBL2	South wall Target Based LiDAR – Epoch 2
STD	Standard Deviation
STD-P	Standard Deviation – Population
STD-S	Standard Deviation – Sample
STL	Software Target LiDAR
sUAS	Small Unmanned Aircraft System
S-VAL1	South Wall Visual-Alignment LiDAR – Epoch 1
S-VAL2	South Wall Visual-Alignment LiDAR – Epoch 2
SWD	Southwest Down
SWU	Southwest Upper
TB	Target-Based
TBL1	Target-Based LiDAR at Epoch 1
TBL2	Target-Based LiDAR at Epoch 2
TIFF	Tagged Image File Format
TLS	Terrestrial LiDAR Scanner
TS	Total Station
UAS	Unmanned Aircraft Systems
UAV	Unmanned Aerial Vehicle
USB	Universal Serial Bus
USft	U.S. Survey Foot

UTM	Universal Transverse Mercator
VA	Visual-Alignment
VAL1	Visual-Alignment LiDAR at Epoch 1
VAL2	Visual-Alignment LiDAR at Epoch 2
WGS84	World Geodetic System 1984

EXECUTIVE SUMMARY

Mechanically Stabilized Earth (MSE) and Modular Block (MB) retaining walls are becoming ubiquitous and significant components of Georgia's highway infrastructure. As these structures age, ensuring their continued stability and safety becomes increasingly critical. Unlike bridges, however, retaining walls currently lack broadly adopted standardized inspection protocols. Across the U.S., over 160 million square feet of retaining walls are constructed annually, yet studies show a concerning number of walls exhibit signs of distress—such as cracking, bulging, leaning, settling, spalling, growth of vegetation or roots, loss of backfill, etc. In response to this growing concern, GDOT is pursuing a practical, data-informed strategy for monitoring and maintaining these structures. To support this effort, GDOT launched Research Project RP 22-17 to develop a nondestructive, noncontact inspection framework using advanced sensing technologies. This study evaluated the capabilities of terrestrial LiDAR, Close-Range Photogrammetry (CRP), and Infrared Thermography (IRT), with an accurate robotic total station (RTS) serving as the reference instrument. These tools were assessed for their effectiveness in detecting structural movement and early signs of deterioration, enabling a more proactive approach to wall maintenance. Timely identification of these issues can help extend the service life of the walls, enhance safety, and reduce the risk of costly repairs.

Key Findings:

- **Terrestrial LiDAR Accuracy and Reliability:** Terrestrial LiDAR techniques particularly Target-Based (TB) LiDAR consistently outperformed Close-Range Photogrammetry (CRP) in

detecting small displacements. At the Control Wall (CW) site, TB LiDAR, using high-resolution field-acquired targets, detected displacements as small as 3 mm. Visual-Alignment (VA) LiDAR delivered comparable accuracy with less field effort, though it required more extensive postprocessing. Nonetheless, VA LiDAR requires highly overlapped scans registered in a close-neighboring pattern, preferably closing a registration loop. An alternative TB LiDAR method, which involved scanning targets in the field but acquiring them via software, offered slightly lower accuracy than the other two approaches but struck a balance by reducing both fieldwork and postprocessing demands.

- **CRP Performance:** Among CRP methods, models created using Agisoft Metashape and DroneDeploy (in this case with auxiliary elevated control points), at the Control Wall, presented estimated noise levels of ~18.5 mm, while the noise for TB and VA LiDAR models was ~7 mm. Nevertheless, multi-epoch comparisons of full CRP models may reveal artifacts—such as surface warping and false displacements, making CRP less reliable for high-precision displacement tracking.

- **Determination of Noise Levels from Multiple Estimations:** Noise thresholds were estimated through point-position and distance-based comparisons (using the accurate RTS instrument) and through full point-cloud comparisons (using the CloudCompare software via its C2C and M3C2 schemes). Measurements completed at the CW and B2-Old River sites resulted in the following estimation of the associated noise levels. TB LiDAR

(9.1 mm), VA LiDAR (11.4 mm), and the 1-second Robotic Total Station (9.8 mm) exhibited lower noise levels compared to CRP models, which reached up to 18.4 mm. These results indicate that LiDAR methods can confidently detect displacements greater than ½ inch (12.5 mm).

- **Control Wall Testing:** Simulated displacements of 3–34 mm at the CW site demonstrated that LiDAR techniques along with CloudCompare could reliably capture fine-scale changes across entire wall surfaces. TB and VA LiDAR showed minimal error spread, whereas photogrammetric models presented larger errors and misidentified static regions as displaced.

- **Infrared Thermography:** IRT was used as a nondestructive method to assess thermal behavior and detect near-surface anomalies in MSE retaining walls. Inspections at Crossgate, Old River Road, and King George Blvd. sites revealed no significant defects affecting structural integrity.

- **Integration of Photographic Data in Wall Inspections:** This study highlights the value of combining photographic imagery with terrestrial LiDAR for retaining wall inspections. LiDAR provides precise spatial data, while photographs capture surface conditions such as cracks, spalling, efflorescence, erosion, and vegetation. Together, they enable more reliable assessments. Though photogrammetric modeling is not essential when LiDAR is used, overlapping images with reference markers can be processed in Agisoft Metashape if needed. Photographs should be collected during each LiDAR epoch via UAVs or handheld cameras to maintain consistency across inspections.

Recommendations:

- **Preferred Modeling Techniques:** For monitoring near-centimeter-level wall displacements, TB LiDAR (with field-acquired targets) is recommended, followed by VA LiDAR (with highly overlapped scans registered in a close-neighboring pattern, preferably closing a loop) and TB LiDAR (with software-acquired targets). All mentioned methods support effective displacement detection via cloud comparison using the CloudCompare software. CRP is suitable for visual documentation but should not be solely relied upon for structural displacement monitoring.

- Photographic imagery should be routinely integrated into retaining wall inspections to capture surface-level indicators such as cracking, efflorescence, and vegetation intrusion that may not be fully visible in LiDAR data.

- **Protocol Development:** To ensure reliable displacement monitoring, it is recommended that GDOT establish and adopt standardized protocols centered on the generation and comparison of multi-epoch LiDAR models, georeferenced to common GCPs, established through well-balanced closed traverses. A summarized, narrated protocol has been developed to guide this process, supported by detailed subprotocols (included in the report appendices) that provide step-by-step instructions for using the relevant instruments and software tools.

- **Workforce Needs:** Effective training is essential for equipping personnel with the skills required to carry out the proposed inspection activities. Key competencies include establishing accurate GCPs, conducting field scans, registering multiple scans into a unified model, and

georeferencing the final product within a consistent local coordinate system for multi-epoch comparison using CloudCompare. Georgia Southern University currently offers an *Introduction to Terrestrial LiDAR* course that covers many of these core topics. Adoption of these skills will improve data accuracy, reduce subjectivity in inspections, and support better infrastructure lifecycle management. As an optional enhancement, close-range photogrammetric modeling can be included in the training to broaden the technical capabilities of inspection personnel.

- **Future Research Directions:** Opportunities include:

    - Comprehensive long-term monitoring and documentation of wall displacements.
    - Integrating AI for automated anomaly detection
    - Real-time UAV monitoring systems
    - IoT sensor integration for surface and subsurface health
    - Evaluating cost-effectiveness vs traditional inspections
    - Adapting and adopting low-cost or open-source alternatives for wider use

Conclusion:

This research confirms that advanced remote sensing technologies particularly terrestrial LiDAR methods supported by accurate reference networks and cloud-based analysis tools offer a reliable, nondestructive framework for monitoring MSE and MB retaining walls. By detecting subtle displacements and surface-level anomalies, these methods enable a shift from subjective visual inspections to objective, data-driven asset management. Among the evaluated techniques, Target-

Based and Visual-Alignment LiDAR approaches demonstrated superior precision in displacement detection. Infrared Thermography, while less effective for identifying structural defects, proved useful as a supplementary tool for detecting near-surface anomalies under favorable conditions. The integration of LiDAR data with photographic imagery further enhances inspection quality by capturing both geometric and visual indicators of deterioration. With standardized protocols and targeted workforce training, GDOT should be well-positioned to proactively manage wall infrastructure, extend service life, and potentially reduce maintenance costs. Continued research into long-term monitoring, AI-driven anomaly detection, and real-time UAV systems will further strengthen this inspection framework.

CHAPTER 1. INTRODUCTION

MSE and Modular Block (MB) retaining walls play a vital role in the transportation infrastructure of Georgia and the broader United States. These wall systems have gained popularity due to their structural reliability, design flexibility, and cost-efficiency in applications such as bridge abutments, roadway embankments, and grade separations (Bathurst, 2019). Since their introduction to the U.S. in the early 1970s, and especially with expanded usage in the 1980s and 1990s, the use of MSE and MB walls has grown rapidly (Mitchell, 1990). Nationally, more than 160 million square ft of retaining walls are constructed annually (Admassu et al., 2024) and NCHRP estimate that over 10 million square feet of MSE and MB walls are constructed each year (NCHRP, 2009). GDOT has utilized these systems extensively across state routes and interstate corridors; however, as these structures—particularly those installed years ago, long-term durability and performance have become a growing concern. A comprehensive 2006 Ohio DOT inspection of 339 MSE walls recorded significant signs of distress: 30% exhibited sand leakage, 32% had vegetation infiltration, 19% showed cracked panels, and 11% had bowing or bulging highlighting pervasive and potentially critical degradation (Raeburn er al., 2008). Similarly, a Michigan DOT study identified numerous deficiencies in its retaining wall inventory, including evidence of face panel movement, joint separations, and excessive batter deviations, concluding that many walls had reached critical aging thresholds and required targeted inspection programs (Athanasopoulos-Zekkos et al., 2020). Additionally, a North Carolina DOT report on MSE wall performance revealed recurring issues with geogrid corrosion, panel misalignment, and settlement-induced damage, noting the lack of a centralized inspection framework to track deterioration over time (NCDOT, 2012). Given the similar construction context of Georgia's walls, many are approaching or exceeding their design

life. Potential concerns include corrosion of steel reinforcements, connection failures, drainage deficiencies, and foundation settlements, most of which are not visible on the surface. A key issue is the lack of a formal inspection framework. Unlike bridges, which are federally mandated to undergo biennial inspections under the National Bridge Inspection Standards (NBIS), retaining walls are often evaluated only in response to observable damage or complaints. This reactive approach lacks consistency, depth, and objectivity. Wall segments located in difficult-to-access areas under bridges, along steep slopes, or near high-traffic lanes are frequently omitted due to safety or logistical challenges. Even when visual inspections are performed, they remain subjective, highly variable, and incapable of detecting subsurface or internal damage. This operational shortcoming creates a significant knowledge gap for agencies like GDOT. Without reliable, repeatable, and high-resolution data on the condition of MSE and MB walls, it is difficult to prioritize maintenance, forecast failure, or make informed investment decisions. There is a clear need for a standardized, technology-driven protocol that can support proactive asset management of Georgia's extensive retaining wall inventory.

To address this gap, GDOT launched Research Project RP 22-17, titled "Nondestructive/Noncontact Inspection Protocols and Technologies for Aging MSE and Modular Block Retaining Walls." The project aimed to develop and validate an inspection framework built on noninvasive sensing technologies that provide objective, scalable, and accurate assessments of wall condition. The overarching goal was to transform MSE wall inspection from a reactive, visual-based process into a proactive, data-informed protocol. This study explored four commercially available and operationally feasible technologies including: Infrared IR(IRT), Robotic Total Station (RTS), and Photogrammetry (UAV and Digital Single-Lens Reflex-DSLR-based). These

technologies were selected for their complementary strengths, established utility in SHM, and adaptability to the geometric and operational constraints of retaining walls. They enable wall condition assessments to be conducted without physical contact, thereby improving inspector safety, minimizing traffic disruption, and capturing both geometric and material-related degradation phenomena.

Each technology addresses a key limitation in traditional inspection. IRT provides thermal imaging that can reveal hidden subsurface defects like moisture ingress, voids, or delamination features not visible to the naked eye. As a qualitative tool, it is especially useful in shaded or thermally dynamic environments where anomalies may become detectable through heat distribution patterns. RTS enables high-precision tracking of CPs with near-centimeter accuracy, making it ideal for long-term displacement and tilting measurements. It also facilitates ground control point (GCP) establishment for georeferencing other data types. LiDAR produces dense, 3D points cloud of the wall surface, capturing subtle deformations such as bowing, cracking, or bulging. It supports large-area coverage and epoch-to-epoch change detection using software such as CloudCompare (CC) or Leica's Cyclone Core. Photogrammetry, whether UAV-based or DSLR-based, provides a cost-effective, visually rich method to create georeferenced 3D surface models. When properly supported by RTS-derived Ground Control Points (GCPs), photogrammetric results can achieve near-centimeter accuracy while remaining accessible and portable. Together, these tools provide a comprehensive inspection suite that bridges the gaps of visual inspections. They are fast to deploy, nonintrusive, and capable of collecting consistent datasets that can be analyzed, compared over time, and archived for future monitoring. The integration of multiple sensing modalities allows GDOT to

capture both geometric deformations and material anomalies, supporting a holistic understanding of wall behavior over time.

The research was implemented in two parts: Part I involved the development of a full-scale Control Wall (CW) on the GSU campus. This structure was used to simulate real-world wall displacement behaviors by attaching Styrofoam plaques with different thicknesses to mimic displacements under controlled conditions. Each sensing method was validated against known displacements, and the resulting datasets were analyzed to determine accuracy, error margins, and optimal workflows. Part II involved field deployment at four selected sites:

- B1- Crossgate: Crossgate Road at Jimmy Deloach Parkway
- B2- Old River: I-16 at Old River Road
- B3- Sandersville: SR-19 at US-319 near Soperton (Sandersville)
- B4- King George: King George Boulevard at Abercorn Street (Georgia State Route 204)

At each location, RTS benchmarks designated as GCPs were established, and the wall surfaces were scanned using LiDAR and photogrammetry. Thermal images were acquired when appropriate conditions existed. Displacement maps and virtual 3D models were generated, and several sites were revisited to support multi-epoch comparisons. These efforts validated the technologies in active highway environments, confirming their ability to operate under time, space, and safety constraints.

The project focuses on four main tasks:

- Task 1: Review Existing Practices – This project comprehensively evaluated the limitations of current GDOT wall inspections and compared them with national practices. It confirmed the absence of a condition rating matrix and the high variability in current inspection frequency, format, and documentation.
- Task 2: Identify and Evaluate Noninvasive Technologies – After reviewing multiple options, the research team identified these four technologies based on availability, technical performance, operational feasibility, and alignment with GDOT resources. All were deployed successfully in the field, validating their appropriateness.
- Task 3: Develop a Standardized Protocol and Rating Matrix – Drawing from data collected across the CW and four field sites, the research team proposed a comprehensive inspection protocol. This includes procedures for setting up control systems, capturing sensor data, post-processing points clouds and imagery, and rating condition based on defined defect indicators.
- Task 4: Conduct Field Verifications and Reporting – Technologies were tested in CW and evaluated at four real-world sites (mentioned above) across Georgia.

This work establishes a comprehensive knowledge base to guide the selection of the most suitable inspection technology under varying conditions. Each method offers distinct strengths: the Robotic Total Station (RTS) provides a highly precise benchmark for detecting millimeter-scale displacements over time; LiDAR scanning excels at capturing both small and large-scale

deformations with high spatial accuracy and dense point cloud coverage; photogrammetry delivers a cost-effective, rapid, and visually intuitive assessment, making it especially useful for routine monitoring or when budgets and equipment access are limited; and infrared thermography (IRT) enables the identification of hidden anomalies such as moisture intrusion, voids, or delamination that geometric techniques cannot reveal. Together, these complementary technologies create a versatile toolkit that can be adapted to diverse inspection scenarios.

By validating and integrating this multifaceted protocol, the project provides GDOT with a clear framework for aligning inspection strategies with site-specific goals, environmental constraints, and available resources. This approach not only addresses existing gaps in retaining wall inspection practices but also supports the development of a proactive, scalable, and standardized inspection program. Such a program strengthens Georgia's infrastructure asset management by ensuring more reliable data collection, timely detection of deterioration, and more informed decision-making for maintenance and rehabilitation planning.

CHAPTER 2. BACKGROUND AND LITERATURE REVIEW

This chapter provides a comprehensive background on the evolution of earth-retaining structures and their inspection methodologies. It traces the historical development of MSE, and MB walls, highlights the limitations of traditional inspection practices, and details the emergence of modern, technology-driven approaches for assessing wall condition and performance.

EVOLUTION OF RETAINING WALL AND INSPECTION

Historical Development of MSE and MB Walls

The modern concept of MSE walls, often referred to as "Terre Armee" or reinforced earth, was pioneered by French engineer Henri Vidal in the 1960s (Vidal, 1969), initially utilizing steel strip reinforcements. A significant parallel development was the emergence of MB walls (also known as Segmental Retaining Walls or SRWs) in the 1980s, which utilized dry-stacked, precast concrete units often in conjunction with geosynthetic reinforcement (Donahue, 2010). Geosynthetic-reinforced soil walls were first constructed in France in the early 1970s and were introduced to the United States in 1974, primarily for applications such as supporting logging roads in the northwestern U.S. (Holtz, 2017). The first modern MSE wall in the U.S. was built in 1971 on State Route 39 near Los Angeles (Bell & Steward, 1977). The period from the 1980s through the 1990s saw a dramatic expansion in the use of these walls, including MB walls, due to their ease of installation, rapid construction, and inherent structural soundness (Bell & Steward, 1977).

Traditional Inspection Methodologies

During this early period, and for many years thereafter, inspections of earth-retaining structures, including MSE walls and the burgeoning MB walls, were largely reactive and relied heavily on conventional visual methodologies (Gong, 1991). Unlike bridges, which are subject to federally mandated biennial inspections under the NBIS, retaining walls often lack the formal, consistent inspection of framework. Visual inspections involved engineers looking for visible defects on the wall face, such as increasing tilt, differential tilt of adjacent panels (or individual blocks in MB walls), vertical cracks, spalling, bulging, misalignment or widening of joints, and blocked drainage channels. They also observed signs in the soil behind the wall, including tension cracks, settlement, gaps between the soil and the wall, lateral cracks in pavement, or excessive ponding. However, these methods were inherently subjective, highly variable, and limited to surface indications, generally only able to detect large, obvious flaws. They provided no information about internal, subsurface, or near-surface defects (Kaartinen et al., 2022). Environmental conditions like poor lighting, thick fog, or heavy rain could also severely hinder defect identification (Chew, 1998). This meant critical issues like corrosion of steel reinforcements (in traditional MSE walls), connection failures (both internal in MSE and between blocks/reinforcement in MB walls), drainage deficiencies, and foundation settlements (which are often not visible on the surface) frequently went undetected (Raeburn et al., 2008).

EMERGENCE OF CONCERNS AND EARLY STANDARDIZED EFFORTS

As MSE walls and MB walls installed in the 1980s and 1990s began to age, their long-term durability and performance became a significant concern (Gerber, 2012). This aging infrastructure

led to the documentation of widespread distress, highlighting the critical limitations of purely visual inspections, especially for hidden defects like inadequate compaction, poor drainage, and insufficient reinforcement, which are common causes of wall failures. For instance, a catastrophic MSE retaining wall failure in Tennessee was linked to issues such as inadequate compaction, poor drainage, and inadequate reinforcement. Similarly, MB walls, despite their ease of installation, also presented challenges related to settlement, bulging, and drainage issues if underlying soil conditions or construction practices were not adequately addressed, leading to concerns about their long-term stability (Tsz et al. 2023; Teshev et al. 2025).

Distress Modes and Associated Causes

The aging of these structures has led to extensive documentation of various distress modes that compromise their performance and longevity. Many of these issues are not readily apparent through conventional visual inspection, underscoring the need for more comprehensive assessment methods. Table 1 summarizes common distress types observed in MSE and MB walls, along with their frequencies and associated causes.

Table 1. Summary of Common MSE Wall Distress Modes and Observed Frequencies

Distress Type	Observed Frequency/Percentage (Source)	Associated Concerns/Causes
Sand Leakage	30% (Ohio DOT, Raeburn, Monkul, & Pyles, 2008)	Loss of backfill, internal erosion, drainage issues (Alimohammadi & Memon, 2023)
Vegetation Infiltration	32% (Ohio DOT, Raeburn, Monkul, & Pyles, 2008)	Root growth damaging panels/joints, moisture retention, aesthetic degradation
Cracked Panels	19% (Ohio DOT, Raeburn, Monkul, & Pyles, 2008)	Material degradation, differential settlement, internal pressure, freeze-thaw cycles (Alimohammadi & Memon, 2023)
Bowing or Bulging	11% (Ohio DOT, Raeburn, Monkul, & Pyles, 2008)	Excessive earth pressure, inadequate reinforcement, foundation settlement, poor compaction (Alimohammadi & Memon, 2023)
Face Panel Movement	Documented (Michigan DOT, Athanasopoulos-Zekkos et al., 2020)	Foundation instability, differential settlement, internal pressure, poor construction (Alimohammadi & Memon, 2023)
Joint Separations	Documented (Michigan DOT, Athanasopoulos-Zekkos et al., 2020)	Movement, settlement, thermal expansion/contraction, poor construction (Alimohammadi & Memon, 2023)
Excessive Batter Deviations	Documented (Michigan DOT, Athanasopoulos-Zekkos et al., 2020)	Foundation settlement, internal pressure, construction errors
Geogrid Corrosion	Documented (North Carolina DOT, NCDOT, 2012)	Material degradation, moisture ingress, chemical attack, inadequate drainage (NCDOT, 2012)
Panel Misalignment	Documented (North Carolina DOT, NCDOT, 2012)	Settlement, internal movement, construction errors
Settlement-Induced Damage	Documented (North Carolina DOT, NCDOT, 2012)	Inadequate foundation, poor compaction, changes in soil properties (Alimohammadi & Memon, 2023)
Corrosion of Steel Reinforcements	Documented (GDOT concern, Raeburn, Monkul, & Pyles, 2008)	Moisture ingress, aggressive soil chemistry, inadequate drainage (Raeburn, Monkul, & Pyles, 2008)
Connection Failures	Documented (GDOT concern, Raeburn, Monkul, & Pyles, 2008)	Material degradation, corrosion, design flaws, overloading (Raeburn, Monkul, & Pyles, 2008)
Drainage Deficiencies	Documented (Case Study of MSE Retaining Wall Failure)	Poor design/construction, clogging, leading to water accumulation (Alimohammadi & Memon, 2023)
Foundation Settlements	Documented (Case Study of MSE Retaining Wall Failure)	Inadequate bearing capacity, poor compaction, changes in soil properties (Alimohammadi & Memon, 2023)

As illustrated in Table 1, common issues such as sand leakage and vegetation infiltration are frequently observed on the surface, while more critical, often hidden defects like bowing or bulging, face panel movement, and especially the corrosion of steel reinforcements or geogrids that indicate

deeper structural compromises. These findings underscore the inherent limitations of relying solely on visual cues for comprehensive assessment.

Early Regulatory and Programmatic Responses

In response to these growing concerns about aging infrastructure and documented distress, some municipalities and state agencies began developing more structured approaches to retaining wall inspection. New York City's Local Law 10, initially for facade inspections, provided a basis for formulating retaining wall inspection programs, recognizing similar deterioration patterns in critical infrastructure (Man, 2024). These nascent programs often defined evaluation categories (e.g., "Safe," "Potentially Unsafe") and mandated periodic inspections by qualified professional engineers, typically on a five-year cycle. A numerical condition rating system (e.g., 1 to 10) also emerged for individual wall elements and overall performance, aiming for greater objectivity than purely ad-hoc visual assessments. However, a National Cooperative Highway Research Program (NCHRP) guide from late 2008 to early 2009 indicated that only 13 out of 40 surveyed highway agencies had Earth Retaining Structure (ERS) asset management programs, and most were still in early stages, though it notably recommended a five-year inspection cycle for ERS (Brutus & Tauber, 2009) This highlights that while concerns were growing, a widespread, standardized framework for retaining wall inspection was still in its infancy.

SHIFT TOWARDS PROACTIVE AND TECHNOLOGY-DRIVEN INSPECTIONS

The recognition that traditional visual inspections were insufficient for detecting critical subsurface defects, coupled with federal mandates like the "Moving Ahead for Progress in the 21st Century

Act," (MAP-21) requiring risk-based asset management plans for the National Highway System, spurred a significant shift in the approach to retaining wall inspection (NCDOT, 2012). This paradigm change led to the exploration and adoption of NDT and non-contact sensing technologies. These advanced methods aim to provide objective, quantitative data on the condition of earth-retaining structures, including both MSE and MB walls, addressing the limitations of purely visual assessments (Kaartinen et al., 2022). Modern NDT techniques are designed to assess damage without compromising the structural integrity, often utilizing principles like sound waves, acoustic impulses, or gamma rays to detect minute cracks, voids, or discontinuities that are invisible to the naked eye.

The Federal Highway Administration (FHWA) and the National Cooperative Highway Program (NCHRP) have played a pivotal role in shaping these advancements. They have provided essential reference manuals and initiated numerous projects specifically aimed at improving the performance assessment of MSE walls and other earth-retaining systems like MB walls, thereby promoting the development and adoption of advanced inspection methods. For instance, NCHRP Topic 42-09 focuses on developing guidelines for using a wider range of backfill materials, acknowledging that some walls have not performed as designed due to backfill quality or construction issues (NCHRP, 2011). To illustrate the progression in inspection practices, Table 2 outlines key milestones in the development of methodologies for assessing earth-retaining structures.

Table 2. Key Milestones in MSE Wall Inspection Practices and Methodologies

Era/Period	Primary Inspection Methodology	Key Characteristics/Limitations	Driving Factors/Developments	Notable Studies/Guidelines
Pre-1970s (Ancient/Early Engineering)	Rudimentary/Ad-hoc Visual	Limited to surface observations; No formal standards; Focus on basic stability.	Ancient principles of reinforced earth; Early building codes focused on basement walls.	NYC Department of Buildings, 2014
1970s-1990s (Modern MSE Adoption)	Reactive Visual, Ad-hoc Visual	Subjective, inconsistent; Surface indications only; Omissions due to access/safety; Lack of centralized framework.	Modern MSE invention (Vidal, 1960s); Rapid U.S. adoption (1971 onwards); Advantages: ease, speed, cost-efficiency. (Bell & Steward, 1977)	Christopher et al., 1990; Allen & Bathurst, 2019
Early 2000s (Aging Infrastructure & Problem Recognition)	Standardized Visual (limited), Early NDT Applications	Still largely reactive; Inability to detect hidden internal/subsurface defects; High variability in frequency/format.	Aging MSE wall inventory; Documented widespread distress (Ohio, Michigan, NCDOT); Growing concerns over long-term durability.	Gerber, 2012 ; Athanasopoulos-Zekkos et al., 2020; NCDOT, 2012
Mid-2000s - Present (Shift to Proactive & Technology-Driven)	Integrated NDT (emerging), Risk-based Asset Management	Objective, quantitative data; Detection of hidden defects; Improved safety/efficiency; Requires specialized equipment/expertise.	MAP-21 federal mandate (risk-based asset management); FHWA & NCHRP research initiatives; Advancements in sensing technologies.	NCHRP, 2009 ; Federal Highway Administration, 2019. ; NCHRP, 2006 ; NCDOT, 2014 ; Federal Highway Administration, 2011

ADVANCED NON-DESTRUCTIVE SENSING TECHNOLOGIES

Several key non-contact technologies have emerged and are being validated for the comprehensive inspection of earth-retaining structures, including both MSE walls and MB walls. These technologies offer distinct advantages in acquiring precise and objective data for structural assessment.

Infrared Thermography (IRT)

Infrared Thermography (IRT), the NDT technique, has been widely adopted in civil engineering since the 1980s. It operates on the principle that damaged or deteriorated areas exhibit distinct heat transfer characteristics, allowing thermal cameras to identify temperature variations indicative of subsurface anomalies such as moisture ingress, voids, or delamination (Rocha & Póvoas, 2017; Sirca & Adeli, 2018). Flaw recognition is possible with varying temperature differences; for instance, studies have observed the detection of subsurface cracks at 7.2°F, various defects including delamination and voids at 7.74°F (Lawal, 2025), and cracks and delamination at 22.5°F (Sirca Jr. & Adeli, 2018). Building on these principles, IRT has proven instrumental in the assessment and monitoring of various retaining structures. For example, Newhart (2020) advanced predictive maintenance for MSE walls by analyzing seasonal thermal data to identify anomalies and proposed routine IRT inspections to preemptively address structural concerns. Complementing this, Omidi (2024) specifically applied IRT to concrete retaining walls, demonstrating its efficacy in detecting surface cracks, voids, and delamination through distinct thermal signatures. Studies by Chen and Zhao (2013) demonstrate IRT's ability to detect surface cracks, voids, and delamination in concrete retaining walls based on distinct thermal signatures. For MSE walls, Cheng et al., (2019) developed predictive maintenance strategies using thermal imaging to identify abnormal heat retention or dispersion, while Cho et al., (2016) successfully applied IRT to detect underground cavities relevant to MSE wall stability. Furthermore, Park et al. (2016) extended IRT's utility by detecting underground cavities through temporal thermal responses on concrete surfaces, thereby validating its non-invasive capability to identify internal anomalies crucial for wall stability. Pan et al., (2023) integrated into the IRT with deep learning (Mask R-CNN) for automated detection and segmentation of hidden defects in Fiber-Reinforced Polymer (FRP)-reinforced concrete structures,

achieving high accuracy. Aljagoub and Cheng (2025) further advanced delamination detection in concrete decks using UAV-based IRT and deep learning. Newer research by Debees and Catbas (2025) and Zou and Liu (2025) combine IRT with neural networks and lightweight models for rapid, automated, and efficient bridge inspection.

Robotic Total Station (RTS)

RTSs are advanced geodetic instruments widely employed in civil engineering for precise SHM, particularly for quantifying deformations and displacements (Pehlivan et al., 2021). These automated systems enable sub-millimeter to millimeter-level accuracy in tracking strategically placed reflective targets on structures, facilitating long-term monitoring of movements such as settlement, tilt, and lateral displacement (Vaidis et al., 2011). Their ability to autonomously collect high-frequency data makes them invaluable for continuous or periodic assessment of large civil infrastructure, including retaining walls, where changes in geometric position can indicate underlying structural issues (Di Cosser et al., 2003). While specific research focusing solely on RTS's direct application to MSE wall detection is less common, its role in deformation monitoring of large retaining structures is well documented. For instance, in a study on the multitemporal monitoring of rocky walls, Catelan et al. (2025) utilized RTS measurements to track displacement trends, effectively confirming slope stability over time. Similarly, Marendić et al. (2025) developed a geodetic monitoring methodology for retaining walls, which inherently involves precise displacement measurements often employing total stations to assess horizontal and vertical movements and identify deformation processes. Zschiesche (2021) provides a comprehensive review, categorizing these instruments into types such as RTSs and image-assisted total stations (IATS), and highlights their evolving capabilities. Studies by Ehrhart and Lienhart (2015)

demonstrate the effectiveness of state-of-the-art IATS for accurate and continuous monitoring of both vibration and displacement. Furthermore, dos Santos et al. (2019) showcase the utility of RTS for detecting dynamic displacements and vibrations in complex structures, such as curved bridge decks, underscoring their precision and versatility in SHM applications.

Terrestrial LiDAR Scanner (TLS)

TLS represents a sophisticated non-contact technology capable of generating dense, three-dimensional point clouds of structural surfaces, thereby enabling the precise detection of subtle geometric deformations such as bowing, cracking, or bulging (Teng et al., 2023). This methodology offers extensive area coverage and facilitates highly accurate epoch-to-epoch change detection through advanced software processing. The inherent advantages of TLS—including rapid data acquisition over expansive areas and the provision of highly detailed geometric information—render it invaluable for comprehensive as-built documentation and meticulous monitoring of structural evolution (Wu et al., 2021). These capabilities underpin its effective application in the SHM of diverse civil engineering assets. Specifically, within the context of MSE walls, TLS has demonstrated considerable utility. Aldosari (2019), for instance, proposed a mobile LiDAR-based monitoring method for MSE walls with panels, showcasing its potential for assessing displacement. Further, Al-Rawabdeh et al. (2020) conducted a detailed evaluation of TLS applicability for monitoring movements of MSE retaining walls at a newly constructed bridge interchange, validating their findings against finite element modeling and traditional total station surveys. More broadly for retaining walls, Bao et al. (2025) experimentally assessed TLS performance in monitoring geometric deformations and proposed methodologies to achieve millimeter-level accuracy for even minor displacements. Extending to other critical infrastructure, Lawal et al.

(2025) explored Artificial Intelligence (AI)-based SHM systems integrating LiDAR imaging for crack detection and segmentation in bridges, underscoring TLS's precision in identifying structural anomalies. Algadhi et al. (2023), in their experimental assessment of TLS for retaining wall deformation, highlights the broader context of precise geometric monitoring a domain where photogrammetry also plays a significant role. Maldonado et al. (2025) examined discrepancies among various LiDAR registration methods for monitoring displacements in MSE walls, highlighting their potential for accurately capturing structural deformations. Several of the methodologies and findings presented in this current report were initially introduced and explored in that earlier study. In a focused application, Adamson (2020) specifically evaluated the use of TLS for monitoring movements of MSE retaining walls associated with a newly constructed bridge interchange, validating findings against finite element modeling and traditional total station surveys, thereby underscoring the potential for image-based techniques in such applications. Furthermore, Oskouie et al. (2016) developed a cost-effective 2D-LiDAR-based system for retaining wall displacement monitoring, demonstrating its capacity for effective three-dimensional displacement estimation. Collectively, these recent investigations affirm TLS's robust effectiveness in acquiring precise geometric data essential for the comprehensive SHM of large-scale civil infrastructure.

Photogrammetry (UAV and DSLR-based)

Photogrammetry, encompassing both Unmanned Aerial Vehicle (UAV) and DSLR-based approaches, represents a highly cost-effective methodology for generating georeferenced 3D-surface models of civil infrastructure (Congress, 2018). UAV photogrammetry offers substantial advantages for SHM by enabling rapid, low-cost data acquisition over extensive structures and

providing safe access to otherwise difficult-to-reach areas (Lee, 2025). When augmented with GCPs or advanced positioning systems such as RTK/PPK, photogrammetric outputs can achieve centimeter-level absolute accuracy. However, it is noteworthy that while photogrammetry excels in visual detail, some comparative studies suggest that LiDAR may offer superior vertical accuracy particularly in challenging environments or when detecting very fine geometric anomalies (Habib et al., 2024). For instance, studies have demonstrated that displacement measurements obtained through photogrammetry are remarkably comparable to those from total station surveys, with reported differences typically within 1–3 centimeters (Oats et al., 2017). This level of accuracy makes photogrammetry a reliable method for the quantitative assessment of wall movement. Hain and Zaghi (2020) emphasized its power in effectively documenting in-situ conditions, enabling early detection of potential failure modes and tracking wall movements over extended periods. Building upon these foundational capabilities, photogrammetry has seen increasing application in the inspection and monitoring of various civil engineering structures, including MSE walls (Hossain, 2025). Furthermore, aerial CRP using UAVs has demonstrated potential for monitoring pile retaining wall deflections, showing good agreement with traditional inclinometer measurements and numerical analysis (Ekinci et al., 2021). A recent experimental evaluation by Wondolowski et al. (2024) further reinforced the efficacy of 3D imaging technologies for structural assessment, specifically focusing on masonry retaining walls. Their findings indicate that both Structure from Motion (SfM) photogrammetry and Structured Light Scanning (SLS) produce accurate 3D models of retaining wall structures. These recent investigations collectively underscore the growing utility and evolving precision of image-based methods for comprehensive structural assessments in civil infrastructure.

State DOTs like North Carolina have begun to recommend data collection procedures that encompass both spatial and attribute data for Earth Retaining Structures, proposing prototype databases for inventory and condition assessment (NCDOT, 2014). Wisconsin DOT's field manual also outlines procedures for assessing visual or NDT defects, coding wall movement and material deterioration (Wisconsin DOT, 2024). FHWA actively promotes the use of Unmanned Aircraft Systems (UAS) for retaining wall inspections, highlighting their utility for condition assessments and the potential for integrating UAS data with AI/ML algorithms for predictive modeling. In summary, the inspection of earth-retaining structures, including MSE walls, has transitioned from a reactive, subjective visual process to a proactive, data-informed approach. This evolution is driven by the aging of the infrastructure, the documented limitations of traditional methods in detecting hidden defects, and advancements in non-destructive and non-contact sensing technologies, supported by national research and federal mandates for comprehensive asset management.

CHAPTER 3. SITE INFORMATION

As part of this study, the research team conducted field surveying and structural assessments of MSE walls serving as bridge abutments at four distinct sites across Georgia. The investigation was carried out in two parts. Part I focused on a CW located adjacent to the Carruth Building on the Statesboro campus of GSU. This wall measures approximately 22 meters (72 feet) in length and 3.8 meters (12.5 feet) in height, as measured from the base at sidewalk level. The geographic coordinates of this CW are 32°25′25.5″N, 81°46′51.5″W. Constructed using red clay bricks arranged in a standard running bond pattern, the wall mimics the structural and visual characteristics commonly seen in institutional building façades. Part II extended the study to four active highway infrastructure sites, each featuring MSE walls functioning as bridge abutments. These sites include the Jimmy Deloach Parkway over Crossgate Rd in Chatham County (Crossgate, B1), the Old River Rd at I-16 Interchange in Effingham County (Old River, B2), the SR 15 over Sandersville Railroad in Washington County (Sandersville, B3), and the SR 204 over King George Blvd in Chatham County (King George, B4). The approximate locations of these sites, in latitude and longitude, are 32°08'49.9"N, 81°10'23.5"W (B1), 32°07'29.5"N, 81°23'13.7"W (B2), 32°58'13.4"N, 82°46'46.1"W (B3), and 31°59'09.7"N, 81°13'03.3"W (B4), respectively. These MSE wall structures were constructed in the last 10 years. The site locations are shown in Figure 1 and additional information about the sites is provided in Table 3.

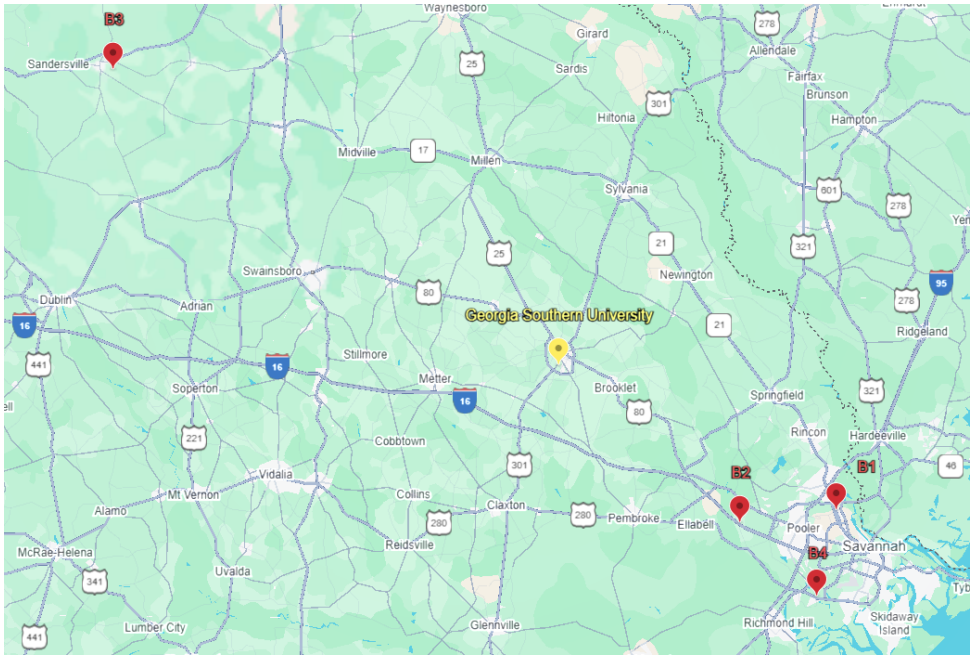

Figure 1. Map. Locations of the study sites

Table 3. Summary of site information

Site No		B1	B2	B3	B4
Name		Crossgate	Old River	Sandersville	King George
County		Chatham	Effingham	Washington	Chatham
GDOT District		5	5	2	5
Location	Latitude	32.147197	32.124867	32.970397	31.986021
	Longitude	-81.173206	-81.387133	-82.779459	-81.217573
Year Built		2015	2020	2024	2018
Lane	Above	4	5	4	3
	Under	2	4	1 (Railroad)	5
MSE Wall	Max. height	~ 22.2 ft	~ 19.8 ft	~ 39.7 ft	~ 32.4 ft
	Facing Type	Large segmental precast panel	Large segmental precast panel	Large segmental precast panel	Large segmental precast panel
	Reinforcement Type	Polyester strip	Steel strip with ribbed pattern	Steel strip with ribs	Uniaxial geogrid
	Design Life (years)	100	100	100	100

Additionally, using design and construction documents obtained from the GDOT, information was collected on key factors influencing the structural stability and integrity of MSE walls. These

include soil characteristics, compaction specifications, reinforcement types and connections, and facing systems. These elements serve as the baseline for comparison throughout this study.

BACKFILL PROPERTIES

Soil properties were a primary focus of the investigation, given their critical role in the performance of MSE walls. Across all four study sites, the backfill material was consistently specified as sand, with no significant variations. Minor differences were noted in parameters such as the internal friction angle and dry unit weight; however, these variations were not substantial enough to be considered influential in the comparative analysis. Similar consistency was observed in foundation soil specifications. A summary of these soil properties is provided in Table 4.

Table 4. Soil Characteristics

Site No	B1	B2	B3	B4
Name	**Crossgate**	**Old River**	**Sandersville**	**King George**
Material	Sand	Sand	M10 Sand	Sand
Max. Fine Contents	0-12%	0-15%	0-12%	N/A
Req. friction angle (degree)	32	30	38	35
Req. unit weight (pcf)	120	120	125	115 (dry) / 130 (moist)
Req. relative Compaction	95% Standard Proctor	100%	95% Standard Proctor	95% Standard Proctor

REINFORCEMENTS

Reinforcement systems were a major area of investigation in this study, as they exhibited the most variability among the four MSE wall sites. At the Cross Gate location, the MSE wall utilized GeoStrap® reinforcements in conjunction with GeoLoop® connections, as illustrated in Figure 2 (Fisher, 2021). GeoStrap® is a synthetic soil reinforcement system composed of a blow-molded, polyolefin, omega-shaped sleeve embedded into precast concrete facing panels (Reinforced Earth). Each strap is approximately 2 inches wide and consists of high-tenacity polyester fibers encased in a durable polyethylene sheath. This configuration provides the necessary tensile strength and long-term durability for structural stability.

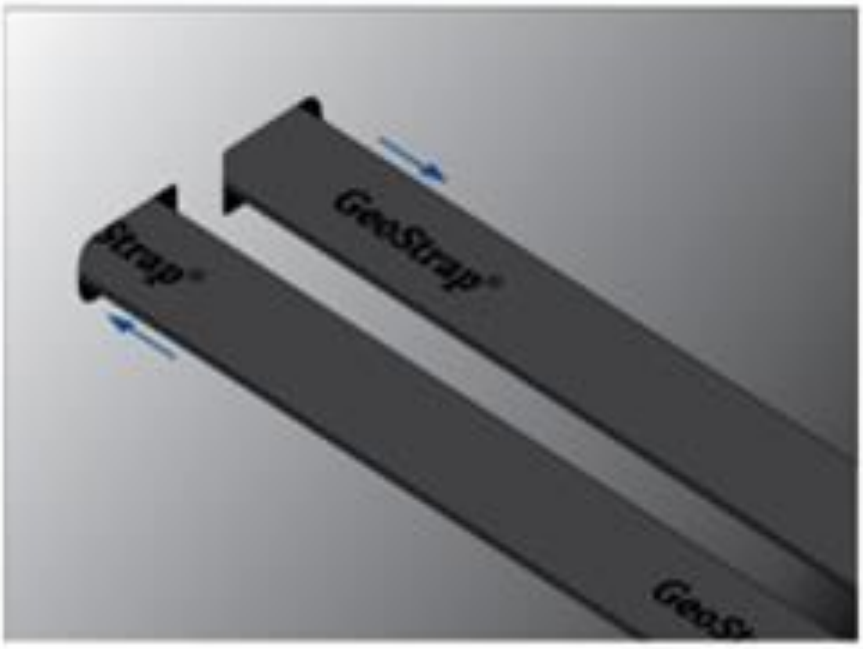

Figure 2. Photo. Reinforcement at Site B1 (From Hansberger, 2019)

At the Old River site, the MSE wall utilized SINEStrip® steel reinforcements with corresponding mechanical connections, as shown in Figure 3 (Hansberger, 2019). SINEStrip® is designed with

surface features (such as ribs or textures) that enhance friction and mechanical interlock with a variety of backfill types. The system is optimized to provide high pull-out resistance and tensile capacity (Reinforced Earth). The strips are galvanized for corrosion protection, contributing to an extended service life and compliance with long-term performance requirements.

Figure 3. Photo. Reinforcement at Site B2-Old River

The MSE wall at Sandersville uses High Adherence Steel Strips, shown in Figure 4 (Fordham, 2019). These steel strips are 2 inches wide and 5/32 inches thick and include a ribbed surface pattern that enhances bonding with compacted backfill. These reinforcements are galvanized for corrosion resistance and long-term durability are bolted to facing elements (Reinforced Earth).

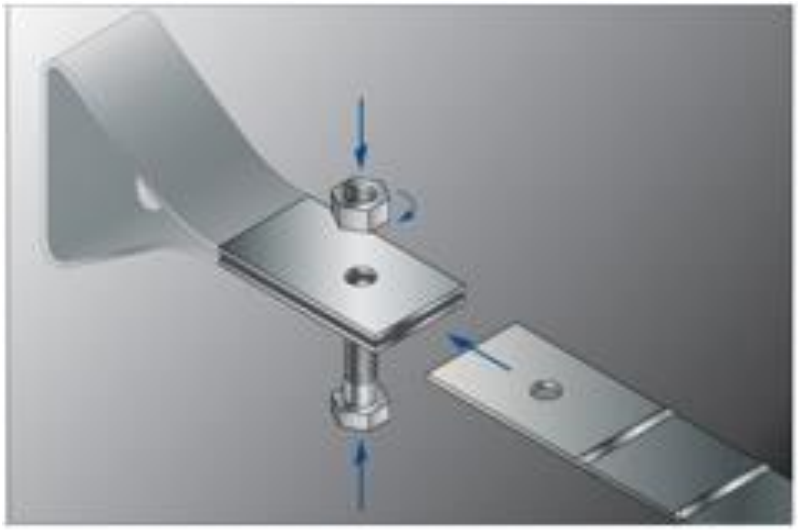

Figure 4. Photo. Reinforcement at Site B3-Sandersville

At the King George site, the MSE walls utilized a Tensar® uniaxial geogrid and a bodkin connector, shown in Figure 5, was used to secure the geogrid to the wall facing (Fuqua, 2016). Manufactured from select grades of high-density polyethylene (HDPE) resin, the uniaxial geogrid resists installation damage and long-term degradation. It can carry high tensile loads and ensures effective load transfer between the soil and reinforcement (Tensar, 2024).

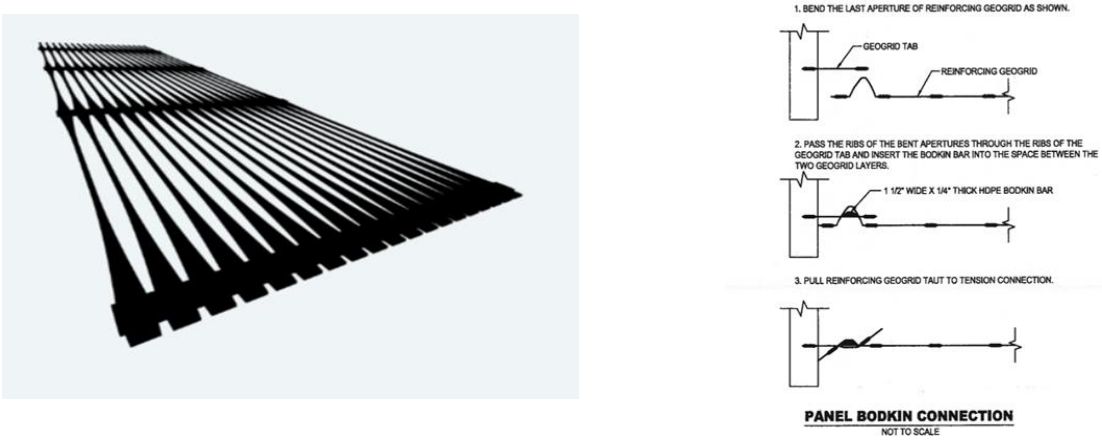

(a) Uniaxial geogrid (b) Bodkin connector

Figure 5. Drawing. Reinforcement at Site B4-King George

Table 5. Summary of Reinforcement Characteristics below summarizes the reinforcement data to easily find information corresponding to each site.

Table 5. Summary of Reinforcement Characteristics

Site No	B1	B2	B3	B4
Name	**Crossgate**	**Old River**	**Sandersville**	**King George**
Types	Polyester strip	Steel strip	High adherence steel strips with ribs	Uniaxial Geogrid
Materials	high tenacity polyester fibers (HTPET) encased in a polyethylene sheath	Grade 50, Galvanized Steel	Grade 65, hot-dip galvanized steel	high-density polyethylene (HDPE) resins
Dimensions (w × t)	2" x 1/8" (GeoMega)	2" wide	2" x 5/32"	N/A
Product brand/model	GeoStrap®	Reinforced Earth Sine Wall®	Reinforced Earth	Tensar® uniaxial geogrids
Connections	Geoloop and GeoMega	SINEStrip®	Bolt	Bodkin

FACINGS

The next component discussed is the panel system of the MSE walls, which includes panel materials, dimensions, number of reinforcement connections, and surface finishes. While each wall contains panels of various sizes and designations, this section focuses on the most common panel types used at each site. A panel key is also provided to explain the labeling system for the panels. At the Crossgate site, the MSE wall primarily consists of A-4 and A-5 panels. These panels measure 4’-10¼” by 4’-10¼” and include four and five reinforcement connections, respectively

(Fisher, 2021). The placement of the reinforcing strips on the A-4 panel is shown in Figure 6 (a). All panels are made of precast concrete and feature a shallow ashlar stone finish (Fisher, 2021). Figure 6 (b) presents the panel key used in this wall design.

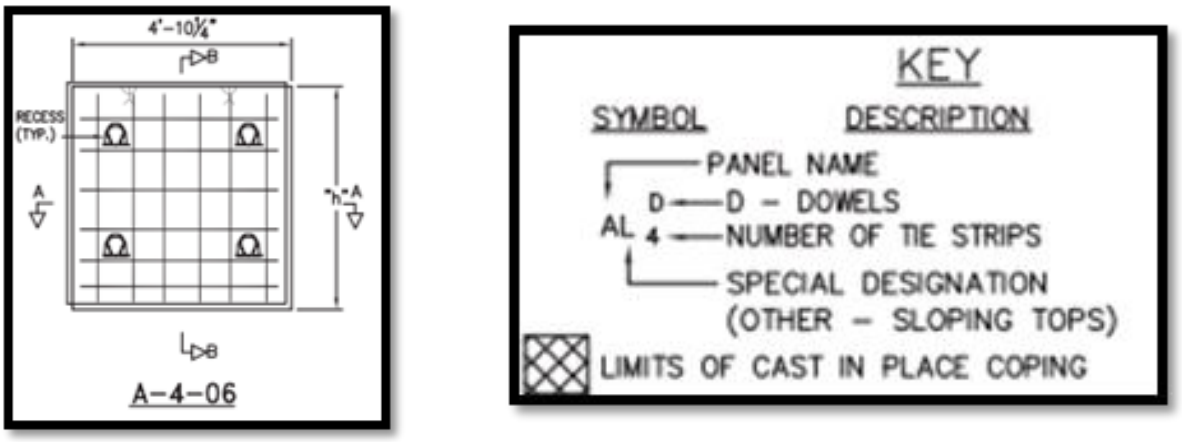

(a) (b)

Figure 6. Drawing. Panel information on Site B1-Crossgate

The Old River MSE wall uses a different panel identification system, with A2-S2 panels being the most common type (Hansberger, 2019). These panels measure 5’-0” by 5’-0”, are made of precast concrete, and feature a shallow ashlar stone finish (Hansberger, 2019). The panel key for this wall is provided in Figure 7.

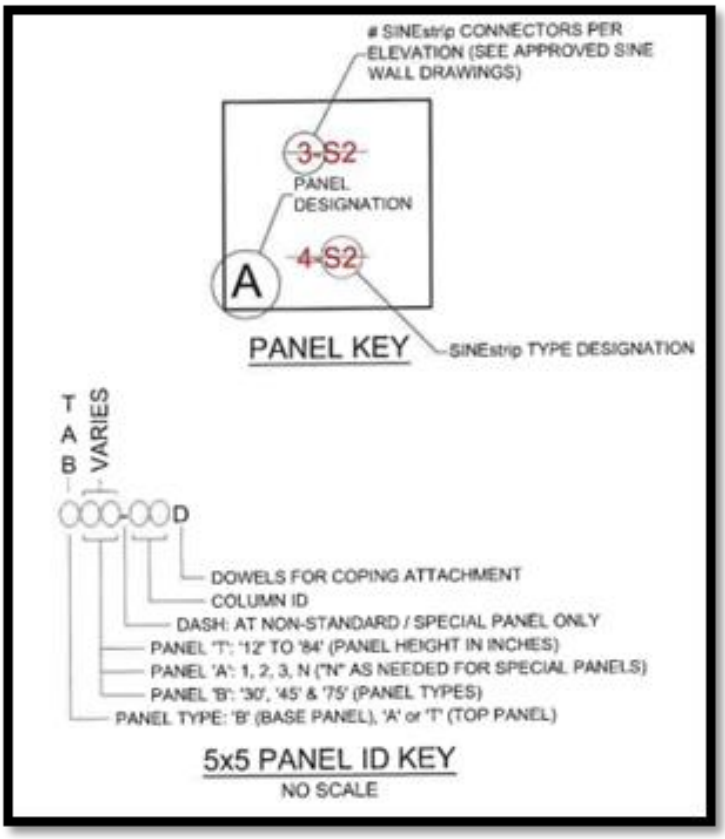

Figure 7. Drawing. Panel information on Site B2-Old River

At the Sandersville site, the MSE wall primarily consists of A-3 and A-4 panels. Similar to those used at Crossgate, these panels measure 4’-10¼” by 4’-10¼” and include three and four reinforcement connections, respectively (Fordham, 2019). The placement of the reinforcements and the panel key are shown in Figure 8. All panels are made of precast concrete and have a plain smooth steel form finish.

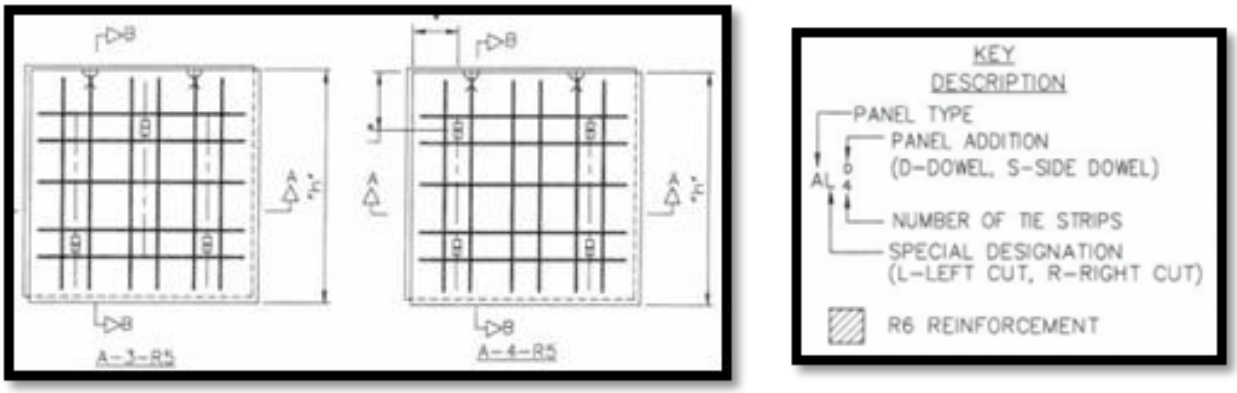

(a) (b)

Figure 8. Drawing. Panel information of Site B3-Sandersville

The MSE wall at the King George site primarily consists of A-2, A-3, and Alignment Factor (AF) panels (Fuqua, 2016). The typical panel size is 4'-9½" by 4'-11¼", as shown in Figure 9, which also provides additional panel details including the panel key. All panels are precast concrete. No information regarding the panel surface was found in the design documents available.

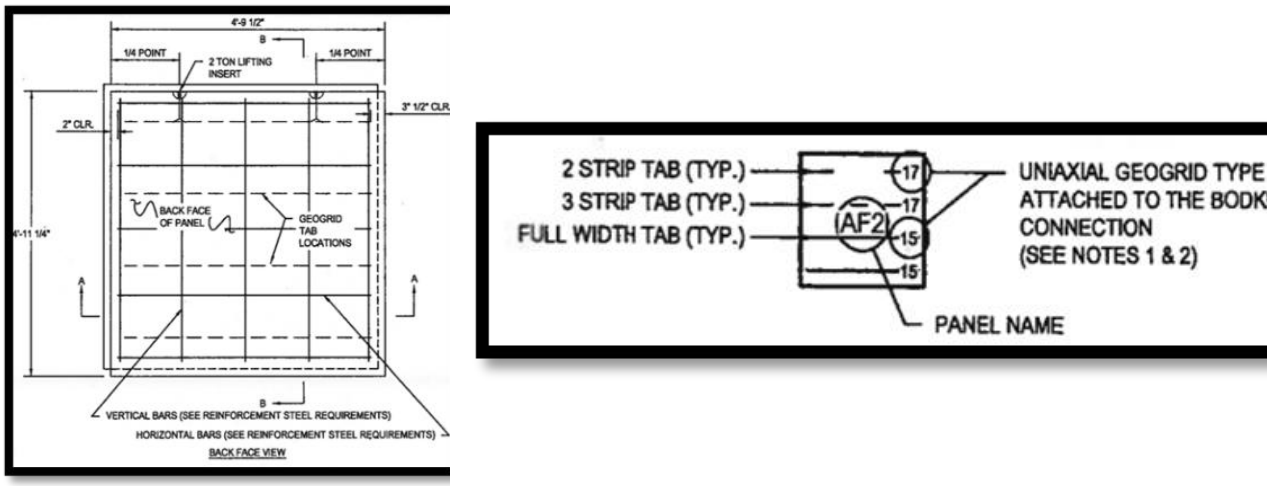

(a) (b)

Figure 9. Drawing. Panel information on Site B4-King George

Geotextile filter fabric is a nonwoven or woven fabric installed behind the facing panels of MSE walls. Its primary function is to allow water to drain from the retained soil while preventing the loss of fine backfill materials through panel joints. It is included in the MSE wall designs at the Crossgate, Sandersville, and King George sites. The layout of the panel geotextile for Crossgate and Sandersville is shown in Figure 10 (a), and the layout for the King George site is presented in Figure 10 (b).

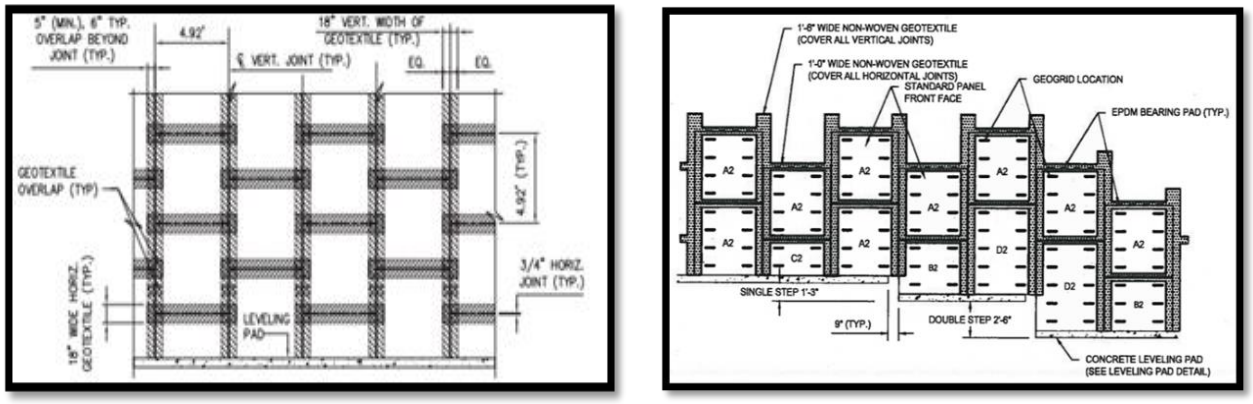

(a) (b)

Figure 10. Drawing. Geotextile filter fabric

Table 6 below summarizes the panel data to easily find information corresponding to each site. The retaining wall sites exhibit consistency in materials and wall thickness, as all four (Crossgate, Old River, Sandersville, and King George) are constructed with precast concrete panels and maintain a minimum thickness of 7 inches. Variations are observed in the standard panel dimensions: Crossgate and Sandersville utilize panels measuring 4′ $10\frac{1}{4}$″ by 4′ $10\frac{1}{4}$″, Old River adopts slightly larger 5′ by 5′ panels, while King George does not have a documented standard

panel size, suggesting either non-standard construction or missing records. Overall, the data indicates a uniform structural approach with minor differences in panel sizing across sites.

Table 6. Facing Panel Dimensions

Site No	B1	B2	B3	B4
Name	Crossgate	Old River	Sandersville	King George
Materials	Precast concrete	Precast Concrete	Precast Concrete	Precast Concrete
Standard Panel Size	4' 10 1/4" by 4' 10 1/4"	5' 0" by 5' 0"	4' 10 1/4" by 4' 10 1/4"	N/A
Wall Thickness	Min. 7"	7"	Min. 7"	7"

CHAPTER 4. INSPECTION AND MAINTENANCE PRACTICES BY STATE AGENCIES AND INDUSTRY

MSE walls have been widely used in the U.S. for decades because they are cost-effective, easy to build, and adaptable to different site conditions. They serve as retaining structures in many applications, with their most extensive use in transportation systems as bridge abutments, wing walls, and highway retaining structures. As these walls approach or exceed their design life, the need for clear inspection and maintenance practices becomes critical. However, most state agencies lack dedicated post-construction guidelines for MSE walls, often grouping them under broader categories like retaining walls or substructures. This leads to inconsistent monitoring and delayed maintenance.

Although states must report bridge data to the National Bridge Inventory (NBI), MSE walls are not included unless they are part of a bridge structure. This leaves many stand-alone walls unmonitored, resulting in lost condition and performance data.

To address this, the research team reviewed inspection practices across all U.S. transportation agencies to identify existing MSE wall guidelines. This chapter summarizes current practices, inspection methods, and frequencies, highlighting gaps and opportunities for standardization. Establishing consistent guidelines will help improve monitoring, ensure long-term wall performance, and support future national standards for managing these critical infrastructure assets.

STATUS OF MSE WALL INSPECTION GUIDELINES

A comprehensive review of state practices was conducted to evaluate how MSE walls are being assessed for post-construction inspection and maintenance. Most of the relevant documents are publicly available through state transportation agency websites. This review focused primarily on technical manuals published by the agencies, supplemented by research articles and project reports. To enhance the accuracy and reliability of the findings, the collected information was cross-checked across multiple sources; however, some data could not be fully verified due to limited or inconsistent documentation.

Based on this review, state agencies can be broadly categorized into three groups according to their approach to MSE wall inspection and maintenance, as illustrated in Figure 11. Unlike bridges, which are subject to mandatory inspections under the Federal Bridge Inspection Program that requires compliance by state governments, there is currently no federally mandated safety inspection program for mechanically stabilized earth (MSE) walls. As a result, many states do not provide post-construction inspection guidelines for MSE walls or even for conventional retaining walls.

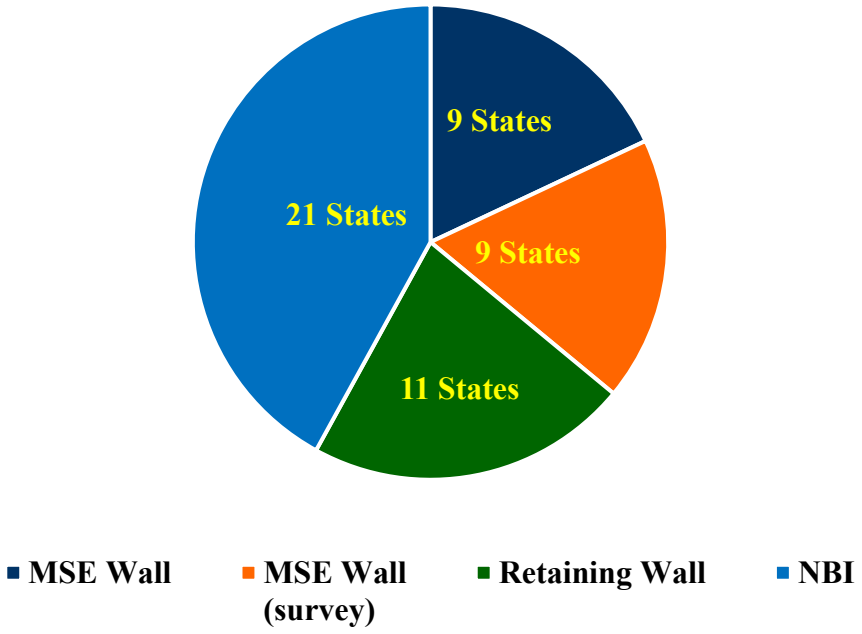

Figure 11. Chart. Adoption status of MSE wall inspection guidelines

The first group consists of nine states (Delaware, Idaho, Kentucky, Louisiana, Nebraska, Ohio, Pennsylvania, Utah, and Wisconsin) that have developed and implemented inspection guidelines or rating systems specifically for MSE walls. These documents typically include condition evaluation criteria, inspection frequencies, and documentation procedures. In these states, MSE walls are treated as distinct geotechnical assets requiring systematic monitoring and maintenance, reflecting a more advanced and proactive approach to geotechnical asset management. Some of these guidelines have been integrated into broader Geotechnical Asset Management (GAM) programs, while others appear to have been developed independently. Table 7 shows the Summary of post-construction inspection guidelines for MSE walls across different states.

Table 7. Summary of post-construction inspection guidelines for MSE walls

States	Source	Rating System	Inspection Frequency (year)
Delaware	Inspection Guidelines for Construction and Post-Construction of MSE Wall (Vankavelarr and Leshchinsky, 2002)	6 check items	N/A
	Bridge Element Inspection Manual (Delaware Department of Transportation -DelDOT, 2021)	11 items with four levels (Good, Fair, Poor and Severe)	N/A
Idaho	Development of an Inventory and Inspection Database Framework for Asset Management of MSE Walls (Sharma et al, 2019)	Recommended Procedures and 12 items	N/A
Kentucky	Evaluation of MSE Walls for Bridge Ends in Kentucky; What Next? (Sun and Graves, 2013)	A visual rating with four levels (Excellent, Good, Fair and Poor) or 10 levels (9 to 0 scale)	N/A
Louisiana	Geotechnical Asset Management Manual (Gavin et al., 2023)	12 items	0.5, 3, or 5
Nebraska	Inspector's Manual for MSE Walls (Jensen, 2009)	14 items (0-9 scales with different multiple levels per item)	N/A
Ohio	Asset Management for Retaining Walls (Athanasopoulos-Zekkos et al, 2020)	20 items with Y/N	N/A
Michigan	Michigan Earth Retaining System Element Inspection Manual (MDOT, 2019)	7 items with four levels (Good, Fair, Poor and Severe)	N/A
Pennsylvania	Bridge Safety Inspection Manual (PennDOT, 2024)	16 items	5
Utah	Development of MSE Wall Inspection Plan and Procedure for Failure Mode Analysis and Risk assessment (Maw, 2009)	67 items with Y/N	N/A
Wisconsin	Structure Inspection Manual (WisDOT, 2020)	4 levels (Good, Fair, Poor and Severe)	< 6

In addition, there are nine other states (Alaska, Colorado, New York, Oregon, Vermont, Maine, Illinois, Florida, and Texas) whose adoption status could not be confirmed through publicly available publications. However, according to a national survey conducted by Sharma et al. (2019), these states reported having MSE wall inspection programs in place. Although the extent of actual implementation in these states remains unclear, the existence of some form of inspection effort is supported by secondary sources. Notably, the Ohio and Utah Departments of Transportation have developed dedicated inspection forms specifically for MSE walls. Copies of these forms, along with Nebraska's condition rating system, are provided in Appendix D for reference.

The next group includes 11 states (Alabama, California, Indiana, Kansas, Maryland, Michigan, Minnesota, Missouri, Montana, North Carolina, and Tennessee) that have developed inventory systems or inspection guidelines for retaining walls. In most cases, these walls are managed under broader asset systems, with some states including subchapters on MSE walls and others grouping them with general retaining structures. MSE walls are often not distinguished in inspections, and general guidelines are applied to all wall types. While this provides basic oversight, the lack of MSE-specific provisions can lead to underreporting issues unique to these systems, such as reinforcement corrosion, connection failures, or panel displacement.

The final group includes 21 states with no publicly available documents addressing post-construction inspections for MSE or conventional retaining walls. Although no MSE-specific guidelines were found, all states must inspect and report on bridges to the NBI every two years, meaning MSE walls that form part of bridge abutments are still inspected under broader bridge protocols. The absence of published guidance does not necessarily indicate no inspection activity;

some states may provide checklists or recommendations during design or construction that indirectly support long-term monitoring.

NATIONAL BRIDGE INVENTORY (NBI)

The NBI is a mandatory program administered by the Federal Highway Administration (FHWA) under the NBIS. The NBI is a federally required database that collects and maintains information on the condition and characteristics of highway bridges across the United States. A summary of the program is provided below in Table 8.

Table 8. Summary of the NBI requirements

Category	Requirement
Responsible Entities	- State DOTs - Federal agencies - Tribal governments
Bridge Types	All public highway bridges > 20 feet in length carrying vehicular traffic
Inspection Frequency	- Every 24 months (standard) - Every 12 months (critical) - Up to 48 or 72 months (based on risk-based assessments)
Report Data	- Structural condition - Load ratings - Geometry - Traffic volumes - Element-level data (especially for NHS bridges)
Data Format	Specifications for the National Bridge Inventory (SNBI) (Full compliance with the SNBI is required by January 1, 2026)

Bridge condition is determined by the lowest rating of the NBI condition ratings for the key components - namely, the deck, superstructure, substructure, and culvert - using a numerical scale from 0 to 9. Bridge conditions are categorized as Good (≥7), Fair (5–6), or Poor (≤4). Although MSE walls are considered part of the substructure, there are no specific guidelines or requirements dedicated to MSE walls in the SNBI.

In addition to state-level practices, several federal and agency-sponsored publications offer useful guidance relevant to the inspection and maintenance of retaining structures, including MSE walls. Butler et al. (2016) developed a comprehensive inspection manual for general retaining walls, which outlines condition evaluation criteria, inspection procedures, and documentation methods as shown in Table 9. While the reference addresses retaining walls broadly, they include elements applicable to MSE systems. Notably, Nebraska stands out as one of the few states with MSE-specific post-construction inspection guidance, issued by the Nebraska Department of Roads in 2009. Table 10 shows evaluation criteria by Nebraska Department of Roads.

Table 9. Evaluation criteria by Butler et al. (2016)

Elements	Criteria	
Wall	1.	Wall or parts of it is visually out of plumb, tilting, or deflecting
	2.	Local bulges or distortion in the wall facing
	3.	Settlement of wall or visible wall elements
	4.	Joints between facing units (e.g., panels, bricks) are misaligned
	5.	Joints between facing units (e.g., panels, bricks) are too wide or too narrow
	6.	Joints between adjacent wall sections are misaligned
	7.	Cracks or spalls in concrete, brick, or stone masonry
	8.	Missing blocks, bricks, lagging, or other facing units
	9.	Timber lagging moderate to highly weathered (splitting or dry rot)
	10.	Staining (water, rust, or evidence of corrosion)
	11.	Root penetration of wall facing
	12.	Damage to the wall from vehicle impact
	13.	Displacement of wall top feature (e.g., coping, parapet, barrier rail)
	14.	Presence of graffiti (slight, moderate, heavy)
Backfill	15.	Settlement and/or tension cracks behind wall
	16.	Evidence of landslide or active earth movement
	17.	Settlement or heaving front of wall
	18.	Evidence of erosion or scour
	19.	Evidence of excessive moisture in backfill
	20.	Material from upslope rockfall or landslide adding to load on wall
Drainage	21.	Drainage outlets (pipes or weep holes) are clogged or not operating properly
	22.	Drainage channels along top of wall not operating properly
Comments	23	Any other observations or concerns not listed above (nearby construction, vegetation, irrigation, excessive runoff, etc.)
1 to 4 (best to worst) scale		

Table 10. Evaluation criteria by Nebraska Department of Roads

Criteria number	Criteria
1.	Wall tilting
2.	Cracking
3.	Facial deterioration
4.	Bowing of the wall
5.	Panel staining
6.	Exposure joints
7.	Loss of backfill
8.	Erosion, front of wall
9.	Erosion, back of wall
10.	Joint spacing
11.	Condition of V-ditch
12.	Coping deterioration
13.	Drainage runoff
14.	Drainage in front of wall
9 to 0 (best to worst) scale	

STATUS OF MSE WALL INSPECTION TECHNOLOGIES

Monitoring the performance of retaining walls is essential for ensuring their long-term structural stability and safety. Parameters such as lateral displacement, vertical settlement, crack development, and pore water pressure provide critical insights into a wall's behavior under load and varying environmental conditions. To accurately measure these parameters, a wide range of geotechnical and structural instruments have been developed and are used in both temporary and permanent monitoring systems. These instruments not only help detect early signs of distress but also support the evaluation of long-term performance and stability. Table 11. Common monitoring techniques for earth retaining structures summarizes commonly used monitoring techniques for earth retaining structures.

Table 11. Common monitoring techniques for earth retaining structures

Parameters	Instruments/Techniques
Condition assessment	Total station Ground based / UAS mounted Light Detection and Ranging (LiDAR) Ground based / UAS mounted photogrammetry Thermal scanning Down-hole cameras Crack Gauges Ground penetrating radar (GPR)
Water in the backfill	Piezometers Pressure transducers
Surface/Wall movement (vertical/horizontal)	Total station Ground based / UAS mounted Light Detection and Ranging (LiDAR) Ground based / UAS mounted photogrammetry Surface monitoring hubs Digital protractors Extensometers Tilt meters / Inclinometers / Slope indicators
Pressure at the back of facing elements	Earth pressure cells Strain gauges Load cells
Reinforcement strain/stress	Strain gauges Induction coil gauges Fiber optic sensors Extensometers
Temperature	Thermocouples Thermistors Fiber optic sensors Resistance temperature detectors
Corrosion of steel reinforcement	Half-cell potential Coupon testing Linear polarization resistance (LPR)

However, many of these technologies must be planned and installed during construction. For MSE walls, post-construction sensor installation can disrupt components and damage the structure, affecting stability and performance. As a result, monitoring surface movement remains the most practical and cost-effective way to assess long-term performance. Tracking displacements enables

early detection of conditions that may impact structural integrity, appearance, or serviceability. Wall face movement is often the clearest indicator of internal issues, especially when no embedded sensors are available.

Traditional ground-based surveys with total stations have long been used, but newer technologies like UAVs and LiDAR now offer improved mobility, safety, accuracy, and cost-effectiveness. LiDAR provides high-resolution 3D mapping for tracking displacement, deformation, and settlement, while UAVs allow safe, efficient inspections of large or hard-to-reach walls without disrupting traffic. Thermal imaging can detect surface and shallow subsurface anomalies through temperature variations, and ultrasonic testing can assess internal conditions like voids and material degradation without damage.

Together, these non-destructive, remote-sensing technologies enhance inspection efficiency, safety, and accuracy while reducing time and cost. They support earlier detection of distress and better maintenance planning. A review of state transportation agency documents showed that, similar to the lack of formal inspection guidelines, most states do not specify official inspection technologies for MSE walls. Many rely on bridge inspection protocols, though a few have begun exploring advanced methods such as LiDAR, photogrammetry, and UAVs. A summary of the findings for these states is provided in Table 12. States with non-contact technology recommendations for retaining walls.

Table 12. States with non-contact technology recommendations for retaining walls

States	Source	Recommendations	Notes
Colorado	Retaining Noise Wall Inspections and Asset Management Manual (CDOT, 2016)	• When the risk grade is below C or D, a special inspection is conducted, and LiDAR or Non-Destructive Testing may be used as needed.	
Idaho	Development of an Inventory and Inspection Database Framework for Asset Management of MSE Walls (Sharma et al, 2019)	• Thermal Imaging • Ultrasonic testing • UAVs with still pictures and videos • To add a measurement component to the UAV surveys, coordination and elevation control must be established along the wall.	Research Report ID RP 270
North Carolina	Retaining Wall Inventory and Assessment System (Rasdorf et al., 2015)	• For critical safety issues that may require additional field evaluation, a more detailed means of measurement may include LiDAR measurements taken at some point in time or at other regular intervals as determined by the NCDOT. • For noncritical ERSs, LiDAR measurements could be taken only when an ERS element is distorted, deflecting, or settling.	Research Report FHWA/NC/ 2014-10
Pennsylvania	Bridge Safety Inspection Manual (PennDOT, 2024)	• For In-depth inspections of retaining walls, a three-dimensional survey must be completed for mechanically stabilized earth walls ≥ 100 ft long and ≥ 20 feet in height. • A three-dimensional survey can be requested for MSE walls to meet these criteria at any time when movement of the wall is suspected regardless of the recommended inspection interval. • The Photogrammetry and Survey Section and Multiple Districts have LiDAR scanners with three-dimensional survey capability available for use in the Engineering Districts.	
Tennessee	Rating and Inventory of TDOT Retaining Walls (Wu et al., 2019)	• UAVs, digital cameras, infrared cameras, LiDAR and cell phone can be used to assist field data collection	Research Report RES 2019-08
Wisconsin	Structure Inspection Manual (WisDOT, 2024)	• For large MSE structures (more than 20 ft in exposed height) where movements are suspected, three dimensional (LiDAR) surveys may be requested at 10-year intervals to ascertain movement by the WisDOT survey crew.	

As indicated earlier, although several research studies have demonstrated the feasibility of using modern non-contact, automated technologies for infrastructure monitoring, most state agencies continue to rely heavily on traditional approaches. In practice, inspection guidelines across different

states still prioritize qualitative assessments, with a primary focus on visual inspections. These inspections are generally limited to identifying surface-level indicators such as bulging, cracks, water stains, and vegetation growth on the wall face. While such visual cues are important for recognizing potential distress in mechanically stabilized earth (MSE) walls, they remain subjective and may not capture subtle or early-stage structural issues that could lead to significant problems over time.

Only a small number of states have incorporated advanced non-destructive testing (NDT) technologies such as LiDAR, UAV-based photogrammetry, or other remote sensing methods into their inspection frameworks. Among these, just one state explicitly mandates the application of LiDAR for MSE wall evaluations under specific conditions outlined in its manual. Two additional states mention the use of these technologies but classify them as optional, leaving their application largely dependent on inspector preference or project needs. The remaining three states have completed promising research studies showcasing the effectiveness of such methods, yet they have not advanced to consistent implementation in practice. Taken together, these findings suggest that while emerging technologies are recognized for their potential, they are still generally treated as supplementary tools, reserved for special cases rather than integrated into routine inspection protocols.

CHAPTER 5. METHODOLOGY AND WORKFLOW

INTRODUCTION

This chapter describes the instruments and methodologies employed to investigate different potential inspection approaches to assess the geometric/structural condition and performance of retaining wall systems. They use a combination of advanced, non-contact, remote sensing technologies and field observations. First, a general description of the employed instruments; their characteristics and capabilities are presented. Then, the different utilized methods are described in general terms. Finally, the general workflows followed at each bridge are explained.

This work typically involves the integration of geospatial data collection from different instruments, such as total stations, laser scanners, and picture cameras, to capture accurate spatial and geometric information of the wall surfaces and surrounding features. Additionally, the use of a thermal camera has been investigated. Most of these technologies enable high-resolution, 3D-modeling for analyzing and monitoring displacement or deformations, without physical contact, ensuring both safety and efficiency. The collected data is then processed and analyzed to identify signs of structural distress, misalignment, or surface anomalies. This process ensures objective, repeatable, and quantifiable evaluation, supporting informed decision-making for maintenance, repair, or further investigation.

FIELD INSTRUMENTS – GENERAL DESCRIPTION

Eight different instruments were employed in this project. Their characteristics are presented in this section.

Robotic Total Station (RTS) – Leica's TCRP 1201+ R1000

This instrument is shown in Figure 12 -A. It is a laser-based device from Leica Geosystems, model TCRP 1201+ R1000. It accurately measures horizontal and vertical angles. According to its manufacturer, (Leica TPS1200+ Series Technical Data), its angular accuracy (standard deviation ISO 17123-3) is one second (0.3 mgon). Because of this, in surveyors' jargon it is commonly referred to as a "one-second gun." Additionally, it measures highly accurate distances, making it the most dependable tool in this study for determining the spatial locations of GCPs and CPs on the walls. When measuring distances in all considered sites in this project, including the CW, the RTS instrument was used in one of the following two modes:

- *Reflector mode*: The employed reflector was 360º prism, GRZ4. In this case, the accuracy (standard deviation ISO 17123-4) indicated by the manufacturer, (Leica TPS1200+ Series Technical Data), for standard distance measurements is σ_d = (1 mm + 1.5 ppm). Its reflector-based range, with the GRZ4 prism, is from 800 m (strong haze, visibility of 5 km (kilometer); or strong sunlight, severe heat shimmer), to 1,500 m (light haze, visibility of 20 km; or moderate sunlight, slight heat shimmer), up to 2,000 m (overcast, with no haze, visibility of 40 km; no heat shimmer). The reflector-based mode was used to measure the sides of the local closed traverses to establish accurate coordinates of the GCPs.

- *Reflectorless mode*: When measuring distances using the reflectorless mode, between 0 m and 500 m, the accuracy (standard deviation ISO 17123-4) indicated by its manufacturer (Leica TPS1200+ Series Technical Data), for standard distance measurements is $\sigma_d =$ (2 mm + 2.0 ppm). The reflectorless range depends on the reflectivity of the objects and on the atmospheric conditions. For example, when aiming at objects with 90% reflectivity, the reflectorless range in strong sunlight, severe heat shimmer, is 600 m. That range increases to 800 m if the object is in shade, or the sky is overcast. Additionally, that range reaches 1000 m for underground, night, and twilight measurements. Conversely, for objects with only 18% reflectivity, each of those three mentioned ranges reduces by approximately 50%. The reflectorless mode was employed to acquire the 3D coordinates of CPs marked on the wall surfaces, at ranges less than 40 m.

Due to its accuracy and long-range capabilities, this device was selected to serve as the benchmarking instrument in this study. Point positions acquired in the field with this device were compared against point coordinates extracted from the georeferenced 3D-virtual models generated via LiDAR and CRP.

Floor Noise Associated with the employed RTS device

In this study, the spatial geometry of MSE retaining walls was monitored using multiple CPs marked on the walls. Each CP was identified with a black-and-white circular target, 6 inches in diameter. Their spatial positions were measured during one or two distinct epochs, spaced one year apart, using Leica's high-precision TCRP 1201+R1000 RTS as the benchmarking instrument. Given the reliance

on this device for reference measurements, it was essential to estimate the magnitude of potential errors associated with its use.

To begin, a baseline floor noise—or minimum expected measurement uncertainty—was established using both manufacturer specifications and standard calculation procedures. Following ISO 17123-4 guidelines from Leica (2006), the theoretical 3D positional uncertainty was estimated using the RTS's angular accuracy of 1 arc second (≈ 4.848×10^{-6} radians) and its reflector-based distance accuracy of ±(1 mm + 1.5 ppm). Since all CPs were located at horizontal distances of approximately 40 meters (40,000 mm) or less, the uncertainty components were calculated as indicated below.

The 3D positional uncertainty (σ_p) was computed using expression 1:

$$\sigma_p = \sqrt{(\sigma_d)^2 + (d * \sigma_\theta)^2}, \qquad (1)$$

Where, σ_p is the total positional uncertainty, σ_d is the distance measurement uncertainty, σ_θ is the angular error in radians, and d is the distance to the target (40,000 mm).

For reflector-based measurements, σ_d = 1 mm + (1.5 ppm × 40,000 mm) = 1.06 mm,

and $d \cdot \sigma_\theta$ = 40,000 mm × 4.848×10^{-6} = 0.194 mm.

$$\sigma_p = \sqrt{(1.06)^2 + (0.194)^2} = 1.08 \text{ mm} \qquad (2)$$

The equation 2 yields a theoretical floor noise of ±1.08 mm under ideal conditions. For a 95% confidence level, the corresponding reflector-based floor noise is:

$$\text{Reflector-based Floor Noise} = z \cdot \sigma_p = 1.96 \times 1.08 = 2.12 \text{ mm}$$

For reflectorless measurements, the manufacturer specifies an accuracy of ±(2 mm + 2.0 ppm) for distances up to 500 m. At 40 m, σ_d = 2 mm + (2.0 ppm × 40,000 mm) = 2.08 mm, and $d \cdot \sigma_\theta$ = 0.194 mm (same as above).

$$\sigma_p = \sqrt{(2.08)^2 + (0.194)^2} = 2.84 \text{ mm} \quad (3)$$

Thus, the 95% confidence floor noise for reflectorless mode is:

$$\text{Reflectorless Floor Noise} = z \cdot \sigma_p = 1.96 \times 2.84 = 5.57 \text{ mm} \quad (4)$$

Since all CP positions in this study were measured in reflectorless mode, this theoretical value (~5.6 mm) represents the minimum expected measurement noise under ideal conditions at the 40 m observation range. However, real-world field conditions including atmospheric variability, imperfect instrument leveling or centering, aiming inaccuracies, and minor shifts or misalignments of CP targets can introduce additional uncertainty.

Therefore, while the values of 2.12 mm (reflector-based) and 5.57 mm (reflectorless) serve as theoretical lower bounds (when measuring at 40 m), a more conservative estimate of Practical

Noise was adopted in this study. This adjusted threshold accounts for real-world imperfections and was derived through supplementary analyses discussed later in the report.

A. Leica's TCRP 1201+ B. Leica's C10 C. Leica's P50

Figure 12. Photo. Measuring and scanning instruments used in this study

Terrestrial Laser Scanner 1 – Leica's ScanStation C10

This instrument is shown in Figure 12. Photo. Measuring and scanning instruments used in this study . Acquired by GSU in 2010, from Leica Geosystems, its maximum scanning rate is 50,000 points per second. According to Leica Geosystems (Leica 2011), the C10 device has a position accuracy of σ=6mm and a distance measurement accuracy of σ=4mm, both at 1-50 m range. Its maximum range is 300 m (at less accuracy). Its horizontal and vertical angular accuracies are 12 seconds. This instrument was employed to generate 3D point-cloud models of retaining walls in two of the four bridges considered in this study.

Terrestrial Laser Scanner 2 – Leica's ScanStation P50

This instrument is shown in Figure 12. Photo. Measuring and scanning instruments used in this study. It was acquired by GSU in summer 2024 from Leica Geosystems. Its maximum scanning rate is 100,000 points per second with a total range of more than 1000 m. This range is divided into smaller selectable segments. According to Leica Geosystems (Leica 2017), the P50 device has a position accuracy (ISO 17123-4) of σ = 1.2mm+10ppm, for ranges in the 120m/270m mode, and σ = 3mm+10ppm, for ranges in the 570m/>1,000 m mode. Its horizontal and vertical angular accuracy is 8 seconds. This instrument was employed to generate 3D point-cloud models of retaining walls in three of the four bridges considered in this study, plus in a CW.

Hand-held DSLR Camera 1 – Nikon's D5300

This instrument is shown in Figure 13. This is a respectable and relatively affordable Digital Single Lens Reflex (DSLR) camera from Nikon with good image quality, manual controls, and useful features. Table 13 lists its main specifications.

Table 13. Specifications of the Nikon D5300 handheld camera.

Features	Nikon D5300
Sensor Resolution (Type)	24.1 MP DX format CMOS sensor (no OLPF)
Autofocus System	39-point AF system (9 sensors cross-type)
ISO Sensitivity	100–12,800 (up to H1: 25,600 expanded)
Display Size/Resolution	3.2", 1.04M-dot vari-angle
Max Framerate (DX Mode)	5 fps
Movie Mode	1080p at 60/30 fps
Battery Life (CIPA)	600 shots
Dimensions	125 × 98 × 76 mm
Weight (no battery)	480 g (16.9 oz)

Figure 13. Photo. DSLR Camera, Nikon 5300

This camera was employed to take pictures, in hand-held mode, to generate photogrammetry models of three of the four bridges considered in this study.

Unmanned Aeiral Vehicle – DJI's Matrice 30

This instrument is shown in Figure 14. The DJI Matrice 30 (M30) is a high-performance enterprise drone designed for industrial inspections and mapping. It combines portability, weather resistance,

and integrated imaging systems suitable for photogrammetric applications. Table 14 lists its main specifications.

Table 14. Specifications of the DJI Matrice 30 (M30) Drone

Features	DJI Matrice 30 (M30)
Integrated Camera	48 MP 1/2" CMOS zoom camera + 12 MP wide camera
Zoom Capability	5x–16x optical, up to 200x digital
Thermal Sensor	640×512 @30 Hz (radiometric)
Laser Rangefinder	Range: 3–1200 m
Max Flight Time and Range	Up to 41 minutes and 15 km
IP Rating	Ingress Protection 55 (IP55) weather resistance (dust and water resistance)
Operating Temp. Range	-20°C to 50°C (-4°F to 122°F)
Transmission System	OcuSync 3 Enterprise (15 km max range)
Weight (with payload)	Approx. 3.7 kg(kilogram) (8.2 lbs(pound))
Dimensions (Folded)	365 × 215 × 195 mm

Figure 14. Photo. UAV (drone), DJI Matrice 30 (M30)

This drone was employed to capture aerial ortho and oblique images over retaining wall structures, supporting the generation of photogrammetric models, and aiding visual inspections in this study. For this project, the DJI RC Pro 2 Enterprise controller was used to operate the DJI Matrice 30

(M30) drone for aerial data collection. This high-performance controller features a 5.5-inch full High Definition (HD) touchscreen with 1000 units of brightness, providing clear visibility in outdoor conditions. It utilizes DJI's OcuSync 3 Enterprise transmission system, offering up to 15 km control range under Federal Communications Commission (FCC) regulations. The controller includes a 5000 mAh battery that supports up to 3 hours of continuous use and fast Universal Serial Bus (USB)-C charging. Additional features include support for Wi-Fi 6, Bluetooth 5.1, and multiple GNSS systems (Global Positioning System - GPS, Global Navigation Satellite System - GLONASS, Galileo, BeiDou), making it a reliable and efficient tool for UAV-based infrastructure inspection

Thermal Camera – Forward Looking Infrared (FLIR)'s T420bx

This instrument is shown in Figure 15. The FLIR T420bx is a professional-grade thermal imaging camera designed for building diagnostics, electrical inspections, and infrastructure condition monitoring. It offers high thermal sensitivity and flexible imaging features, making it suitable for noncontact inspection of retaining walls and structural elements. Table 15 lists its main specifications.

Table 15. Specifications of the FLIR T420bx Thermal Camera

Features	FLIR T420bx
Infrared Resolution	320 × 240 pixels
Thermal Sensitivity, Noise Equivalent Temperature Difference (NETD)	< 0.045°C (degree celcius) @30°C
Temperature Range	–20°C to 650°C (–4°F to 1202°F)
Accuracy	±2°C or ±2% of reading
Detector Type	Uncooled microbolometer
Display	3.5” Liquid Crystal Display (LCD) touchscreen with autorotation
Frame Rate	60 Hz (hertz)
Focus	Manual and automatic
Image Overlay (Multi-Spectral Dynamic Imaging (MSX)®)	Yes (visual + thermal fusion)
Battery Life	Up to 4 hours of continuous use
Weight	0.88 kg (1.94 lbs) with battery
Dimensions	106 × 201 × 125 mm

Figure 15. Photo. Thermal Camera, FLIR T420bx

This camera was used to collect thermal images of wall surfaces to detect temperature anomalies, potential moisture intrusions, and material inconsistencies, enhancing the non-destructive inspection approach employed in this project.

Auto Level – Topcon's AT-B2

This instrument is shown in Figure 16. The Topcon AT-B2 is a precision auto level commonly used in surveying and construction for establishing height references and conducting elevation checks. With superior optics and a rugged, water-resistant design, it offers reliable performance under demanding site conditions. Its rapid, self-leveling magnetic damping compensator enhances accuracy and stability, making it ideal for use in establishing control points and monitoring elevation changes at retaining wall sites. Table 16 lists its main specifications.

Table 16. Specifications of the Topcon AT-B2 Auto Level

Features	Topcon AT-B2
Magnification	32×
Accuracy (1 km double run)	±0.7 mm
Compensator Type	Magnetic damping
Compensator Range	±15 arc minutes
Field of View	1°20′ (2.3 m at 100 m)
Minimum Focus	0.3 m
Water Resistance	IPX6 (protected against powerful jets)
Operating Temperature	–20°C to +50°C
Weight	1.85 kg
Dimensions	215 × 130 × 140 mm

Figure 16. Photo. Auto Level, Topcon AT-B2

The Topcon AT-B2 auto level was employed in this project to establish and verify elevation benchmarks with high precision, ensuring reliable reference points for repeated surveys across the retaining wall sites. By providing accurate height measurements, the instrument supported the detection of subtle vertical displacements such as settlement, heaving, or tilting of wall panels, which are critical indicators of potential structural or geotechnical distress. Its integration into the ground control network not only enhanced the accuracy of deformation tracking but also provided a trusted survey-grade validation framework for advanced sensing methods like photogrammetry and LiDAR, thereby strengthening the overall monitoring and georeferencing process.

Emlid RS2+ GNSS

This instrument is shown in Figure 17. The Emlid Reach RS2+ is a multi-band GNSS receiver designed for high-precision surveying applications, offering centimeter-level accuracy in RTK and PPK workflows. It supports all major global navigation satellite systems (GNSS) and offers robust performance even in challenging environments. In this project, the RS2+ was used in combination with the DJI Matrice 30 (M30) drone and connected to the DJI RC Pro 2 Enterprise controller to enhance geolocation accuracy during aerial surveying and image acquisition. Its integrated LTE modem, Bluetooth, and Wi-Fi connectivity enables seamless base-rover operation and real-time data correction. With its rugged construction, long battery life, and compatibility with mobile applications, the RS2+ was ideal for establishing GCPs and Check Points to support accurate photogrammetric reconstruction. Table 17 lists its main specifications.

Table 17. Specifications of the Emlid Reach RS2+ GNSS Base

Features	Emlid Reach RS2+
GNSS Support	GPS, GLONASS, Galileo, BeiDou, Quasi-Zenith Satellite System (QZSS), Satellite-Based Augmentation System (SBAS)
Channels	184 channels
Positioning Accuracy (RTK)	Horizontal: ±7 mm; Vertical: ±14 mm
Update Rate	Up to 10 Hz (real-time output)
Correction Format	RTCM3 (RTK), RINEX (PPK)
Connectivity	LTE, Wi-Fi, Bluetooth, RS-232, LoRa radio
Internal Storage	16 GB
Battery Life	Up to 22 hours (on one charge)
IP Rating	IP67 (dustproof and waterproof)
Operating Temperature	–20°C to +65°C
Weight	~950 g

Figure 17. Photo. GNSS Receiver, Emlid Reach RS2+

The RS2+ was utilized in this project to accurately geolocate control and check points essential for aligning photogrammetric models and validating structural displacements on highway retaining walls.

Summary of Equipment and Software

This project employed a diverse suite of field instruments and software platforms to ensure accurate data collection, robust processing, and comprehensive analysis across all inspection sites. The Table 18 below provides a summary of all equipment and software utilized, including their specific versions, manufacturers, and official product information for reference.

Table 18. Summary of all equipment and software used in the project

Name of Equipment/Software	Version	Company	Official Product Link
Leica RTS (TCRP 1201+)	1201+	Leica Geosystems (Hexagon)	https://hts-3d.com/brochures/Leica-TS1201-Total-Station.pdf
Leica ScanStation P50	P50	Leica Geosystems (Hexagon)	https://leica-geosystems.com/products/laser-scanners/scanners/leica-scanstation-p50
DJI Matrice M30	M30	DJI (Da-Jiang Innovations)	https://www.dji.com/matrice-30
DJI Matrice M350	M350 RTK	DJI (Da-Jiang Innovations)	https://www.dji.com/matrice-350-rtk
Nikon D5300 DSLR Camera	D5300	Nikon Corporation	https://www.nikonusa.com/en/nikon-products/product/dslr-cameras/d5300.html
Agisoft Metashape	v2.1.0	Agisoft LLC	https://www.agisoft.com/
DroneDeploy	Cloud-based (2024)	DroneDeploy Inc.	https://www.dronedeploy.com/
Pix4D Mapper	v4.8.4	Pix4D SA	https://www.pix4d.com/product/pix4dmapper-photogrammetry-software
Leica Cyclone Core	v2023.1.0	Leica Geosystems (Hexagon)	https://leica-geosystems.com/en-us/products/laser-scanners/software/leica-cyclone/user-coordinate-system-and-control
CC	v2.13.2	CC (Open-Source Project)	https://www.cloudcompare.org/
Microsoft Excel	Office 365	Microsoft Corporation	https://www.microsoft.com/en-us/microsoft-365/excel
Topcon AT-B2 Auto Level	AT-B2	Topcon Corporation	https://global.topcon.com/products/auto-levels/at-b-series/
Emlid Reach RS2+ GNSS Receiver	RS2+	Emlid Ltd.	https://emlid.com/reachrs2plus/
DJI RC Pro 2 Controller	RC Pro 2	DJI (Da-Jiang Innovations)	https://www.dji.com/rc-pro

GENERAL METHODOLOGIES

Establishment of GCPs – Closed Traverse

At each studied location, the four bridge sites and the CW site, GCPs were established near the MSE retaining walls to support accurate spatial modeling. These GCPs were physically marked using steel or magnetic nails and were typically located along the shoulders of the lower-crossing roadway, adjacent to the walls. To determine their local coordinates with high precision, the GCPs were used as the vertices of a closed polygonal traverse that defined a site-specific reference system. The traverse was carefully designed to align with the walls under investigation, with half of the GCPs positioned near each wall (except at the CW site, where only one wall was present).

Before traverse data collection, an on-site visit was generally conducted to select optimal vertex locations. In cases where a site visit was not possible, traverse geometry was developed based on available site documentation or as-built plans. A minimum of three (3) GCPs is required for LiDAR georeferencing; however, four (4) or more are typically necessary for CRP platforms such as DroneDeploy. Some CRP workflows, especially those requiring high spatial fidelity, also benefit from the use of Elevated (EACPs) to further improve model accuracy. To account for redundancy and ensure robustness against point loss or occlusion, five to seven (5–7) GCPs were established at each site in this study. Larger or more complex sites may warrant the use of additional GCPs.

Traverse surveying was performed using a high-precision, one-second RTS, specifically Leica's TCRP 1201+ R100. This RTS instrument was used to measure both horizontal and vertical

distances between traverse vertices. Each leg (i.e., the distance between two adjacent vertices) was measured multiple times typically between three to five repetitions to reduce random error through averaging. Elevation differences among GCPs were calculated via trigonometric leveling at most sites; however, differential leveling was used at the B4–King George site. Angular measurements followed a rigorous process to ensure accuracy. At each vertex, both the internal and external angles were measured twice and averaged. These values were used to compute the Local *Angular Error of Closure* (LA_{EC}) using expression 5:

$$LA_{EC} = Internal\ Angle + External\ Angle - 360° \quad (5)$$

The LA_{EC} at each vertex was corrected by equally adjusting the angular discrepancy between the internal and external angle measurements. Once all internal angles were locally balanced, they were summed up to evaluate the Global Angular Error of Closure (GA_{EC}) with equation 6 for the entire n-sided traverse:

$$GA_{EC} = \left(\sum_{i=1}^{n} (Locally\ Balanced\ Internal\ Angle)_i\right) - [(n-2) \times 180°] \quad (6)$$

The GA_{EC} was then corrected by uniformly adjusting all internal angles across the traverse to restore geometric closure.

For linear balancing, the Bowditch Method, also known as the Compass Rule, was applied to the traverse. This method assumes that longitudinal errors in a traverse are proportional to the length of each leg. The total longitudinal error of closure was adjusted proportionally to refine the measured distances and directions, ensuring that the traverse loop closes precisely and that the final vertex

aligns with the starting point. The longitudinal precision of the traverse was quantified by the following expression 7:

$$Longitudinal\ Precision = \frac{1}{\left({}^{L_{EC}}/_{P}\right)} \qquad (7)$$

where L_{EC} is the Longitudinal Error of Closure and P is the total perimeter of the traverse.
A precision ratio of 1:20,000 was established as the minimum acceptable standard for this study, while 1:30,000 to 1:40,000, or even better, were preferred for high-precision applications. The following three cases illustrate typical values associated with these precision levels:

For 1/20,000, a max error of 0.01 ft (3.05 mm) corresponds to a length of 200 ft (60.96 m).
For 1/30,000, a max error of 0.01 ft (3.05 mm) corresponds to a length of 300 ft (91.44 m).
For 1/40,000, a max error of 0.01 ft (3.05 mm) corresponds to a length of 400 ft (121.92 m).

For example, a traverse leg of 40 meters measured with 1:20,000 precision would correspond to a relative positional error of no more than 2.0 mm, which is smaller than the floor noise of the RTS instrument employed in this study. According to Leica's technical specifications, its TCRP 1201+ R100 yields positional noise levels (at 40 meters, with 95% confidence) of 2.1 mm using a reflector, and 5.6 mm in reflectorless mode. While these values represent theoretical limits, actual measurement errors are typically higher due to contributing factors such as instrument and prism centering, prism aiming/targeting, atmospheric conditions, and setup stability, among others. Nevertheless, achieving a traverse precision of 1:30,000 or 1:40,000 corresponds to errors of

1.3 mm and 1.0 mm, respectively, at 40 m. Both of which fall well below the RTS floor noise. As such, these high-precision traverses ensure that the GCP framework does not impose any significant limitations on the accuracy of LiDAR or CRP models.

Determination of Coordinates at CPs

Several CPs were established at each worksite to serve two primary purposes:

- to detect potential future displacements of the walls, and
- to assess the spatial accuracy of the resulting point clouds by comparing model-derived coordinates against field measurements taken with a high-precision, one-second RTS instrument.

At each bridge site, a total of 12 CPs were painted on the two MSE walls six per wall except for the B4–King George site, where 16 CPs were established (eight per wall). At the CW site, six CPs were marked. All CPs were painted as 6-inch-diameter circles, divided into alternating black-and-white quadrants, to ensure high visibility and precise targeting. The CPs on each wall were arranged in vertical pairs, with one pair member marked near the bottom of the wall and its corresponding pair member marked higher up. When three vertical pairs were used, they were typically distributed as follows: one near each wing of the wall and one at the central region. At the B4–King George site, four vertical pairs were used per wall two placed centrally and one near each wing to provide more detailed coverage.

The local spatial coordinates of each CP were measured in the field using the RTS instrument. For that purpose, the RTS device was positioned on a nearby GCP and used another GCP as a

backsight. Since the GCP coordinates were defined in a local site-specific reference frame, the resulting CP coordinates were also expressed within the same system. Correspondingly, the 3D coordinates of the same CPs were later extracted from the geo-referenced point cloud models, which were aligned to the same local coordinate system. This shared reference frame enabled direct and accurate comparison between model-derived coordinates and RTS-acquired measurements, supporting both accuracy assessment and displacement detection.

Laser Scanning

At each site, this task involved the use of terrestrial laser scanning to collect spatial data for generating full virtual 3D point cloud models of the considered wall(s). At all locations, the MSE walls were scanned at least once; in some cases, a second scan was performed later to produce two temporally distinct models, referred to as Epoch 1 and Epoch 2. For these scanning operations, either the older Leica C10 scanner or the newer Leica P50 scanner was employed, depending on availability. Appendix C1 presents a protocol to operate the P50 scanner. White spherical targets, either 6-inch or 9-inch in diameter, were used during scanning. These spheres were mounted on top of vertical poles, which were placed and carefully verticalized on top of each GCP. The height of each pole was measured precisely, as it was necessary to determine the true location of the GCPs. The scanner recorded the center of each spherical target; by subtracting the height of the pole, the actual GCP location can be identified within the resulting point cloud.

Prior to conducting the full scan at each station, these spherical targets were captured individually at high resolution. This step served two purposes: (i) enabling the option to register individual scans

using the TB registration method, and (ii) allowing the geo-referencing of the final 3D point cloud model within a common coordinate system.

The number of STs varied by site: 4 at the CW, 6 at both B1-Crossgate and B2-Old River, 8 at B3-Sandersville, and 16 at B4-King George. The number of scans depended on the size of the walls to be covered. The selection of scanning locations was flexible and did not require permanent markers such as nails. Typically, 3 to 8 stations were positioned near each wall, at approximately 4 to 6 meters, to ensure the wall surfaces were captured with high point density. At each scanning station, the scanner was first properly verticalized. Scanning parameters were then selected, and all visible spherical targets were acquired at high resolution. Following this, a complete scan was performed at medium resolution, covering a full horizontal field of view (360°) and a vertical range of approximately 270°, excluding only the cone-shaped area directly beneath the scanner containing the tripod.

All scans were conducted at medium resolution to manage scan duration effectively, as high-resolution scanning significantly increases data acquisition time. When using the Leica C10, medium resolution provided a point spacing of approximately 10 mm at a distance of 10 meters from the scanner. In contrast, the Leica P50 was configured to achieve a point spacing of approximately 6.3 mm at the same distance, resulting in denser and more detailed point clouds.

Post-Processing of LiDAR Data

Postprocessing of LiDAR data was performed by using Leica's Cyclone Core software. It involved several key steps to convert raw scan data into georeferenced, analyzable, and comparable 3D point clouds. The typical workflow includes:

1. Importing Scan Data: Raw data from the Leica C10 or P50 scanner was downloaded from the scanner and imported into Cyclone Core. Each scan represented a separate "ScanWorld" containing spatial point coordinates, color coordinates, and reflectivity (light intensity) information.

2. Target Identification: Spherical (or alternatively planar) targets captured during field scanning were identified within each scan. Cyclone detected those previously acquired targets, and they were automatically positioned at their respective locations, within the captured point cloud. These targets were used for both TB registration and georeferencing purposes.

3. Registration (stitching) of Scans: Multiple STs were aligned using either:
    - *Target-Based (TB) Registration*: This swift process automatically aligns scans by matching identified targets (e.g., spheres placed on GCPs). To enable accurate registration, the TB LiDAR approach requires each scan to capture at least three common spherical targets that are also visible in an adjacent scan. In exceptional cases, when both scans are precisely verticalized, this minimum may be reduced to two targets, though this is not generally recommended. For optimal accuracy,

all target acquisitions should ideally be performed in the field at high resolution, which ensures precise target localization but increases both field time and workload. As an alternative, targets may be scanned at standard resolution along with other objects in the scene and later identified during postprocessing using software tools. A protocol to acquire targets via the Cyclone Core software is presented in Appendix C6. While this alternative approach significantly reduces time spent in the field, it may lead to slightly lower positional accuracy for the targets and requires additional time in the lab for target extraction. Despite this trade-off, the TB LiDAR method remains efficient during scan registration, as the software automates much of the alignment process with minimal user input. A protocol for TB registration, independently of whether they were acquired in the field or via software, is in Appendix C4.

- *Visual-Based Registration*: This alternative registration approach manually aligns two scans at a time. Leica's has now improved the original visual registration by substantially facilitating user's alignment of overlapping scans. This new approach is called Visual Alignment (VA) and could be highly accurate when involving well-overlapped scans. A protocol for Visual-Alignment registration is in Appendix C3. In contrast, the VA LiDAR technique does not rely on physical targets for scan registration. Instead, it requires substantial overlap between adjacent scans and depends on geometric features for alignment. The registration process begins with the manual alignment of two well-overlapped scans. Leica's Cyclone software assists the user by offering both plan view (horizontal) and

elevation view (vertical) windows for precise alignment. After an initial alignment is performed manually, the software refines the result by maximizing the number of spatially coincidence points and minimizing residual gaps between near-matching features. Once the first two scans are aligned, a third scan, with sufficient overlap, is added to the registered set. This iterative process continues until all scans are stitched together into a full point cloud. Since it does not need targets for registration (stitching) purposes, it presents reduced time in the field but still requires a minimum of 3 targets for georeferencing purposes. While the VA method is generally considered less accurate than the TB approach, it can yield comparable results when scans are well planned, strongly overlapped, and registered in a logical sequence, following a successive close-neighboring registration pattern of highly overlapped scans, preferably forming a closed loop. In smaller or more controlled environments, VA registration has, in some cases, produced results that are slightly more accurate than those obtained through TB registration, likely due to improved scan coverage, high overlap, and point cloud consistency.

In this investigation, both registration methods TB and VA were applied and evaluated. Their relative accuracies were compared against measurements obtained in the field with the benchmarking RTS instrument. Additionally, the study also assessed the effectiveness of each method in detecting small wall displacements ranging from 3 mm to 30 mm, providing insight into their suitability for structural monitoring applications.

4. Noise Filtering and Cleanup: Unwanted artifacts such as stray points, scanner reflections (including solar beams), vehicle and/or pedestrian traffic, or vegetation can be manually or semi-automatically filtered to improve model clarity. Leica's Cyclone Core software provides several tools and workflows for noise removal and data cleaning in LiDAR point clouds. These tools help improve model clarity and accuracy by eliminating unwanted or irrelevant points. Additionally, Cyclone Core allows users to clean individual ScanWorlds before registering them, minimizing the propagation of noise during scan alignment and georeferencing. Appendix C2 presents protocols for noise removal via Cyclone Core.

5. Georeferencing: This process transforms the coordinate system of a registered scan dataset (originally in a scanner-centric coordinate system) into a real-world coordinate system, typically a local, site-specific, coordinate frame defined by GCPs. This procedure is based on knowing the coordinates of three GCPs at least. Because of those known coordinates, in 3D computer vision techniques, this procedure is usually referred to as “Known Point Registration.” It aligns the scan data to physical GCP coordinates through matched spherical targets. If GCPs were measured using total-station or GNSS devices, their known coordinates can be input to transform the registered point cloud into a local or global coordinate system. In this project, no GNSS data was employed. All GCP coordinates were accurately determined via a properly balanced local traverse at each site. Once applied, this transformation situates the 3D point cloud into the desired reference frame, enabling model comparisons at different times and even cross-technology comparisons. This assists in deformation monitoring, and high-precision engineering analysis, in general. Appendix C5 presents a protocol for georeferencing via Cyclone Core.

6. Merging and Exporting: The registered and cleaned scans may be unified into a single point cloud. It is common that full models need to be exported in standard formats (e.g., .e57, .pts, .las) for further analysis or modeling in other software platforms like CC or AutoCAD.

This process ensures the creation of accurate, high-resolution 3D models suitable for structural monitoring, deformation analysis, and documentation.

Extraction of CP Coordinates from LiDAR Models

After the LiDAR data has been fully registered and georeferenced within the local coordinate system defined by the GCPs, the next critical step is the extraction of checkpoint (CP) coordinates from the resulting 3D point cloud. This process is essential for evaluating the geometric accuracy of the model and for comparing model-derived coordinates to those measured independently by instruments such as an RTS.

The procedure generally involves the following steps:

1. Visualization and Navigation:

   The georeferenced point cloud is opened in Leica's Cyclone Core or compatible software (e.g., CC or Autodesk ReCap). The user navigates each painted checkpoint on the MSE or MB wall. These CPs were painted in the field as distinct circular targets (typically 6 inches in diameter, divided into black and white quadrants), which appear clearly in the point cloud due to their geometric and radiometric contrast.

2. Cross-Sectioning or Slicing (Optional):

   To increase precision, a thin cross-sectional slice (e.g., 1–2 cm thick) is created through the plane of the checkpoint using slicing or clipping tools. This reduces background clutter and isolates only the point data that intersects the CP marker.

3. Point Selection:

   Points corresponding to the CP are manually or semi-automatically selected. In high-resolution scans, the circular boundary of the target is often distinguishable, allowing for the identification of a symmetrical point cluster.

4. Center Coordinate Estimation:

   The most common method for determining the center of the CP is to apply a best-fit geometric function, such as a circle or ellipse fitting algorithm, to the selected points. The software calculates the center of the fitted shape and reports its 3D coordinates (X, Y, Z) in the same local coordinate system as the GCPs and RTS measurements. Alternatively, the centroid of the selected point cluster can be used if the target geometry is incomplete or partially occluded.

5. An alternative and practical method for extracting the CP coordinates is by selecting the point or set of points nearest to the perceived center of the circular target.

   This process typically is characterized by:

   - Navigating to the Checkpoint:

     The user locates the circular CP on the wall within the point cloud visualization.

     Depending on scan density and surface texture, the CP target should appear as a dense cluster of points, usually forming a round or oval shape.

- Estimating the Visual Center:

  The user visually estimates the center of the CP by rotating the 3D view and using orthographic projections (top view, front view) to identify the geometric middle of the visible target area.

- Point Proximity Selection:

  Using point selection tools, the analyst selects one or a few points located closest to the estimated center of the CP. In high-resolution scans, this can be a single point clearly at the visual center. In medium-resolution scans, it may involve averaging the coordinates of 3–5 nearby points to mitigate noise and increase accuracy.

- Human judgment in estimating the target's center may lead to a systematic bias, especially if the target is not perfectly orthogonal to the scanner or is partially occluded. Even a 1–2 cm misjudgment of the center can introduce spatial errors in the final coordinate, depending on scan resolution and point spacing.

6. Coordinate Logging:

   The extracted coordinates are recorded, typically exported to a spreadsheet or Comma-Separated Values (CSV) file for further comparison. This dataset is then used to compute residuals between point cloud-derived coordinates and those obtained via RTS measurements, enabling the quantification of absolute spatial accuracy.

7. Quality Control:

   Visual inspection and statistical analysis may be performed to ensure that the extracted positions are repeatable and not biased by shadowing, scan angle, or surface irregularities. If necessary, outlier points are removed, and the process is repeated.

In this study, all CPs were extracted using the proximity method which carried some errors. They were compared against RTS-acquired data to assess relative discrepancies. By using high-density LiDAR scans and precise geometric extraction methods, this process can yield positional accuracy on the order of millimeters, provided that the scan resolution, registration, and georeferencing steps were performed with care. This approach is instrumental in validating the reliability of 3D models for SHM and displacement detection.

Acquisition of Images for CRP

Images from UAV

To ensure accurate 3D reconstruction of MSE or MB retaining walls using CRP, images captured via an UAV must be acquired under carefully controlled flight conditions and imaging parameters. UAV photogrammetry introduces specific constraints and advantages compared to hand-held acquisition, most notably aerial perspective, consistent platform motion, and automated flight planning. However, achieving survey-grade model quality still requires attention to detail in flight design, camera orientation, overlap, resolution, and lighting conditions. Prior to data collection, the UAV platform should be properly configured to operate with stabilized camera settings. Most UAVs used for CRP include high-resolution RGB sensors with fixed lenses and gimbals. If camera settings are adjustable, they should be locked to manual exposure mode to ensure consistent lighting across all images. Typical configurations include a low ISO (100–200) to minimize noise, moderate aperture (if available), and a shutter speed fast enough to eliminate motion blur caused by UAV vibration or wind gusts. The focus should be set to manual or infinity, depending on the lens

type, and white balance should be fixed (e.g., daylight) to ensure color uniformity throughout the image set.

Flight planning is a critical aspect of UAV-based image acquisition. Unlike conventional aerial mapping missions that focus on nadir (downward-looking) images, the photogrammetric inspection of retaining walls requires oblique and vertical perspectives of near-vertical surfaces. Accordingly, the flight path should be designed to maintain a consistent distance typically 4 to 8 meters from the wall's surface, with the camera oriented to face the wall at approximately 90 degrees (perpendicular). This allows the wall surface to be captured in maximum detail, with minimal distortion. Depending on wall height, multiple vertical tiers may be necessary to fully cover the structure from top to bottom. High image overlaps are essential. Along-track (forward) overlap should exceed 80%, and side overlap should be maintained at 60–70%. This ensures sufficient parallax between frames to support dense point cloud generation. Overlapping images must share identifiable features such as wall textures, joints, or control targets visible across multiple frames to allow for robust tie point matching in photogrammetric processing. If the wall includes structural transitions (e.g., step-backs, embedded elements, guardrails), the flight plan should include extra passes from alternative angles to resolve complex geometry.

Lighting conditions play a significant role in UAV-based image acquisition. Ideal flights are conducted under overcast skies or during periods of soft lighting (early morning or late afternoon), which help reduce shadows and glare. Harsh sunlight can create unwanted reflections or deep shadows, especially on concrete or modular block surfaces, which may impede feature matching.

UAV flights should also avoid windy conditions that can destabilize the platform and introduce image misalignment or blur.

The use of GCPs is especially important for scaling and georeferencing UAV-derived models. GCPs should be placed along the base and near the top of the wall and must be clearly visible in the aerial images. These can include high-contrast circular or checkerboard markers, with their 3D coordinates measured using a total station or RTK GNSS. For best results, the GCPs should be evenly distributed across the wall surface and captured in multiple overlapping images. When the walls are tall, additional markers may be installed at mid-height or on nearby elevated surfaces to assist in vertical alignment. In cases where RTK or PPK UAV systems are used, image geotags will be associated with centimeter-level accuracy. However, even with RTK-enabled drones, GCPs remain critical for verifying absolute accuracy and resolving potential errors introduced by Inertial Measurement Unit (IMU) drift or GNSS signal degradation.

Throughout the mission, the UAV operator must monitor flight stability, image quality, and overlap coverage in real-time, if the interface allows. After the mission, all images should be reviewed for sharpness, consistent exposure, and completeness. Any gaps or compromised images (due to blur, occlusions, or exposure issues) should be identified, and additional flights may be conducted to supplement the dataset. By adhering to these principles, maintaining appropriate flight geometry, overlap, lighting, and control point integration, UAV-based image acquisition can produce highly accurate, detailed 3D photogrammetric models suitable for structural monitoring, surface deformation analysis, and integration with LiDAR, RTS, or Computer-Aided Design (CAD)-based reference systems.

Images from Hand-Held Camera

To ensure high-quality 3D reconstructions from CRP, image acquisition must be carefully planned and executed. When using a DSLR camera like the Nikon D5300, it is essential to configure the camera with full manual control. Consistency across all images is critical for successful photogrammetric processing. The camera settings should include a medium aperture (typically between f/8 and f/11) to achieve sharpness and sufficient depth of field. ISO should be kept low preferably between 100 and 400—to minimize noise, and shutter speed should be adjusted to prevent motion blur, depending on ambient lighting conditions. Manual focus should be used and fixed throughout the image set, with the focus point set based on the estimated average distance to the wall. White balance should also be set manually (e.g., to "Daylight") to ensure color consistency across all photos.

The camera lens should remain fixed in focal length during the entire capture session. Using a prime lens is preferred due to its reduced distortion and sharper optics; however, if a zoom lens is used, it must remain locked at a single focal length to maintain internal calibration integrity. It's also advisable to disable any in-camera lens corrections, allowing the photogrammetry software to perform properly calibration and correction during processing. Image capture should be carried out by walking slowly and steadily along the length of the wall, maintaining a consistent distance typically between 3 and 6 meters from the surface. Images must have substantial overlaps to allow for accurate feature matching. Generally, at least 70% forward overlap and 50% side overlap is recommended. This can be achieved by photographing horizontal passes, where each subsequent image covers most of the previous image's content. For taller structures, the photographer should

work in vertical tiers or multiple rows to fully capture the height with sufficient vertical overlap between rows.

Photographs should be taken not only from front-facing (normal) angles, but also from oblique and slightly angular viewpoints (15°–45°) to introduce parallax—essential for generating accurate depth information in 3D models. This strategy is particularly important when capturing textured or uneven wall surfaces, cracks, tilts, or damage patterns. The field of view should comprehensively cover both general features and critical details such as joints, seams, and structural defects.

Environmental conditions must be considered. Ideal lighting is soft and diffused, such as during overcast weather or in shaded conditions. This reduces harsh shadows and contrast that can interfere with feature detection. Direct sunlight should be avoided, as it can create glare or sharp shadows that hinder reconstruction. Care should also be taken to avoid capturing moving objects, such as vehicles, pedestrians, or vegetation swaying in the wind, which can introduce ghosting artifacts or reduce processing accuracy. For improved model scale and positional accuracy, GCPs should be established in the scene. These should be clearly visible, high-contrast markers (such as checkerboards or circular targets) placed on or near the structure, with their 3D coordinates independently measured using a total station or GNSS. When georeferencing is planned, GCPs must be placed such that they cover the area evenly in three dimensions and are visible in multiple overlapping images.

Throughout the image acquisition process, it is important to monitor image quality in real-time. All captured photos should be reviewed for sharpness, exposure balance, and focus consistency. Any

blurry or poorly lit images should be immediately reshot while on-site. Additionally, field notes documenting image sequences, camera settings, and any anomalies or unique features at the site will facilitate organized processing later. By following these principles, handheld DSLR photogrammetry can yield high-quality, geometrically accurate 3D models of retaining walls, suitable for structural assessment, displacement monitoring, and integration with other spatial datasets such as LiDAR and RTS measurements.

Post-Processing of Photogrammetric Data

Photogrammetric postprocessing platforms Agisoft Metashape, DroneDeploy, and Pix4Dmapper share the core objective of reconstructing accurate 3D models from overlapping imagery. All three platforms rely on similar underlying photogrammetric principles: camera alignment through feature matching, multi-view stereo reconstruction for dense point clouds, and optional georeferencing via GCPs or image geotags. However, they differ considerably in terms of workflow design, user control, automation, and suitability for specific applications such as vertical structures and engineering-grade analysis.

Agisoft Metashape is a desktop-based, professional-grade software known for its flexibility and control over all processing steps. It is well suited for detailed structural modeling, especially when data is collected with non-standard configurations, such as handheld cameras or UAVs capturing steep, vertical surfaces. Users are able to customize nearly every aspect of the workflow from sparse cloud generation to mesh optimization and orthophoto projection. Importantly, Metashape allows the use of custom coordinate systems and custom projection planes, making it ideal for

modeling vertical structures like retaining walls. It also supports precise GCP integration with residual tracking and robust error reporting. However, this flexibility comes with a steeper learning curve and longer processing times, especially at high-quality settings. A full protocol for processing photos in Metashape is presented in Appendix C7.

DroneDeploy, by contrast, is a cloud-based platform emphasizing automation, speed, and ease of use. Its interface is streamlined for UAV-based workflows, automatically generating dense point clouds, orthomosaics, and elevation models shortly after image upload. This makes it particularly effective for large-scale horizontal surveys, but less ideal for capturing and processing near vertical structures. While DroneDeploy supports GCPs, manual marking is simplified, and the platform does not allow for detailed adjustments of projection planes or internal processing parameters. Consequently, while fast and user-friendly, DroneDeploy sacrifices some degree of control and precision in favor of scalability and simplicity. It is highly effective when UAVs equipped with RTK/PPK are used and when time efficiency is critical. The full DroneDeploy image processing and coordinate transformation workflow is documented in Appendix C10. Pix4Dmapper lies somewhere between the two. It is a desktop application like Metashape but emphasizes semi-automated workflows with structured processing stages. Users are guided through the photogrammetric pipeline (initial alignment, GCP calibration, dense cloud generation, mesh/ Digital Surface Model (DSM)/orthophoto creation) while still being able to intervene or customize each step. Pix4D offers strong GCP handling and excellent tools for reprojection error analysis, making it a trusted tool in civil engineering and surveying. A detailed guideline outlining the processing procedures in Pix4D Mapper is available in Appendix C9. Like Metashape, it allows the definition of custom orthoplanes, which is essential when generating orthophotos of vertical

surfaces such as MSE or MB walls. Processing is generally faster than Metashape but less automated than DroneDeploy. It strikes a good balance between control, usability, and accuracy.
In terms of outputs, all three platforms can produce:

- Dense point clouds (.las, .xyz)
- Orthophotos (.tif)
- Digital surface/elevation models
- 3D meshes (.obj)
- Measurement and accuracy reports

But only Metashape and Pix4Dmapper offer full control over projection planes, multi-epoch analysis, and advanced filtering or editing of the point cloud. DroneDeploy, while limited in this regard, excels at rapid turnaround and integrates easily with cloud-based workflows, including asset tagging, annotation, and project sharing.
In summary:

- Metashape offers maximum customization and precision, ideal for research-grade modeling of complex structures.
- DroneDeploy is optimized for ease and speed, best suited for wide-area UAV inspections with minimal postprocessing effort.
- Pix4Dmapper balances automation with control, making it a strong candidate for professional infrastructure surveys requiring both efficiency and accuracy.

Each has a place depending on the needs of the project—whether it's time-sensitive aerial surveying, detailed deformation monitoring, or repeatable structural analysis.

Comparison of Results

Comparison of results – Discrepancies in Positions

When evaluating wall displacements, modeling techniques, and measurement precision, position comparisons play a vital role for several interrelated reasons. First, they enable the quantification of actual displacements over time by identifying spatial changes at CPs or across wall surfaces between different epochs—essential for validating the occurrence and extent of physical movement. Second, modeled positions can be compared with benchmark measurements (e.g., RTS data) to directly assess the performance and inherent noise of each technique. The magnitude of resulting discrepancies serves as a diagnostic metric for evaluating accuracy and reliability. Those position discrepancies (PDs) have been determined as explained in the following paragraphs.

The position of a given CP, say point *P*, is defined by its three spatial coordinates (x_p, y_p, z_p). They represent a position vector $\overrightarrow{V_p}$, from the origin of the adopted local system of reference (*0*, *0*, *0*) to that point (x_p, y_p, z_p). That adopted system is the same used by the local, closed traverse and its vertices, the GCPs. The magnitude of the position vector $\overrightarrow{V_p}$ represents the distance from the origin to that point. It is Pythagorically calculated as follows in equation 8:

$$\left|\overrightarrow{V_p}\right| = \sqrt{(x_p - 0)^2 + (y_p - 0)^2 + (z_p - 0)^2} = \sqrt{{x_p}^2 + {y_p}^2 + {z_p}^2} \qquad (8)$$

First, the coordinates/positions of each CP were obtained in the field using the benchmarking RTS instrument. For example, for a given CP, let's call its RTS-based position vector as $\overrightarrow{V_{RTS}}$, defined by coordinates $(x_{RTS}, y_{RTS}, z_{RTS})$. Additionally, the coordinates of the same CP were extracted from one of the generated models, which was georeferenced in the same adopted local system of reference. This second set of coordinates, for the same point, define a slightly different position vector, $\overrightarrow{V_{Mod}}$, with coordinates $(x_{Mod}, y_{Mod}, z_{Mod})$. In general, the model-extracted coordinates do not coincide with the ones measured in the field. This is because diverse postprocessing tasks are involved in the generation, georeferencing, and coordinate extraction in the different modeling techniques. The difference between these two position vectors, for the same point, is vector: $\overrightarrow{V_{Dif}} = \overrightarrow{V_{Mod}} - \overrightarrow{V_{RTS}}$. In this study, we define the position discrepancy (PD) as the magnitude of that difference vector with equation 9:

$$\text{Position Discrepancy} = \left|\overrightarrow{V_{Dif}}\right| = \sqrt{(x_{Mod} - x_{RTS})^2 + (y_{Mod} - y_{RTS})^2 + (z_{Mod} - z_{RTS})^2} \qquad (9)$$

Since these PDs are magnitudes of vectors, they are always positive values.

Additionally, position discrepancies were evaluated between comparable point clouds, each aligned to the same coordinate reference system, but produced using different modeling techniques.

Comparison of results – Discrepancies in Distances

When evaluating wall displacements, modeling accuracy, and measurement precision, analyzing Distance Discrepancies (DDs) between CPs is essential for identifying spatial inconsistencies and quantifying modeling noise. Unlike position-based comparisons, which focus on individual point deviations, distance-based analyses examine how inter-CP separations change across epochs or relative to benchmark measurements or across different modeling techniques. By comparing inter-CP distances derived from each model against those measured in the field using the RTS instrument, it is possible to assess the fidelity of spatial relationships within each model. The resulting discrepancies serve as a diagnostic indicator of geometric distortion, offering a complementary perspective on model quality and error distribution. This approach is particularly useful when physical displacements affect relative CP spacing, or when scan registration and surface modeling may introduce stretch, compression, or warping—effects that are not easily captured through position-only metrics. Thus, DDs provide an additional layer of validation for evaluating the precision and reliability of modeling techniques used in displacement detection. Those DDs have been determined as explained in the following paragraphs.

Distances were defined between pairs of CPs on the CW. They were Pythagorically determined. For example, given the coordinates of two CPs, P (x_p, y_p, z_p) and Q (x_q, y_q, z_q), the distance between points P and Q was calculated by equation 10:

$$Distance\ PQ = \sqrt{(x_p - x_q)^2 + (y_p - y_q)^2 + (z_p - z_q)^2} \qquad (10)$$

First, that distance was calculated using RTS coordinates, this resulted in distance PQ_{RTS}. Then, the distance between the same points was calculated using coordinates extracted from a point-cloud model. In most cases, this yielded a different value, PQ_{Mod}. The discrepancy between both distances was determined by equation 11 by subtracting the benchmarking value, PQ_{RTS}, from the model value PQ_{Mod}.

$$DD = DDs = PQ_{Mod} - PQ_{RTS} \qquad (11)$$

Note that DDs can either be positive or negative.

Certainly. Here's a rephrased version with a different structure and tone:
DDs were further examined across models produced by distinct techniques, provided they operated within an identical coordinate reference system.

Comparison of results – CC C2C and Multiscale Model-to-Model Cloud Comparison (M3C2) distances (Model Discrepancies)

In the CC software, C2C and M3C2 are two methods used to compare 3D point clouds and evaluate spatial changes or discrepancies between them:

- C2C: This method calculates the distance from each point in one cloud to the nearest point in another. It’s simple, fast, and effective for identifying general changes—but it doesn't account for surface orientation or local geometry, which can lead to noisy results if the point density is uneven.

- M3C2: This is a more advanced approach that compares clouds based on surface normal and local neighborhoods. Instead of nearest neighbors, M3C2 projects distances along the estimated normal direction for each point, offering greater accuracy—especially in detecting subtle displacements or changes on irregular surfaces.

In essence, C2C provides a quick overview of differences, while M3C2 offers a more reliable metric for precision analysis in complex modeling scenarios. The full CC workflow is documented in Appendix C8.

METHODS AND WORKFLOW FOR CW

Purpose and Rationale for CW

The CW experiment was designed to validate the studied, non-invasive, potential inspection approaches, for MSE MB walls, in a controlled setting. However, this wall was not part of the initial plan in this project. The original idea consisted in measuring/modeling twice, at two separate times, or epochs, the spatial geometry of the same existing MSE walls in two different bridge sites, B1-Crossgate and B2-Sandersville. The purpose of this double modeling was to capture undesired wall displacements that could occur during the time between those two epochs. Due to limitations in the duration of this investigation, those two epochs were planned to be one year apart. However, the MSE walls at the assigned bridge sites were built several years ago and remained without apparent displacement/deformation during the year considered. In addition, after having measured/modeled the walls at B1-Crossgate, in summer 2023, the research team visited it again, in summer 2024, to perform a second set of measuring/modeling tasks, but they could not be

accomplished. During that year, GDOT completed some shoulder modifications and pavement work along those walls and inadvertently removed the GCPs that were established by the research team in 2023. Nevertheless, this initial inconvenience did not affect the progression of the research work, as is explained in the following sentences. Regarding B2-Old River, both measuring/modeling tasks were completed without inconveniences, in fall 2023 and fall 2024.

Nevertheless, no measurable wall displacements were captured at this second site. Similarly, after visiting two additional bridges, B3-Sandersville and B4-King George, it was apparent that they did not present any signs of observable previous wall settlements or displacements, and it was unlikely that new measurable deformations were to occur and be potentially captured during an additional one-year period. Therefore, to properly validate the techniques studied in this project, it was decided to simulate wall displacements in a controlled experiment using CW. This imitation wall is part of the actual façade wall of the Carruth Building, at the Statesboro Campus of GSU. This building houses the Built Environment and Modeling (BEaM) laboratory where all data postprocessing tasks, associated with this project, were completed.

The purpose of the CW experiment is to test and validate various remote sensing, non-invasive, methods considered in this research project. They are being analyzed and compared to develop a proper inspection protocol for MSE or MB walls in GDOT bridges. Additionally, the CW assisted in testing the performance, a long time, of the employed techniques before they were adopted to be applied on actual retaining wall structures. Validating those techniques in a laboratory-controlled environment, with known simulated displacements, ensures that they can accurately capture actual displacements and deformations. The CW was designed to mimic real-world displacements by

introducing Styrofoam attachments, with different measurable thicknesses, on their external surface. By comparing the outputs of different technologies against known displacements on the CW, this research project ensures that the proposed inspection protocol is not only theoretically sound but also practically measurable and repeatable. This process supports refinement of accuracy thresholds and validates the suitability of the proposed protocol for eventual deployment in GDOT inspection operations.

The CW was measured and modeled twice using the studied approaches. First, the undeformed wall was fully captured, and then, after simulated displacements were introduced with foam shims, it was measured again. The two models were spatially compared to assess the sensitivity and accuracy of each method in detecting wall displacements. The evaluated technologies included (i) a Robotic Total Station (RTS) as the benchmark, (ii) terrestrial LiDAR, (iii) DSLR-based photogrammetry with a hand-held camera, and (iv) UAV-based photogrammetry. Each method captured two data epochs—before and after displacement—to compare performance through multiple indicators, including RMSVs of position and DDs. These analyses helped define noise levels, instrument or processing errors, and the limitations of each method. Infrared thermography was excluded from this experiment due to its dependency on real thermal conditions and was evaluated separately during field investigations. The CW study was essential in validating the effectiveness of these technologies for developing an inspection protocol for MSE and MB retaining walls.

This section summarizes the CW site fieldwork, which deployed non-contact technologies including RTS, terrestrial LiDAR, and CRP using both DSLR and UAV cameras. The objective was to produce accurate 3D models of the wall in two configurations—Epoch 1 (original) and

Epoch 2 (displaced)—to assess the ability to capture small, simulated displacements. Figure 18. Flowchart. Workflow summary of fieldwork and postprocessing steps for the CW validation experiment.illustrates the complete workflow, including field and postprocessing steps for each technology, and compares the resulting model measurements against the RTS reference to evaluate reproducibility and relative accuracy

Task 1 – Robotic Total Station (RTS)

The fieldwork began with the establishment of 5 GCPs near the wall, and 6 CPs on the wall. GCPs were inserted on the concrete ground surface, using steel nails. They are the 5 vertices of a polygonal, closed traverse serving as reference in this site. CPs were marked on the wall by affixing circular (6-inch diameter), black-&-white, paper stickers, covered with protective plastic tape to resist weather conditions, during the data acquisition period. These 6 circular CPs were placed at different locations to monitor surface deformation at both vertical and horizontal sections of the wall. They can be observed in Figure 18. The coordinates of the GCPs were determined by measuring angles and distances and balancing the errors of closure in the closed traverse they define. All needed angular and longitudinal measurements were conducted using the accurate RTS instrument, Leica's TCRP 1201+ R1000. Each measure was repeated twice for swift identification of mistakes and their avoidance. Additionally, if the double measurements were close to each other, they were averaged to obtain the adopted value. If they were substantially different, that was an indication of mistaken measurements and required revision. After obtaining the coordinates of the GCPs, they were employed to determine the coordinates of the CPs with the RTS instrument. In this case, the instrument was stationed on one of the GCPs, used another GCP as a backsight, and captured the coordinates of the CPs in the same system of reference used by the GCPs.

Figure 18. Flowchart. Workflow summary of fieldwork and postprocessing steps for the CW validation experiment.

Task 2 – Laser Scanning

Laser Scanning of the full wall was performed at two different times using Leica's ScanStation **P50**, one time to capture the original CW configuration (Epoch 1) and one time to model its simulated deformed configuration (Epoch 2). This instrument was chosen for its accuracy and long-range capacity. Four scanning stations were selected at strategic locations to properly capture the geometric features of the full CW. Prior to scanning at each station, all 5 spherical targets (each on one of the 5 GCPs) were accurately acquired at high resolution, following the target-acquisition procedure recommended by the manufacturer. This was necessary to enable TB registration and proper georeferencing for both registration workflows, TB and VA. At each station, the scanning parameters were set to medium resolution (6.3 mm point spacing at 10 meters from the scanner). Scans were performed under consistent lighting to reduce external interference. Each scan captured not only desired spatial geometry, but also unsought noise, i.e., solar beams and pedestrian/vehicular traffic. Additionally, each scan used its own system of reference. This required several postprocessing tasks, as indicated below in the subsection entitled *Workflow for Postprocessing of the CW*. The full guide for P50 workflows is documented in Appendix C1.

Task 3(a) – CRP with Hand-Held Camera

During this task, images for photogrammetric modeling were acquired using a hand-held DSLR camera, Nikon's D5300. This was done at Epoch 1 for the non-displaced wall, and at Epoch 2 for the simulated displaced wall. A planned image capture sequence was followed, with consistent lighting and assuring high superposition of neighboring images. In this regard, photos were taken with approximately >80% side overlap, at the same focal length, and preferably along orthogonal

directions to the wall face. In general, the photographer moved one step sidesway between pictures to assure that the location of the camera was different for each picture. The distance from the camera to the wall ranged from ~ 4 m to ~ 15 m (from ~ 13 ft to ~ 15 ft). Additionally, radial shooting patterns from the same point were avoided. For later georeferencing purposes, previously established GCPs are to be captured in several of the acquired images. This was facilitated by identifying each GCPs on the ground with 2ft×2ft, square, black-&-white, markers. A total of 1080 and 1018 pictures were taken during this activity in Epochs 1 and 2, respectively. Postprocessing was required to generate final models, extract measurements, and to complete comparisons. This is described in the following subsection, entitled *Workflow for Postprocessing of the CW*.

Task 3(b) – CRP with DJI's Matrice 30

CRP was also conducted using UAV, at Epochs 1 and 2. This flying device is commonly referred to as a drone. In this case, DJI's Matrice 30 (M30) UAV was employed. It was operated with DJI's RC Pro Enterprise controller. To attain accurate positions of the UAV-borne, moving, camera, at the instant that pictures were taken, and so assist in the generation of the corresponding 3D photo-based models, Emlid's RS2+ GNSS receiver was used as an accurate RTK base. As was the case when images were taken with a hand-held camera, the drone camera must capture the locations of the GCPs for georeferencing purposes. This was facilitated by marking the GCPs on the ground with the previously referred 6ft×6ft, square, black-&-white markers. Drone pictures were taken at Epochs 1 (non-displaced wall) and 2 (displaced wall). Flight missions were performed at an altitude of ~ 33.5 m (~ 110 ft), with both nadir (downward and vertical) and oblique imaging strategies. High front and side overlap (>80%) ensured optimal feature matching when stitching the pictures. Undesired environmental conditions, such as shadows at different times of the day and wind were

avoided to enhance image clarity and model precision. The number of pictures acquired for Epochs 1 and 2 were 192 and 196, respectively. The necessary postprocessing tasks are described in the following section on *Workflow for Postprocessing of the CW*.

All field-acquired data, including RTS measurements, LiDAR scans and photogrammetric images required postprocessing activities to generate comparable 3D models, extract measurements and assess the performance of the different measuring/modeling techniques. The resulting, virtual, 3D models were compared against themselves, and against field measurements completed with the accurate benchmarking RTS device. This was done to study the capacities of different methods to capture small wall displacements, and to determine their relative accuracy.

For proper comparison purposes, each model was georeferenced in the same system of coordinates, the one employed by the GCPs. This system of reference was selected and determined by balancing the errors of the closed traverse while obtaining accurate coordinates of its vertices, the GCPs. The positions of 6 CPs, and 15 non-repeated distances among them, were compared across the considered measuring/modeling techniques. The statistics of position and DDs were determined. Additionally, full point-cloud comparisons were performed using the CC software, including two of its comparison analyses for positional discrepancies: C2C “absolute” distances, and Multiscale Model to Model Cloud Comparison (M3C2) “signed” distances. The different postprocessing activities are described in the following subsections.

Task 4 – 3D Point Cloud via Cyclone Core

The generation of LiDAR-based, 3D point-cloud models, using Leica's Cyclone Core software, followed a structured postprocessing workflow in both Epochs, 1 (original nondisplaced wall) and Epoch 2 (simulated displaced wall).

The first step in postprocessing involved noise removal. Unwanted elements such as solar beams, background clutter, pedestrian and vehicular traffic were filtered out to preserve only the meaningful geometry of the wall and its immediate surroundings. As indicated in Appendix C2, each cleaned scan was properly saved independently to avoid the need to repeat the cleaning in later steps.

Once the noise was removed, scan registration (stitching) was performed using two different techniques: TB registration and VA registration. In the TB method, spherical targets, placed on GCPs during field scanning, were used as common points where scans were made to coincide. At least three common targets are necessary per scan to align the point clouds using an error-minimization algorithm within Leica's Cyclone Core software. In this case, we used 4 targets TA, TB, TC and TD for the registration (Target TA at vertex A, target TB at vertex B, Target TC at vertex C, and target TB at vertex C). If there were no errors in target naming and positions, the TB registration approach would be fast and only take a few seconds to complete. On the other hand, the VA registration scheme, also known as manual alignment, consists in identifying overlapping features between two neighboring scans and in refining their alignment, first by an approximated visual matching in two planes (plan view and side view), and then by invoking the corresponding refinement algorithm via software. The VA approach takes more postprocessing time than the TB

technique. This is because VA only registers two scans at a time. After a pair forms a group of registered scans, another scan is added to that group by stitching the new scan to one of the scans already included in the registered group. That is, the VA registration progresses much slower than the fast TB scheme.

After registration, the integrated point cloud model was georeferenced into the selected local coordinate system defined by the closed traverse and its GCPs. This georeferencing step ensured that all LiDAR-derived spatial data were directly comparable to other measurements and/or 3D models attained by the different employed techniques, including RTS measurements.

Taks 5 – 3D Point Cloud via Metashape, DroneDeploy and Pix4D

As previously mentioned, photogrammetry-based 3D models were generated using imagery from two different sources: a DSLR camera, Nikon's D5300, and DJI's Matrice 30 UAV. Pictures taken with the drone camera were geotagged. That is, they contained camera location information which was enhanced by assisting DJI's Matrice 30 with an accurate, fixed RTK GNSS base, Emlid RS2+. To compare the capabilities of currently popular CRP technologies, the images were processed using two different software platforms, Agisoft's Metashape and DroneDeploy.

DJI's Matrice 30 UAV imagery was processed using both software platforms, Agisoft's Metashape and DroneDeploy. The DSLR images lack position information (geotagging) and they were processed exclusively in Agisoft's Metashape, as this software does not require geotagging. Nevertheless, Metashape can process geotagged pictures as well. This software provides a customizable desktop-based photogrammetry workflow. Both sets of images, from the DSLR

camera and from the UAV camera, were used in Metashape to generate different models. First, the software aligns overlapped pictures by using feature detection algorithms. Then, the process is followed by dense point cloud generation, mesh creation, and texture mapping. Finally, scaling and georeferencing in a selected system of reference is completed. The detailed processing guideline for Metashape is provided in Appendix C7. For this project, Pix4D Mapper was also utilized for the post-processing of DSLR images, employing a workflow like that of Metashape. A detailed guideline outlining the processing procedures in Pix4D Mapper is available in Appendix C9.

DroneDeploy, a cloud-based automated platform, enabled streamlined processing of the geotagged UAV images. The workflow included automatic alignment, sparse point cloud generation, mesh reconstruction, and final point cloud export. Initially, DroneDeploy models were georeferenced in a global system (WGS84 or UTM). However, this was not the selected local system of reference. Therefore, for proper comparison purposes against other models in this study, the initial georeferencing was changed to the selected local system of reference. For this purpose, a comma-separated-variable (CSV) file was generated and uploaded to the software. That file contained the coordinates of the GCPs in the selected local system of reference. The software used these coordinates to complete the coordinate transformation. The full DroneDeploy image processing and coordinate transformation workflow is documented in Appendix C10. Positions and distances were later extracted from the final georeference models to complete discrepancy analysis between the employed measuring/modeling techniques.

This dual-source, dual-platform strategy, including automated cloud processing for UAV data and accurate desktop processing for both UAV and DSLR imagery, allowed for an extensive

comparison of current popular CRP techniques. The integration of data from both image sources also strengthened the analyses at the CW to assess non-contact potential inspection technologies under simulated displacement conditions.

Taks 6(a) – Position and via Microsoft Excel

After several different models of the CW were generated and georeferenced in the same selected local coordinate system, for Epochs 1 (non-displaced wall) and 2 (wall with simulated displacements), point positions, and distances between points, were extracted from them for comparison and performance evaluation purposes. The extracted coordinates were compared in Microsoft Excel against the corresponding field-measured values acquired by the accurate benchmarking RTS instrument.

Two primary types of analyses were conducted: PD and DD. The PD investigation consisted in determining the spatial deviation between the positions of 6 CPs extracted from a 3D georeferenced model and the positions of the corresponding 6 CPs determined, in the field, by the accurate RTS instrument. DD analysis involved spaces between pairs of CPs. A set of 15 non-repeated distances between the 6 CPs were calculated with the CP coordinates extracted from the final georeferenced models and they were compared against the 15 distances between the same CPs but calculated using the field-acquired RTS coordinates of those 6 CPs. These analyses provided insight into the effectiveness and relative accuracy of each modeling technology to detect subtle wall displacements with respect to measurements completed with the accurate benchmarking RTS instrument.

A Microsoft Excel spreadsheet was used to calculate statistical measures of the position and DDs. For instance, means (μ), medians, standard deviations (STD = σ), and RMSVs (RMSV) were determined. This structured analysis enabled clear visualization and interpretation of the relative performance of each modeling technique, supported by tables and comparative plots. These comparisons assisted in identifying the most effective of the considered modern remote-sensing technologies to capture small wall displacements. In turn, these results presented evidence for the proper selection of an inspection protocol to monitor undesired displacements at MSE and MB walls along time.

Taks 6(b) – Positional Discrepancies via CC

This last stage of the workflow for the CW consists in employing CC software, an open-source code designed for 3D point-cloud processing and comparison. This allowed us to perform detailed, full-surface comparisons of selected point-cloud models of the CW. This comparison complemented the previous numerical spatial assessments of the CPs by enabling spatial visualization and a comprehensive analysis of the geometric discrepancies between the full wall surfaces in Epochs 1 and 2. The analysis focused on comparing 3D point clouds derived from two sensing technologies, TB LiDAR and DSLR-based photogrammetry. During this process, two position-discrepancy schemes were utilized, C2C and Multiscale Model to Model Cloud Comparison (M3C2). The C2C technique involved the “absolute” distances between corresponding points in the two compared surfaces. The distance of a point in the reference point cloud (typically Epoch 1) is determined with respect to its nearest neighbor in the compared point cloud (Epoch 2). The result was a color-coded deviation map that highlighted the magnitude of positional discrepancies (displacement) across the wall surface along the two epochs. This visual feedback

assisted in quickly localizing deformations such as bulging, settling, or shifting caused by artificial interventions applied to the CW between epochs. The M3C2 scheme uses an improved algorithm that increases reliability and reduces noise sensitivity in surface comparisons. Unlike C2C, which is sensitive to point density and surface orientation, M3C2 uses directions normal to the local surface and a defined neighborhood scale to measure orthogonal distances between cloud surfaces. This method is better suited for detecting directional or "signed" displacements, especially when comparing models with different densities or noise levels. The output of both schemes consisted of visual displacement maps and quantitative metrics, such as mean shifts, standard deviations, RMSVs, maximum deviations between the two compared surfaces, distribution spread, histograms, and cumulative distribution functions. Through the combination of C2C and M3C2, the spatial discrepancies between LiDAR and photogrammetry models were assessed. The findings reinforce the applicability of CC for nondestructive displacement monitoring and highlight the value of both schemes, C2C and M3C2, to capture wall displacements in practical inspection workflows. The full CC workflow is documented in Appendix C.

METHODS AND WORKFLOW IN BRIDGE B1-CROSSGATE

The bridge is at the intersection of Jimmy Deloach Parkway and Crossgate Road, in Port Wentworth, GA. It has 2 MSE walls, one at each abutment. In this report, they are referred to as the North (N) and South (S) walls. The data collection and analysis occurred during the academic summer term of 2023. Measurements and modeling were carried out using the accurate, benchmarking RTS instrument, Leica's TCRP 1201+ R1000, one laser scanner, Leica's ScanStation C10, and an UAV, DJI's Matrice 30. The tasks included the establishment of GCPs, capture of

checkpoint coordinates, laser scanning of both walls, capturing drone images, generation of georeferenced virtual 3D LiDAR-based and photogrammetry-based models, extraction of data from final models, and comparison of results extracted from the models against field measurements completed with the accurate RTS device.

The original plan was to collect data and model both walls at two or even three different times, summer 2023, summer 2024, and summer 2025. This double or triple time was intended to capture potential wall displacements occurring during one and/or two years. However, only the first measurements/modeling were accomplished, in summer 2023. When the bridge was visited one year later, in summer 2024, it was realized that, during the intervening time, GDOT carried out shoulder modifications and pavement work along the site, inadvertently removing the GCPs established by the research team in 2023. Despite this setback, the overall progress of the research was not hindered, as explained in the following sentences. The research team learned from practitioners that most of the undesired displacements in MSE/MB walls occur during or immediately after construction. Since all bridges considered were built several years ago, it was possible that additional settlements/displacements may not be captured during the time window of this research project. Therefore, to effectively validate the techniques developed in this project, the research team opted to simulate wall displacements in a controlled environment, using a selected CW with artificial displacements. Additionally, at site B2–Old River, both rounds of measurements and modeling—conducted in fall 2023 and fall 2024—were completed without issue. However, no measurable wall displacements were detected at this location. Similarly, inspections of two additional bridges, B3–Sandersville and B4–King George, revealed no visible signs of prior wall settlement or displacement, and it was deemed unlikely that any significant deformation would

occur within an additional one-year observation period. These facts lead to mostly using the selected CW to study the ability of various remote-sensing modeling techniques to capture small displacements.

The research tasks completed at this site are divided into two areas: Field Work and Postprocessing. Both are described in the following sections and are schematically presented in Figure 19.

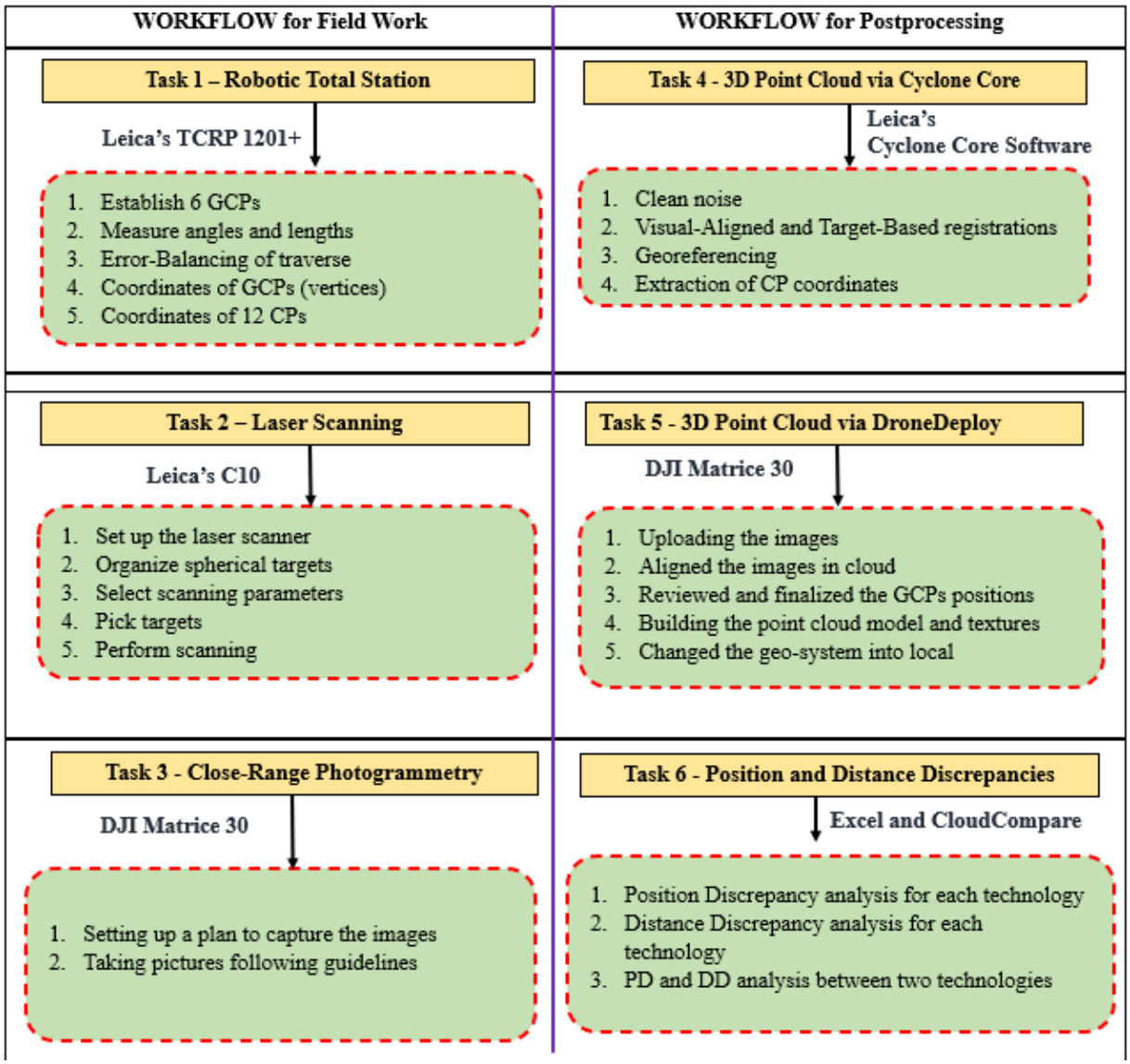

Figure 19. Flowchart. Schematic of methodology and workflow for analyses at B1-Crossgate

During summer 2023, the N and S walls at B1-Crossgate were modeled via LiDAR. Unlike the studies at the CW and B2-Old River sites, at B1-Crossgate only one epoch of data was collected and processed. One objective of the modeling effort was to generate dense 3D point cloud models of both retaining walls to support accuracy evaluation of the scanning techniques, TB LiDAR and visual-aligned LIDAR, with respect to field measurements completed with the accurate, benchmarking RTS instrument. An additional objective was to study the relative accuracy of a CRP model generated via DroneDeploy software. The tasks involved in LiDAR-based and photo-based modeling are divided into two areas: Field Work and Postprocessing. Both are described in the following sections and are schematically presented in Figure 19.

Task 1 – RTS Surveying

At this site, 6 GCPs, labeled A through F, were established using magnetic steel nails to form a closed 6-sided polygonal traverse. These GCPs, strategically placed near both MSE walls, served as reference points, in the custom local coordinate system, for determining the field coordinates of 6 CPs on each wall. Using the accurate RTS instrument, the research team measured all 6 internal angles and 6 side distances each multiple times for accuracy, including both horizontal and vertical components. Trigonometric leveling was used to determine relative elevations.

Each internal and external angle at the 6 vertices was measured twice and averaged, allowing for the calculation of the Local Angular Error of Closure at each vertex. These local errors were balanced between internal and external angles, and their sum was used to compute the Global Angular Error of Closure for the six-vertex traverse. Then, this error was evenly distributed among

all internal angles. To further refine the traverse, the Bowditch Method (Compass Rule) was applied to adjust the 6 side lengths, proportionally correcting for measurement errors based on leg length. This ensured a geometrically closed and accurate traverse, leading to an accurate set of coordinates for its 6 vertices, the 6 GCPs employed at this site.

Task 2 - Terrestrial Laser Scanning

A single epoch of laser scanning was conducted at this site during the field campaign of summer 2023. Leica's C10 scanner was used to collect spatial data for generating three-dimensional point cloud models of both MSE walls. Six white spherical targets (6-inch or 9-inch in diameter) were mounted on vertical poles positioned over each of the 6 GCPs. These targets were used for a double purpose: (i) for scan registration in the TB LiDAR approach, and (ii) for georeferencing both investigated LiDAR approaches, TB and visual-aligned. Scanning was performed from 6 stations, with three stations near each wall. Each scanning station was selected close to a preceding neighboring station to assure proper continuous overlapping of scans. The location of these scanning stations did not require permanent marking. A full 360° horizontal scan was completed at each station using medium resolution, resulting in point densities of one centimeter spacing at ten meters from the scanner. These scans were postprocessed to create a single, georeferenced 3D point-cloud model of the site, including the façade geometry of both MSE walls. As only one epoch of scanning was performed at B2-Crossgate, no time-based displacement analysis or C2C comparison was conducted at this location.

Task 3 - CRP at B1-Crossgate

At this site, UAV-based CRP model was generated using a UAV, the DJI's Matrice 30 (M30) drone. All images captured by the camera mounted on this drone were processed via DroneDeploy software. In this regard, after some initial trial-&-error modeling attempts, two additional auxiliary elevated control points were added on the walls, to improve model scaling and vertical accuracy. The M30 UAV was equipped with its integrated imaging system and was employed to capture high-resolution images of the MSE walls at B1-Crossgate. It was operated using the DJI RC Pro Enterprise controller, enabling precise manual and semi-automated flight with live video monitoring and flight parameter adjustments.

Unlike the process completed at the CW site, no external GNSS system, such as the Emlid RS2+, was employed at this site. Instead, the drone's built-in RTK module was used in conjunction with Auxiliary AECPs placed directly on the wall surface. Two CPs were selected, and temporarily designated to function as AECPs, enhancing vertical scaling and model accuracy during photogrammetric processing. Image acquisition followed a structured protocol ensuring more than 80% front and side overlap, with photos taken from a combination of nadir and oblique angles to cover the entire wall surface uniformly. The UAV was flown at low altitude and safe distances to reduce distortion and improve feature clarity. Environmental conditions such as lighting and wind were carefully considered to avoid image inconsistencies. The full DroneDeploy workflow is documented in Appendix C10.

The captured images were processed using DroneDeploy's cloud platform, where automated image alignment, 3D point cloud generation, and model scaling were completed. The AECPs played a

crucial role in reducing vertical distortion and aligning the model more closely to the local coordinate system established via the closed traverse. The final model was visually inspected and used to assess coverage, resolution, and structural feature detail. Although no temporal displacement comparison was conducted at this site, the photogrammetric model serves as a relatively reliable spatial record of the MSE walls at Crossgate Road.

Task 4 – Development of 3D Point Clouds by Cyclone Core

At the B1-Crossgate site, 6 LiDAR scans were completed. Each of them captured millions of points and recorded their coordinates in its own coordinate system. That is, each of the 6 scans captured points in different frames of reference. These individual point clouds needed to be aligned (stitched), or registered into the same system of reference, to form a unified 3D point-cloud model.

The first step in postprocessing consisted in removing noise, such as unwanted returns from vehicles, pedestrians, or solar reflections. This cleaning was conducted using Leica's Cyclone Core software. Appendix C2 includes instructions on the scan-cleaning procedures employed in this project. To prevent repeating cleaning tasks in subsequent processing activities, each cleaned scan was properly saved in its "Model" and "Control" spaces, within the Cyclone Core software. Next, the scans were registered using the TB registration method. This method relied on 6 spherical white targets, positioned on vertical poles fixed over each GCP. These targets were acquired in all 6 scans and were used to align the data using a least-squares optimization routine built into Cyclone Core. Additionally, the 6 scans were registered following the visual-alignment (VA) method, a C2C registration approach. This was done to compare the relative accuracies of the TB and VA

approaches with respect to measurements completed in the field with the benchmarking RTS instrument.

Following both registration approaches, the resulting 2 full point-cloud models were georeferenced using the coordinates of all 6 GCPs in the selected local coordinate system, which was defined by the closed traverse. This ensured that the models were in the same system of reference employed by field-measured data, allowing for accurate extraction of spatial information from the models and their comparison against field measurements.

Task 5 – Development of 3D Point Cloud via DroneDeploy

At the B4–King George site, a CRP model was developed using 313 images captured by a DJI Matrice 30 (M30) drone. The flight was manually operated with high front and side image overlapping (>80%) and a mix of nadir and oblique views to ensure full wall coverage. No external GNSS base was used; the drone's built-in RTK and four Auxiliary AECPs placed on the walls improved scaling and vertical accuracy.

All images were processed in DroneDeploy, which performed automatic alignment, reconstruction, and point cloud generation. The final model was georeferenced to the local coordinate system established by a closed RTS traverse. After processing, 3D coordinates of 16 wall CPs were extracted and compared against RTS benchmarks for position and DD analysis. The photogrammetry processing workflow using Agisoft Metashape is described in Appendix C7, while the DroneDeploy workflow is covered in Appendix C10.

Task 6 - Position and Distance Discrepancy Analysis

Since only one set of data was collected at King George (summer 2024), this task focused solely on evaluating the relative accuracy of the Epoch-1 models. The 3D coordinates of 16 CPs (8 per MSE wall) were extracted from the georeferenced point-cloud models—generated via LiDAR (TB and visual-alignment) and DroneDeploy-based photogrammetry—and compared against field measurements completed with the accurate, benchmarking RTS instrument. Two types of analysis were performed:

A. PD Analysis: For each checkpoint, its spatial position derived from each model (LiDAR TB, LiDAR VA, and DroneDeploy) was compared to the corresponding RTS-measured coordinates. The magnitude of the difference between model and field measurements represented the PD at that checkpoint. Summary statistics such as average, maximum, and RMSV of these discrepancies were calculated.

B. DD Analysis: All 120 non-repeated pairwise distances among the 16 CPs were computed using both model-derived and RTS-measured coordinates. Discrepancies between these distances were quantified for all three modeling approaches (LiDAR TB, LiDAR VA, and DroneDeploy) using metrics such as mean values, standard deviations, and RMSVs. These analyses helped evaluate the geometric accuracy and internal consistency of each 3D model.

METHODS AND WORKFLOW IN B2-OLD RIVER

The tasks corresponding to laser scanning were completed in two different epochs. Epoch 1 was during fall 2023 and epoch 2 in fall 2024.

The MSE walls at Bridge 2 were modeled via laser scanning (LiDAR) at two different times, Epochs 1, during the Fall 2023 academic term, and Epoch 2, during the Fall 2024 term. The purpose of this double modeling, separated by one year, was to attempt the detection of potential non-desirable wall displacements that may have occurred throughout that year. The tasks involved in this LiDAR modeling and analysis are divided into two areas, Field Work, and Postprocessing. Both are described in the following sections and are schematically presented in Figure 20.

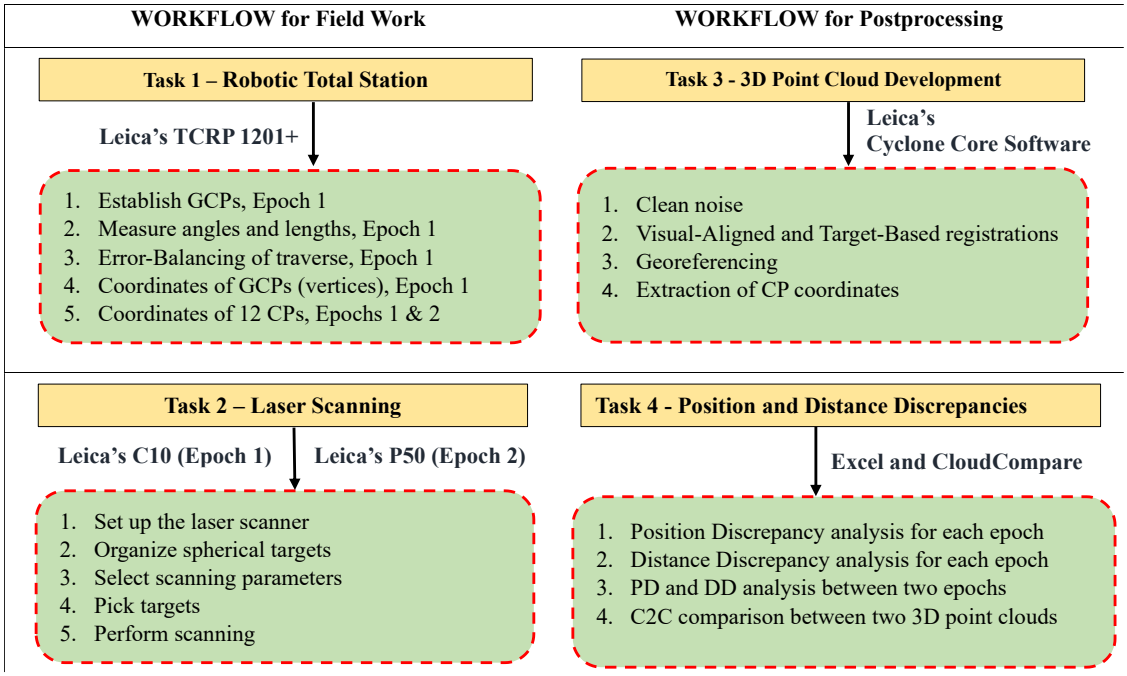

Figure 20. Flowchart. Schematic of the methodology and workflow employed for LiDAR analysis at B2-Old River

Task 1 – Robotic Total Station

First, during Epoch 1, in the academic term of fall 2023, the bridge was visited, and 6 GCPs were established to serve as the customized local system of reference for this site. Those points were strategically established on the lower crossing roadway, near and below the bridge, and materialized with magnetic steel nails through the pavement. A pair of GCPs were placed near each of the 2 retaining walls existing at the abutments of the bridge. These 4 points were established near the walls so later they were employed as stationing locations to capture the position of 12 nearby CPs, 6 on each wall. The 6 GCPs defined the vertices (A, B, C, D, E, and E) of the 6-sided, closed, polygonal traverse employed to determine accurate coordinates for all 6 GCPs.

Task 2 – Laser Scanning

This task consisted in using a terrestrial laser scanning instrument to collect spatial data to later generate full, 3D, point-cloud models of both MSE walls in this bridge. The full scanning of the MSE walls was performed twice to generate two models of the same walls at different times, during Epoch 1 (fall 2023), and during Epoch 2 (fall 2024). The older Leica's C10 scanner was employed in fall 2023 and the newer Leica's P50 scanner was used in fall 2024. During these activities, white spherical targets were employed. They were 6-in or 9-in in diameter. These spheres were attached at the top of vertical poles, which were placed and verticalized on each GCP. The height of each of those poles is to be properly measured. Then, during each scan, all these spherical targets were acquired. The acquisition of those targets has a double purpose: (i) to have the option to use them for stitching the individual scans; and (ii) to employ them for georeferencing the full, 3D, point-cloud models into a common coordinate system. Six scanning stations were selected. In this regard,

there is flexibility in selecting their actual locations and there is no need to mark them with nails. Three of them were selected near each MSE wall. At each scanning station, the scanner was verticalized, the scanning parameters were selected, and the spherical targets were acquired, one by one at high resolution. Then, a full scan was completed at each station covering a full horizontal angle of 360° at medium resolution. During Epoch 1, the medium resolution of the C10 scanner captured the positions of points separated by 1 cm when they were located at 10 m from the scanner. During Epoch 2, the P50 scanner was set up to capture point positions separated by 6.3 mm at 10 m from the scanner. That is, denser point clouds were captured in Epoch 2 by the P50 scanner.

Task 3 – 3D Point-Cloud Development

Once each scan is completed, the spatial x-y-z coordinates of each acquired point (out of several million points) are expressed in a frame of reference associated with those scans. Typically, that system of reference differs from scan to scan. These multiple systems are to be aligned when point clouds from different scans are stitched together to form a full model. That is, the acquired spatial data is to be processed for proper generation of the final full model under a single system of reference. This postprocessing stage involves several steps to ensure accuracy and reliability of the results. First, the noise captured in the acquired data is to be removed. Mostly, this noise consists of non-desired pedestrian and vehicular traffic acquired by each scan. Moreover, if scans are performed during a sunny day, non-existing "solar beams" (point clouds shaped as beams pointing towards the Sun) could be captured as well. Leica's Cyclone Core software presents various tools to remove noise. After cleaning, each scan must be properly saved to avoid having to repeat the noise

removal process in subsequent tasks. This requires following an appropriate procedure in the Cyclone Core software, involving the Model and Control spaces of each scan. Once the noise is removed, the point cloud of each scan is stitched into the full model. This stitching process consists of translating and rotating scans so that their common points coincide. Nevertheless, this coincidence is not perfect and is attained with minor flaws. Usually, this stitching procedure is referred to as the registration process, meaning the registration of the point cloud from each scan into a common system of reference. Two different registration approaches have been considered in this study. They are the TB scheme and the visual-aligned (VA) technique. The TB registration needs a minimum of three common points (designated as targets) to stitch together the point clouds of two neighbouring scans. Exceptionally, it may only need two common targets when stitching two scans that are perfectly verticalized, but this may result in a larger stitching error. In this bridge, 6 common targets (TA, TB, TC, TD, TE, and TF) were captured by each of the 6 scans completed in each epoch to generate the models of the MSE walls for Epochs 1 and 2. Those targets were previously described as white spherical ones, attached to vertical poles standing on each of the 6 GCPs. Leica's TB registration procedure employs a least-squares-based optimization algorithm implemented via its Cyclone Core software. This was accomplished with computer workstations at the BEaM lab at the Civil Engineering and Construction Department of GSU. The TB technique requires the acquisition of numerous stitching targets in the field, and this delays field operations. However, the required postprocessing time is less and faster than in alternative approaches. The other registration technique, the VA approach, does not require stitching targets, but it uses already acquired points in the two scans that are to be registered. Because of that, it is considered as a visual registration technique. The original visual scheme required the user to identify a minimum of

3 common points in each of the two scans to be stitched at a time. However, those points are not necessarily at the same location in both scans, and this introduced some error. Leica's VA registration approach improves this method by allowing the user to visually align, in an approximate fashion, both scans using a horizontal plan view and a vertical lateral view. After this approximate alignment, the software improves the registration by identifying and minimizing the distance between potentially coincident points. The VA method does not require the acquisition of stitching targets in the field. This makes it faster in the field than the TB one. However, the TB technique is faster during the postprocessing stage, at the computer laboratory. This is the case because the TB scheme registers all scans at once while the VA technique only allows the stitching of 2 scans at a time, with time-consuming user intervention. Additionally, the successive stitching required by the VA approach increases the possibility of error propagation while successively registering scans to complete a full model. This could result in final models that are more inaccurate. After each scan is registered into a common system of reference, the full point-cloud model is completed. However, the system of reference resulting from the registration process may not be a desired one. In this study, for proper comparison, the full models produced in Epochs 1 and 2 were registered on the same system of reference. That is, registered full models from Epochs 1 and 2 are to be transformed into a common system of reference. This final coordinate-transformation process is designated as georeferencing. In this study, the selected common system of reference is the one employed by the GCPs and defined by their associated closed traverse calculations. Therefore, after this georeferencing of a full point-cloud model, the spatial coordinates of all its points are in the same system of reference as the employed by the GCPs. Once the models generated in Epochs 1 and 2 are georeferenced in the same system, the coordinates of their check points (same 12 CPs from each Epoch) are extracted to compare them, point by point, and

potentially detect any wall displacements that may have occurred between those two Epochs. This comparison is described in the following section.

Task 4 – PD and DD analysis

After the final, virtual, 3D, georeferenced models for each epoch were completed, the coordinates of the CPs were extracted from them, and various comparisons were performed. Additionally, full clouds were compared. These comparisons are described as follows:

(1) PD Analysis for each Epoch: this analysis consisted of comparing the positions of the CPs extracted from two 3D, LiDAR models (TB and VA), where each of them was considered independently against the positions of the same points determined in the field with the RTS instrument. For each CP, two sets of coordinates were employed to determine two position vectors. One vector was defined using the coordinates extracted from the virtual 3D model and the other using the field coordinates acquired via the RTS instrument. These two vectors were subtracted to define a PD vector. Then, the magnitude of that discrepancy vector was determined. The statistics of those magnitudes, for all 12 CPs, were calculated.

(2) DD Analysis for each Epoch: This analysis used the coordinates of the 12 CPs to calculate all possible 66, non-repeated distances among them, and compared those distances. In this case, distances calculated with coordinates extracted from the virtual, 3D models (TB and VA) were compared independently against distances determined by coordinates measured in the field with the RTS instrument. All possible non-repeated distances between the 12 CPs were

compared to determine their discrepancies. Then, the statistics of those discrepancies were calculated.

(3) Discrepancy Analysis between Epochs: After the analysis in above points (1) and (2) were completed for each epoch, a PD and DDs comparison was also performed, Epoch 2 vs Epoch 1. These last discrepancy analyses were conducted to detect any structural displacements or deformations over time.

(4) C2C Analysis between Epochs: In this case, the comparison was made between the point clouds of two TB LiDAR models, one from Epoch 2 and one from Epoch 1, which served as reference. The purpose of this full C2C comparison was to observe, in a graphical sense, position discrepancies between point clouds of the full retaining walls (Epoch 2 vs Epoch 1). The two involved 3D point-cloud models, from Epochs 1 and 2, were compared against each other by using the open-source, CC software. To transfer the LiDAR model from the Cyclone Core software into the CC software, the point cloud RGB model in Cyclone Core was exported as a ".las" file and then imported to the CC. This program determined the distances between corresponding points in the two involved clouds and showed the magnitudes of those distances by using an active scalar field (i.e., a color scale). Additionally, the software provided information on the distribution density function of those distances and permitted to generate the corresponding cumulative density function. This latter function identifies the percentage of points separated by more than a selected distance.

Together, these post-processing techniques enhance the assessment of the techniques considered and support detailed evaluation of the retaining wall.

METHODS AND WORKFLOW IN B3-SANDERSVILLE

In B3-Sandersville, this study consisted of the generation and analysis of several virtual, 3D models generated by two approaches: laser scanning and CRP. The corresponding tasks were mainly divided into two areas, Field Work and Postprocessing and completed in summer 2024, with one additional collection and postprocessing of pictures in spring 2025. The following section describes both approaches.

In Summer 2024, the MSE walls at Bridge 3 were modeled twice via laser scanning (LiDAR), once employing the TB approach and once using the VA technique. Additionally, during the same time, one CRP model was generated using the Agisoft Metashape software, employing pictures taken with the hand-held Nikon D5300 camera. Later, in spring 2025, another photogrammetric model was completed with the same software but using pictures taken with an UAV, the DJI Matrice T30. The purpose of using two different modeling techniques was to compare their relative accuracy with respect to measurements completed with the accurate, one-second, benchmark instrument, Leica's RTS device. The tasks involved in the LiDAR and photogrammetric modeling/analyses are described in the following sections and are schematically presented in Figure 21. They are divided into two major parts, Fieldwork and Postprocessing.

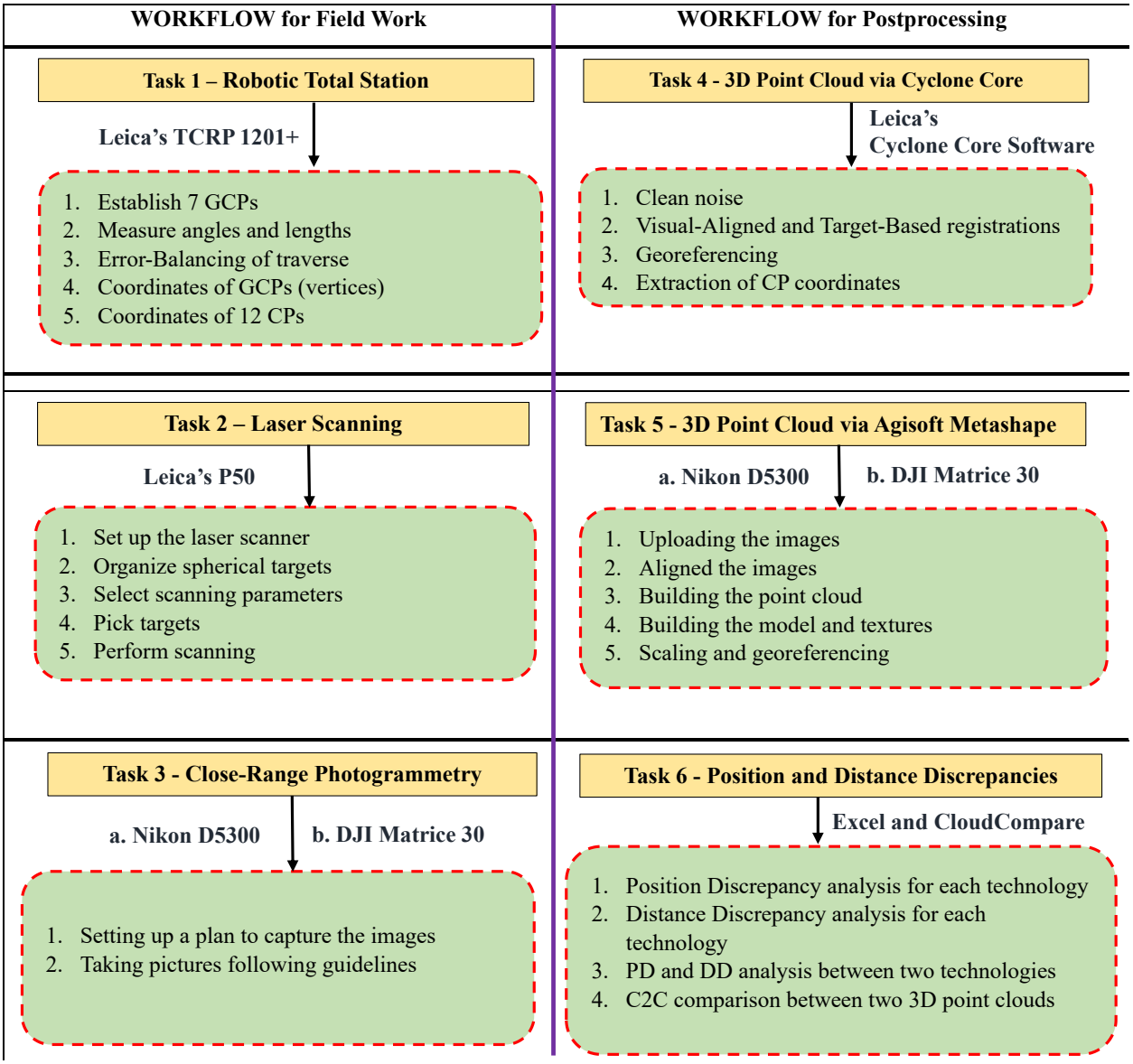

Figure 21. Flowchart. Schematic of the methodology and workflow employed for LiDAR and Photogrammetry analyses at B3-Sandersville

The work completed in the field consisted of 3 main tasks, involving the collection of field data. First, the RTS instrument was used to accurately determine the position of GCPs and CPs. The GCPs serve to define the local system of reference selected in this site. The CPs were established to track potential future deformations of the involved MSE walls. Then, LiDAR was employed to rapidly scan the wall surfaces and surrounding environment, generating dense, virtual, 3D, point-

cloud models providing comprehensive relative spatial information. The CPs captured in those point clouds were used to compare the relative accuracy of their positions with respect to the positions captured in the field with the benchmark RTS instrument. Finally, CRP was employed to complement these methods and to also compare its relative accuracy with respect to measurements completed with the RTS device. Together, these tools allow for efficient, and non-invasive data collection, making field work a critical step in assessing the condition and stability of MSE walls. These 3 field work tasks are described in the following subsections.

Task 1 – Robotic Total Station

This first task is characterized by using the benchmark instrument, Leica's RTS device. In summer 2024, 7 GCPs were established to serve as the customized local system of reference for this site. Those 7 points were strategically placed near the railway running underneath the bridge. These points were marked with steel nails and constituted the vertices of a selected, 7-sided, closed, polygonal traverse. That traverse was calculated and balanced to accurately determine the coordinates of its vertices, the 7 GCPs. Additionally, the selection of the locations of the GCPs was influenced by the need to employ them later to acquire field coordinates of the CPs, with the RTS instrument. A total of 12 CPs were painted on the 2 MSE walls at this site. That is, 6 on each wall. Those CPs were painted as 6-inch-diameter circles with alternating black & white quadrants. They have a double purpose: (i) to capture undesirable potential future displacements, and (ii) to compare the accuracy of the resulting point clouds with respect to measurements performed by the accurate, one-second, RTS instrument. The 6 CPs on each wall followed a 3 pair pattern, with one member of

each pair placed at a low level (~3 ft above ground) and the other member at a higher location (~ 8 foot higher) than the low member.

Task 2 – Laser Scanning

This task involved the acquisition of spatial data to later generate detailed 3D point-cloud models of the 2 MSE walls at this bridge site, using terrestrial LiDAR technology. This was carried out using the Leica P50 scanner, which was deliberately placed at 6 different strategic scanning positions near the railroad and underneath the bridge. To ensure accurate integration of each scan into the full model, spherical targets were positioned on each GCP. All 6 spherical targets were captured by every single scan. Leica Geosystems refers to this target-capturing action as "picking" targets. At each scanning station, targets are to be picked before starting the full scan. These targets played a crucial dual role. They not only assisted later in merging the individual scans into a unified model but also facilitated the final georeferencing process by accurately aligning the full 3D point-cloud model within the selected coordinate system, defined by the GCPs. At each scanning station, the scanner was properly set up, and necessary parameters were adjusted, including the selection of a relatively medium resolution (capturing points spaced by 6.3 mm at 10 meters from the scanner). Then, at each station, all 6 targets were individually picked (one at a time) before a full scan was performed. Each full scan completed 360 horizontal coverage, ensuring that the collected spatial data was both detailed and presented considerable superposition to later facilitate the use of the VA registration (stitching) approach for comparison against the usually more accurate TB registration technique.

Task 3a – CRP with Hand-Held Camera

This task consists of following a structured methodology for capturing images using a hand-held camera (in this case a DSLR Nikon D5300 camera), adhering to specific guidelines to ensure the subsequent generation of a full and accurate virtual 3D model. The process begins with setting up a detailed plan for capturing needed images. To achieve optimal results, several factors, such as lighting, angles, and distances from the camera to the surfaces to be captured, should be properly considered. The use of a hand-held camera presents the advantage of allowing precise control over the photographic process, ensuring that each image meets the required standards for subsequent analysis. However, this manual process is slower than the automatic process that can be completed with cameras on-board of UAVs. Additionally, the photographer may not be able to access all preferred camera positions. The images from hand-held cameras should follow a standardized procedure that minimizes variability. This includes taking neighboring pictures with large amount of side overlapping (more than 80%, if possible), varying the camera position for each picture, and using the same focal length for all pictures. Additionally, it is important that, for each picture, the camera points approximately perpendicularly towards the surface to be captured. However, this may not always be possible with a hand-held camera. It is also advisable to avoid taking pictures in a radial fashion, from the same camera position. This could make the stitching algorithm fail during the postprocessing and model-generating stages. By adhering to those guidelines, the captured images provide a reliable foundation for close-range photogrammetric processing, enabling the generation of high-quality spatial data.

Task 3b – CRP with UAV

This task involved the use of a UAV, specifically the DJI Matrice 30 (M30) equipped with its integrated imaging system, to collect high-resolution images for photogrammetric reconstruction of the CW surface. The UAV was operated using the DJI RC Pro Enterprise controller, which provides advanced control, real-time video feedback, and automated mission planning capabilities. To support precise georeferencing and enhance positional accuracy, a GNSS-based control system (Emlid RS2+) was deployed during data acquisitions. The Emlid RS2+ operated in RTK mode, allowing for high-accuracy collection of GCP coordinates, which were later used to scale and anchor the photogrammetric models generated from UAV imagery.

The photogrammetric workflow using the UAV began with flight mission planning, where coverage, overlap, and flight altitude were configured based on the dimensions and geometry of the CW. Care was taken to optimize image capture for both top-down (nadir) and angled (oblique) perspectives to ensure full façade coverage. The onboard camera of the DJI M30 provided both zoomed and wide-angle images, which were captured at a constant resolution and fixed camera parameters for consistency. Image acquisition was executed with substantial overlap typically more than 80% front and side overlap to ensure robust feature matching in the post-processing stage. The UAV was flown manually and semi-autonomously at low altitude, maintaining a safe horizontal distance from the wall to minimize parallax distortion and maximize surface detail resolution. To reduce image variability and maintain data quality, consistent lighting conditions were considered, and flight operations were avoided during strong shadows, overcast sky glare, or high wind speeds. Unlike hand-held photogrammetry, UAV photogrammetry allows for systematic and repeatable

coverage of hard-to-reach vertical surfaces, though it may suffer from slightly higher vertical positioning error if elevated GCPs are not well-distributed. Captured images were processed in Agisoft Metashape where camera alignment, dense point cloud generation, and model scaling were performed. GCPs measured using the Emlid RS2+ GNSS were integrated to improve georeferencing accuracy. The resulting 3D model was analyzed alongside RTS and LiDAR data to assess completeness, RMSV, and displacement detection.

By following these procedures, UAV-based photogrammetry produced a comprehensive, model-ready image set of the CW, supporting both quantitative and visual comparisons between epochs and across different sensing technologies.

Task 4 – 3D Point Cloud via Cyclone Core

The generation of virtual, 3D, point-cloud models, using Leica's Cyclone Core software, involves several steps. First, all scans are to be transferred from the laser scanner to a workstation with the installed software. Then, all scans are imported into a selected project database in Leica's Cyclone Core software. Next, unwanted elements such as vehicle or pedestrian traffic and solar beams, which are commonly referred to as "noise", are to be removed from each scan. Once the noise is deleted, each cleaned scan is saved in 2 spaces used by the software for this project, the Model and the Control spaces. This must be completed following a proper procedure to prevent the need for repeated cleaning in subsequent tasks. After noise removal, the scans are to be registered (stitched together) into a common system of reference by following two different approaches, TB and VA registrations. These two techniques are employed because each takes a different amount of time to

complete, and their resulting models may have different accuracies. This study compares their relative accuracy against field measurements completed with the RTS benchmark instrument. The TB method requires 3 common targets, at least, per scan, to register them into a full model. Exceptionally, if all scans are perfectly verticalized, a minimum of 2 common targets per scan suffices, but this may increase the registration error. The TB technique is a fast process that uses a least-squares optimization algorithm to quickly align the scans in a single action. On the other hand, the VA method is a slow C2C scheme, based on the manual identification of several common points in two overlapping neighboring scans to stitch them together. It requires user intervention to align (stitch) only two scans at a time. Fortunately, Leica has improved the original C2C technique by initially allowing the user to approximately align two scans in a horizontal plan view and in a vertical side view. Once the two scans are visually aligned, Leica's software optimizes and improves that initial alignment. Since only two scans are registered at a time, the VA approach takes more processing time, in a computer laboratory, than the TB method to register all individual scans into a full model. However, during data acquisition in the field, the VA technique is faster than the TB approach. This is because the TB method requires acquiring numerous field targets for two different purposes: (i) to stitch scans, and (ii) to georeference the final model. Conversely, the TB approach only requires the acquisition of a few field targets for georeferencing the final model. After registration of all scans, the resulting full models are georeferenced into the selected local system of reference. This georeferencing consists in assigning the coordinates of the GCPs (defined by the closed traverse) to their corresponding target points acquired by the scans. After georeferencing, the spatial coordinates of all points in a final model are expressed in the same system of reference employed by the GCPs. This ensures consistency for further analysis and comparisons with field measurements. Then, the coordinates of the CPs are extracted from the

georeferenced full models to estimate the spatial relative accuracy of the resulting models with respect positions and distances determined by the benchmarking RTS instrument in the field. These comparisons are described in the following subsection.

Task 5a – 3D Point Cloud via Agisoft Metashape with Hand-Held Camera

This task consists of generating 3D point cloud models using Agisoft Metashape software with images captured with a hand-held camera. For this, the DSLR Nikon D5300 camera was employed. First, the captured images were uploaded into the computer program. Then, these images were aligned by a software algorithm that identifies and matches common features across multiple photographs, establishing precise spatial relationships. After this alignment, the software constructs the point cloud, representing the 3D geometry of the spatial scene captured by the pictures. The point cloud is further refined to build a detailed model, with textures applied to enhance visual realism. The final steps involved scaling the model to real-world dimensions and georeferencing it to align the coordinates of all its points with a selected local coordinate system. This scaling and georeferencing assures the compatibility and comparability of the model with other spatial data using the same system of reference. The use of Agisoft Metashape facilitated this process through advanced photogrammetric algorithms, resulting in 3D models suitable for various applications.

Task 5b – 3D Point Cloud via DJI Matrice 30 Camera

This task is very similar to the previous one, 3a. The main difference is that it uses pictures captured by the onboard camera of a DJI Matrice 30 UAV. The resulting photogrammetric models from this alternative approach are georeferenced in the same system of coordinates as all previous models.

This allows the team to compare the relative spatial accuracy of the resulting models against other models and with respect to field measurements attained in the field with the benchmarking RTS instrument. In the DroneDeploy-based photogrammetry workflow using UAV imagery, the inclusion of elevated GCPs positioned directly on the wall played a critical role in enhancing model accuracy and scaling. These auxiliary GCPs provided additional vertical and planar constraints that significantly improved the geometric integrity of the 3D reconstruction. Comparative analysis showed that models incorporating elevated GCPs achieved 10 to 15 times higher accuracy than those relying solely on ground-level references. This underscores the importance of strategic GCP placement particularly in vertical structures for achieving reliable and precise photogrammetric results.

Task 6 – Position and Distance Discrepancy

This task aims to evaluate the spatial accuracy of the resulting 3D point-cloud models by comparing them with field measurements obtained using the accurate, one-second, Leica's RTS instrument. Additionally, it involves a comparative analysis of selected full point-cloud models, considering the spatial discrepancies in the entire surfaces of the MSE walls. At this stage, multiple sets of coordinates have been obtained for the CP points marked on the MSE walls. One set was previously extracted from each georeferenced full point-cloud model, including TB LiDAR, VA LiDAR, Nikon Photogrammetry, and Matrice 30 Photogrammetry. Since all these 3D models are georeferenced within the same system, it is possible to spatially compare them. Additionally, another set of CP coordinates was collected in the field using the referred Leica's high-precision, RTS device, which served as the benchmarking instrument. This latter set provided the reference for comparison. Using this data, spatial discrepancy analyses were conducted to assess the relative

accuracy of the resulting 3D point-cloud models. These analyses included PD and DD evaluations, which identified and quantified relative positional differences and variations between corresponding points across different datasets. In this bridge, the coordinates of 12 CPs were considered in the discrepancy studies mentioned. Statistical analyses, including mean, standard deviation, and RMSVs, were performed to assess the relative accuracy of the resulting 3D point-cloud models with respect to RTS measurements. To streamline data management, visualization, and reporting, the analyzed information was organized and processed in Excel spreadsheets. For the comparative analysis of entire wall surfaces, the open-source CC software was utilized. It measures and allows the visualization of differences between two virtual, 3D point-cloud models: one generated via TB LiDAR and the other through photogrammetry using Agisoft Metashape, with images captured by a handheld DSLR Nikon D5300 camera. The CC software computed absolute distances between corresponding points in 2-point clouds, enabling a detailed spatial comparison of the wall surfaces. This analysis assists in identifying geometric differences or structural details between the compared surfaces. The results were presented through a color-coded distance map, where different colors indicated the magnitude of differences between the point clouds. This visualization allows users to quickly pinpoint areas of significant deviation or close alignment. Additionally, key metrics including C2C distance, standard deviation, cumulative distribution function, and maximum distance—were provided, offering a quantitative assessment of the comparison.

METHODS AND WORKFLOW IN BRIDGE B4 – KING GEORGE

The bridge is located at the intersection of King George Boulevard and Abercorn Street in Savannah, Georgia. It features two MSE walls positioned at the northwestern and southeastern

abutments of the overpass. In this report, these walls are referred to as the Northwest (NW) and Southeast (SE) walls. All data collection and analysis for this site were conducted during the summer of 2024. The fieldwork utilized a combination of instruments, including the Leica TCRP 1201+ RTS for capturing precise benchmark coordinate measurements, the Leica ScanStation P50 for terrestrial laser scanning, and the Nikon D5300 DSLR camera for CRP. In addition to horizontal and angular measurements, the Topcon AT-B2 auto level instrument was used to determine the relative elevations of the GCPs. This leveling process established vertical relationships between all traverse stations. Each vertical angle was measured twice, and the averaged values were used to compute elevations. UAV-based photogrammetry was not performed at this site due to limited vertical clearance under the overpass, which posed a safety risk for drone operations.

The workflow began with the establishment of GCPs and the placement of CPs directly on the MSE walls. Using the RTS, precise local coordinates were recorded to serve as reference benchmarks. Laser scans of the wall surfaces were then conducted with the Leica P50, followed by systematic image capture using the DSLR camera. These datasets were processed to produce georeferenced 3D models derived from both LiDAR and photogrammetry. To assess the quality and accuracy of the models, spatial comparisons were made using both point-based and cloud-based techniques, referencing the RTS-derived coordinates as ground truth. Initially, the research team planned to return to this site in a subsequent year to conduct a second round of data collection for multi-epoch analysis, which would have enabled the detection of any potential wall displacement over time. However, this follow-up survey, scheduled for summer 2025, was not feasible due to the project's final report deadline in July 2025. As a result, no second-epoch measurements were taken at this location. Despite this limitation, the King George site provided valuable insights into the

performance and reliability of remote sensing technologies under real-world field conditions. During the inspection and scanning activities, the walls exhibited no visible signs of settlement, tilting, or structural displacement. Considering the apparent stability and age of the MSE walls, significant deformation was not expected within the limited timeframe of this study. Similar outcomes were observed at other study locations. At site B2–Old River, two full rounds of measurements and 3D modeling were completed in Fall 2023 and Fall 2024, respectively, yet no measurable wall displacements were detected. Likewise, inspections at site B3–Sandersville and site B1–Crossgate revealed no evidence of prior wall settlement or displacement. It was therefore concluded that further measurable movement was unlikely to occur within an additional one-year observation period.

Given these findings, the research team shifted focus to using a dedicated CW, built in a controlled environment, to simulate artificial displacements for validation purposes. This approach allowed for the evaluation of the sensitivity and effectiveness of different modeling techniques in detecting minor deformations that might not have occurred naturally within the project's timeline. Consequently, the King George site served as a valuable benchmark for evaluating the single-epoch accuracy of various 3D modeling approaches. The research activities at this location are divided into two main phases, Field Work and Postprocessing, which are described in detail in the following sections and schematically illustrated in Figure 22.

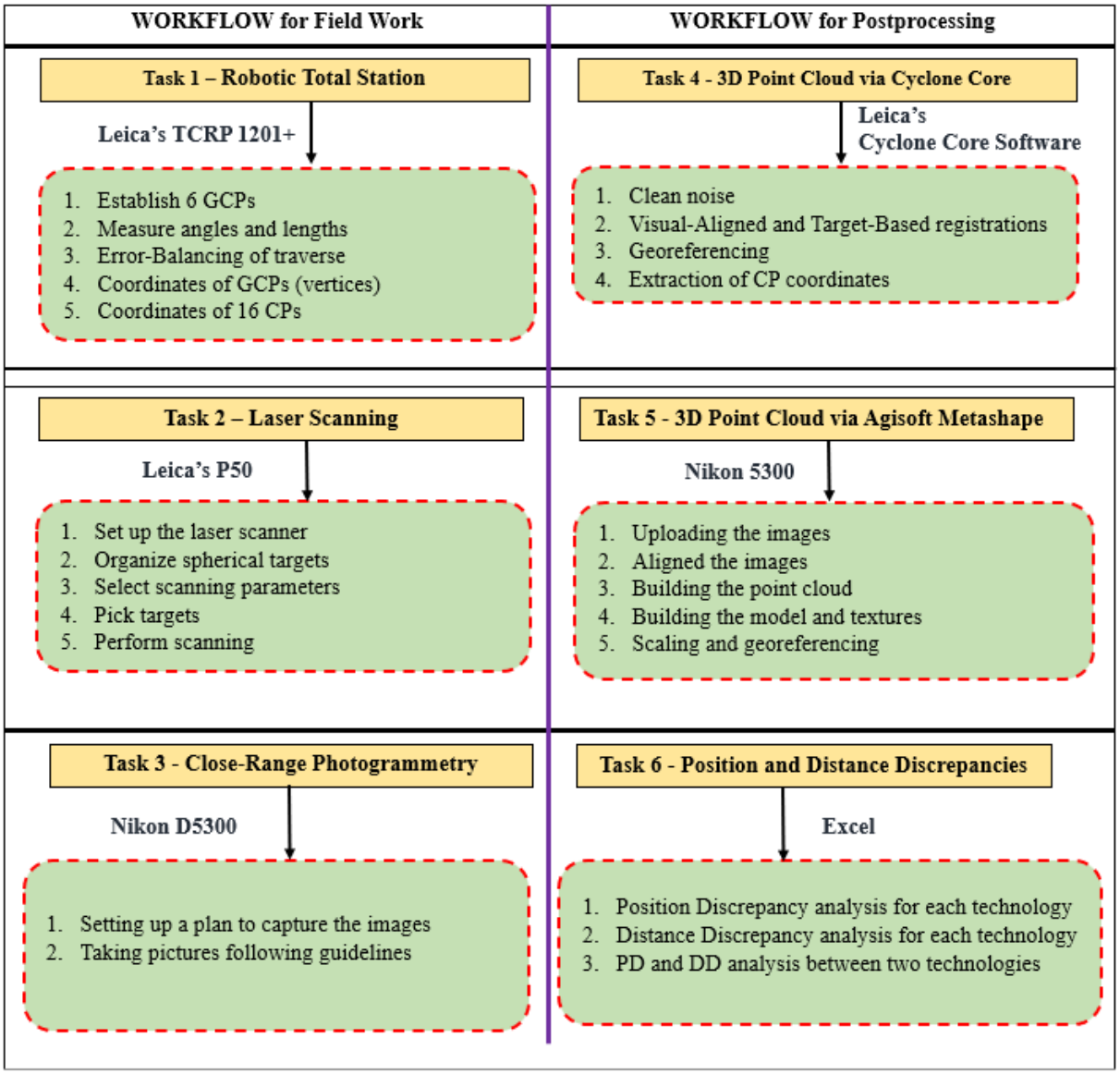

Figure 22. Flowchart. Schematic of methodology and workflow for analyses at B4-King George

During summer 2024, the NW and SE retaining walls at B4 – King George were modeled using both terrestrial LiDAR and DSLR-based photogrammetry. Unlike the CW and B2 – Old River sites, only a single epoch of data was collected and analyzed at this location. The primary objective was to generate accurate 3D point cloud models of both walls to evaluate the spatial performance of non-contact sensing techniques. Two terrestrial LiDAR modeling approaches TB and visual-aligned

(VA)—were investigated. In addition, CRP using the Nikon D5300 DSLR camera was employed, with all images processed in Agisoft Metashape to create high-resolution 3D models. UAV-based photogrammetry was not feasible at this site due to insufficient vertical clearance beneath the overpass, which limited safe drone operation.

The modeling workflow focused on comparing the spatial accuracy of point clouds from both sensing technologies with benchmark coordinates acquired using the Leica TCRP 1201+ RTS. The tasks involved in the LiDAR and photogrammetric modeling are organized into two areas: Field Work and Postprocessing. Both phases are discussed in the following sections and are schematically illustrated in Figure 22.

Task 1 – RTS Surveying

At B4 – King George, six GCPs, labeled A through F, were established using magnetic steel nails to form a closed 6-sided polygonal traverse. These GCPs were strategically located near both MSE walls and served as anchors for defining the site's custom local coordinate system. The RTS instrument was used to measure the six internal angles and corresponding side lengths of the traverse, including repeated horizontal and vertical observations to ensure precision.
Each angle at the traverse vertices was recorded twice and averaged to improve reliability. Local angular errors were computed and adjusted to balance internal and external angles at each station. The sum of internal angles was checked for closure, and any global angular error was evenly redistributed across the network. To finalize the traverse geometry, the Bowditch Method (Compass Rule) was applied to correct horizontal distances proportionally according to leg length, thereby achieving a balanced and closed traverse. The resulting GCP coordinates, defined in the local

reference frame, were then used to determine the 3D coordinates of 16 circular CPs (8 on each wall), enabling subsequent accuracy comparison with point cloud outputs from both LiDAR and photogrammetric datasets.

Task 2 – Laser Scanning

This task involved using terrestrial laser scanning to collect high-resolution spatial data and generate 3D point-cloud models of the MSE walls at Bridge 3 – King George Blvd. The scanning was conducted during a single campaign in Summer 2024 (Epoch 1) using the Leica ScanStation P50. This instrument was selected for its long-range capabilities and high point density output, making it well-suited for capturing fine details on large vertical surfaces. White spherical targets, either 6-inch or 9-inch in diameter, were mounted atop vertical poles and precisely placed on each of the six previously established GCPs. The elevation of each target above its GCP was carefully measured to ensure accurate registration. These targets served a dual role: (i) to support TB registration for merging individual scans, and (ii) to enable georeferencing the resulting 3D model into the local coordinate system defined by the closed traverse from the RTS measurements.

A total of 16 scanning stations were used across the site to ensure complete coverage of both retaining walls and surrounding features. Each station was carefully verticalized, and the scanning parameters were optimized for maximum accuracy. The spherical targets were manually “picked” at high resolution before initiating the full 360° horizontal scans. The P50 scanner was configured to capture point intervals of approximately 6.3 mm at 10 meters, resulting in dense and detailed point clouds of the MSE wall surfaces. The collected scan data were subsequently processed using both

TB and visual-aligned (VA) registration techniques and later evaluated through position and DD analyses. The full LiDAR scanning workflow using the Leica P50 is outlined in Appendix C1.

Task 3 – CRP with Hand-Held Camera

CRP was conducted using a Nikon D5300 DSLR camera, following established best practices for hand-held image capture. No UAV-based photogrammetry was conducted at this site due to limited overhead clearance beneath the overpass, which restricted safe drone flight. A total of 2,449 photographs were captured around the two MSE walls, ensuring comprehensive coverage for 3D reconstruction.

The image acquisition strategy emphasized high overlap (greater than 80%) between neighboring photos, consistent camera orientation perpendicular to the wall surface, and uniform camera settings (focal length, exposure) to reduce variability. Images were taken from varying positions to avoid radial clustering, which can negatively impact model stitching. This photogrammetric dataset was processed entirely in Agisoft Metashape, where the images were aligned, dense point clouds were generated, and the model was georeferenced using the RTS-derived GCP coordinates. The resulting 3D photogrammetric model was later used for spatial accuracy comparison against the terrestrial LiDAR models and RTS-based benchmarks.

Task 4 – Development of 3D Point Clouds via Cyclone Core

At the B4 – King George site, a total of 16 terrestrial LiDAR scans were completed using the Leica P50 scanner. Each scan independently captured millions of spatial data points, storing them within

its own local coordinate frame. To develop a unified 3D model of the two MSE walls, these scans required precise registration into a common system of reference. The postprocessing began with noise removal, eliminating extraneous points caused by vehicles, pedestrians, shadows, or reflective surfaces. This cleaning process was carried out in Leica's Cyclone Core software. Appendix C2 provides a detailed protocol outlining the noise-filtering techniques used. Cleaned scans were saved in both "Model" and "Control" spaces within Cyclone Core to avoid redundancy during subsequent tasks.

Once the scans were cleaned, registration was performed using the TB method. This method used spherical white targets mounted on vertical rods over GCPs. Each of the 16 scans captured these targets, allowing alignment through a least-squares optimization routine built into Cyclone Core. For comparative analysis, the scans were also registered using the visual-alignment (VA) method, a C2C registration technique. This enabled an evaluation of both TB and VA methods in terms of spatial accuracy, particularly in comparison to field measurements from the benchmarking RTS. After registration, the two full 3D point-cloud models, one using TB registration and the other using VA were georeferenced using the local coordinates of all six GCPs, as defined by the closed traverse. This georeferencing ensured full consistency between the point cloud models and the RTS-derived field measurements, allowing for accurate spatial analysis and cross-validation of results.

Task 5 – 3D Point Cloud via Agisoft Metashape with Hand-Held Camera

At the B4 – King George site, a total of 2,449 DSLR images were captured using a Nikon D5300 camera to generate high-resolution 3D photogrammetric models of the two MSE walls. These

images were collected following a close-range structured photogrammetry protocol, ensuring high overlap (≥80%), appropriate lighting, and consistent camera-to-wall distances for effective reconstruction. UAV deployment was not feasible at this location due to insufficient vertical clearance under the overpass, which restricted safe flight operations. The image processing was conducted in Agisoft Metashape, beginning with photo alignment through feature matching across overlapping images, followed by the generation of sparse and dense point clouds. Subsequent steps included mesh creation and texture mapping. For accurate spatial referencing, GCPs established during the RTS field survey were imported into Metashape and manually marked on multiple images, enabling precise local georeferencing of the final model to the coordinate system defined by the closed traverse.

Once the point cloud model was georeferenced, the 3D coordinates of all 16 CPs (8 per wall) were extracted directly from the model. These checkpoint coordinates were then compared against the benchmark RTS-measured values for the same points, allowing for a detailed PD and DD analysis. This cross-comparison provided insights into the geometric accuracy and reliability of the DSLR-based photogrammetric model relative to traditional field-survey data and supported the broader objective of evaluating non-contact inspection techniques for aging retaining wall structures.

Task 6 – PD and DD Analysis

Since only one set of LiDAR and photogrammetric data was collected at the B4–King George site (during Summer 2024), the analysis focused on evaluating the relative spatial accuracy of the generated 3D models with respect to field benchmarks obtained via the RTS. Two independently developed 3D models were analyzed, a LiDAR-based point cloud, generated and processed in

Cyclone Core using 16 terrestrial laser scans and a photogrammetry-based point cloud, developed in Metashape using 2,449 DSLR images captured with a Nikon D5300 camera. To evaluate the models, two types of spatial error analysis were conducted:

(i) **PD Analysis**: A total of 16 CPs, eight placed on each of the two MSE walls—were used to extract spatial coordinates from each 3D model. These coordinates were compared against the field-measured RTS values, which serve as the benchmark. For each checkpoint, the spatial difference vector between the model-derived and RTS-derived coordinates was calculated. The magnitude of this vector represented the PD for that CP. Summary statistics including minimum, maximum, mean, standard deviation, and RMSV were computed to evaluate the overall spatial fidelity of each model.

(ii) **DD Analysis**: From the same 16 CPs, 120 non-repeated pairwise distances were computed using each model and compared with the corresponding distances derived from RTS field data. The differences between each model-measured and RTS-measured distance represented the DDs. These values were used to assess internal geometric consistency and deformation artifacts in each 3D model. Metrics such as mean discrepancy, standard deviation, and RMSV were calculated to quantify accuracy.

Both the Point Displacement (PD) and Distance Difference (DD) analyses were conducted independently for the Cyclone Core–processed LiDAR model and the photogrammetry-derived model, with each referenced to the same local coordinate system established through the ground control point (GCP) traverse. By applying identical control frameworks, this dual-analysis strategy

ensures a consistent basis for evaluating the spatial reliability of the two techniques. The parallel comparison not only highlights the relative accuracy, precision, and noise characteristics of LiDAR versus photogrammetry but also demonstrates how each method performs under identical field and environmental conditions, thereby providing a more rigorous foundation for selecting the most suitable technology for retaining wall inspections.

CHAPTER 6. RESULTS AT CW

This chapter presents the results obtained at the CW site, where numerous modeling techniques were investigated. Those techniques are divided into two categories: (a) Terrestrial LiDAR and (b) CRP. In the Terrestrial LiDAR component, the performance of two modeling methods was analyzed: (i) TB LiDAR; and (ii) Visual-Alignment (VA) LiDAR.

The CRP component investigated the performance of the following 6 approaches: (i) use of Agisoft's Metashape with a large number of pictures captured by a hand-held DSLR camera; (ii) use of Agisoft's Metashape with a medium number of pictures captured by a hand-held DSLR camera; (iii) use of Agisoft's Metashape with a small number of pictures captured by a hand-held DSLR camera; (iv) use of Agisoft's Metashape with pictures captured by a drone camera; (v) use of DroneDeploy with pictures captured by a drone camera and with GCPs on a relatively flat surface; (vi) use of DroneDeploy with pictures captured by a drone camera and with GCPs plus auxiliary elevated control points AECPs.

WALL DESCRIPTION, DIMENSIONS AND MATERIALS

The selected control is located at the Carruth building on the Statesboro campus of GSU. It is approximately ~22 m (72 ft) long and 3.8 m (12.5 ft) tall, measured from the base of the wall at sidewalk level. The wall is constructed with red clay bricks bonded in standard running bond pattern, typical of building façades in institutional settings. Although this wall is not a true MSE or MB retaining wall, its uniform surface, vertical continuity, and unobstructed façade made it suitable

for displacement simulation and spatial data capture. No backfill or embedded reinforcements were introduced, as the purpose of this CW was only geometric simulation rather than structural behavior. As shown in Figure 23, the CW is equipped with circular and rectangular Styrofoam attachments. Some of them, the circular ones in black & white, served as CPs. All attachments were considered for displacement detection. These attachments were of different thicknesses, ranging from 3 mm to 34 mm (from ~0.1 in to ~ 1.4 in) to simulate relatively small outward displacements.

Figure 23. Photo. CW with circular and rectangular Styrofoam attachments

GCPS AND CPS

To ensure accurate georeferencing of the CW models, a total of five ground-level, GCPs were established as vertices (A, B, C, D, and E) of a closed, polygonal traverse, as shown in the aerial view in Figure 24. The GCPs materialized by steel nails on the sidewalks and their positions were marked using 2ft×2ft, square, black-and-white, checkerboard targets placed securely on the paved sidewalks, near the wall. Their locations allowed optimal coverage of the CW from multiple angles. Two ACP were affixed to the building fascia near the top corners of the CW. They were 6in×6in, square, black-and-white, checkerboard stickers. They were added, just in case they were needed to

potentially further improve vertical accuracy and to support camera calibration in drone flights. Additionally, six circular CPs were attached to the wall using high-contrast, black-&-white, 6-inch-diamaeter sticker markers. These CPs were distributed across the wall face, spanning from left to right and top to bottom. Their purpose was to serve as consistent, high-visibility reference points across both data collection epochs. The CPs were used for extracting their 3D coordinates via the accurate RTS benchmarking instrument, and from the resulting LiDAR and photogrammetry point-cloud models, to compare positions and distances. This combination of five ground GCPs, two elevated ACPs, and six wall-mounted CPs provided a geospatial framework for aligning all sensor data and performing accurate comparative analyses.

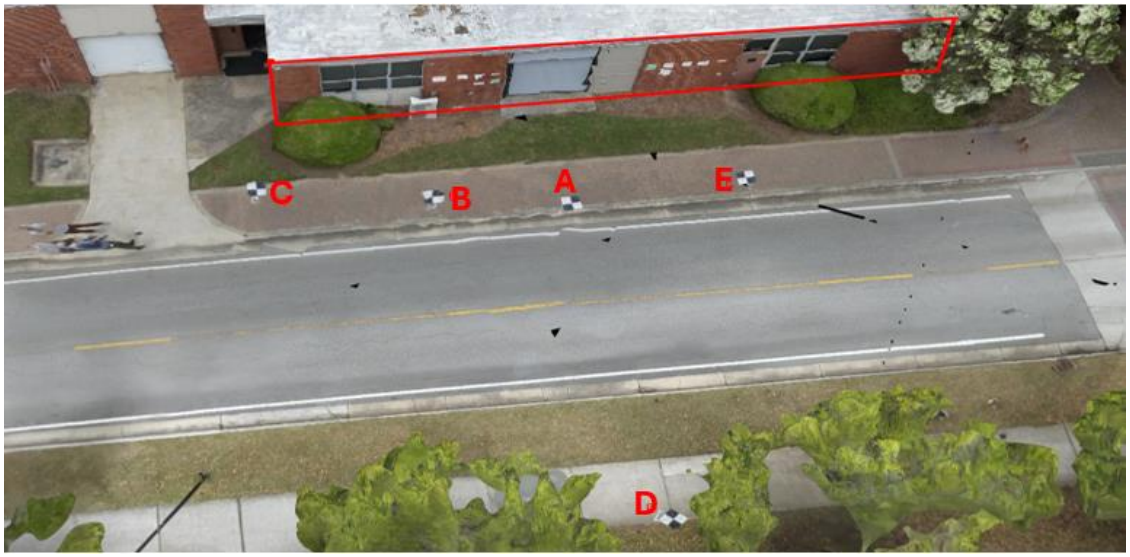

Figure 24. Photo. Aerial view of the CW site with the test section outlined in red and GCPs A–E marked for spatial referencing

DISPLACEMENT SIMULATION STRATEGY

To simulate realistic structural displacements, controlled offsets were introduced to the wall surface using expanded polystyrene (EPS) foam panels of various thicknesses. These foam pieces were

selected to mimic wall displacements, which are symptoms of distress in MSE and MB retaining walls.

The displacement simulation was divided into two types, rectangular and circular foam panels. A set of twelve rectangular EPS panels—with thicknesses of 3 mm, 5 mm, 11 mm, 17 mm, 24 mm, and 34 mm—were used. The varying thickness of the foam boards used in the experiment are illustrated in Figure 25. The range of these thicknesses was selected to determine the minimum displacement that can be captured by the considered modeling techniques. These EPS boards were applied in two distinct vertical areas on the CW:

- Left side: Two rows—four panels in the upper row and two panels in the lower row.
- Right side: Two rows—five panels in the upper row and one panel in the lower row.

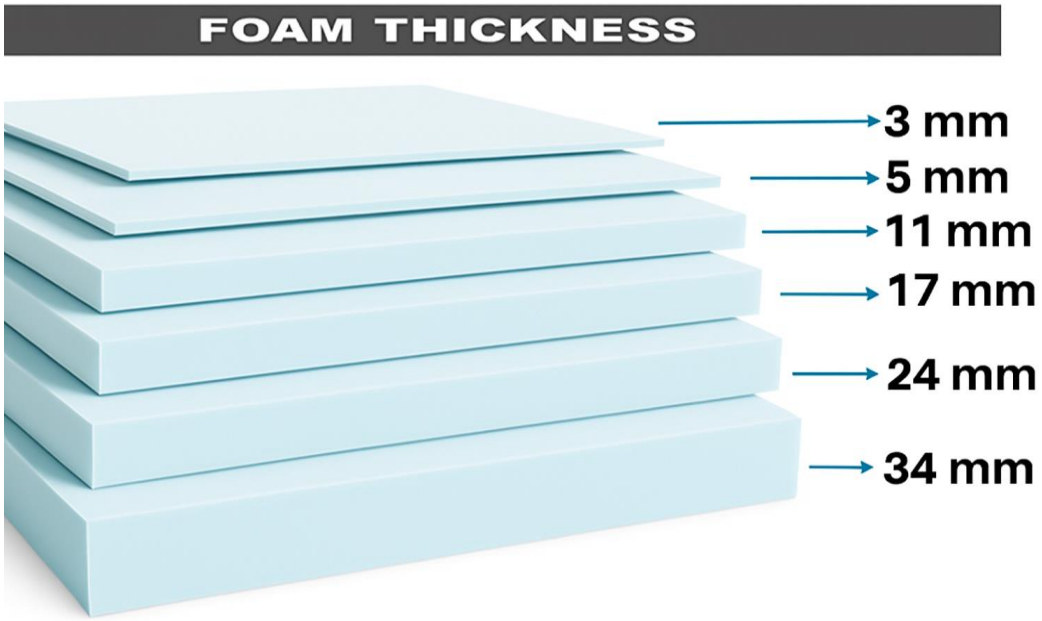

Figure 25. Photo. Styrofoam Sheets with Varying Thicknesses: 3 mm, 5 mm, 11 mm, 17 mm, 24 mm, and 34 mm.

The panels were affixed directly to the wall surface using non-damaging liquid adhesives, simulating gradual or localized protrusions. This arrangement created measurable, spatially distributed displacement zones, with known geometric offsets, used to assess detection sensitivity and noise in the 3D modeling workflows. Other 6 circular foam panels of known measured thicknesses were also attached to each of the 6 circular CPs. This was done to simulate displacement at those CPs. The names of the CPs and the thicknesses for their circular displacements were as follows:

- LU (Left-Upper) – 24 mm
- LD (Left-LoCPs.– 11 mm
- MU (Middle-Upper) – 5 mm
- MD (Middle-Lower) – 30 mm
- RU (Right-Upper) – 3 mm
- RD (Right-Lower) – 17 mm

Initially, at Epoch 1, the wall only contained the CPs marked by flat paper stickers on its surface to capture the baseline data. The foam pieces were then carefully added to the corresponding areas to generate a new “displaced” configuration, Epoch 2. This setup enabled high-fidelity temporal comparisons between sensor outputs and proper assessment of the minimum detectable displacement by each method.

EXPERIMENTAL STRATEGY AND EPOCH PLANNING

All activities at the CW were conducted under laboratory-controlled field conditions. The location, situated alongside a paved access road, allowed for safe instrument setup and repeatable measurements. Personnel adhered to university safety protocols for drone operation, tripod-based LiDAR scanning, and RTS work near the roadway. Because no excavation, backfill, or structural modification were involved, the validation experiment posed no structural risk and was logistically simple to repeat as needed. The use of foam along with removable adhesives ensured that the displacement simulation was both reversible and damage-free, maintaining wall integrity while providing controlled ground truth data for validation of photogrammetry, LiDAR, and RTS measurements. The measuring and modeling were conducted over two epochs: Epoch 1, baseline data collection without any induced displacement, and Epoch 2, data acquisition after the foam displacement simulation was applied.

This two-epoch setup allowed comparison between baseline and displaced models using C2C and RMSV analyses. The consistent use of the same GCPs, similar scanning stations, and environmental conditions across both epochs ensured reliable comparison. The length of the wall, ~22 m (~72 ft), enabled realistic GCP positioning and wide sensor coverage, while the ~3.7 m (~12 ft) height provided sufficient vertical span to test LiDAR and photogrammetry (with drone and DSLR pictures) modeling capacity against high-placed and low-placed CPs. Its relatively clean façade minimized the impact of surface irregularities or vegetation on data quality. As shown in Figure 26, the CW was modified between the first and second epochs by adding multiple planar targets to simulate wall displacements.

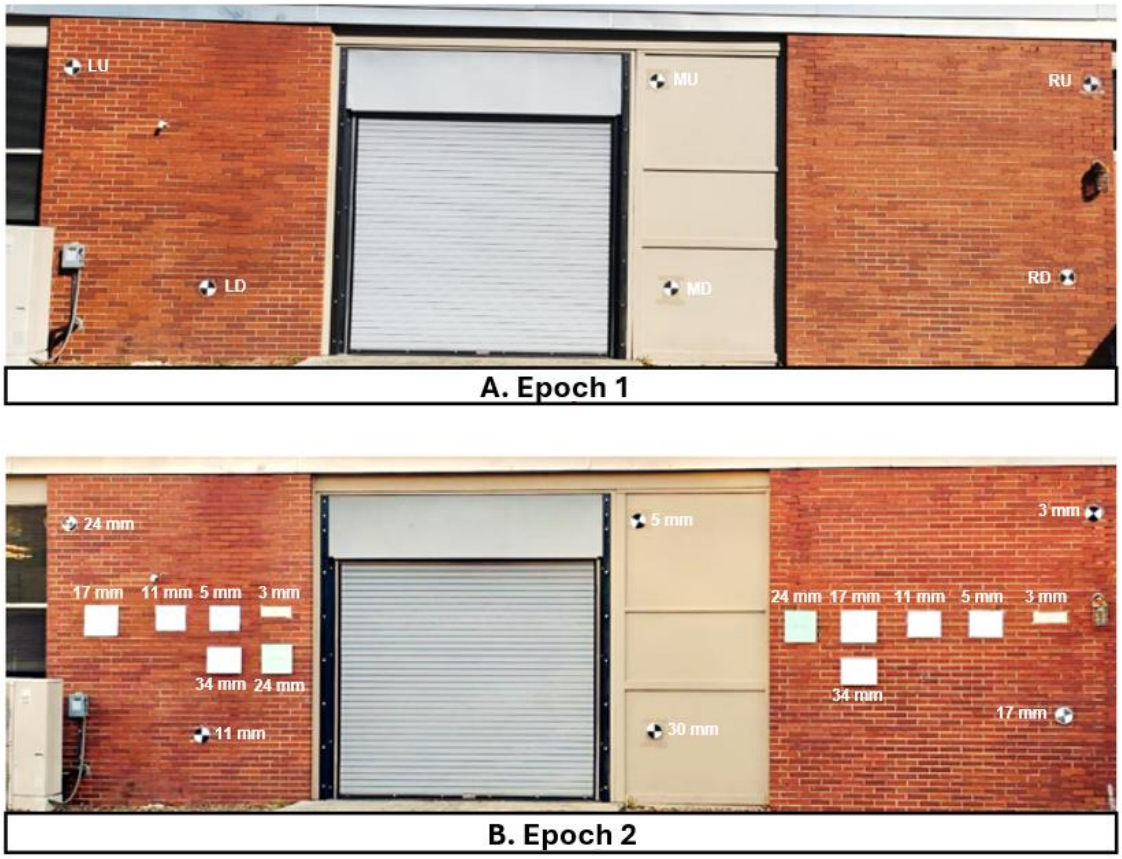

Figure 26. Photo. Visual comparison of the CW at Epochs 1 (baseline) and 2 (with added displacements).

SURVEY AND MODELING TECHNOLOGIES

To study the appropriateness of different modeling techniques under controlled conditions for potential adoption as a non-invasive inspection protocol, four key field instruments were deployed at the CW. These technologies represent the primary sensing methods used throughout the research project for capturing accurate geometric information, generating 3D virtual models, and monitoring wall displacements.

RTS – Leica's TCRP 1201+ R1000

Leica's accurate TCRP 1201+ R1000, robotic total-station instrument, RTS, was used as the benchmarking device for all distance, angular and coordinate-based measurements completed in the field for the CW. The main characteristics and accuracies of this device were described earlier in this chapter, in the "FIELD INSTRUMENTS – GENERAL DESCRIPTION" section. This instrument was used to perform all necessary measurements required to define and balance the local traverse, and to accurately determine the coordinates of all GCPs. Additionally, this RTS device was employed to capture, in the field, the spatial coordinates of all CPs on the CW.

Terrestrial LiDAR Scanner – Leica's ScanStation P50

Leica's ScanStation P50 was the primary, static, terrestrial LiDAR system used for high-resolution 3D scanning of the CW. The main characteristics and accuracies of this device were described earlier in this report, in the "FIELD INSTRUMENTS – GENERAL DESCRIPTION" section.
To capture the entire CW, 4 scanning stations were used. During scanning, 4 spherical targets (2 with 6-inch diameters and 2 with 9-inch diameters) were placed on 4 of the 5 GCPs. This was necessary to stitch/register the individual scans via the TB LiDAR approach, and to georeference all models completed by both LiDAR techniques, TB and visual-aligned. All indicated 4 targets were captured by each scan. The dense point-cloud data produced by the P50 scanner allowed highly detailed surface modeling and posterior C2C displacement comparisons between Epochs 1 and 2.

TB and VA LiDAR Models for Epochs 1 and 2 at CW

At the CW, two virtual 3D point-cloud models were developed using static terrestrial LiDAR. The objective was to compare their abilities to accurately capture small, simulated wall displacements. These models were generated during two separate sessions Epoch 1, conducted before placing the Styrofoam inserts, and Epoch 2, after the inserts were added to simulate wall movement. Each model was built using 4 LiDAR scans, planned to ensure adequate wall surface coverage and sufficient overlap for properVA. After removing pedestrian and vehicular noise, including ambient interference or reflective anomalies (such as solar beams), the scans were registered using two methods: TB and Visual-Alignment (VA). The TB registration employed four white spherical targets—labeled TA, TC, TD, and TE—mounted on GCPs and captured consistently in all scans. These targets served as fixed common points for stitching the scans with high spatial accuracy. Figure 27 and Figure 28 show finalized point-cloud models of the CW at Epochs 1, and 2, respectively. They were generated via the TB LiDAR registration approach.

For VA registration, the scans were aligned based on geometric overlaps, particularly between two close neighboring and adjacent scans. This method did not rely on physical targets but required consistent scan overlap. Both TB and VA models from each epoch were georeferenced using the selected local coordinate system, defined by the GCPs, which coordinates were accurately determined via a balanced, closed traverse. From these georeferenced point clouds, the coordinates of 6 CPs were extracted and compared across epochs to determine displacement. PD and DD analyses were performed to evaluate the sensitivity of each registration method in detecting simulated wall movement.

Figure 27. Photo. TB LiDAR point-cloud model of the undeformed CW in Epoch 1

Figure 28. Photo. TB LiDAR point-cloud model of deformed CW in Epoch 2

DSLR-Based Photogrammetry – Nikon D5300

One of the two photogrammetric evaluations of the CW was performed using a hand-held DSLR camera, Nikon's 5300. This camera was selected for its cost-efficiency and high image resolution (24.1 MP). Its main characteristics were described earlier in this report, in the "FIELD INSTRUMENTS – GENERAL DESCRIPTION" section. Images were captured manually following strict overlap and coverage protocols. Those images were processed in Agisoft's

Metashape to generate 3D photogrammetric models of the CW. To evaluate displacement detection sensitivity and relative accuracy, positional data and measurements were extracted from the models and compared with field measurements obtained using the benchmark RTS. Additionally, measurements from the LiDAR models were analyzed by performing position and DD assessments, along with C2C and M3C2 analyses. For the CW, 1080 and 1018 photos are taken by the NIKON D500 camera respectively for Epoch 1 and Epoch 2.

UAV-Based Photogrammetry – DJI Matrice 30 (M30)

An additional photogrammetric evaluation of the CW was performed using pictures taken with an UAV, DJI's Matrice 30. Its main characteristics were described earlier in this report, in the FIELD INSTRUMENTS – GENERAL DESCRIPTION section. This UAV was deployed to collect aerial imagery of the CW from two different altitudes and angles. The main flight was at a 110-ft altitude, and pictures were taken orthogonally to the ground (0 degree). Then, the UAV was flown at a lower altitude, 25 ft, to take oblique (45 degree) pictures closer to the wall. This facilitated fast large-scale image acquisition, particularly from oblique and top-down perspectives. UAV imagery was processed using DroneDeploy and Agisoft's Metashape software platforms for 3D model generation. Although more susceptible to vertical error, due to limited differences in elevation of the GCPs, the UAV-based photogrammetry still provided valuable data for model completeness and displacement detection comparisons. For the CW, at Epochs 1 and 2, the number of pictures taken by the UAV camera were 192 and 196, respectively.

LOCAL SYSTEM OF REFERENCE AT CW

For local reference purposes, a five-sided polygonal traverse was established near the CW. This was completed in Epoch 1 and served as reference for both Epochs, 1 and 2. The vertices of this traverse constituted the 5 GCPs used in this wall. They were identified as A, B, C, D, and E. The already indicated RTS instrument was employed to measure all angles and distances of this traverse. At each of the five traverse vertices, both internal and external horizontal angles were measured twice to identify potential mistakes and ensure repeatability and accuracy. If these repeated values were close to each other, they were averaged to reach their adopted values. If the difference between those two initial measurements was relatively large, then a mistake was detected, and measures were repeated. Likewise, each horizontal distance such as from point A to B and from B to A was measured four times (two in each direction) and averaged. Figure 29 & Figure 30 shows a plan view of the closed traverse, indicating the relative horizontal location of all GCPs, in feet. Please note that the selected reference North direction does not coincide with the true North.

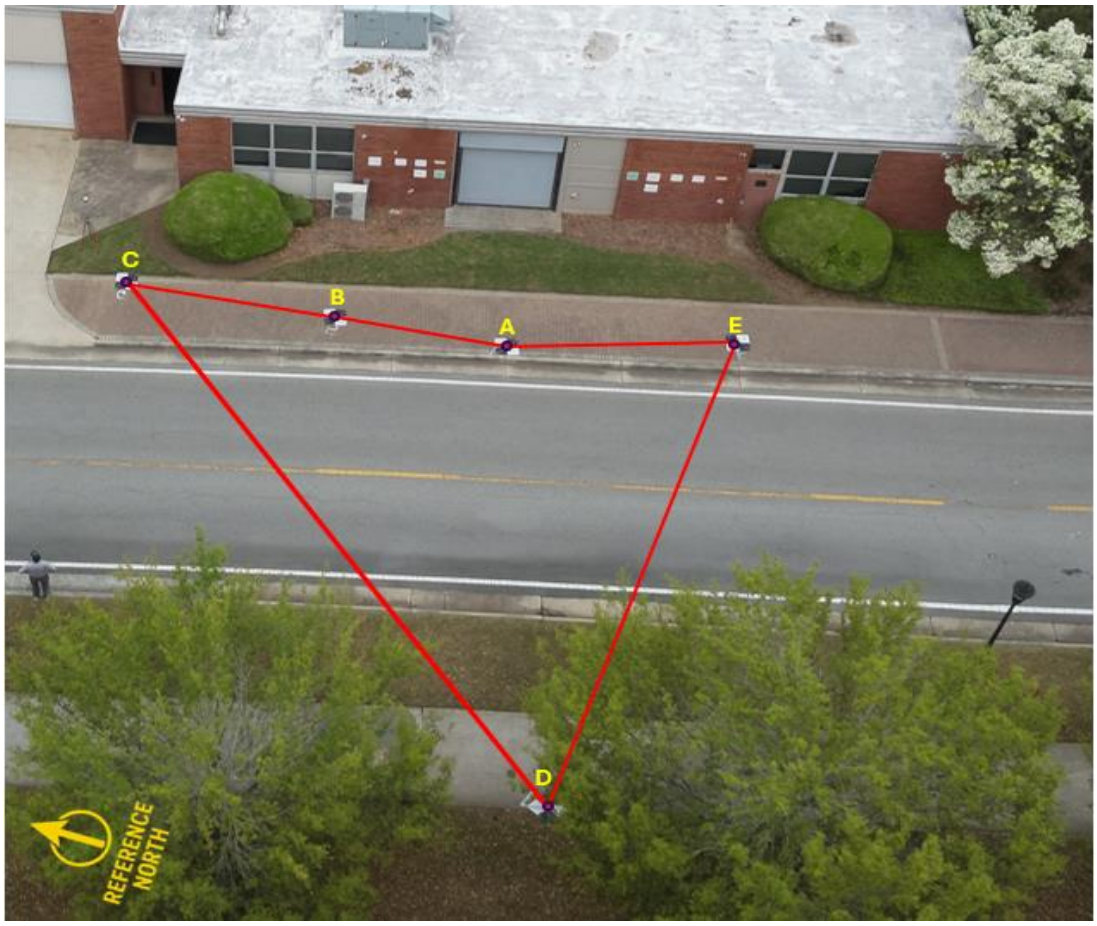

Figure 29. Photo. Aerial view of 5-sided closed traverse near CW

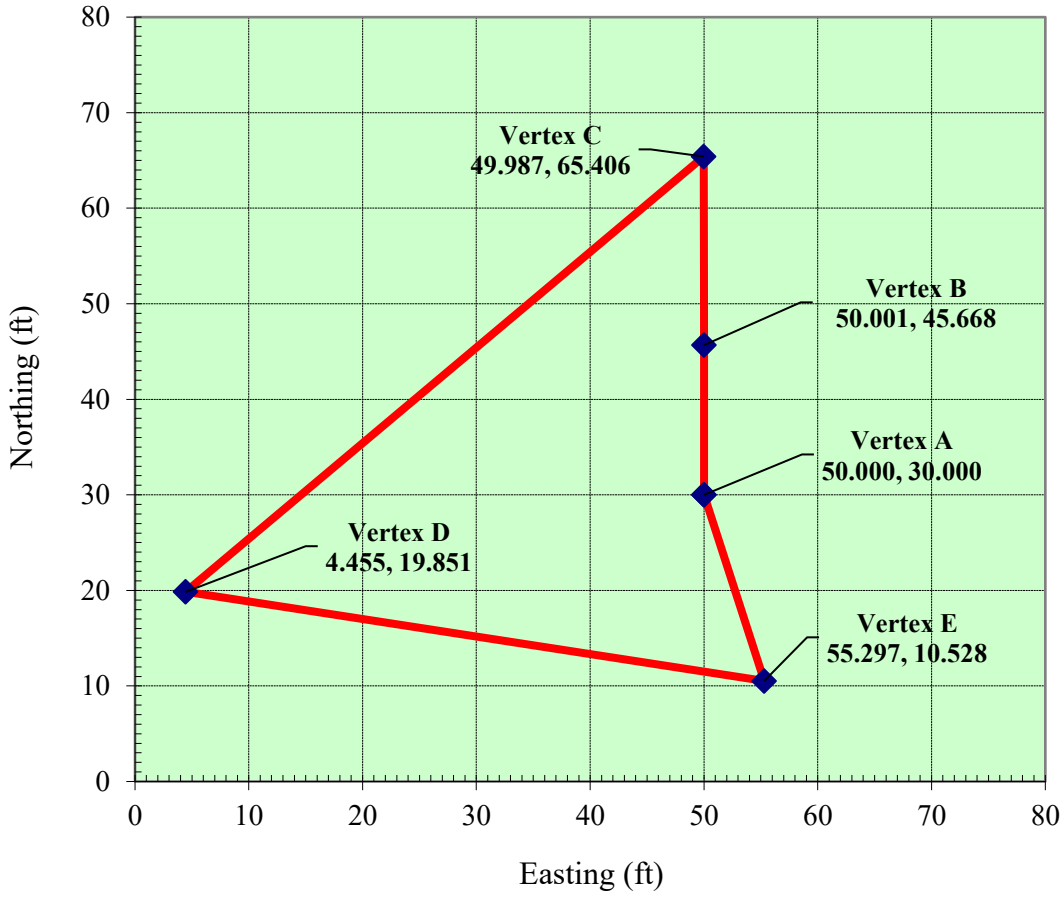

Figure 30. Graph. Horizontal coordinates of 5-sided closed traverse at CW

To adjust the angular measurements, at each vertex, the pair of internal and external angles was added and that sum compared against 360°. Then, the resulting minor local angular error (difference with respect to 360°) was equally balanced between both internal and external angles, ensuring consistency at each vertex. After this local adjustment, a global adjustment was applied across all five internal angles. The sum of the locally adjusted internal angles was found to be 539.99333°, which is 24.0 seconds less than the theoretical exact sum of 540° for a five-sided polygon. To correct this global angular misclosure, 4.8 seconds were evenly added to each internal angle.

The final 5 adjusted internal angles were then used in combination with the average side lengths to compute the local coordinates of the five vertices, 5 GCPs. The traverse had a perimeter of 52.329 m (171.684 ft) and resulted in a linear misclosure of only 2.3 mm (0.0076 ft). This yielded a longitudinal precision of 1 in 22,590, exceeding the 1:20,000 precision requirement specified in the GDOT Survey Manual (GDOT, 2022). Elevation differences were similarly determined using trigonometric leveling, which required vertical angle measurements. The elevation misclosure was -2.2 mm (-0.007 ft). The final adjusted internal angles, paired with the measured horizontal and vertical side lengths, produced a highly accurate local coordinate system. These GCP coordinates served as the foundational reference for georeferencing all spatial models of CW, via LiDAR, and via DSLR-based and UAV-based photogrammetry. Table19 presents a summary of the characteristics of the resulting traverse calculations, including their errors of closure and attained longitudinal precision. Table 20 shows the resulting spatial coordinates (X, Y, Z) of all 5 GCPs.

Table 19. Characteristics of 5-sided, closed traverse at CW

Traverse at Bridge	Perimeter	Total Horizontal Angular Error of Closure	Attained Longitudinal Precision	Elevation Error of Closure
	ft ; [m]	seconds	Ratio	ft ; [mm]
CW	171.684 ; [52.33]	-24.00	1/22,590	-0.007 ; [-2.2]

Table 20. Local spatial coordinates of GCPs at CW

GCPs	Easting (ft)	Northing (ft)	Elevation (ft)
	X	Y	Z
A	50.000	30.000	0.000
B	50.001	45.668	0.010
C	49.987	65.406	0.067
D	4.455	19.851	0.336
E	55.297	10.528	0.418

CPS AT CW

Six CPs were marked on the CW to monitor simulated displacements between Epochs 1 and 2. Each CP was a circular, 6-inch-diameter, black & white sticker, for easy and precise detection in both LiDAR and photogrammetry models. The CPs were arranged in three vertical pairs left, center, and right—each consisting of one upper and one lower marker, providing complete coverage for tracking deformation in both horizontal and vertical directions. Figure 31 illustrates the configuration and appearance of a typical CP pair on the CW.

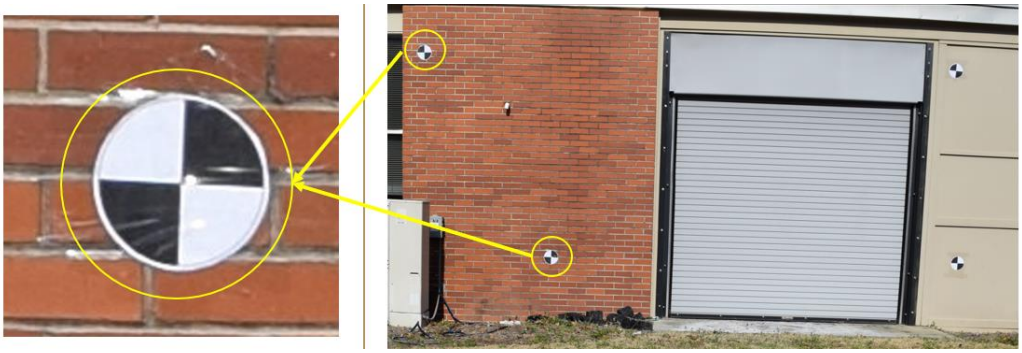

Figure 31. Photo. Black-and-white CPs on CW

The 3D coordinates of each CPs were measured using the RTS instrument from two different GCPs to detect mistakes and enhance accuracy. Again, the coordinates from both observations were averaged to adopt final coordinates. This procedure was repeated for both Epoch 1 and Epoch 2, enabling accurate comparison for displacement evaluation. RTS-based CP coordinates from Epoch 1 served as the benchmark for comparing non-contact sensing technologies, including LiDAR, and both UAV-based, and DSLR-based photogrammetry. These RTS values ensured consistent comparison across different 3D models developed in the study. Table 21 and Table 22 summarize the raw RTS measurements from each station and the final average values, respectively.

Table 21. CPs – Raw RTS-based Coordinates from Two different GCPs

CPs	Easting ft	Northing ft	Elevation ft
LU from A	65.210	46.764	10.876
LU from D	65.213	46.758	10.869
LD from A	65.968	42.141	3.607
LD from D	65.970	42.133	3.591
MU from A	68.791	27.570	10.920
MU from D	68.791	27.559	10.913
MD from A	68.906	27.024	3.794
MD from D	68.909	27.018	3.793
RU from A	70.795	13.021	10.969
RU from D	70.794	13.014	10.962
RD from A	70.620	13.923	4.418
RD from D	70.620	13.917	4.413

Table 22. CPs - Final Averaged RTS-based Field Coordinates

Locations of CPs	Name of CPs	Easting ft	Northing ft	Elevation ft
Left & up	LU	65.212	46.761	10.873
Left & down	LD	65.969	42.137	3.599
Medium & up	MU	68.791	27.565	10.917
Medium & down	MD	68.908	27.021	3.794
Right & up	RU	70.795	13.018	10.966
Right & down	RD	70.620	13.920	4.416

The comparison between these modeling techniques and the RTS reference enables quantification of positional discrepancies for their proper evaluation and potential adoption as an inspection methodology under controlled conditions.

EPOCH-1 ANALYSIS OF CW MODELS

To evaluate the relative accuracy of the developed models, the RTS field data from Epoch 1 was used as the reference dataset. Each of the 6 circular CPs, on the CW, served as evaluation targets. First, their position coordinates were measured in the field by using the accurate benchmarking RTS instrument. This set of RTS-based CP coordinates, from Epoch1, was referred to as Robotic Total Station Data from Epoch 1 (RTS1). Additionally, the coordinates of all 6 CPs were extracted from the finalized, different, point-cloud models, generated by using various technologies and processing workflows. The 6 CP positions, and 15 non-repeated distances among them, were compared between each model and the reference RTS1 set. A total of seven model types were assessed for Epoch 1:

- ML1 – Metashape model with a large number (1080 photos) of DSLR images
- MM1 – Metashape model with a medium number (590 photos) of DSLR images
- MS1 – Metashape model with a small number (295 photos) of DSLR images
- LV1 – LiDAR model using VA
- LT1 – LiDAR model using TB alignment
- MD1 – Metashape model generated from UAV images (192 photos)
- DG1 – DroneDeploy model generated from UAV images with CGPs in ground only (192 photos).
- DE1 – DroneDeploy model generated from UAV images with auxiliary elevated GCPs (192 photos).
- PL1 – Pix4D Mapper model with a large number (1080 photos) of DSLR images

PD at CW in Epoch 1

In this study, the position of each checkpoint (CP) is defined by a vector $\overrightarrow{V_p}$ = (x_p, y_p, z_p), originating from the adopted local reference system (0, 0, 0). Its magnitude, representing the distance from the origin, is calculated with equation 12:

$$\left|\overrightarrow{V_p}\right| = \sqrt{{x_p}^2 + {y_p}^2 + {z_p}^2} \qquad (12)$$

RTS field measurements provide the reference vector defined by coordinates $\overrightarrow{V_{RTS}} = (x_{RTS}, y_{RTS}, z_{RTS})$, while model-based coordinates yield, $\overrightarrow{V_{Mod}} = (x_{Mod}, y_{Mod}, z_{Mod})$. Due to differences in modeling and postprocessing, these vectors rarely match. The discrepancy between them is represented by equation 13:

$$\overrightarrow{V_{Dif}} = \overrightarrow{V_{Mod}} - \overrightarrow{V_{RTS}}. \qquad (13)$$

The PD (position discrepancy) is defined as the magnitude of this difference is calculated by equation 14:

$$\left|\overrightarrow{V_{Dif}}\right| = \sqrt{(x_{Mod} - x_{RTS})^2 + (y_{Mod} - y_{RTS})^2 + (z_{Mod} - z_{RTS})^2} \qquad (14)$$

PDs are always positive and serve as a metric for evaluating modeling accuracy relative to benchmark data.

The extraction of position coordinates from each final georeferenced model may incorporate user-induced noise, especially if the users are not experienced. That is, different software users may generate slightly different scaled/georeferenced models and may identify different coordinate positions for each CP. This was investigated for the photogrammetry models generated via Metashape (ML1, MM1, MS1, and MD1) in Epoch 1. The CP coordinates from each of those 4 models were compared against the corresponding ones obtained in the field, with the benchmarking instrument, Epoch 1, RTS1. Those 4 models were assigned to 4 different groups of students, with 3 or 4 members each, who were taking a graduate-level course on Intro to CRP at GSU. Each student group was designated as User 1, 2, 3, and 4. Each group generated, scaled, and georeferenced its own 4 photogrammetric models. Additionally, they extracted the positions of the 6 CPs from each model and compared them against the corresponding RTS1 coordinates. The following statistical metrics for all 6 CP samples were determined: MIN (minimum PD value), MAX (maximum PD value), MAE (mean absolute error = mean PD), MED |X| (median of absolute values = median of PD), STD-S (standard deviation of PD – sample), STD-P (standard deviation of PD – population), and RMSV (RMSV of PD). These statistics are compared among users in Figure 32, and Figure 33. Each of these figures, respectively, show PDs determined as [ML1-RTS1], [MM1-RTS1], [MS1-RTS1], and [MD1-RTS1]. In addition, each of those figures includes bars representing the average values of all 4 users. An analysis of these figures indicates that there are small differences between different users, especially for the [ML1-RTS1], [MM1-RTS1] and [MS1-RTS1] comparisons. However, larger deviations are observed in the [MD1-RTS1] comparison, not only among different users, but also with respect to RTS1 values.

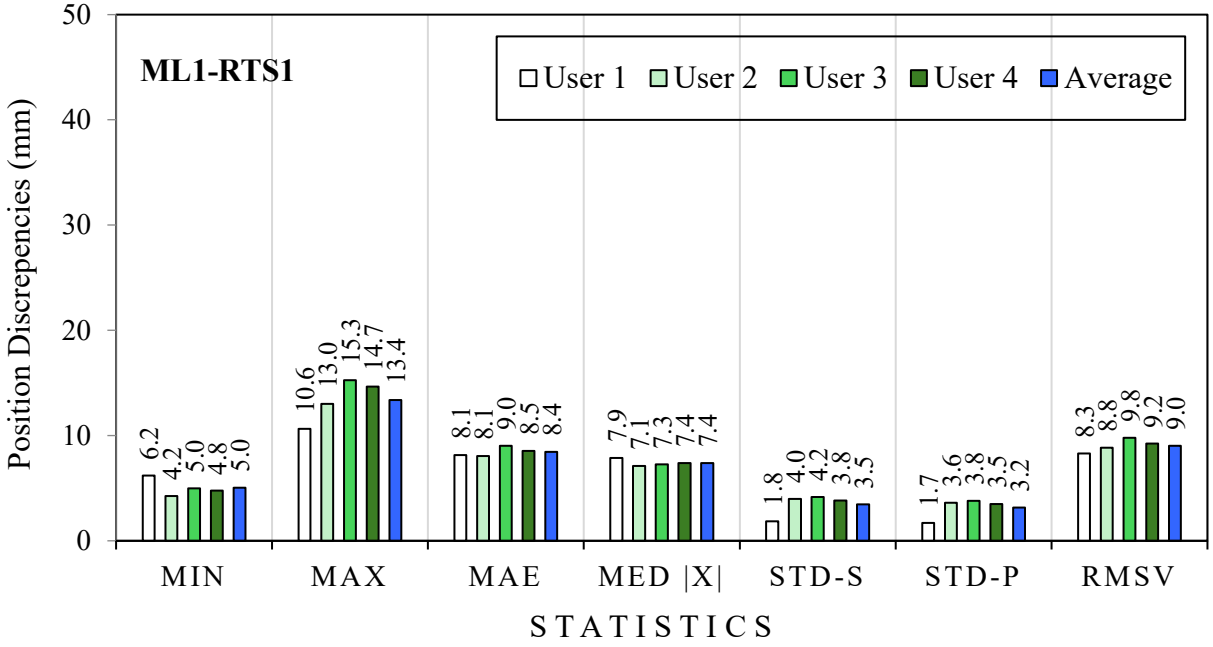

Figure 32. Chart. Comparison of PDs [ML1-RTS1] of 4 Different User Groups

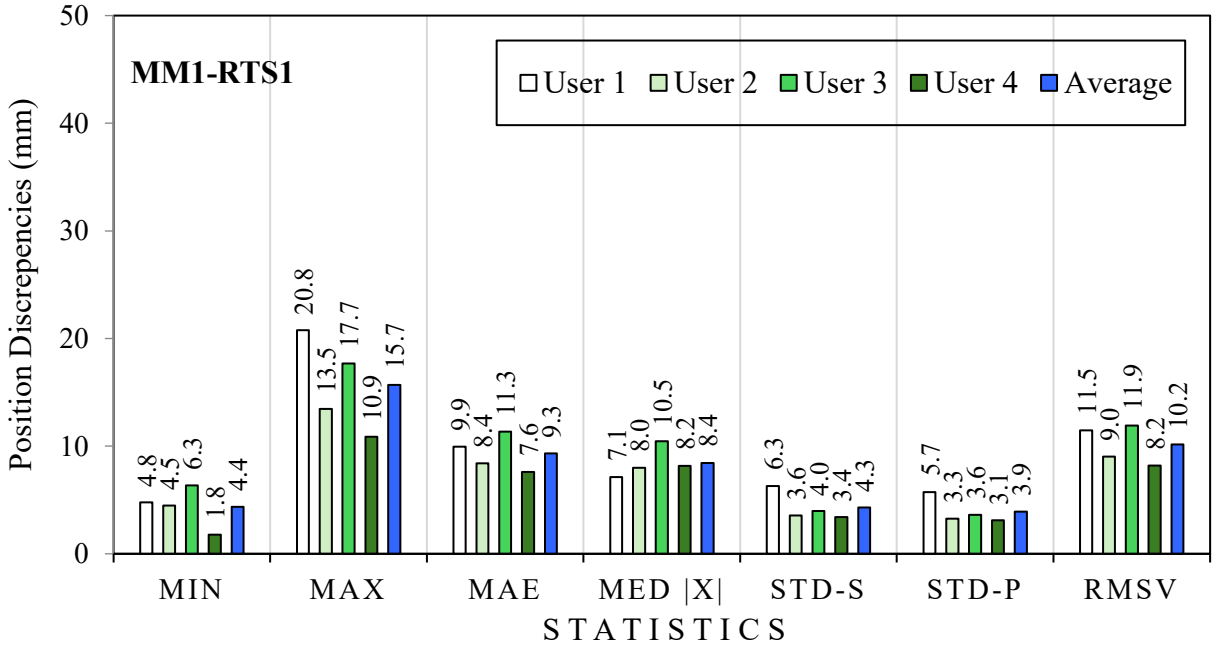

Figure 33. Chart. Comparison of PDs [MM1-RTS1] of 4 Different User Groups

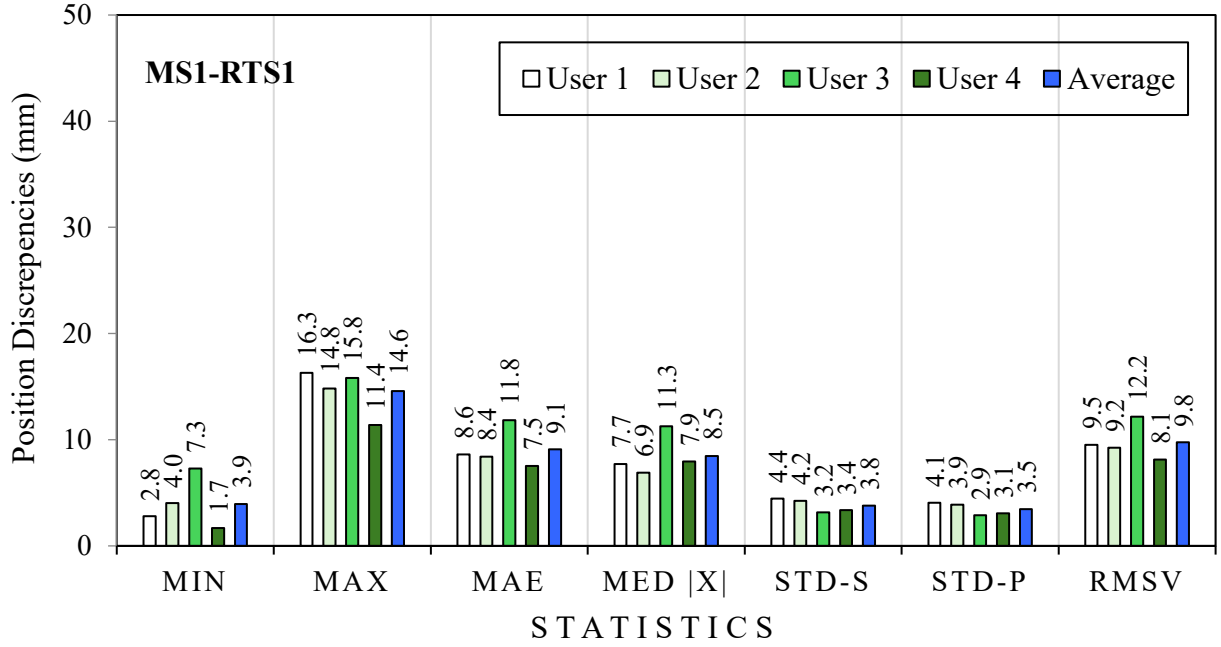

Figure 34. Chart. Comparison of PDs [MS1-RTS1] of 4 Different User Groups

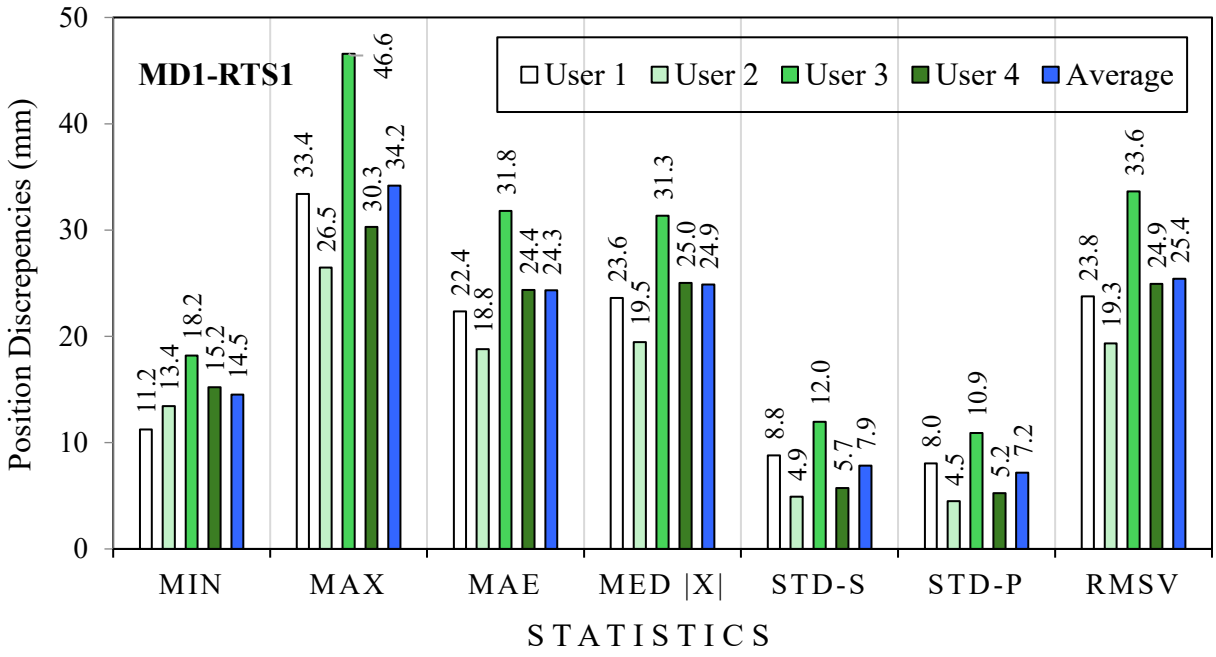

Figure 35. Chart. Comparison of PDs [MD1-RTS1] of 4 Different User Groups

Figure 36 compares PDs statistics of 6 CPs which coordinates were extracted from 6 different models in Epoch 1 (ML1, MM1, MS1, LT1, LV1, and MD1) and were compared against those measured with the benchmarking instrument in Epoch 1, RTS1. For the 4 Metashape models, ML1, MM1, MS1, and MD1, the averaged statistics obtained by 4 different user groups are reported in this figure. Regarding the 2 LiDAR-based models, LT1 and LV1, no multi-user analysis was carried out this time. In this case, two experienced graduate students generated and georeferenced the LiDAR models to extract CP positions, minimizing potential user-induced differences. In summary, the following PDs are presented in Figure 36: [ML1-RTS1], [MM1-RTS1], [MS1-RTS1], [LT1-RTS1], [LV1-RTS1], and [MD1-RTS1].

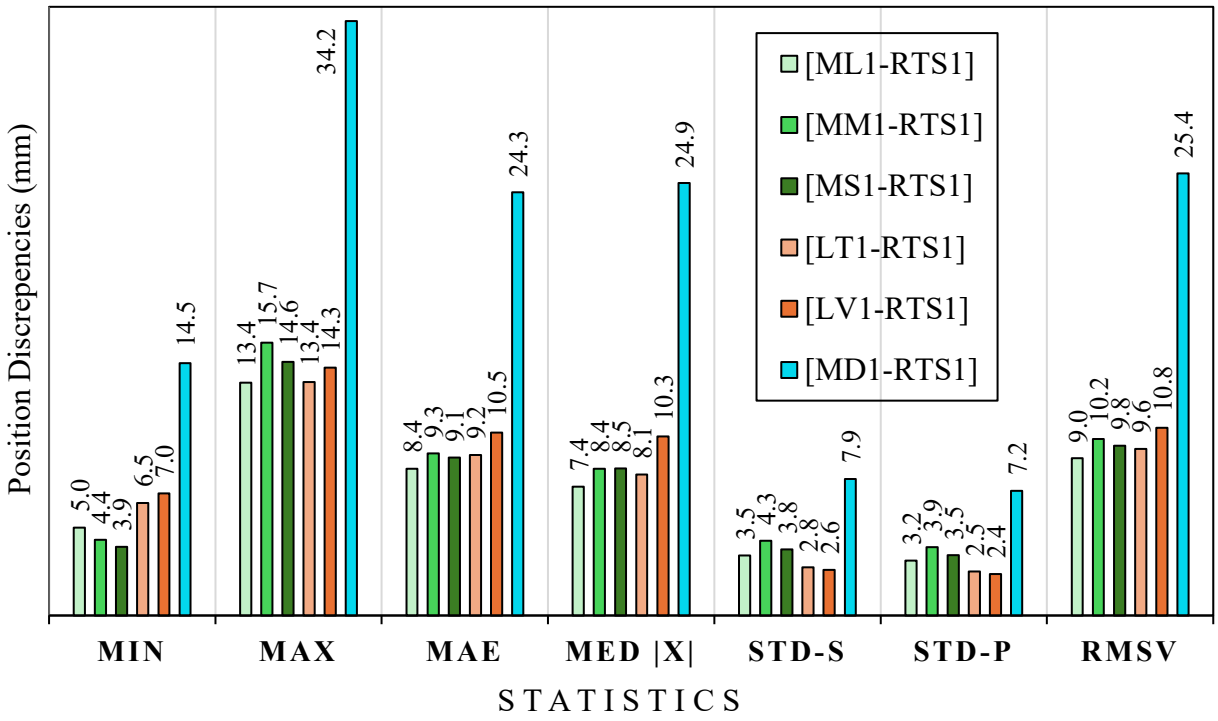

Figure 36. Chart. Statistical Analysis of 6 PDs between Epoch-1 Models and RTS1.

By considering Figure 36, among all methods, the Metashape model with a large number of DSLR images (ML1) performed best, exhibiting the lowest RMSV of 9.0 mm, but slightly larger standard deviations than LiDAR, with respect to RTS1 measurements, confirming its ability to generate accurate models. The photogrammetry performance slightly declined for medium (MM1) and small (MS1) number of image sets, indicating that image density influences photogrammetric accuracy, but not substantially. In contrast, the LiDAR models also showed strong performance, with the TB registration (LT1) slightly outperforming the visual-aligned version (LV1) in most metrics, except in the standard deviations. This emphasizes the benefit of employing TB registration or highly overlapped scans when successively visually aligning close-neighbor scans, preferably following a closed loop, as indicated in the study corresponding to bridge B2-Old River.

In stark contrast, the UAV-based Metashape model (MD1) showed the highest spatial difference with respect to the benchmarking measurements, RTS1. Its maximum discrepancy of 34.2 mm (1.35 in), its RMSV of 25.4 mm (1.00 in), and its STDs near 7.5 mm (0.30 in) highlight the limitations of aerial imagery without sufficient ground elevation control or dense image overlapping. These results underscore that DSLR-based photogrammetry in Metashape, when executed with high image volume and precise GCPs, can deliver accuracy comparable to or better than LiDAR. However, UAV photogrammetry must be carefully designed and supported with robust control data to avoid larger errors than those presented by the other considered techniques. Overall, this comparison validates the reliability of non-contact methods for displacement detection, with DSLR photogrammetry, TB and VA LiDAR emerging as the most accurate options for monitoring displacements in MSE/MB walls.

DD at CW in Epoch 1

Distances between pairs of control points on the CW were calculated using the Euclidean formula. For any two points, P (x_p, y_p, z_p) and Q (x_q, y_q, z_q), their spatial separation was computed with equation 16:

$$Distance\ PQ = \sqrt{(x_p - x_q)^2 + (y_p - y_q)^2 + (z_p - z_q)^2} \qquad (16)$$

Initially, this distance was derived from RTS field measurements, yielding PQ_{RTS}. The same calculation was repeated using coordinates extracted from a point-cloud model, producing PQ_{Mod}. The DDs (distance discrepancy) were then defined with equation 17, as the difference between these two:

$$DDs = PQ_{Mod} - PQ_{RTS} \qquad (17)$$

Since DDs reflect a directional difference, values may be either positive or negative depending on the model's deviation from the benchmark.

Since there were 6 CPs on the CW, a total of 15 non-repeated distances were calculated among all 6 of them. Then, for each model, 15 DDs were determined with respect to the same distances measured in the field, with the benchmarking RTS instrument.

In Epoch 1, a comparative assessment of DDs between various 3D modeling techniques (ML1, MM1, MS1, LT1, LV1, and MD1) and benchmark measurements, RTS1, was conducted using the 15 non-repeated distances among the 6 circular CPs on the CW. As summarized in Figure 37, the

considered DDs are [ML1-RTS1], [MM1-RTS1], [MS1-RTS1], [LT1-RTS1], [LV1-RTS1], and [MD1-RTS1].

Figure 37 indicates that both LiDAR models, with TB registration (LT1) and with visual-alignment registration (LV1), showed the best and almost similar performance with respect to RTS1 benchmarking measurements. They presented the smallest DDs, near symmetric minimum and maximum values, almost zero mean values, low STD-P values (~1.7 mm) and low RMSVs (~1.75 mm). Regarding the DSLR-based Metashape models (ML1, MM1, MS1), they can be considered as the second set of best performers with STD-P values ranging from 4.6 mm to 5.1 mm and RMSVs from 6.6 mm to 7.4 mm. All three of them showed a slight positive bias with small positive mean values, ranging from 2.6 mm to 5.5 mm. Unexpectedly, model MS1 (with the lowest number of images) slightly outperformed ML1 and MM1. It presented the lowest STD-Ps and RMSVs, showing slightly less deviations despite having fewer images. This suggests diminishing improvements beyond a certain image density when target placement is optimal.

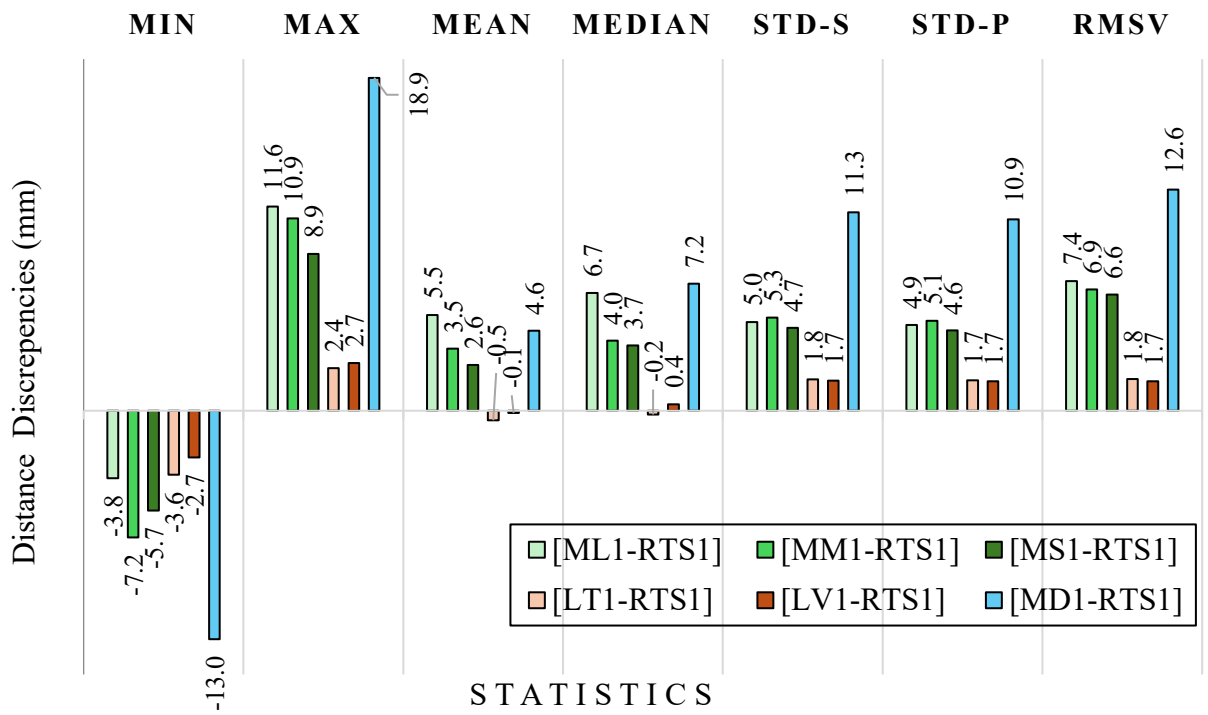

Figure 37. Chart. Statistical Analysis of 15 DDs between Epoch-1 Models and RTS1.

In contrast, the UAV-based Metashape model (MD1) exhibited the highest DDs, with RMSV = 12.6 mm, significantly higher than other models. This was followed by DroneDeploy (DS1, not shown in this chart), highlighting even greater variability in spatial consistency when using UAV imagery alone, with most GCPs on the ground at almost the same level. These findings almost align with those from the PD results (Figure 36), That is, both LiDAR techniques, TB and visual alignment (with high overlapping), are accurate. DSLR photogrammetry (even with moderate image sets) offers less accuracy but still can capture relatively small displacements while monitoring MSE/MB walls. On the other hand, UAV photogrammetry, while efficient, may introduce greater geometric error without proper horizontal and elevation control and/or high image overlap.

The data presented in Figure 37 can be used to estimate the noise level associated with DDs. These discrepancies were calculated by extracting 15 unique inter-point distances from each model—spanning all six control points —and comparing them to the corresponding field-measured distances obtained during Epoch 1 using the RTS instrument (RTS1 distances). Assuming the discrepancies follow a Gaussian distribution, the 95% confidence interval for expected variation which is expressed by equation 18 and variation is approximated as follows:

$$\{\mu - 1.96 \times \sigma \ , \ \mu + 1.96 \times \sigma\} \qquad (18)$$

Where μ is the MEAN value and σ is the STD-P.

For [ML1-RTS1]: $\{5.5 - 1.96 \times 4.9 \ , \ 5.5 + 1.96 \times 4.9\} = \{-4.1 \ , \ 15.1\}$ mm

For [MM1-RTS1]: $\{3.5 - 1.96 \times 5.1 \ , \ 3.5 + 1.96 \times 5.1\} = \{-6.5 \ , \ 13.5\}$ mm

For [MS1-RTS1]: $\{2.6 - 1.96 \times 4.6 \ , \ 2.6 + 1.96 \times 4.6\} = \{-6.4 \ , \ 11.6\}$ mm

For [LT1-RTS1]: $\{-0.5 - 1.96 \times 1.7 \ , \ -0.5 + 1.96 \times 1{,}7\} = \{-3.8 \ , \ 2.8\}$ mm

For [LV1-RTS1]: $\{0.4 - 1.96 \times 1.7 \ , \ 0.4 + 1.96 \times 1.7\} = \{-2.9 \ , \ 3.7\}$ mm

For [MD1-RTS1]: $\{7.2 - 1.96 \times 12.6 \ , \ 7.2 + 1.96 \times 12.6\} = \{-17.5, \ 31.9\}$ mm

From the above expressions, the noise level is estimated as the maximum absolute limit of each interval. This results in the following levels:

For [ML1-RTS1]: 15.1 mm

For [MM1-RTS1]: 13.5 mm

For [MS1-RTS1]: 11.6 mm

For [LT1-RTS1]: 3.8 mm

For [LV1-RTS1]: 3.7 mm

For [MD1-RTS1]: 31.9 mm

POSITION AND DDS ANALYSIS OF PIX4D MAPPER (PL1)

For this project, GDOT facilitated the use of a license for the Pix4D Mapper software to assess the viability and usability of this alternative 3D modeling technique, based on CRP. In Epoch 1, one model of the CW was generated with this software package. It is referred to as PL1.

For comparison purposes, Figure 38 shows the statistics of position discrepancies attained by PL1, ML1 and LT1 at all 6 CPs on the CW, all with respect to positions RTS1, measured in the field with the benchmarking instrument. In the figure, it is observed that the discrepancies associated with PL1 are much larger than those obtained with the ML1 and LT1 models.

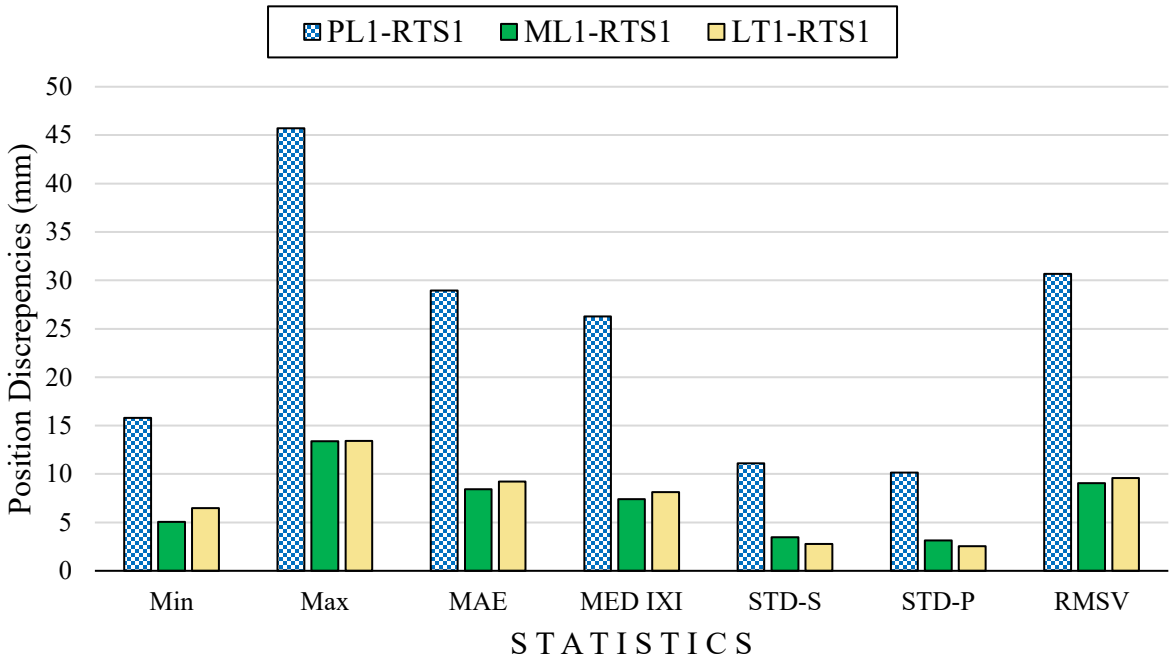

Figure 38. Chart. Statistical Analysis of 6 PDs between Epoch-1 Models and RTS1.

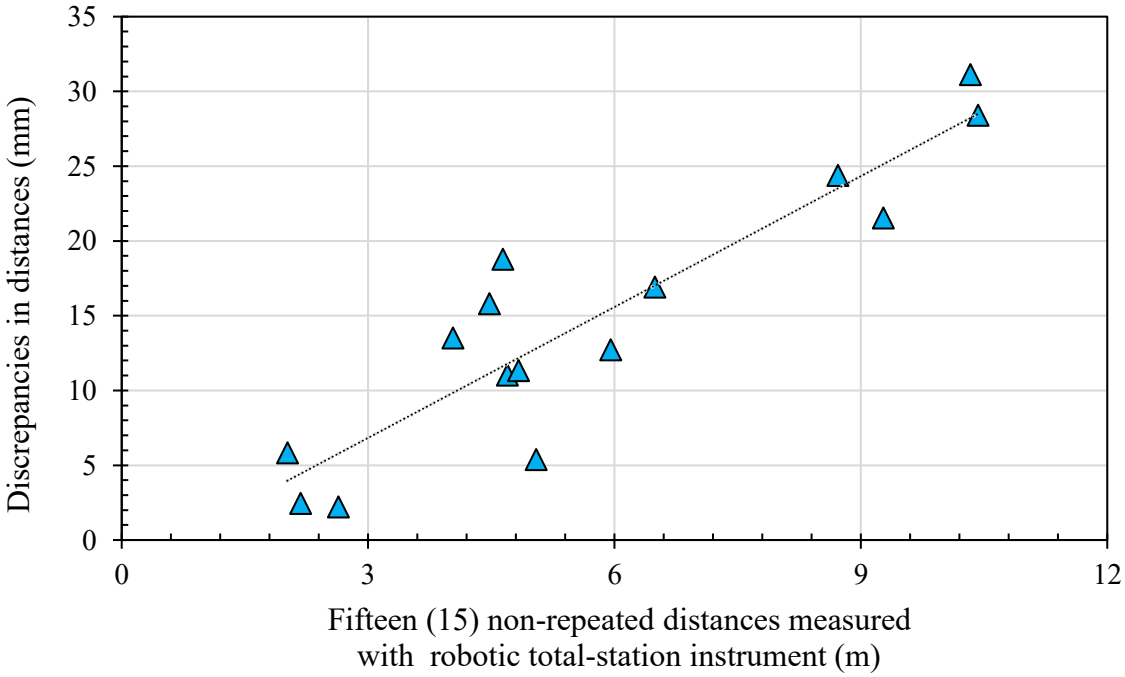

Figure 39. Graph. Discrepancies in 15 non-repeated distances between PL1 and RTS1.

Additionally, Figure 39 presents discrepancies in all possible 15 non-repeated distances among all 6 CPs on the CW. These discrepancies were determined by subtracting RTS1 field distances from the corresponding ones extracted from the georeferenced final model PL1. Apparently, the resulting PL1 model shows increased DDs with increased lengths.

EPOCH-2 ANALYSIS OF SIMULATED DISPLACEMENTS AT CW

This section evaluates the performance of each model in attempting to capture wall displacements during Epoch 2. To this end, a series of relatively small horizontal displacements ranging from 3 mm to 34 mm were simulated by attaching flat Styrofoam inserts of varying thicknesses to each CP, along with larger rectangular blocks affixed to other sections of the CW. These additions produced artificial displacements normal to the wall surface, defining the deformed configuration of the CW in Epoch 2.

At each CP, the imposed displacement was represented by a circular black-and-white foam insert (6 inches in diameter), centered precisely on the original CP location established in Epoch 1. Table 23 lists the thicknesses of the foam inserts applied to each CP, which correspond to the *true* horizontal displacements normal to the wall introduced in Epoch 2.

Table 23. Thicknesses of Attached Foam Inserts on the CPs

Position of CP	Name of CP	Attached Foam Thickness
Right & up	RU	3 mm
Medium & up	MU	5 mm
Left & down	LD	11 mm
Right & down	RD	17 mm
Left & up	LU	24 mm
Medium & down	MD	30 mm

Additionally, foam inserts were strategically placed across the wall to simulate realistic, graduated surface displacements. The configuration provided a reliable ground truth for assessing the sensitivity and accuracy of various non-contact sensing technologies, including terrestrial LiDAR and CRP. Figure 40 shows the distribution of all Styrofoam inserts on the CW, along with their corresponding thickness.

Figure 40. Photo. Styrofoam Inserts Simulating Displacements at CW

Several different models of the deformed CW in Epoch 2 were generated and are referred to as follows:

- ML2 – Metashape model with a large number (1018 photos) of DSLR images
- MM2 – Metashape model with a medium number (509 photos) of DSLR images
- MS2 – Metashape model with a small number (259 photos) of DSLR images
- LV2 – LiDAR model using VA
- LT2 – LiDAR model using TB alignment
- MD2 – Metashape model generated from UAV images (196 photos)
- DG2 – DroneDeploy model generated from UAV images with ground GCPs only (196 photos).

- DE2 – DroneDeploy model generated from UAV images with auxiliary elevated GCPs (196 photos).

Epoch-2 Displacements via Benchmarking RTS Instrument, [RTS2-RTS1]

In Epoch 2, following the application of simulated displacements to the CW, the new displaced positions of the six CPs measured normal to the wall were determined in the field using the benchmarking RTS instrument. This updated set of CP coordinates is referred to as Robotic Total Station Data from Epoch 2 (RTS2). To assess the measurement of repeatability and identify potential errors, the positions were recorded twice. The first and second measurements are denoted as Robotic Total Station Data from Epoch 2 Attempt 1 (RTS21) and Robotic Total Station Data from Epoch 2 Attempt 2 (RTS22), respectively. For reference, the original CP positions from Epoch 1 are labeled RTS1. Figure 41 compares the displacements derived from [RTS21 − RTS1], [RTS22 − RTS1], and their average values against the true displacements represented by the foam insert thicknesses.

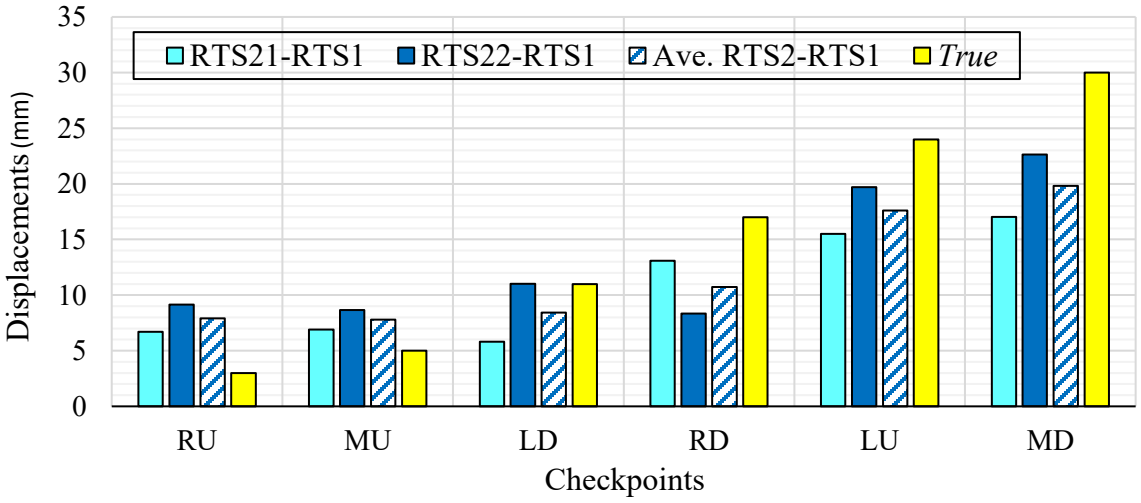

Figure 41. Chart. Displacements at 6 CPs [Epoch 2 – Epoch 1]

Figure 41 reveals that even the high-precision benchmarking RTS instrument encounters challenges in detecting small displacements in the 3–5 mm range. Moreover, while larger displacements are generally identified, their magnitudes tend to be slightly underestimated. As discussed later in this report (see section "Establishment of Floor Noise Associated with the Employed RTS Device"), the floor noise of the RTS instrument when operating in reflectorless mode at a distance of 40 meters is approximately 5.6 mm. However, this baseline may be elevated by various sources of error, including those related to instrument stationing, vertical alignment, aiming precision, atmospheric conditions, and inaccuracies in the coordinates of the reference GCPs. Consequently, small actual displacements (e.g., 3–5 mm) may fall within this noise threshold and thus remain indistinguishable using the RTS under the practical conditions of this study.

Despite these limitations, the strong consistency between the RTS21 and RTS22 measurements demonstrates excellent repeatability, reinforcing the reliability of the RTS device as a reference standard. The average values closely follow the expected trend of increasing displacement across the control points, confirming the RTS instrument's suitability for providing ground-truth data in the validation of other sensing technologies.

Subsequent analysis compared user-interpreted displacement results from each model type against both the RTS1 measurements of the non-displaced configuration (Epoch 1) and the *true* simulated displacements represented by the foam insert thicknesses. Figure 42 through Figure 45 present visual comparisons of displacement estimates reported by five different user groups, each consisting of 2–4 students enrolled in the "Introduction to CRP" graduate course at GSU. These

multiple user interpretations offer valuable insight into user-induced variability and the potential subjectivity inherent in data processing and model interpretation.

Epoch-2 Displacements via Models ML2 (Metashape with Large Image Set), [ML2 – RTS1]

Figure 42 illustrates the displacements determined by 4 or 5 users, at 6 CPs on the CW, using models ML2, which were generated at Epoch 2 via Metashape with a large DSLR image set (1018) pics). Those displacements are compared to the actual simulated displacements, indicated as *True* values. Overall, Figure 42 shows that models ML2 overestimated the actual displacements, especially the small ones (i.e., 3, 5, and 11 mm), with a better approximation to the larger ones (17, 24, and 30 mm). Among all participants, user 3 demonstrated the most consistent alignment with the *True* values of the largest displacements (RD, LU, and MD), indicating strong processing accuracy. These results confirm the ability of the ML2 models to capture displacements larger than 11 mm. However, some user sensitivity is observed when different individuals use Metashape.

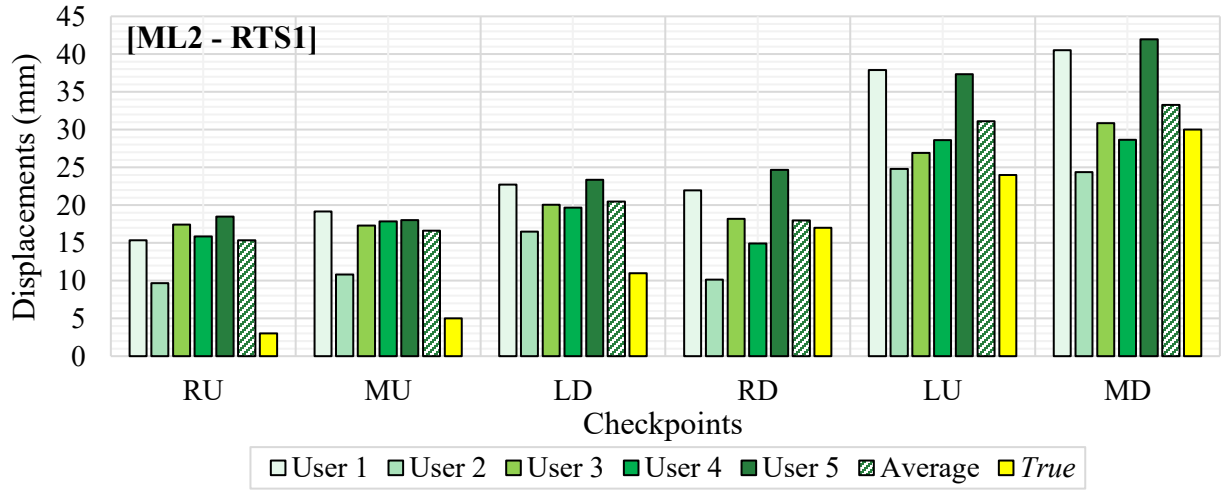

Figure 42. Chart. Displacements Captured at Epoch 2 via Models ML2 by Different Users [ML2 – RTS1]

Epoch-2 Displacements via Models MM2 (Metashape with Medium Image Set), [MM2 – RTS1]

Figure 43 presents similar displacement results as those in Figure 42, but derived from the MM2 model, processed with a medium number of DSLR images (509 photos) in Agisoft's Metashape. The results from five users are compared against the known *True* displacement values at the CPs. In this case, it is observed less user variability. On average, users accurately determined the largest four displacements (11, 17, 24, and 30 mm) at LD, RD, LU, and MD. User 3 being closest to most of those *True* values. Again, the smallest displacements (3, 5, and 11 mm) were overestimated by all users, especially the two smallest ones (3 and 5 mm). In general, models MM2 performed well, with marginally less user-to-user variation, and slightly more accuracy than models ML2. This indicates that Metashape remains effective to capture displacements larger than 11 mm with a medium image count. It even showed slightly more accuracy than when using a denser dataset.

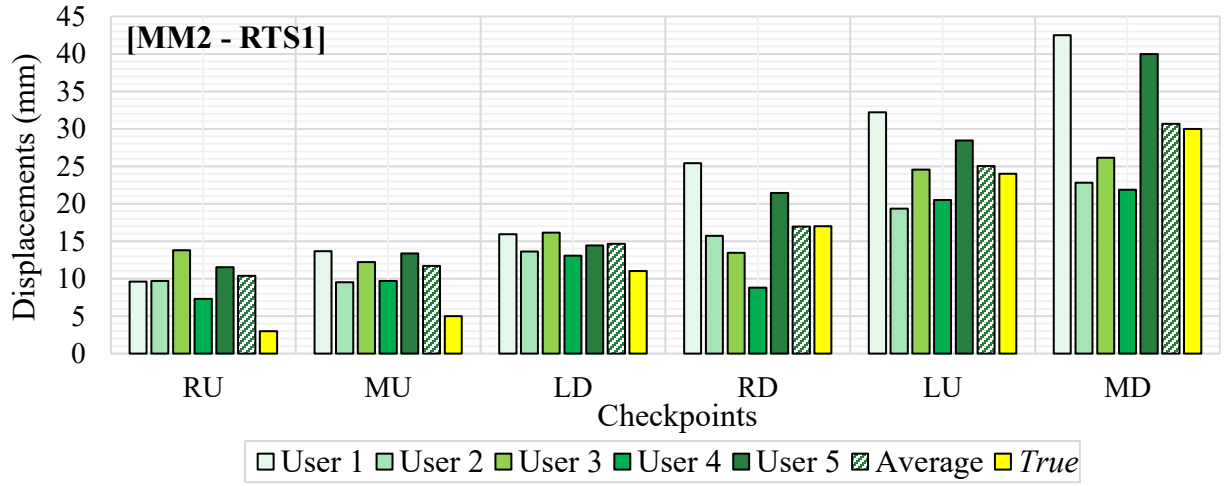

Figure 43. Chart. Displacements Captured at Epoch 2 via Models MM2 by Different Users [MM2 – RTS1]

Epoch-2 Displacements via Models MS2 (Metashape with Small Image Set), [MS2 – RTS1]

Figure 44 shows displacement results at 6 CPs derived from MS2 models, generated using a small number of DSLR images (259 photos in Epoch 2) in Agisoft's Metashape. The plot compares results from five users against true displacement values. This time, more user variability has been observed than those resulting from the ML2 and MM2 models. On average, the small displacements (3 and 5 mm) continued to be excessively overestimated, and the larger displacements (11, 17, 24, and 30 mm) were more accurately determined. Overall, the MS2 model demonstrated that while Metashape can still deliver meaningful displacement trends with fewer images, the reduction in photo count increases sensitivity to user judgment and can result in larger deviations, especially at higher-deformation CPs. This highlights the need for denser image datasets for improved accuracy and consistency in CRP

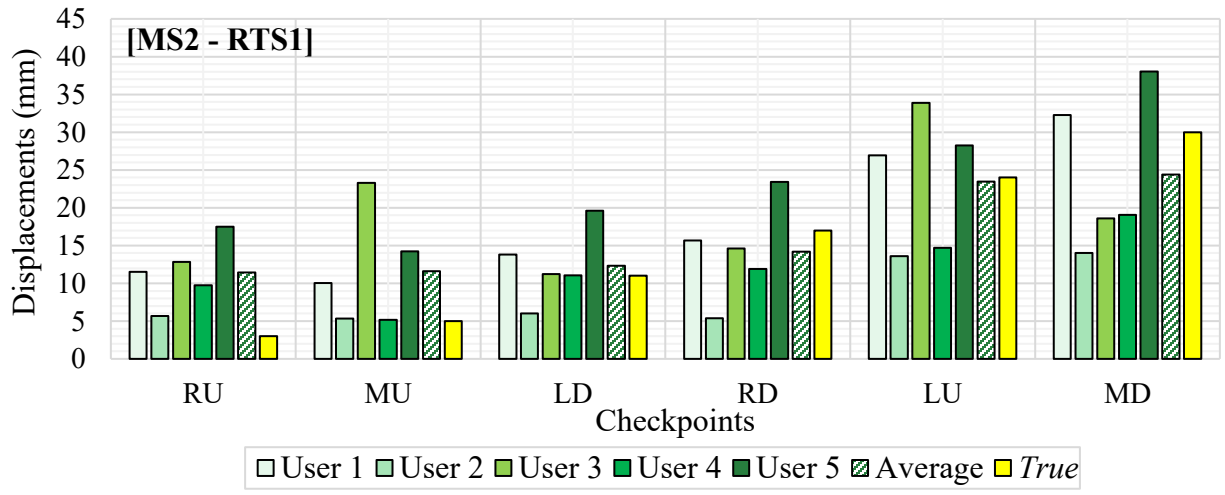

Figure 44. Chart. Displacements Captured at Epoch 2 via Models ML2 by Different Users [ML2 – RTS1]

Epoch-2 Displacements via Model DG2 (DroneDeploy without Elevated GCPs), [DG2 – RTS1]

Figure 45 presents displacement results extracted from the DG2 model. This model was generated via the DroneDeploy software platform, using UAV images without elevated GCPs. That is, the employed GCPs were those defined by the closed traverse, at ground level, on the sidewalks near the CW. As explained earlier in this report, in Epoch 2, 196 aerial pictures were taken from 2 different altitudes (110 ft, and 25 ft) and 2 angles (0° vertically, and 45° oblique). This figure compares displacements determined by four users, at 6 CPs (RU, MU, LD, RD, LU, MD), against the *True* values derived from the thicknesses of the Styrofoam inserts attached to each CP to simulate horizontal displacements, normal to the CW. The model demonstrated large deviations from actual displacements. Across all CPs, the displacements reported by most users were drastically overestimated, exceeding 700 mm at several CPs (RU, MU, LU), when all *True* displacements were ≤ 30 mm. User 1 reported the largest errors, with 3 values reaching over 1100 mm at RU, MU and LU. Even the lowest estimates provided by User 4 remain excessively higher than the *True* values. This widespread overestimation highlights limitations of UAV photogrammetry, using the number of pictures taken as previously indicated (see section on *UAV-Based Photogrammetry – DJI Matrice 30 (M30)*), and more critically, when elevated GCPs are not used. The vertical inaccuracy is severe, especially at CPs located higher on the wall, indicating poor Z-axis control. In summary, the so generated DG2 models, without elevated GCPs, are not reliable for precise displacement analysis in MSE/MB walls. The models failed to approximate the *True* values at any checkpoint, emphasizing the necessity of vertical GCPs distribution in UAV-based modeling workflows.

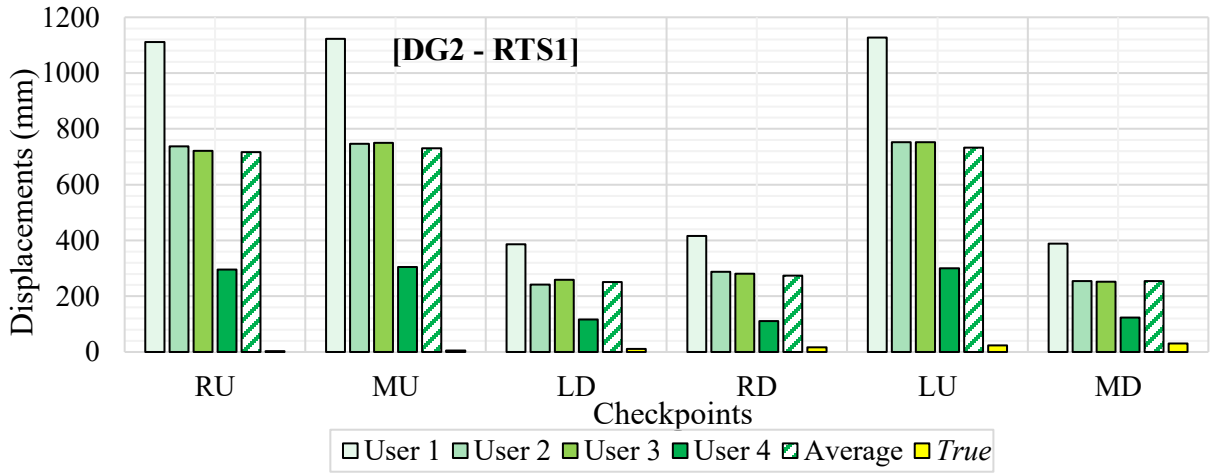

Figure 45. Chart. Displacements Captured at Epoch 2 via Models DG2 by Different Users [DG2 – RTS1]

Epoch-2 Displacements via Model DE2 (DroneDeploy with Elevated GCPs), [DE2 – RTS1]

Since the previous DG2 models showed deficient accuracy, it was decided to analyze the performance of UAV-based photogrammetric models using elevated GCPs. The expectation was to improve vertical and overall positional accuracy on MSE/MB walls. In this case two EACPs were considered, one at each upper corner of the CW. Their coordinates were obtained in the field by using the accurate RTS instrument stationed at a nearby GCP and using a second GCP as backsight. This was done twice, using different GCPs. Each pair of corresponding coordinates were averaged. That is, the coordinates of the EACPs were not as accurate as those of traverse-derived GCPs but were still carefully determined.

Figure 46 shows displacement results from one DE2 model (DroneDeploy with Elevated GCPs) for Epoch 2. It compares values from User 5 against the averaged values obtained with 2 RTS2

measurements ([RTS21-RTS1] and [RTS22-RTS1]), and with the *True* displacements at 6 CPs on the CW. Unlike the version without EACPs, this model shows substantial improvement. Even though the smaller displacements (3, 5, and 11 mm) are still extensively overestimated, the larger displacements (17, 24, and 30 mm) are more closely approximated, especially the largest one (35.8 mm vs 30 mm). This shows that the added elevated control points substantially improved the accuracy of the resulting DE2 model when compared to the earlier version without elevated control points. Overall, this result validates the critical role of properly placed elevated GCPs in enhancing the vertical accuracy of UAV-based models. The DE2 model with EACPs demonstrates that DroneDeploy can be viable for displacement analysis, especially when vertical control is correctly implemented.

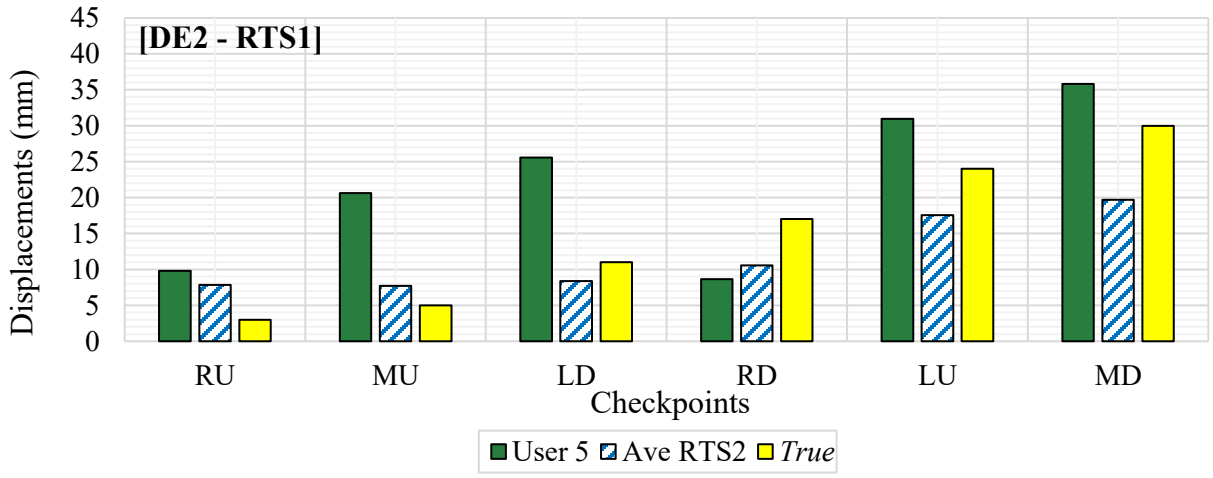

Figure 46. Chart. Displacements Captured at Epoch 2 via Model DE2 by One User [DE2 – RTS1]

Epoch-2 Displacements via Model LT2 (LiDAR with TB Alignment), [LT2 – RTS1]

Figure 47 presents displacement measurements extracted from the LT2 model, which used terrestrial LiDAR point-cloud data registered with TB alignment. The figure shows User 5's results compared against the averaged values obtained with 2 RTS2 measurements ([RTS21-RTS1] and [RTS22-RTS1]), and against the *True* simulated displacements across 6 CPs. The model exhibits strong agreement with *Ture* values across most CPs, except with the smallest displacement (determined as 12.6 mm instead of 3 mm at RU). For the larger displacements at LU and MD, the results tracked closely to True, though values were slightly lower than actual ones. These results affirm the reliability of LiDAR when paired with TB registration. The consistent alignment across most displaced CPs, especially in higher displacement areas, demonstrates low error with a performance like that of the accurate RTS instrument. The LT2 model performed even fine while capturing a 5-mm displacement as 8.1 mm. TB LiDAR is well-suited for monitoring spatial geometry requiring accuracy and repeatability. There is minimum human influence in these results as the employed spherical targets were captured in the field by the scanning instrument. If those targets were properly located and verticalized on the GCPs, the operator-induced error should be minimized.

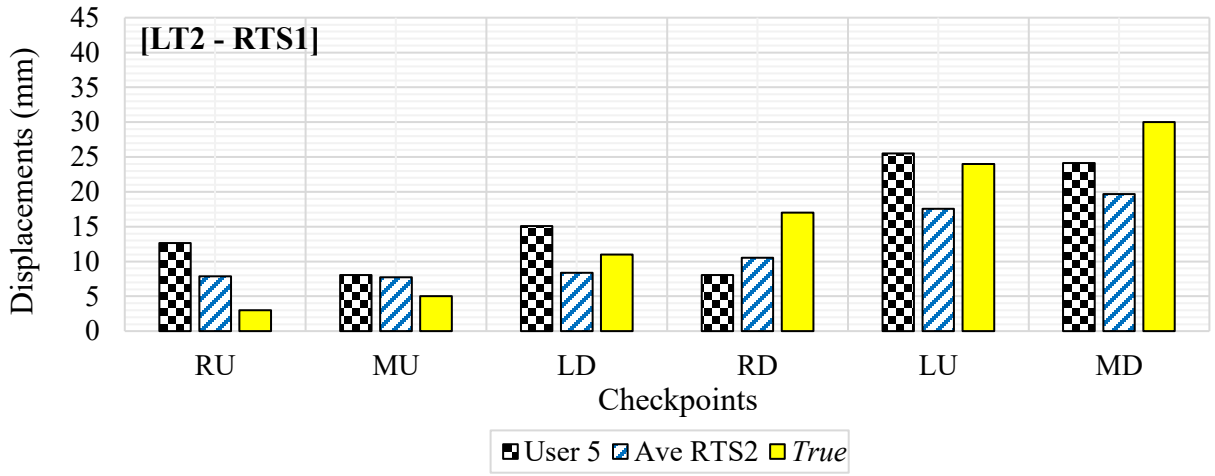

Figure 47. Chart. Displacements Captured at Epoch 2 via Model LT2 by One User [LT2 – RTS1]

Epoch-2 Displacements via Model LV2 (LiDAR with Visual-Alignment), [LV2 – RTS1]

Figure 48 illustrates displacement measurements derived from the LV2 model, where LiDAR scans were registered using Leica's VA technique. The graph shows User 5's results compared to the averaged values obtained via 2 RTS2 measurements ([RTS21-RTS1] and [RTS22-RTS1]), and to the *True* simulated displacements at 6 CPs. User 5's estimates generally follow the correct trend. Nevertheless, as has been the case with all other modeling techniques, the small displacements at RU (3 mm) and at MU (5 mm) are highly overestimated (15.1 and 13.1 mm), with RU showing the largest deviation. LD shows good agreement, while RD is underestimated (10.0 vs 17 mm). For the high-displacement CPs, LU (24 mm) and MD (30 mm), the determined values are under the *True* ones by approximately 5–8 mm, though still directionally consistent.

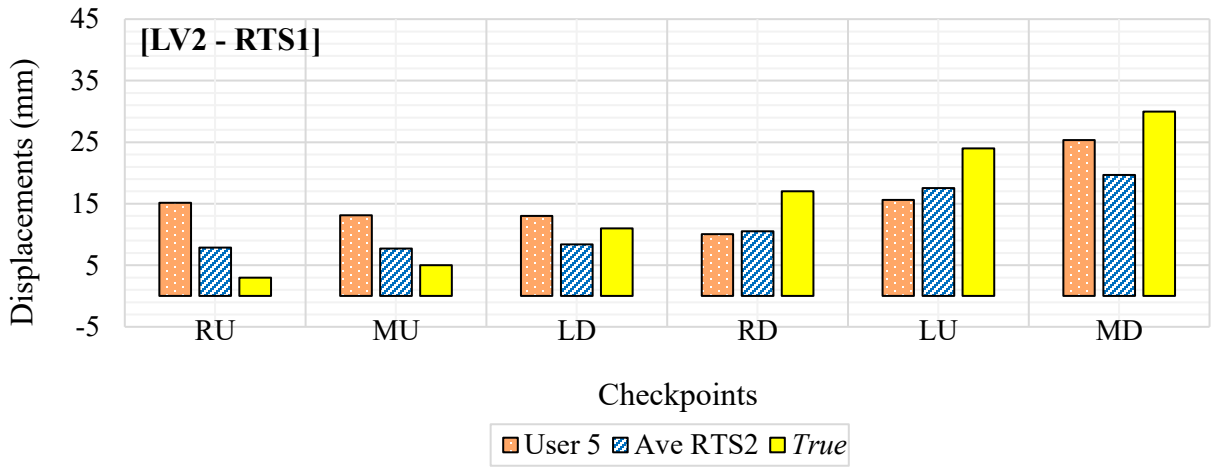

Figure 48. Chart. Displacements Captured at Epoch 2 via Model LV2 by One User [LV2 – RTS1]

For a direct comparison between TB and VA LiDAR, Figure 49 shows displacements captured by the LT2 and LV2 against the *True* values. This figure shows that the overall performance of both LiDAR techniques is similarly acceptable, with LT2 showing slightly more accuracy in the larger displacements (24 and 30 mm). However, LV2 presents captured more accurately the medium displacements (11 and 17 mm). The visual-based alignment process introduces some subjectivity, which may explain the observed slightly larger discrepancies. Nevertheless, the LV2 model remains a viable option when target placement is not feasible or when time in the field is to be minimized, albeit with slightly reduced accuracy.

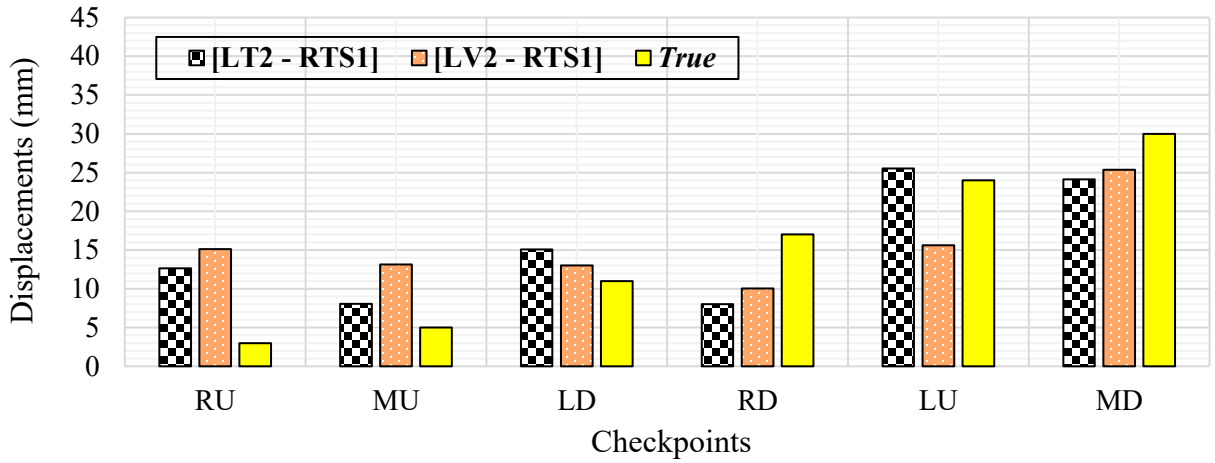

Figure 49. Chart. Displacements Captured at Epoch 2 via Models LT2 and LV2 by One User

Epoch-2 Displacements via Model MD2 (Metashape with Drone Imagery), [MD2 – RTS1]

Figure 50 presents the displacement analysis of the MD2 model, which was generated using Metashape with 196 images captured from the DJI Matrice 30 drone. No EACPs were used in this model. The results from 5 users are compared with the *True* displacement values across all 6 CPs. Again, each of those users was a group of 2-4 students taking a graduate course on Intro to CRP course, at GSU. This model shows some variability between users. At RU, the minimally displaced CP (3 mm), the range of reported displacements was wide, with User 1 significantly overestimating it (25.4 mm) and User 4 being the closest (5.2 mm) to the *True* value. Nonetheless, the accurate capture of small displacements (3-5 mm) has been difficult for all considered measuring/modeling methodologies in this project. At MU, User 1 provides the best match (5.3 mm vs *True* =5 mm), while others overestimated the values, with User 3 deviating the most (23.3 mm vs *True* =5 mm). At the 4 remaining CPs, the averaged value from all 5 users was rather accurate: 12.0 mm vs *True* = 11 mm; 18.8 mm vs *True* = 17 mm; 30.8 mm vs *True* = 24 mm; and 26.6 mm vs *True* = 30 mm. Overall, while the MD2 model is correct in identifying ≥ 11mm displacements, it shows some user variability

as it was the case in DSLR-based photogrammetry (see previous results for ML2, MM2, and MS2). This suggests that Metashape requires not only an appropriate number of GCPs and adequate image overlap, but also careful modeling, including satisfactory scaling, georeferencing and proper extraction of positional coordinates. For UAV-based photogrammetry, strict control over flight parameters should be added to that previous list, to improve accuracy and reduce user sensitivity.

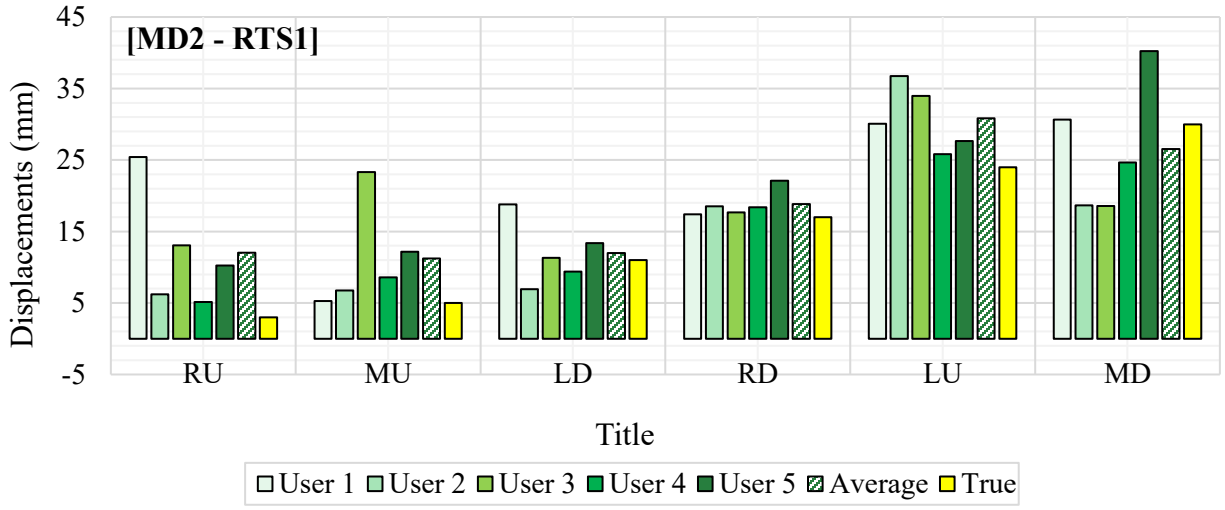

Figure 50. Chart. Displacements Captured at Epoch 2 via Models MD2 by Different Users [MD2 – RTS1]

Epoch-2 Overall Displacement Analysis and Estimation of Noise Levels

Figure 51 shows a comparison of the displacements determined by the best performing models against the *True* displacements at the 6 CPs. It includes the following sets of displacements: (i) user-averaged values for the DSLR-based Metashape models MS2, MM2, and ML2; (ii) single-user values for DroneDeploy model DE2; (iii) user-averaged values for the UAV-based Metashape model MD2; (iv) single-user values for both LiDAR models, LT2 and LV2; and (v) *True* displacement values at CPs.

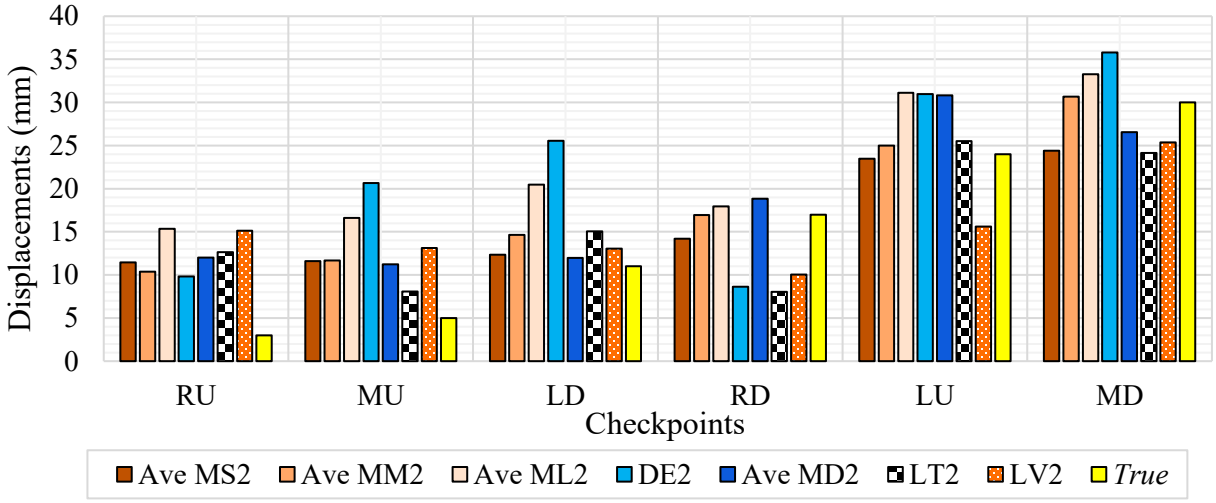

Figure 51. Chart. Displacements Captured at Epoch 2 via Various Models. User Averaged Values [Epoch 2 – RTS1]

As observed in Figure 51, all models overly estimated the small displacements (3 and 5 mm) at RU and MU. Overall, for displacements larger than 5 mm, the photogrammetry model MM2 is showing excellent performance, with all other Metashape models (ML2, MS2, and MD2) performing relatively well. Additionally, the LiDAR models showed a relatively good performance as well, with LT2 being marginally better than LV2. The DroneDeploy model, DE2, also presented good results at the points with the largest displacements, LU (24 mm) and LD (30 mm).

In all 4 Metashape models (MS2, MM2, ML2, and MD2), the comparison values reported in Figure 51 resulted from averaging the measurements obtained by 5 different users. This introduced some statistical bias. Therefore, the following graph, in Figure 52, shows the statistics corresponding to the displacement errors shown in Figure 51, but incurred by all users. Consequently, it is observed that all models presented similar displacement error dispersion (σ = STD-P), with MM2 showing less scattering, followed by slightly more spreading ML2 and LT2. Additionally, the errors incurred by LT2 and MM2 have almost the same lowest magnitudes (RMSV), 6.3 mm and 6.6 mm, respectively.

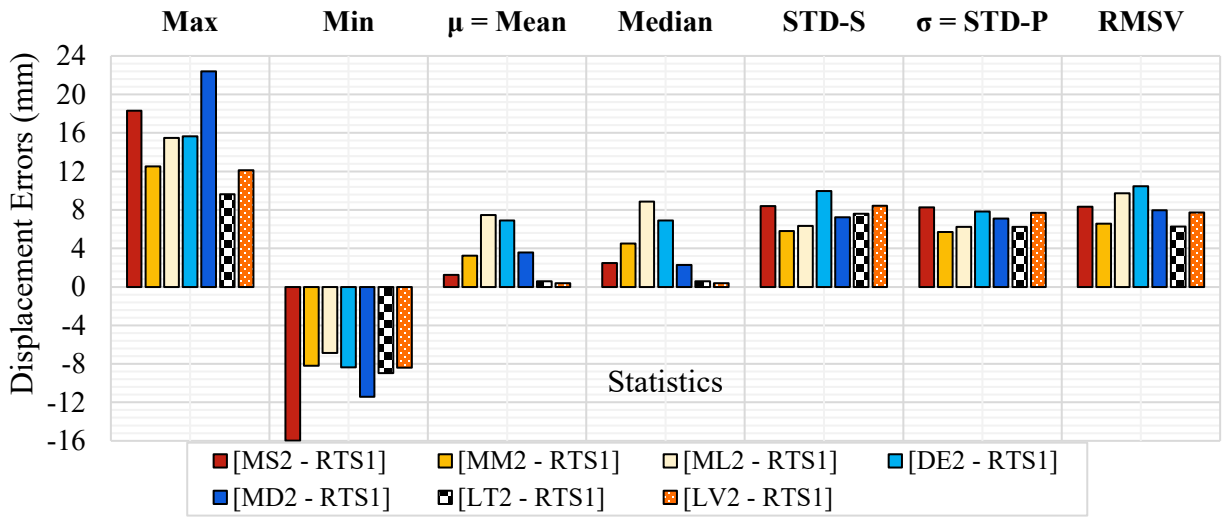

Figure 52. Chart. Statistics of Errors in Displacements Captured at Epoch 2 via Various Models by all Users [Epoch 2 – RTS1]

Assuming the referred displacement errors follow a gaussian distribution, 95% of those errors will be in the interval {μ - 1.96 σ, μ + 1.96 σ}. For the models considered in Figure 52, those intervals are:

For [MS2-RTS1]: = {1.2 - 1.96×8.4, 1.2 + 1.96×8.4} = {-15.3 mm, 17.7 mm}

For [MM2-RTS1]: = {3.2 - 1.96×5.7, 3.2 + 1.96×5.7} = {-8.0 mm, 14.4 mm}

For [ML2-RTS1]: = {7.5 - 1.96×6.2, 7.5 + 1.96×6.2} = {-4.7 mm, 19.7 mm}

For [DE2-RTS1]: = {6.9 - 1.96×7.8, 6.9 + 1.96×7.8} = {-8.4 mm, 22.2 mm}

For [MD2-RTS1]: = {3.6 - 1.96 * 7.1, 3.6 + 1.96 * 7.1} = {-10.3 mm, 17.5 mm}

For [LT2-RTS1]: = {0.6 - 1.96 * 6.2, 0.6 + 1.96 * 6.2} = {-11.6 mm, 12.8 mm}

For [LV2-RTS1]: = {0.4 - 1.96 * 7.7, 0.4 + 1.96 * 7.7} = {-14.7 mm, 15.5 mm}

After ordering the above models in increasing maximum absolute values of their observed displacement errors, it is noticed that their maximum expected errors (with a potential 95% probability) are: (1) LT2: 12.8 mm; (2) MM2: 14.4 mm; (3) LV2: 15.5 mm; (4) MD2: 17.5 mm;

(5) MS2: 17.7 mm; (6) ML2: 19.7 mm; and (7) DE2: 22.2mm. These values could serve as estimates of the noise level associated with each of those modeling techniques.

DISPLACEMENTS DIRECTLY CAPTURED BY LIDAR-BASED MODELS [EPOCH 2 – EPOCH 1]

Table 24 presents the displacements at the six CPs independently captured by the RTS instrument and the LiDAR-based models, between Epochs 1 and 2. The RTS2 values shown represent the average of two measurements, RTS21 and RTS22. The table also includes the corresponding errors relative to the *true* displacement values defined by the foam insert thickness.

Table 24. Epoch-2 Displacements captured by RTS instrument and LiDAR-based Models, [Epoch 2 – Epoch 1].

CPs		*True* Displ. (mm)	[RTS2-RTS1] Displ. (mm)	[RTS2-RTS1] Error (mm)	[LT2-LT1] Displ. (mm)	[LT2-LT1] Error (mm)	[LV2-LV1] Displ. (mm)	[LV2-LV1] Error (mm)
CW	**RU**	3	7.9	**4.9**	1.2	**-1.8**	3.4	**0.4**
	MU	5	7.8	**2.8**	3.4	**-1.6**	6.4	**1.4**
	LD	11	8.4	**-2.6**	16.5	**5.5**	14.6	**3.6**
	RD	17	10.7	**-6.3**	10.7	**-6.3**	10.7	**-6.3**
	LU	24	17.6	**-6.4**	25.6	**1.6**	18.6	**-5.4**
	MD	30	19.8	**-10.2**	28.7	**-1.3**	30.8	**0.8**

For ready visualization, Figure 53 shows a graph presenting the data in Table 24. This figure indicates that the LiDAR-based models, [LT2-LT1] and [LV2-LV1], capture more accurately the smaller displacements (3 and 5 mm) than the benchmarking RTS instrument. Regarding mid-range displacements (11 and 17 mm), all three measuring/modeling techniques show similar errors.

However, on the larger displacements (24 and 30 mm) the LiDAR techniques, particularly the TB LiDAR models, are more accurate. Overall, Figure 53 indicates that both LiDAR approaches, TB and visual-aligned perform well, even outperforming the benchmarking RTS instrument.

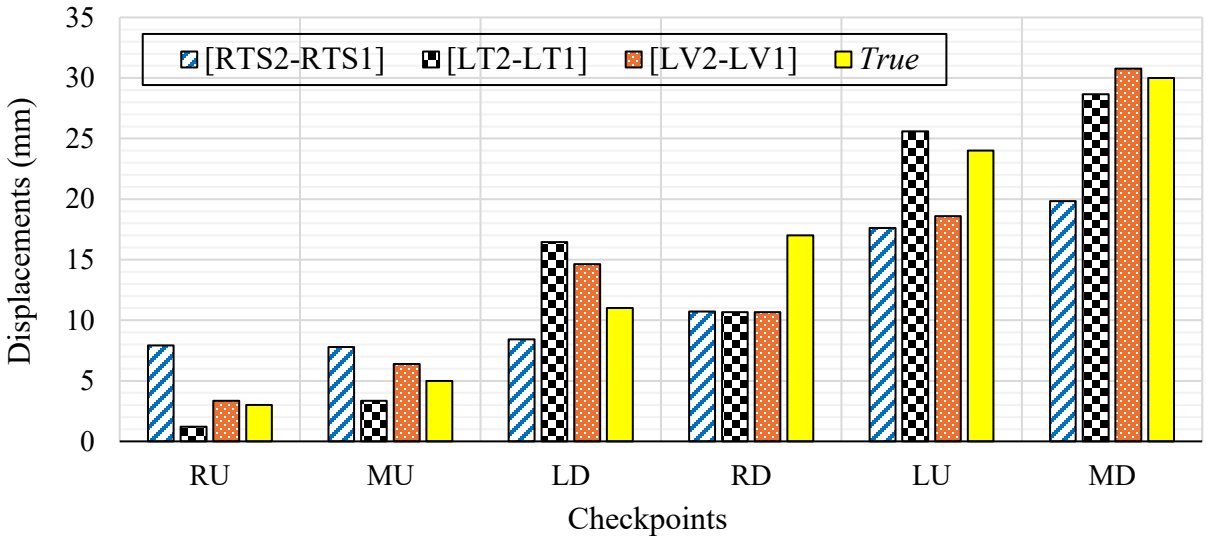

Figure 53. Chart. Displacements directly measured by RTS instrument and by LiDAR-based models.

A statistical analysis of the displacement measurement errors at all six CPs is presented in Table 25 and Figure 54. The table also includes the estimated noise interval derived from these six observations. Assuming Gaussian-distributed errors, the interval was calculated to encompass 95% of all potential measurements using the expression $\mu \pm 1.96 \times \sigma$. The maximum absolute value between the lower and upper bounds of this interval was then taken as the estimated noise level.

Table 25. Statistical analysis of errors incurred when measuring 6 displaced CPs, and noise estimation with this limited number of samples.

Statistical Function	[RTS2-RTS1] mm	[LT2-LT1] mm	[LV2-LV1] mm
Max	4.9	5.5	3.6
Min	-10.2	-6.3	-6.3
μ = Mean	-3.0	-0.7	-0.9
Median	-4.4	-1.5	0.6
STD-S (Standard Deviation – Sample)	5.8	3.9	4.0
σ = STD-P(Standard Deviation – Population)	5.3	3.6	3.7
RMSV	6.1	3.7	3.8
	Estimated Noise Interval Limits (mm) [95% Prob. Interval = μ ± 1.96 × σ]		
	Lower -13.4	**Lower** -7.7	**Lower** -8.1
	Upper 7.5	**Upper** 6.4	**Upper** 6.2
	Estimated Noise Level (mm) (Maximum Absolute Lower/Upper Limit)		
	13.5	7.7	8.1

Therefore, based on this analysis using only six control points, the estimated noise levels were as follows: (i) 13.5 mm for RTS measurements; (ii) 7.7 mm for TB LiDAR measurements; and (iii) 8.1 mm for visual-aligned LiDAR measurements. Although this revised noise estimation relies on a limited sample size, it notably excludes RTS1 measurements (which introduce their own inherent noise) from the LiDAR comparison. Interestingly, the RTS-derived noise in this analysis was unexpectedly higher than that of the LiDAR-based methods.

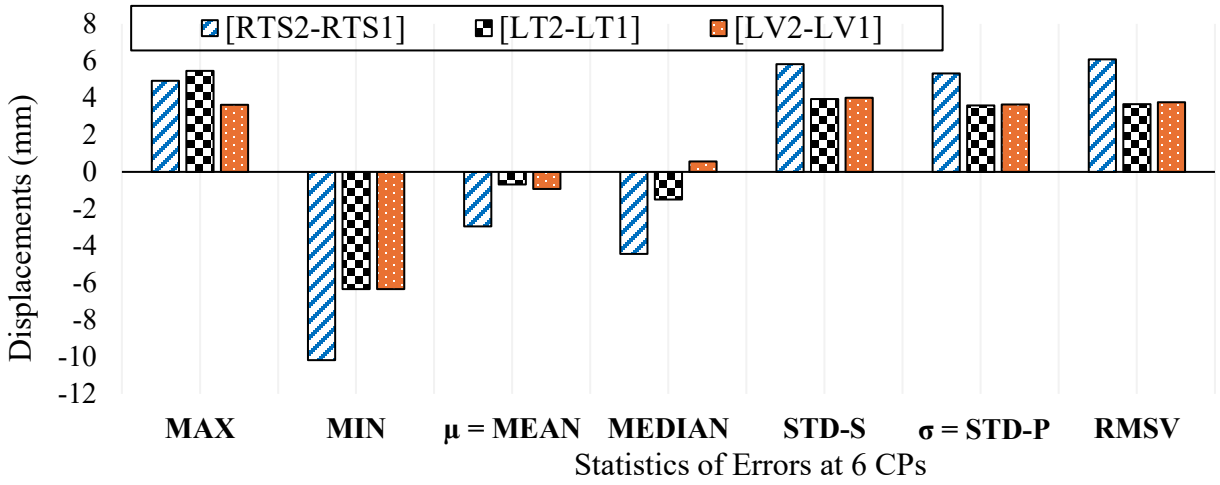

Figure 54. Chart. Statistics of displacement errors attained at 6 CPs between Epochs 1 and 2.

DISPLACEMENTS DIRECTLY CAPTURED BY PHOTOGRAMMETRY-BASED MODELS [EPOCH 2 – EPOCH 1]

The displacements captured at the 6 CPs, by the different photogrammetric models, between Epochs 1 and 2, are presented in Table 26. Each model was generated using a specific technique, DSLR-based Metashape models with varying image counts (ML2, MM2, MS2), UAV-based Metashape model (MD2), and the DroneDeploy model (DE2). Table 2626 also shows the errors incurred with respect to the TRUE displacement values, which were introduced using known thickness foam blocks. These values serve as the benchmark to evaluate the performance of each modeling approach.

Table 26. Displacements captured by photogrammetric models, [Epoch 2 – Epoch 1]

CPs	*True* Displ.	[ML2-ML1]		[MM2-MM1]		[MS2-MS1]		[MD2-MD1]		[DE2-DE1]	
		Displ.	Error	Displ.	Error	Displ.	Error	Displ.	Error	Displ.	Error
	(mm)	(mm)	(mm)	(mm)	(mm)	(mm)	(mm)	(mm)	(mm)	(mm)	(mm)
RU	3.0	**25.6**	22.6	**13.0**	10.0	**23.6**	20.6	**10.2**	7.2	**5.1**	2.1
MU	5.0	**18.5**	13.5	**12.2**	7.2	**14.5**	9.5	**12.2**	7.2	**24.5**	19.5
LD	11.0	**21.7**	10.7	**12.4**	1.4	**16.5**	5.5	**13.4**	2.4	**16.2**	5.2
RD	17.0	**35.7**	18.7	**27.2**	10.2	**30.1**	13.1	**22.1**	5.1	**15.2**	-1.8
LU	24.0	**27.3**	3.3	**21.2**	-2.8	**19.6**	-4.4	**27.6**	3.6	**37.8**	13.8
MD	30.0	**45.2**	15.2	**39.5**	9.5	**38.6**	8.6	**40.2**	10.2	**24.4**	-5.6

To facilitate visualization, Figure 55 illustrates the displacement results from Table 26, comparing the inherent accuracy of various photogrammetric models. The DSLR-based Metashape model using the largest image set [ML2–ML1] noticeably overestimated small displacements (3 mm and 5 mm), with errors exceeding 10 mm. In contrast, the medium [MM2–MM1] and small [MS2–MS1] image sets provided better accuracy in the mid-range (11 mm–17 mm), though all three showed increased variation as displacement magnitude increased. The UAV-based Metashape model [MD2–MD1] performed reasonably well in detecting mid- and high-range displacements (at LD, RD, LU, and MD), with errors mostly under 6 mm. However, for the smallest movements (at RU and MU), it tended to overestimate by 7 mm or more, underscoring its reduced sensitivity to subtle shifts in the absence of high-density image coverage or strong ground control. The DroneDeploy model [DE2–DE1] produced the best estimate for the smallest displacement (only 2 mm error at RU) but showed inconsistent behavior at higher displacements, such as at MU and MD, where both over- and underestimation occurred.

Overall, Figure 55 shows that while photogrammetric models can reliably detect displacements above ~10 mm, their sensitivity and precision vary significantly. Image count, resolution, and

acquisition method all influence performance. DSLR-based photogrammetry, especially with higher image volumes and closer perspectives, outperformed UAV-based methods. Nevertheless, none of the photogrammetric techniques achieved the sub-millimeter resolution and noise control demonstrated by terrestrial LiDAR models in earlier analyses.

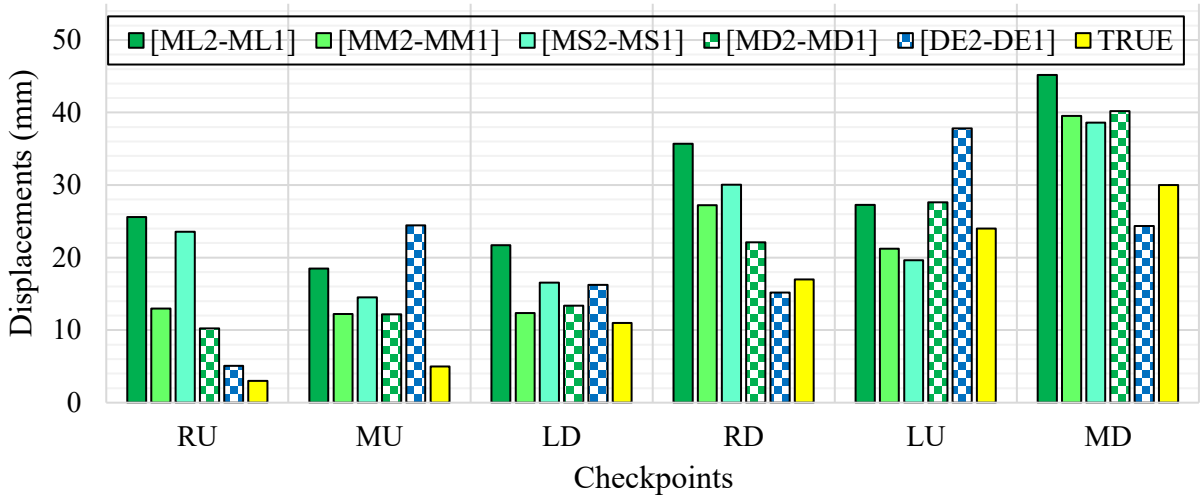

Figure 55. Chart. Displacements directly measured by photogrammetric models [Epoch 2 – Epoch 1]

A statistical evaluation of measurement errors for the six control points is provided in Table 2727 and illustrated in Figure 55. This table and figure specifically pertain to the comparison of photogrammetric models between Epoch 2 and Epoch 1. The table also includes the estimated noise interval derived from these six observations, assuming a Gaussian (normal) distribution. To determine this interval with 95% confidence, the standard formula $\mu \pm 1.96 \times \sigma$ was applied, where μ represents the mean error and σ the standard deviation. The maximum absolute value between the upper and lower bounds of this interval was taken as the estimated noise level.

Table 27. Statistical analysis of errors incurred when measuring the 6 displaced CPs, and noise estimation with this limited number of samples.

Statistical Function	[ML2-ML1]	[MM2-MM1]	[MS2-MS1]	[MD2-MD1]	[DE2-DE1]
	(mm)	(mm)	(mm)	(mm)	(mm)
MAX	22.6	10.2	20.6	10.2	19.5
MIN	3.3	-2.8	-4.4	2.4	-5.6
μ = MEAN	14.0	5.9	8.8	6.0	5.5
MEDIAN	14.3	8.4	9.1	6.1	3.7
STD-S	6.7	5.4	8.3	2.8	9.5
σ = STD-P	6.1	4.9	7.5	2.6	8.7
RMSV	15.3	7.7	11.6	6.5	10.3
	Estimated Noise Interval Limits (mm)				
	[95% Prob. Interval = μ ± 1.96×σ]				
	Lower	**Lower**	**Lower**	**Lower**	**Lower**
	2.0	-3.8	-6.0	0.9	-11.5
	Upper	**Upper**	**Upper**	**Upper**	**Upper**
	26.0	15.6	23.6	11.0	22.6
	Estimated Noise Level (mm)				
	(Maximum Absolute Lower/Upper Limit)				
	26.0	15.6	23.6	11.0	22.6

Therefore, from this analysis, considering only 6 CPs, the level of noise was estimated as: (i) 26.0 mm for the [ML2–ML1] photogrammetric model; (ii) as 15.6 mm for the [MM2–MM1] model; (iii) as 23.6 mm for the [MS2–MS1] model; (iv) as 11.0 mm for the [MD2–MD1] UAV-based model; and (v) as 22.6 mm for the [DE2–DE1] UAV-based model. Even though a reduced set of samples has been considered in this new noise estimation analysis, it does not involve the use of RTS1 measurements which carry their own noise. In this analysis, the estimated noise from the photogrammetric models particularly [ML2–ML1] and [MS2–MS1] resulted significantly larger than that from the UAV-based models such as [MD2–MD1] and [DE2–DE1].

CLOUDCOMPARE (CC) ANALYSIS OF DISPLACEMENTS BETWEEN EPOCHS 1 & 2

Previous displacement analyses for the CW focused solely on 6 CPs and on 15 non-repeated distances among them. While informative, this small set of data points provides only limited information about displacements that may occur at any other location on the wall facing. To gain a more comprehensive assessment of displacements, it was decided to employ the CC software. This is a robust open-source platform that compares 2-point clouds to detect spatial discrepancies between them. CC was employed to analyze 2 point-cloud models of the full surface of the CW generated at two different times, Epochs 1 and 2. By comparing point clouds over time, CC allows a much more granular and holistic evaluation of geometric changes that may occur during a selected period, surpassing the capabilities of visual inspections or sparse checkpoint-based methods. By expanding the analysis beyond a few Checkpoints (CPs) to the full surface of the wall, this approach supports the development of a robust inspection protocol for aging infrastructure using LiDAR or photogrammetry.

Since, in the previously reported displacement analysis, the TB LiDAR model (LT2) and the Metashape model with medium size dataset (MM2) provided the smallest errors with respect to accurate RTS1 measurements, it was decided to explore the use of these two modeling techniques along with CC to capture displacements occurring between two epochs. Therefore, 2 full-surface model comparisons were performed as follows:

- LT2 vs LT1: Evaluates terrestrial LiDAR-based displacements, where the Epoch-1 model, LT1, served as the reference cloud and the Epoch-2 model, LT2, as the compared cloud. Both were exported from Leica Cyclone Core as "*.las*" files.

- MM2 vs MM1: Assesses displacements captured via DSLR-based photogrammetry. Here, the Epoch-1 Metashape model, MM1, serves as the reference cloud, and Epoch 2, MM2, as the compared cloud, with both exported from Agisoft's Metashape as "*.las*" files.

The purpose of this comparison was to determine which of these two modeling techniques use more effectively CC to detect small structural displacements in retaining walls under controlled deformation scenarios.

CC offers several types of point cloud comparison analysis. In this study, C2C and Multiscale Model to Model Cloud Comparison (M3C2) were employed. C2C calculates absolute (unsigned) Euclidean distances between each point in the reference cloud and its nearest neighbor in the compared cloud. Though useful, this method can sometimes overestimate displacements because the nearest neighbor may not lie directly along the normal vector of the surface. M3C2 is a more advanced method that projects each point in the compared model along the normal direction of the reference cloud, allowing calculation of signed distances. It also considers multiple scales of local roughness, making it highly effective for evaluating surfaces with variable textures and for minimizing noise sensitivity. This multiscale capability enables M3C2 to detect both small and large changes across the wall façade.

In both analyses, the reference and compared models were required to share the same spatial units (ft) and the same coordinate system of reference. All point cloud files, whether exported from Cyclone Core or Metashape were standardized accordingly prior to being imported into CC. For

proper comparison, the cloud segment containing the wall facing was extracted (segmented) from the two full point-cloud models to make them geometrically comparable.

These comparisons not only validated the simulated displacements imposed on the CW but also offered clear insights into which 3D sensing technique best supports accurate, non-contact geometric monitoring.

C2C "absolute" distance comparisons, [LT2 vs TBL1] & [MM2 vs MM1]

The C2C comparison was performed using CC software to estimate absolute point-to-point distances (interpreted as position discrepancies, PDs) between two comparable 3D point cloud models from Epoch 1 and Epoch 2 of the CW. These models were developed using different sensing technologies across two epochs. Appendix C8 outlines the specific protocol, settings, and parameters used in executing the C2C workflow within CC.

All point clouds were georeferenced in the same local coordinate system, established via the RTS-based closed traverse, and used ft as the spatial unit. This consistency eliminated the need for additional transformations before importing into CC. The C2C method then computed "absolute" distances from each point in the reference cloud to its nearest neighbor in the compared cloud. These distances are visualized in a color-coded scale and represent displacements across the wall surface between the two epochs.

Part A of Figure 56 shows the simulated deformed configuration of the CW at Epoch 2. Part B, displays a color field illustrating the C2C analysis results for LT2 vs LT1, confirming accurate detection of zones with relatively small displacements.

A. CW with simulated displacements and their magnitudes at Epoch 2.

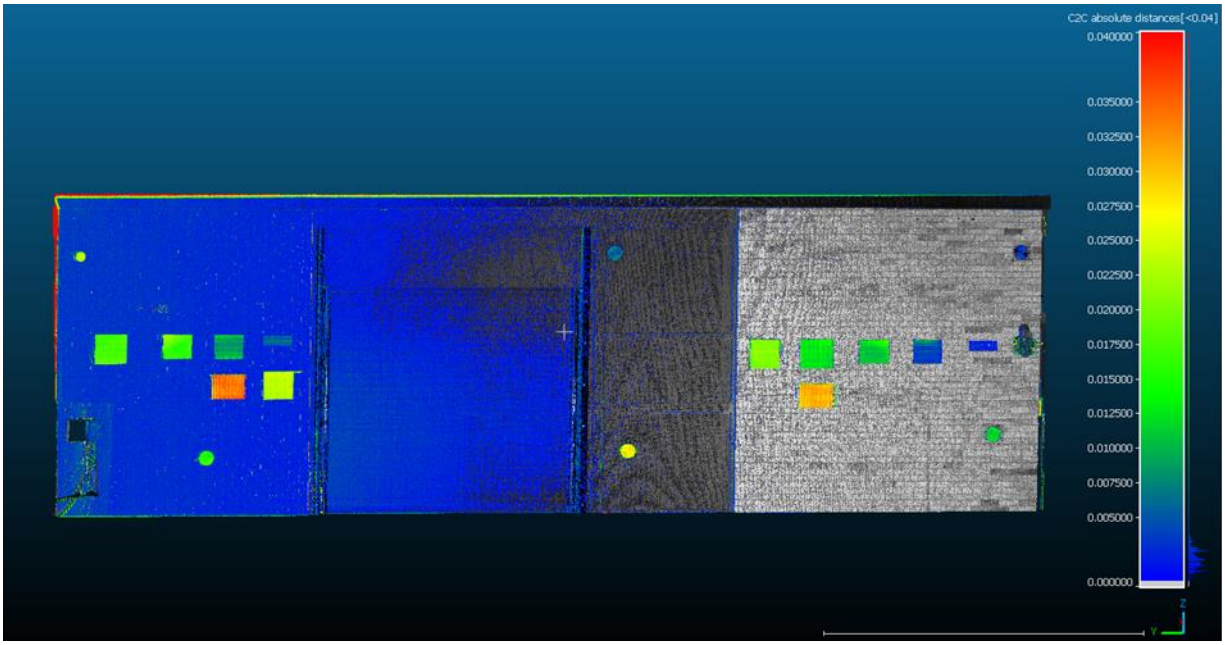

B. C2C "Absolute" Distance Comparison – [LT2 vs LT1]

Figure 56. Photo. CC C2C Comparison of TB LiDAR Models

Figure 57 presents the comparison between the MM2 and MM1 models, revealing how DSLR-based photogrammetry performs in identifying wall changes.

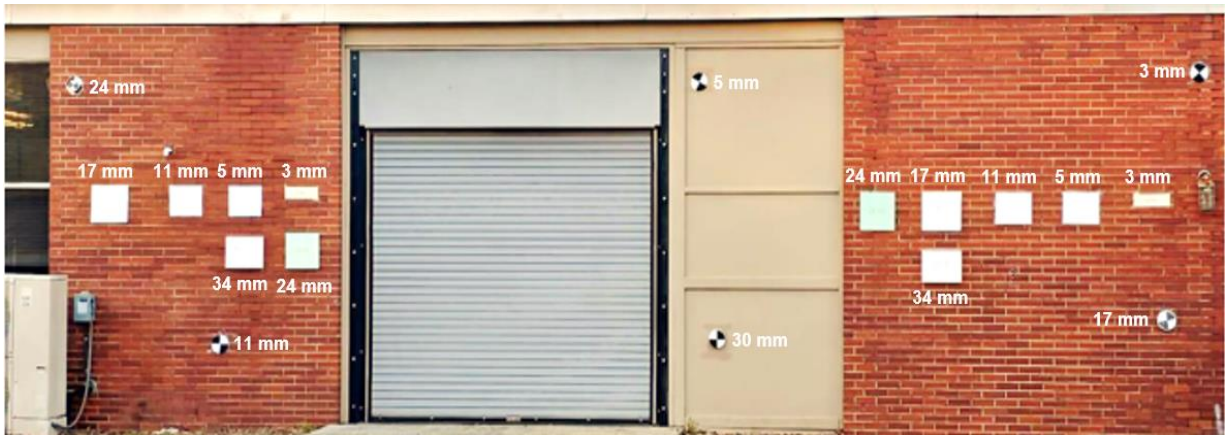

A. CW with simulated displacements and their magnitudes at Epoch 2.

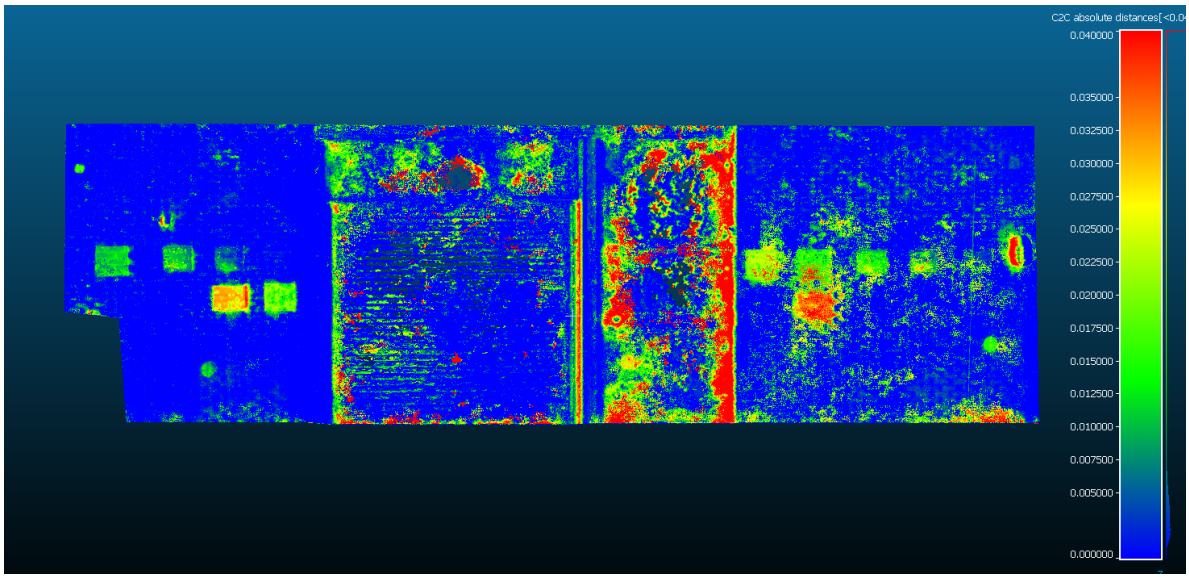

B. C2C "Absolute" Distance Comparison – [MM2 vs MM1]

Figure 57. Photo. CC C2C Comparison of DSLR-based Metashape models

In all C2C visualizations, the gray color indicates regions with zero or negligible displacement. Slight positional discrepancies ranging up to 5 mm are shown in blue to blueish tones. As deviations increase, the color transitions from green to greenish, followed by yellow, and ultimately to red which represents the highest levels of detected displacement. This progressive color scale allows intuitive identification of deformation zones. Notably, areas where foam blocks or structural shifts were introduced between epochs, exhibit red or yellow highlights, validating the simulated

displacements and demonstrating the effectiveness of the C2C method for detecting subtle surface changes on the CW.

By directly comparing parts B of Figure 56 and Figure 57, it is evident that the terrestrial LiDAR model, captured with Leica's P50 scanner, demonstrates exceptional accuracy in detecting surface deviations. All simulated displacements, regardless of size, were correctly identified and localized, including the smallest 3 mm changes, as shown by consistent color matches across the wall. This confirms that terrestrial LiDAR can detect sub-centimeter changes with precision, making it ideal for SHM and deformation tracking. In contrast, Figure 57 reveals considerable noise and low fidelity. The surface is heavily scattered, presenting irregularities, imperfections and showing areas with non-existing larger displacements. This interferes with the proper detection of small displacements. That is, our best performing photogrammetry-based model fails to clearly detect minor or moderate wall shifts. This C2C comparison between terrestrial LiDAR and DSLR-based photogrammetry proves that LiDAR performed significantly better in accuracy, resolution, and noise suppression, especially for detecting small-scale deformations. This makes it a recommendable tool for precise non-contact inspection of aging infrastructure like MSE/MB walls.

C2C Histogram Analysis

The histogram shown in Figure 58 presents the distribution of C2C absolute distances between the LT1 and LT2 models of the CW. That is, it shows the distribution of displacements that occurred between Epochs 1 and 2. Approximately 6.01 million-point pairs were analyzed. Most of the resulting absolute distances (PDs) were found to be less than 5 mm, with a significant concentration in the lower intervals of the histogram, all rendered in blue. The tallest bar, representing the highest

point count, occurs at the 4th interval, between1.4 mm and 1.7 mm, with a point count of approximately $1{,}142\times10^3$, suggesting that most of the wall surface remained unchanged between epochs. Notably, a short red bar appears at the far right of the chart, at around 40 mm, as the final red interval. These elevated distance values do not represent meaningful displacements but rather stem from non-overlapping edge zones between the two-point clouds, where the algorithm matched unmatched boundary points to the nearest available surfaces. Such outliers were disregarded in the displacement evaluation. The consistent blue distribution across most of the histogram confirms the high accuracy and sensitivity of the terrestrial LiDAR models.

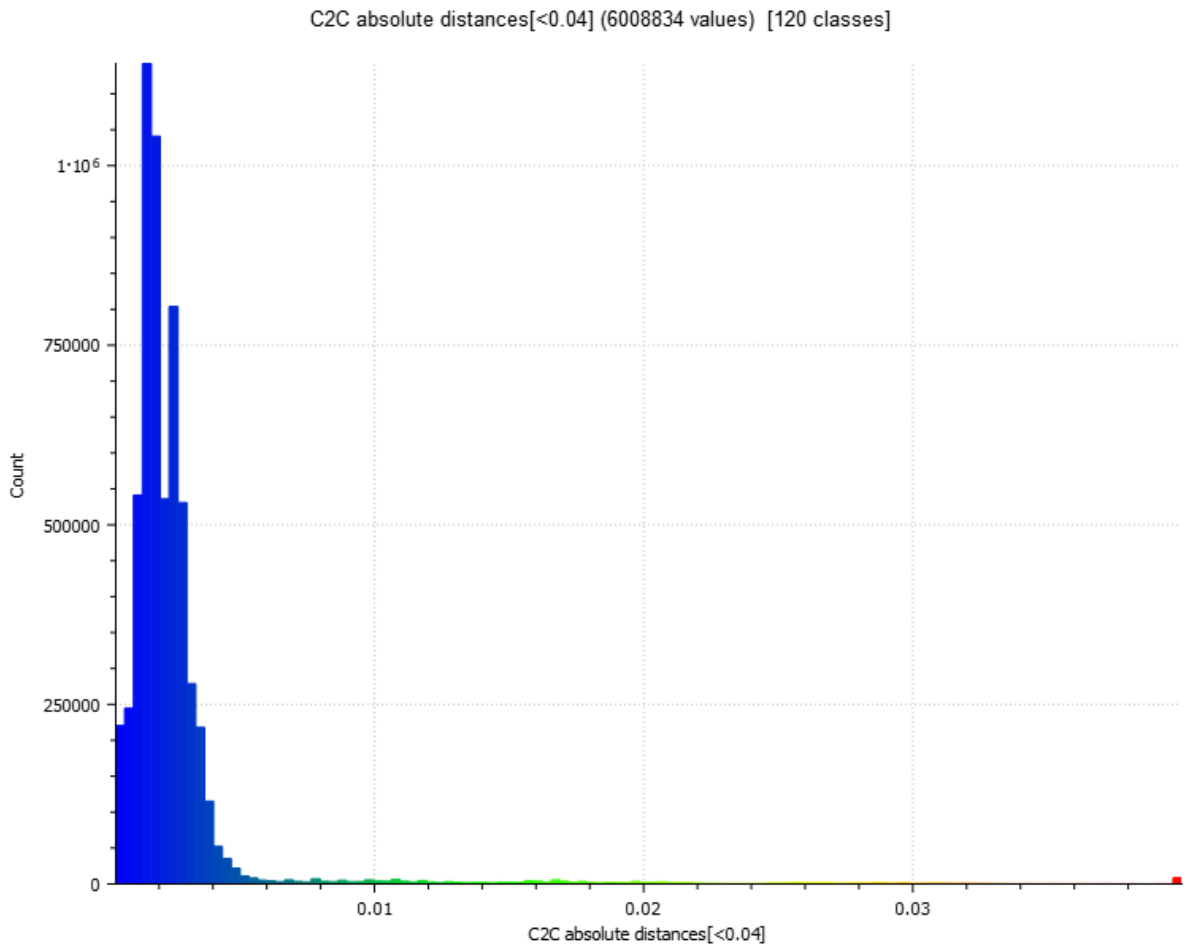

Figure 58. Graph. Histogram of C2C absolute distances (displacements), LT1 vs LT2 (m)

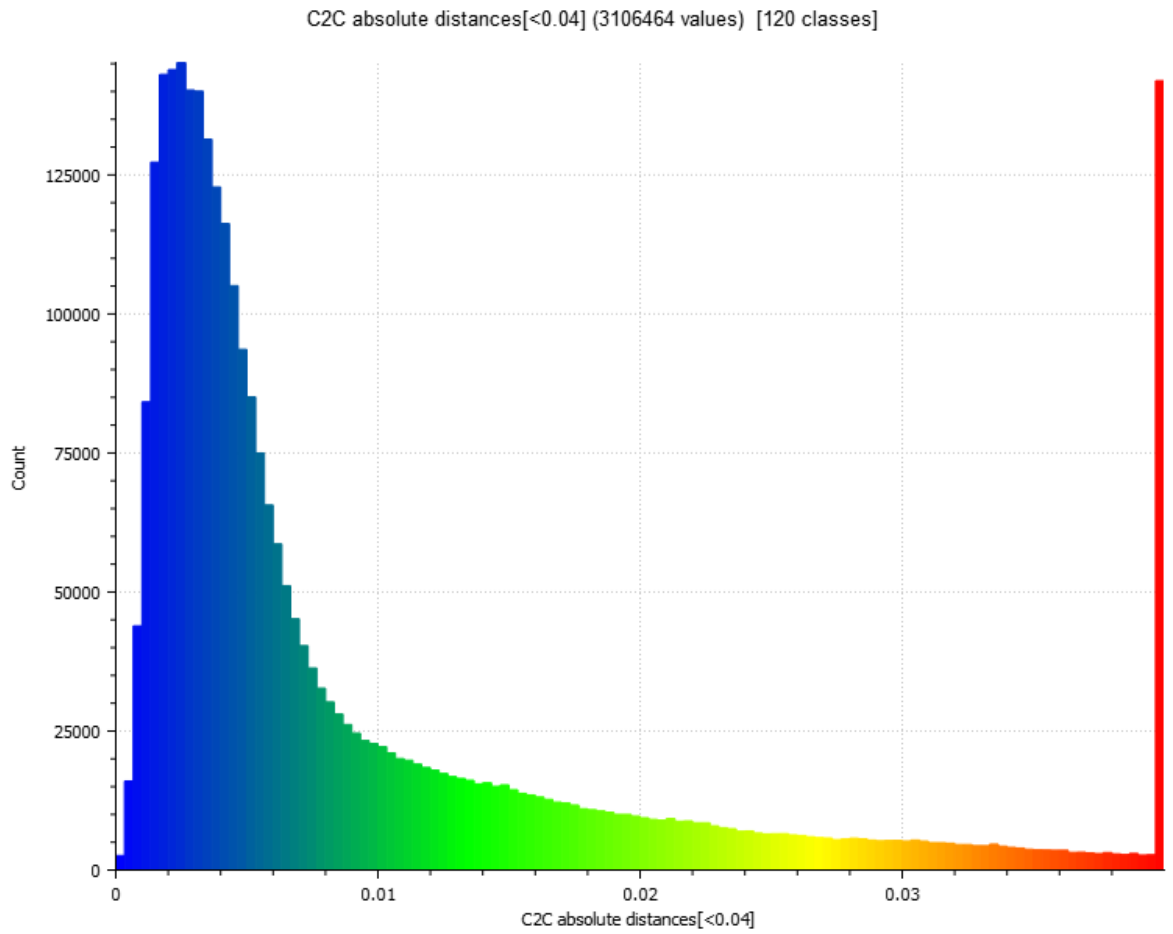

Figure 59. Graph. Histogram of C2C absolute distances (displacements), MM1 vs MM2 (m)

Figure 59 displays the histogram of C2C absolute distances between the MM1 and MM2 photogrammetric models of the CW. A total of approximately 3.11 million pairs of points were analyzed. Compared to the terrestrial LiDAR results in part A, this histogram demonstrates a much broader and asymmetrical distribution of absolute distances, or PDs (i.e., displacements) between the models in Epochs 1 and 2, extending across the entire 0–40 mm range. The highest bar is concentrated at the 8th interval, from 2.3 mm to 2.6 mm, with 145×10^3 points, yet the overall distribution shows a gradual slope extending through green (10–20 mm), yellow (25–30 mm), and even orange reaching the large red spike at 40 mm. This final red interval representing the largest

number of mismatches includes over 140,000 points, likely arising from noise, edge mismatches, or registration inconsistencies, especially in less textured areas or surface occlusions. These red-zone values were excluded from final displacement interpretations, as they likely do not reflect actual geometric changes.

While the blue regions do indicate some accuracy in parts of the model, the long tail and elevated noise floor suggest that the photogrammetric models struggled to detect subtle wall displacements and wrongly captured non-existing ones. These inaccuracies may be attributed to several factors (i.e., lower spatial resolution, camera calibration limits, or inconsistencies in image alignment and dense reconstruction). In summary, while general trends are visible, the photogrammetry-derived models demonstrate less sensitivity and precision in detecting fine-scale movements compared to terrestrial LiDAR-derived models.

C2C Cumulative Distribution Functions (CDFs) at CW

Figure 60 displays the cumulative distribution functions of the C2C "absolute" distances, which can be interpreted as point position discrepancies (PDs) or displacements observed on the CW between Epochs 1 and 2. The figure includes two curves: one representing the TB LiDAR comparison [LT2 vs LT1], and the other corresponding to the photogrammetry-based Metashape comparison [MM2 vs MM1].

In that figure, the x-axis denotes displacement values in millimeters, ranging from 0 to 40 mm, while the y-axis indicates the cumulative probability that a displacement is less than or equal to a given value. In other words, for any displacement value on the x-axis, the corresponding y-axis

value reflects the proportion (or percentage) of observations in the dataset that fall below that threshold. For example, the [LT2 vs LT1] comparison shows that approximately 95.0% of all detected displacements were ≤ 3.6 mm, whereas the [MM2 vs MM1] comparison indicates, more erroneously, that about 95.0% of displacements were ≤ 27.7 mm.

Assuming that displacement observations are uniformly distributed across the wall surface, the cumulative probability values on the y-axis can also be interpreted as the percentage of the wall area exhibiting displacements equal to or less than a given threshold. Under this interpretation, the [LT2 vs LT1] curve suggests that roughly 91.1% of the wall experienced displacements ≤ 3.0 mm. This aligns with the fact that the actual simulated displacements on the CW—ranging from 3 mm to 34 mm—were confined to a small portion of the wall. Specifically, the Styrofoam inserts used to simulate movement covered only ~7.61 ft² out of a total ~217.63 ft², or approximately 3.5% of the wall area. In other words, a true 96.5% of the wall experienced no displacement.

This analysis demonstrates that the TB LiDAR models effectively captured most of the simulated displacements on the CW, including those near the 3 mm threshold. However, the presence of modeling noise resulted in indicating that ~ 91.1% of the wall experienced some displacement (≤ 3.0 mm), when in reality 96.5% of the wall did not displace between Epochs 1 and 2.

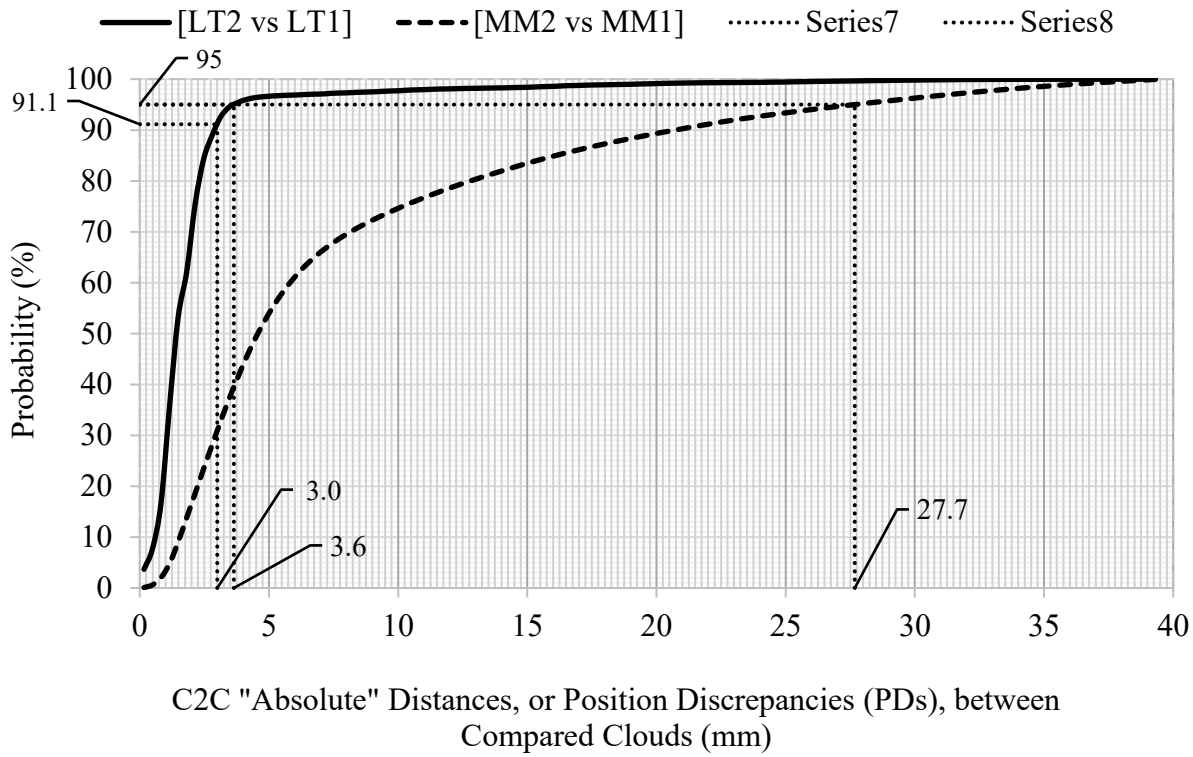

Figure 60. Graph. Cumulative distribution function of C2C "absolute" distances, between Epochs 1 and 2, for [LT2 vs LT1] & [MM2 vs MM1]

Nevertheless, the CC C2C analysis of the TB LiDAR models effectively and colorfully identified all simulated displacements on the CW, including the smallest ones (3 mm), as seen in Figure 56. This outcome suggests that the estimated 12.8 mm noise level—derived from 6 observations and representing the 95th percentile of potential measurement error for TB LiDAR (relative to RTS1 measurements) during the CW study, as shown in Figure 52. However, when the noise was estimated from the [LT2–LT1] comparison independent of RTS1 measurements the value decreased to 7.7 mm. This reduced estimate was obtained from information in Table 25 in the subsection titled *Displacements Directly Captured by LiDAR-based Models [Epoch 2 – Epoch 1]*. Despite these variations in estimated noise levels, the CC C2C analysis of the TB LiDAR models from Epochs 1 and 2 proved highly effective in detecting all simulated displacements, ranging from 3 mm to 34 mm. Remarkably, several of the smaller displacements (3 mm, 5 mm, and even 11 mm)

which were expected to fall within or below the noise threshold were still successfully detected. This underscores the sensitivity and robustness of the TB LiDAR method in capturing subtle spatial changes, even in the presence of modeling noise.

In contrast, the CC C2C comparison of the photogrammetry models, [MM2 vs MM1], suggests that displacements ≤ 27.7 mm were detected across 95% of the CW. This value appears unusually high—especially considering that the same graph indicates approximately 30% of the wall experienced displacements ≤ 3 mm, while about 90% fell below 34 mm. This would imply that roughly 60% of the wall (90% – 30%) exhibited displacements within the simulated range of 3–34 mm. However, this interpretation is clearly misleading, as only ~3.5% of the wall contained simulated displacements. This inaccuracy is likely the result of imperfections in the photogrammetry models, which may have introduced artifacts or inconsistencies (e.g., wavy or rippled surfaces where none exist, floating textures or disconnected fragments, non-existent bulges, pits, holes, etc.) Such issues could explain the presence of numerous red areas in the [MM2 vs MM1] comparison, indicating large, non-existent displacements that were not part of the simulation.

Additionally, the estimated noise level associated with the photogrammetry model MM2—based on the [MM2–RTS1] comparison shown in Figure 52 was 14.4 mm. This value increased slightly to 15.6 mm when the noise was estimated from the [MM2–MM1] comparison, which was conducted independently of RTS1 measurements. See Table 27 in the subsection titled *Displacements Directly Captured by Photogrammetry-based Models [Epoch 2 – Epoch 1]*.

According to the CC C2C analysis, the photogrammetry comparison [MM2 vs MM1] is not as effective as the TB LiDAR comparison [LT2 vs LT1] to detect wall displacements, especially when they are small.

M3C2 "signed" distance comparisons, [LT2 vs LT1] & [MM2 vs MM1]

The Multiscale Model to Model Cloud Comparison (M3C2) algorithm, implemented in CC, was employed to assess directional surface displacements on the CW using both terrestrial LiDAR and DSLR-based photogrammetry models. For each method, the Epoch 1 model was designated as the "reference", and the Epoch 2 model as the "compared". Specifically, the comparisons included [LT2 vs LT1] for terrestrial LiDAR, and [MM2 vs MM1] for DSLR photogrammetry. The goal was to quantify and visualize surface-level deviations under identical conditions, enabling a direct evaluation of each technique's sensitivity to small-scale displacement.

The M3C2 algorithm first computed directions normal to the wall surface on the reference model and then measured signed (±) distances between corresponding points, in the Epochs 1 and 2 models, along those normal directions. These signed values provide information on both magnitude and direction: positive distances (red hues) indicate outward displacement, while negative distances (blue hues) signal inward movement. Areas of negligible change are shown in green, representing surface regions where no significant displacement occurred. A consistent ±40 mm color scale (total range of 80 mm) was applied to both comparisons for visual parity. Appendix C8 outlines the specific protocol, settings, and parameters used in executing the M3C2 workflow within CC.

Figure 61 and Figure 62 presents the M3C2 displacement maps for both comparisons [LT2 vs LT1] and [MM2 vs MM1], respectively. The LiDAR-based comparison demonstrates highly localized and accurate detections of the simulated displacements, matching known ground truth values with high resolution and minimal noise. In contrast, the comparison of photogrammetry models [MM2 vs MM1] reveals a noisier surface response with less distinct deformation zones and broader color transitions. While the general displacement regions are still captured, the DSLR-based photogrammetry approach shows reduced clarity and sensitivity compared to the terrestrial LiDAR data. This dual analysis highlights the robustness of the M3C2 scheme in differentiating performance between sensing methods under identical experimental conditions.

A. CW with simulated displacements and their magnitudes at Epoch 2.

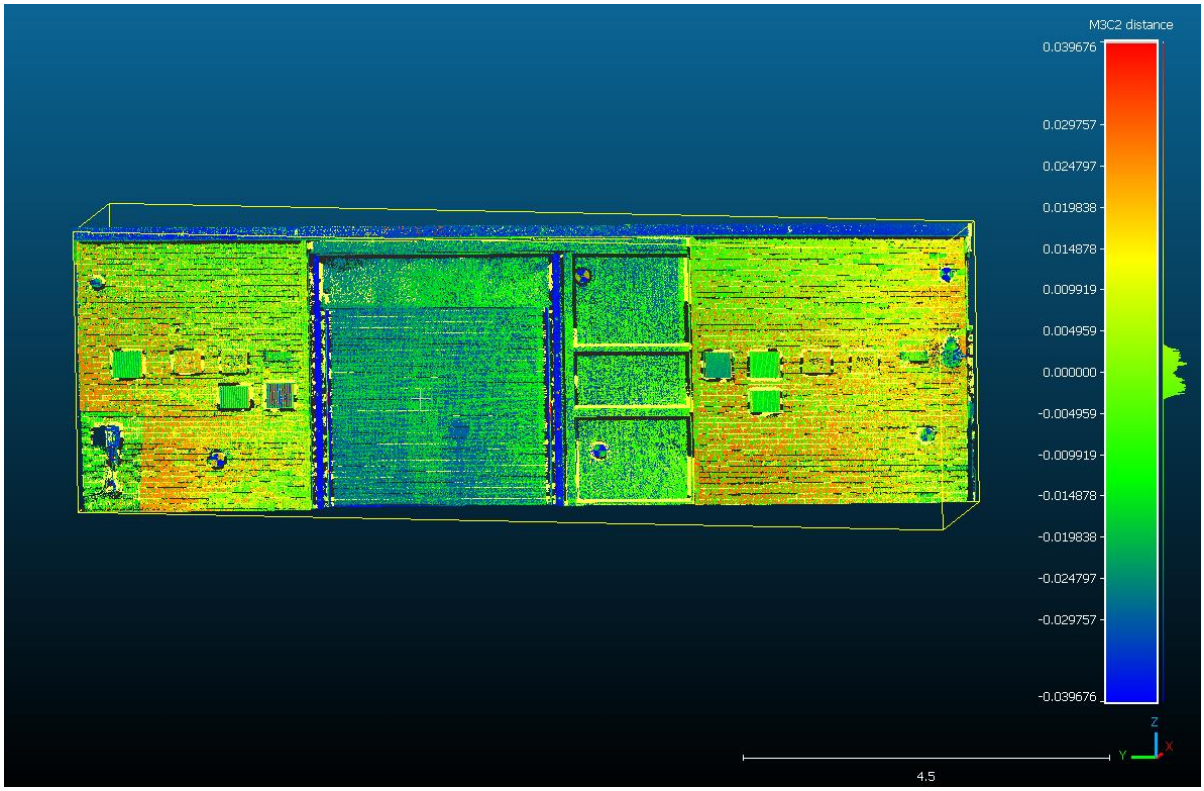

B. M3C2 "Signed" Distance Comparison – [LT2 vs LT1]

Figure 61. Photo. CC M3C2 Comparison of TB LiDAR Models

A. CW with simulated displacements and their magnitudes at Epoch 2.

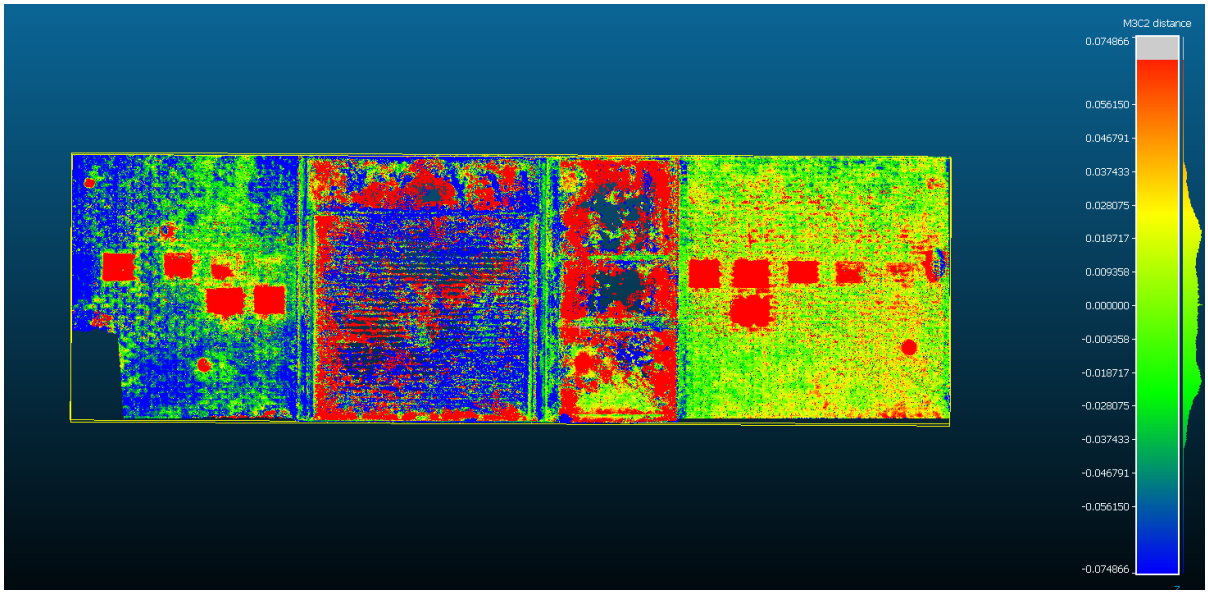

B. M3C2 "Signed" Distance Comparison – [MM2 vs MM1]

Figure 62. Photo. CC M3C2 Comparison of DSLR-based Metashape models

M3C2 Histogram Analysis

The two histograms in Figure 63 and Figure 64 display the distribution of M3C2 "signed" distances interpreted as directional position discrepancies (±PDs), between Epoch 1 and Epoch 2 for the CW. In both comparisons, the surface of Epoch 1 was treated as the reference point cloud, and the Epoch 2 surface as the compared model. In part A of that figure, the histogram corresponds to the terrestrial LiDAR comparison [LT2 vs TBL1], while the histogram in part B reflects the DSLR-

based photogrammetry comparison [MM2 vs MM1]. In both cases, M3C2 computed distances along directions normal to the surface of the reference wall and discarded distances associated to unmatched or poorly defined points, leading to fewer point pairs than in the C2C analysis.

In Figure 63, approximately 4.94 million distances (displacements) were calculated by the M3C2 algorithm for the LiDAR models. The distribution is sharply centered around 0 mm, with most values concentrated between –3 mm and +3 mm. This tight clustering near zero is in good agreement with the fact that 96.5% of the CW did not displace. The remaining 3.5% of the wall displaced 3, 5, 11, 17, 24, 30, and 34 mm. This histogram demonstrates good geometric modeling capabilities of the TB LiDAR technique and minimal noise (between 0-3 mm) in areas with zero displacements. The quasi-symmetric peaks near zero also indicates that both inward and outward noise-related displacements were equally minor, possibly marking the remaining noise level associated with these LiDAR models when evaluated via the M3C2 signed distance scheme. This validates the LiDAR system's sensitivity to sub-centimeter shifts across the wall surface.

In contrast, Figure 64, which compares MM2 and MM1 (photogrammetry models generated in Metashape), presents a much wider, but still symmetrical histogram. In this case, only ~0.16 million distances (displacements) were computed between both photo-based clouds from Epochs 1 and 2. Most of those distances are heavily concentrated in the ±45 mm range, with the largest peaks near 21 mm and +20 mm. However, this is misleading as the CW only experienced simulated displacements (0-34 mm) in only 3.5% of its surface. That is, 96.5% of the surface did not displace. So, theoretically, a large peak near zero-displacement should have been observed, as was the case when comparing the LiDAR models.

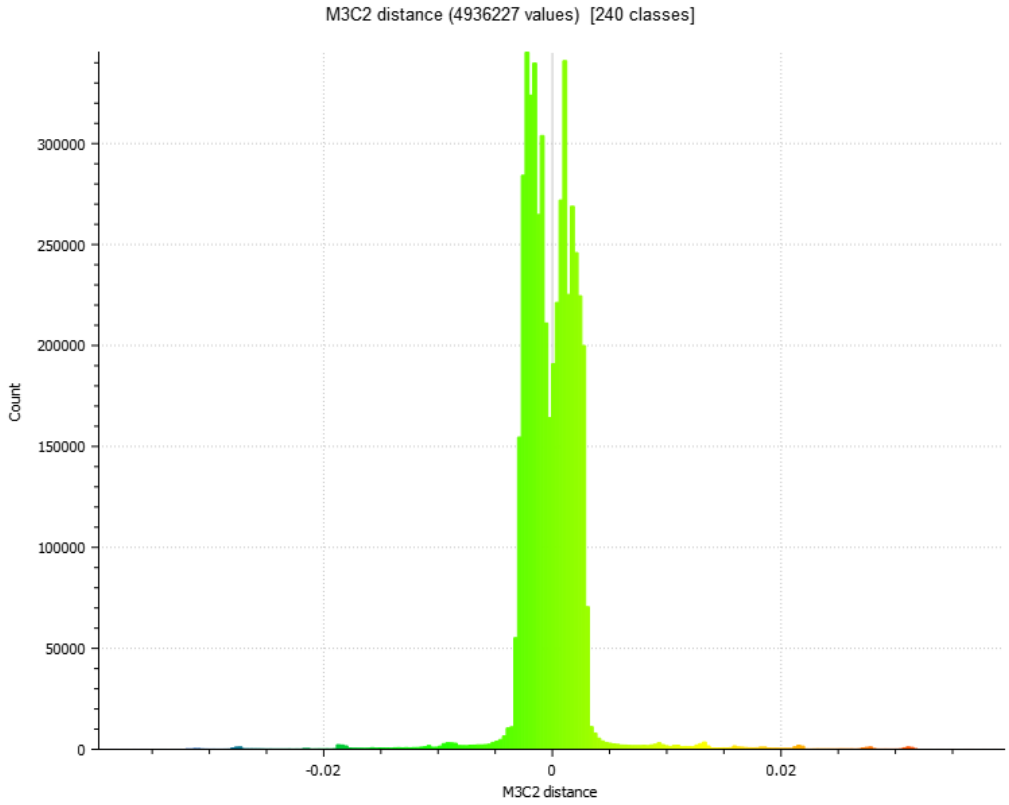

Figure 63. Graph. Histogram of M3C2 “signed” distances (displacements), [LT1 vs LT2], (m)

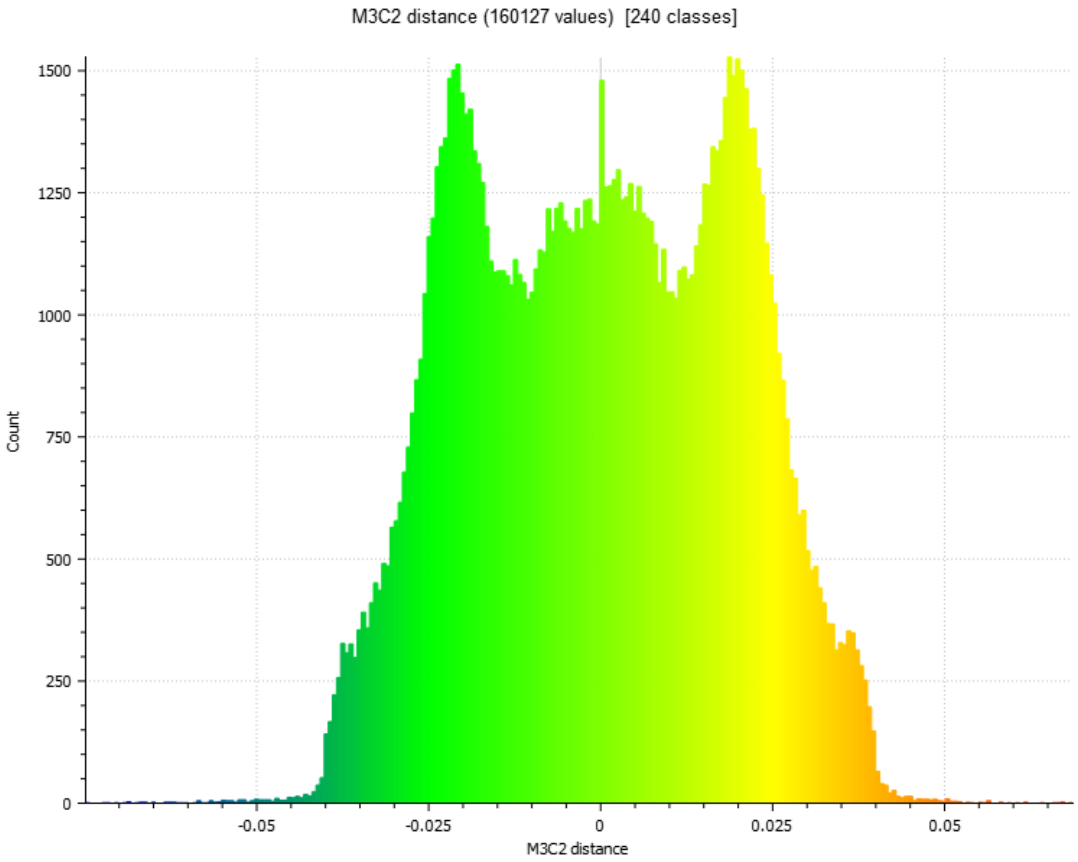

Figure 64. Graph. Histogram of M3C2 "signed" distances (displacements), [MM1 vs MM2], (m)

Analysis of M3C2 CDF

Figure 65 illustrates the cumulative distribution functions of M3C2 "signed" distances (±PDs, or ±displacements) between 2 point-cloud models generated by the same technique at Epochs 1 and 2. The dashed line corresponds to the comparison between TB LiDAR models [LT2 vs LT1], and the solid line represents the comparison between photogrammetric models [MM2 vs MM1], generated via Metashape with pictures taken with a hand-held DSLR camera.

Each CDF curve visualizes the probability that determined M3C2 "signed" distances (±displacements), fall within a given range. The x-axis denotes the signed displacements (mm)

computed using the M3C2 algorithm, while the y-axis shows the cumulative probability that displacements are equal or less than a given value (x value).

Since in the previous C2C "absolute" distance analysis, the discrepancy range was selected between 0 and 40 mm, now for proper comparison, in the current M3C2 "signed" distance analysis, the range was selected from –40 to +40 mm. Additionally, since in the C2C "absolute" analysis, the maximum magnitude of displacements with a 95% probability of occurrence was determined, now in the M3C2 "signed" analysis, that 95% probability was considered between the 2.5% and 97.5% levels. Accordingly, for the [LT2 vs LT1] comparison, Figure 65 indicates a 95% probability that all displacements are in the [-3.8 mm, +2.7 mm] interval. Similarly, for the [MM2 vs MM1] comparison, that 95% corresponds to the [-34.5 mm, 33.5 mm] interval. Those ranges are translated into "absolute" magnitudes of position discrepancies, resulting in the following two statements: (i) For the TB LiDAR comparison, there is a 95% probability that the magnitude of all displacements, between Epochs 1 and 2, be equal or less than 3.8 mm. Similarly, for the photo-based Metashape comparison, that amplitude is equal or less than 34.5 mm. These amplitudes are larger but still similar to the values obtained in the previous C2C analysis, 3.6 mm and 27.7 mm, respectively (see Figure 60). Therefore, in this regard, there is not a marked difference between the results obtained by the C2C and M3C2 schemes. That is, both C2C and M3C2 schemes show that LiDAR-based comparison [LT1 vs LT2] is more accurate than the photo-based comparison [MM1 vs MM2]. This could also be observed from an alternative point of view, as explained in the following paragraph.

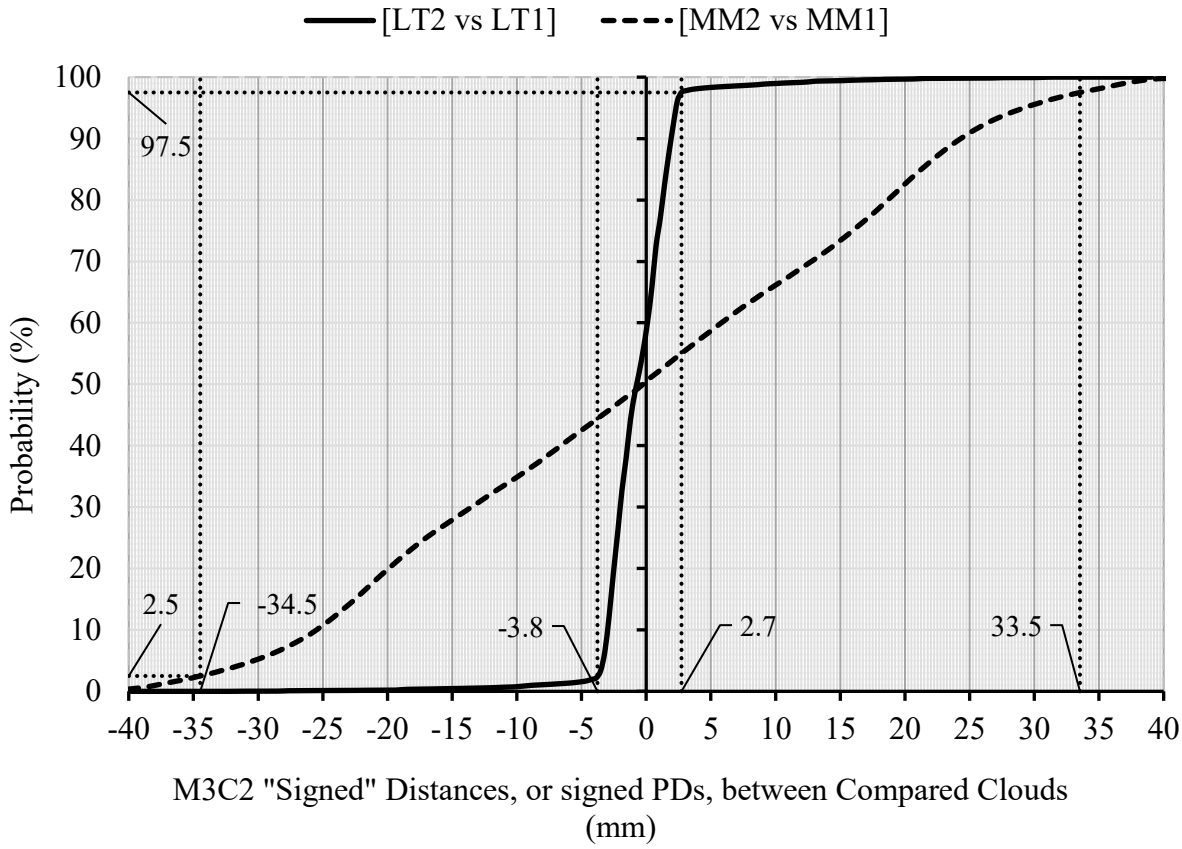

Figure 65. Graph. Cumulative distribution function of M3C2 "signed" distances, between Epochs 1 and 2, for [LT2 vs LT1], and [MM2 vs MM1]

By assuming that the C3M2-determined displacements are equally distributed on the full surface of the compared walls, a value in the y-axis of Figure 65, can be interpreted as the percentage of the wall area having displacements equal or less than a given value (x value). Under this alternative interpretation, the [LT1 vs LT2] comparison indicates that 95% of the wall area (97.5%-2.5%) experienced displacements in the [–3.9 mm, 2.7 mm] interval. This is in close agreement with the fact that, at the CW, the simulated displacements (3-34 mm) only affected ~3.5% of the wall. That is, 96.5% of the wall remained displaced between Epochs 1 and 2. In contrast, the [MM1 vs MM2] comparison shows that 95% wall area displaced within the [–34.5 mm, 33.5 mm] interval, which is highly inaccurate. Therefore, under the assumption of equally distributed CC-determined

displacements, the analyzed TB LiDAR technique outperforms the photogrammetry model considered in this CC analysis.

ESTIMATION OF NOISE ASSOCIATED WITH VARIOUS MEASURING AND MODELING TECHNIQUES AT THE CW

During the analysis of the CW across Epochs 1 and 2, multiple noise estimates were derived from discrepancies in observed positions and distances, reflecting the inherent variability of the applied measurement and modeling techniques. To develop these estimates, most of the data collected was carefully evaluated and interpreted. The final noise values summarized in Table 28 correspond to the following measurement and modeling approaches:

RTS# = Leica's RTS instrument employed in this study.

MS# = Metashape model with a small number of pics from a hand-held camera.

MM# = Metashape model with a medium number of pics from a hand-held camera.

ML# = Metashape model with a large number of pics from a hand-held camera.

MD# = Metashape model with pics taken from a drone camera.

DE# = DroneDeploy model with pics taken from a drone camera and with EACPs.

LT# = TB LiDAR model

LV# = Visual-Alignment LiDAR model

Table 28. Estimated noise level associated with the different measuring/modeling techniques studied at the CW

See Notes [1]-[15] & Color Codes			ABBREVIATED MAMES OF CONSIDERED MODELS							
			RTS# (mm)	**MS#** (mm)	**MM#** (mm)	**ML#** (mm)	**MD#** (mm)	**DE#** (mm)	**LT#** (mm)	**LV#** (mm)
From **PDs**	[Ep2-RTS1], [1] →		17.7	14.4	19.7	17.5	22.2	12.8	15.5	
	[Epoch2 - Epoch1]	[2]	10.2	20.6	10.2	22.6	10.2	19.5	6.3	6.3
		[3]	13.5	23.6	15.6	26.0	11.0	22.6	7.7	8.1
		[4]	6.1	11.6	7.7	15.3	6.5	10.3	3.7	3.8
		[5]			27.7				3.6	
		[6]			34.5				3.8	
		[7]	*9.9*	*18.4*	*18.4*	*20.9*	*11.3*	*18.7*	*6.3*	*8.4*
From **DDs**	[Epoch 1 - RTS1]	[8]		8.9	10.9	11.6	18.9		3.6	2.7
		[9]		11.6	13.5	15.1	31.9		3.8	3.7
		[10]		6.6	6.9	7.4	12.6		1.8	1.7
		[11]		*9.0*	*10.4*	*11.4*	*21.1*		*3.1*	*2.7*
Noise Estimates			COMBINED ESTIMATES							
		[12]	9.9	13.7	14.4	16.1	16.2	18.7	4.7	5.6
		[13]	9.9	18.4	18.4	20.9	21.1	18.7	6.3	8.4
		[14]	13.5	23.6	34.5	26	31.9	22.6	12.8	15.5
			ESTIMATED NOISE LEVEL							
			RTS#	**MS#**	**MM#**	**ML#**	**MD#**	**DE#**	**LT#**	**LV#**
		[15]	**9.9**	**18.4**	**18.4**	**20.9**	**21.1**	**18.7**	**6.3**	**8.4**

Notes for Table 28:

[1] = PDs, [Epoch2-RTS1], 5 Users, 6 CPs, 95% Prob. = |μ±1.96×σ|
[2] = PDs, [Epoch2-Epoch1], 6 CPs, Coarse Estimate = Abs Max PD
[3] = PDs, [Epoch2-Epoch1], 6 CPs, 95% Prob. = |μ±1.96×σ|
[4] = PDs, [Epoch2-Epoch1], 6 CPs, RMSV (discrepancy magnitude)
[5] = PDs, [Epoch2-Epoch1], C2C "absolute" dist., 95% Prob. = Abs Max of 1 wall
[6] = PDs, [Epoch2-Epoch1], M3C2 "signed" dist., 95% Prob. = Abs Max of 1 wall
[7] = PDs, [Epoch2-Epoch1], Averaged values from PDs
[8] = DDs, [Epoch1-RTS1], 15 non-repeated dist. (among 6 CPs), Coarse Estimate = Abs. Max
[9] = DDs, [Epoch1-RTS1],15 non-repeated distances (among 6 CPs), 95% prob. = |μ±1.96×σ|
[10] = DDs, [Epoch1-RTS1],15 non-rep. dist. (among 6 CPs), RMSV (discrepancy magnitude)
[11] = [Epoch1-RTS1], Averaged Values from DDs
[12] = Average of [7] & [11]
[13] = Moderately Conservative Estimate = Max of [7] & [11]
[14] = Conservative Estimate = Max of all
[15] = Estimated Noise Level (at CW site)

Note For Table 28,
Color Codes:

Light Brown = From Figure 52
Light Yellow = From Table 25
Light Green = From Table 27
Light Blue = From Figure 37
Light Purple = From Figure 60
Light Orange = From Figure 65

To maximize the utility of the available data in estimating the practical noise level associated with each modeling technique, Table 28 presents noise values derived from both positional and DDs. These individual estimates were systematically analyzed and consolidated to determine the noise level observed at this site for each modeling approach.

The physical PDs (position discrepancies) observed at the CPs between Epochs 1 and 2 represent the true simulated displacements applied at those locations: 3, 5, 11, 17, 24, and 30 mm. Each modeling technique estimated these displacements with some degree of error, making it possible to calculate displacement errors for each method based on the [Epoch2 – Epoch1] comparison. The magnitude of these errors served as a key indicator of each method's sensitivity and reliability in detecting small-scale displacements within the 3–30 mm range. These error values were instrumental in establishing the practical noise level inherent to each modeling approach, with supporting data extracted from Table 25 and Table 28.

In addition, displacement values for the CPs were calculated by comparing each model's Epoch 2 positions with the corresponding RTS1 benchmarks [Epoch2 – RTS1], as illustrated in Figure 52. Further noise estimates were also derived from the CC analyses using both the C2C and M3C2 methods.

DDs, DDs, were also evaluated at the CW site. At Epoch 1, a total of 15 unique inter-CP distances were identified among the 6 CPs. Following the simulated displacements in Epoch 2, these inter-point distances changed and were no longer directly comparable to their Epoch 1 counterparts. Consequently, the analysis focused on benchmarking the Epoch 1 distances extracted from each model against those measured in the field using the RTS instrument. The resulting differences denoted as [Epoch1 – RTS1] formed on the basis of the DDs values presented in Figure 37.

Together, the combined PD- and DD-based evaluations provided a comprehensive framework for quantifying model reliability at the Control Wall. The PD analysis directly captured each model's ability to resolve localized, point-specific displacements in the 3–30 mm range, while the DD analysis offered a broader perspective on how accurately relative geometries among checkpoints were preserved. By integrating these two complementary approaches, the study not only identified the practical noise thresholds associated with LiDAR and photogrammetry but also revealed the relative strengths and weaknesses of each technique under identical test conditions. This dual framework ensured that both absolute and relative deformation patterns were rigorously assessed, providing a more holistic understanding of model sensitivity and enabling GDOT to benchmark these technologies against the RTS standard with higher confidence.

Based on these error analyses, and applying a moderately conservative approach, the estimated noise levels for each modeling technique, at the CW site, are as follows:

For RTS# measurements:	~9.9 mm
For MS# modeling:	~18.4 mm

For MM# modeling: ~18.4 mm

For ML# modeling: ~20.9 mm

For MD# modeling: ~21.1 mm

For DE# modeling: ~18.7 mm

For TB LiDAR modeling: ~ 6.3 mm

For visual-alignment LiDAR modeling: ~ 8.4 mm

CHAPTER 7. RESULTS AT BRIDGE B1-CROSSGATE

Bridge B1-Crossgate is equipped with two MSE walls, one at each abutment. The research conducted at this site centered on generating high-fidelity 3D virtual models to assess their effectiveness in capturing the spatial configuration of the MSE walls with precision. Unlike other locations investigated across two different epochs, this bridge was evaluated only during a single data acquisition period, Epoch 1, conducted in the Summer 2023 academic term. Consequently, temporal displacements could not be assessed. However, the relative accuracy of the generated models (with respect to accurate RTS field measurements) and their geometric consistency were rigorously evaluated using high-precision field data.

Two primary modeling techniques were employed during Epoch 1: (i) static terrestrial LiDAR and (ii) drone-based photogrammetry. For the LiDAR method, two point-cloud registration approaches were examined using Leica's C10 scanner: TB registration and Visual-Alignment (VA) registration. Each scan captured spherical targets affixed to GCPs, and the resulting 3D models were georeferenced to a locally defined coordinate system established via a balanced closed traverse. Leica's TCRP 1201+ RTS was utilized to measure traverse distances and angles, as well as to determine the precise positions of all involved CPs. The LiDAR-derived datasets are labeled Target-Based LiDAR at Epoch 1 (TBL1) and Visual-Alignment LiDAR at Epoch 1 (VAL1) (both representing Epoch 1. RTS-derived measurements are designated RTS1, serving as the reference for all discrepancy analyses.

Additionally, UAV photogrammetry was conducted using a DJI Matrice 30 (M30) drone and processed via the DroneDeploy software platform. The drone's built-in RTK system was used without a GNSS base station. Four ground-level GCPs were used for photogrammetry, along with two EACPs placed on each wall to improve vertical accuracy. A total of 313 images (246 exterior and 67 interior) were captured. The processed model, referred to as DS1, was transformed into the selected local coordinate system to enable comparisons with RTS and LiDAR models.

As only one epoch was recorded, the main goal was to assess how well these non-contact methods (LiDAR TB, LiDAR VA, and photogrammetry DS1) aligned with RTS benchmark coordinates. Any differences between them were interpreted as methodological noise or inherent limitations in the modeling systems rather than true structural displacements. These discrepancies may stem from random and systematic errors both in the field and during postprocessing. Field-related sources of error include slight misplacement of instruments on GCPs, imperfect leveling, aiming inaccuracies, and variations in lighting or surface reflectivity. Postprocessing errors may arise from inconsistencies during feature matching, target detection, scan registration, and georeferencing steps. For photogrammetry models, errors can also result from limitations in image overlap, GCP recognition, or the lack of base-station correction in the drone RTK data.

The sections that follow provide detailed descriptions of the survey setup, modeling workflows, and the discrepancy analyses conducted at bridge B1-Crossgate. These analyses include PD and DD comparisons between the virtual models (TBL1, VAL1, and DS1) and RTS1 data.

LOCAL SYSTEM OF REFERENCE AT B1-CROSSGATE

At this bridge site, a 6-sided, polygonal, closed traverse was implemented and carefully balanced to establish a reliable local coordinate system. For this purpose, the precise 1-second RTS instrument was employed. The traverse consisted of 6 vertices, labeled A, B, C, D, E, and F. During traverse calculations, each internal horizontal angle was balanced twice: first locally, by comparing each internal angle to its adjacent external angle at the same vertex, and then globally to ensure that the total sum of internal angles matched the theoretical sum for a hexagon, 720°.

Horizontal distances were measured multiple times and adjusted using the Compass (Bowditch) Rule to distribute longitudinal corrections to balance the closure error. Each vertical angle was also measured twice, and the average was used to determine the relative elevation of each GCP vis trigonometric leveling. The total elevation error of closure was then distributed proportionally across all traverse legs based on their respective horizontal lengths.

Appendix A present detailed horizontal traverse and elevation calculations, respectively. Figure 66 shows an aerial view (not to scale) of B1-Crossgate, illustrating the approximate layout of the 6 GCPs. Figure 67 displays the relative horizontal arrangement and local coordinates (X = Easting, Y = Northing) of those GCPs within the selected local reference system. The adopted reference "North" direction does not coincide with true geodetic North. Nonetheless, this orientation was consistently applied throughout the modeling and analysis process at this site.

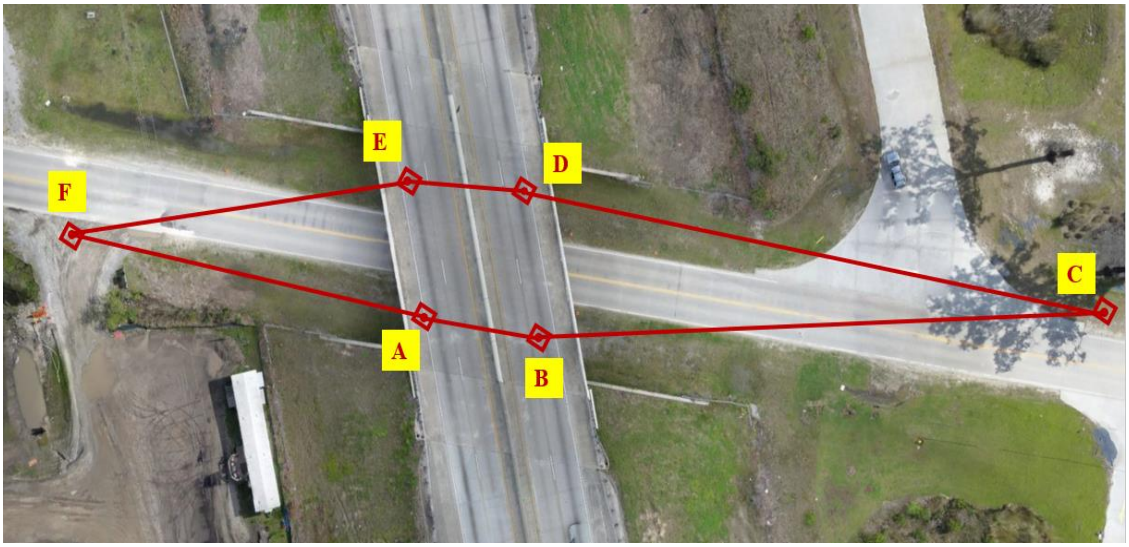

Figure 66. Photo. Aerial view of 6-sided closed traverse near B1-Crossgate

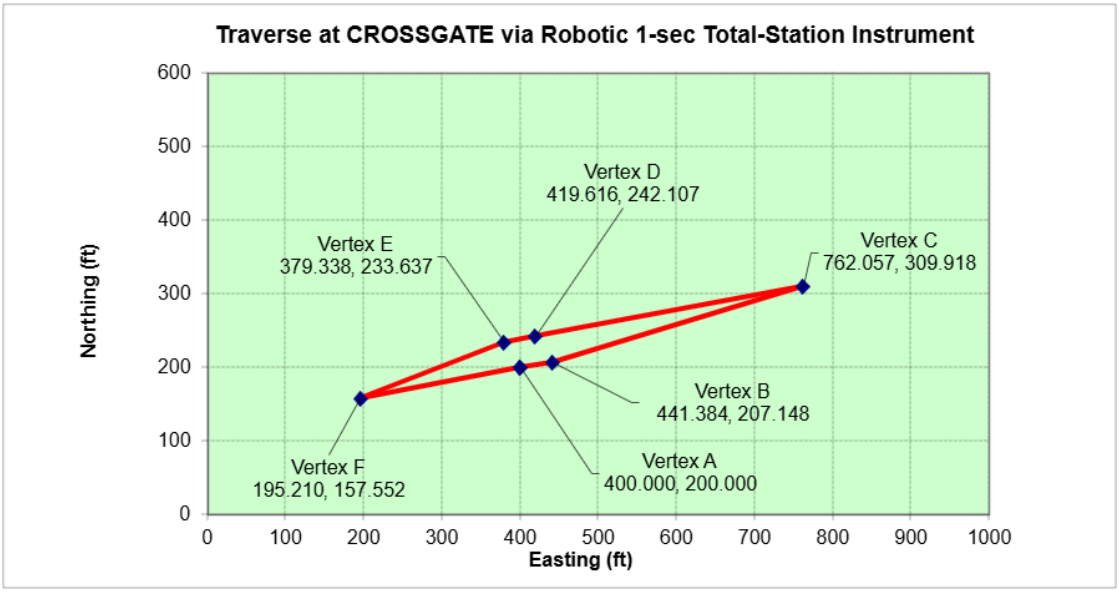

Figure 67. Graph. Horizontal coordinates of 6-sided closed traverse near B1-Crossgate

Table 29 summarizes the key properties of the closed traverse established at B1-Crossgate. The Compass Rule (Bowditch method) was used for horizontal balancing, resulting in a total perimeter of 1,177.355 feet (358.876 meters) and a longitudinal error of closure of 0.0136 ft (4.15 mm). The attained longitudinal precision was 1:86,406, which far exceeds the minimum standard of 1:20,000

(GDOT, 2022), confirming the accuracy of the traverse. The elevations of the GCPs were determined using trigonometric leveling. This resulted in a vertical error of closure of just 0.009 ft (2.7 mm), indicating good leveling accuracy as well.

Table 29. Properties of 6-sided, closed traverse in B1-Crossgate

Traverse at Bridge	Perimeter	Total Horizontal Angular Error of Closure	Attained Longitudinal Precision	Elevation Error of Closure
	ft ; [m]	seconds	Ratio	ft ; [mm]
Crossgate Rd	1177.355; [358.876]	+56	1/86406	0.009; [2.7]

Table 30. Local spatial coordinates of seven GCPs near Bridge 1 – Crossgate

Name of the GCPs	Easting (ft)	Northing (ft)	Elevation (ft)
	X	Y	Z
A	400.000	200.000	100.000
B	441.384	207.148	100.043
C	762.057	309.918	98.187
D	419.616	242.107	99.616
E	379.338	233.637	99.655
F	195.210	157.552	100.587

CHECKPOINTS AT B1-CROSSGATE

A total of 12 CPs were established on the MSE walls at B1-Crossgate to support spatial accuracy analysis and monitoring efforts. These CPs were distributed equally between the North and South walls, with 6 CPs on each wall. As shown in Figure 68, each CP was marked using a 6-inch-diameter, black-and-white circles, designed for easy visibility in both LiDAR and photogrammetric datasets.

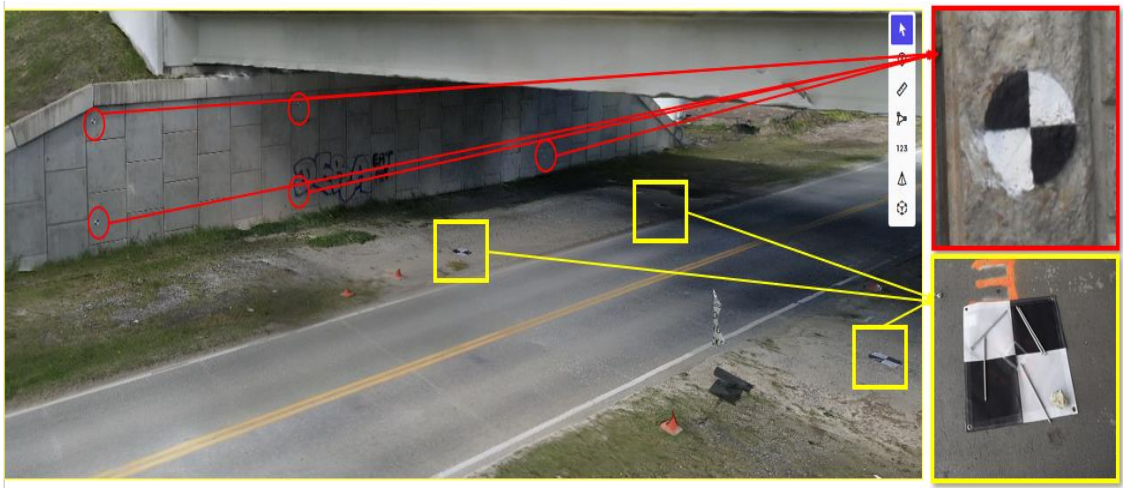

Figure 68. Photo. Black-&-white rectangles for GCPs and circles for CPs on MSE walls

The CPs were arranged following a structured layout: three vertical pairs per wall, with each pair consisting of an upper (U) and a lower (D) checkpoint. These were spaced near the beginning, middle, and end sections of each wall to ensure broad spatial coverage and capture potential displacements across the entire wall face. The RTS instrument was used to determine the coordinates of all CPs. For this, angular and linear measurements between the GCPs and each CP were completed. For quality control, those RTS measurements were performed twice using different GCPs as station and backsight, and the results were averaged to obtain the final coordinates. This redundancy helped mitigate observational error and ensured precision in the derived data. All CP coordinates were expressed in the selected local coordinate system defined by the previously established 6-point closed traverse. These RTS-derived coordinates serve as the benchmark (RTS1) for evaluating discrepancies in position and distance when compared to LiDAR and photogrammetry-derived models. The finalized local coordinates of all twelve CPs are presented in Table 31 and referred to as RTS1 values.

Table 31. RTS1 Coordinates of 12 CPs near B1-Crossgate

Wall	CPs	Easting (ft)	Northing (ft)	Elevation (ft)
		X	Y	Y
NORTH	N1U	485.604	192.095	112.648
	N1D	485.552	191.958	103.078
	N7U	456.233	186.180	112.664
	N7D	456.354	186.141	103.065
	N18U	401.989	175.498	112.535
	N18D	401.982	175.379	102.236
SOUTH	S1U	335.734	248.242	112.005
	S1D	335.799	248.224	102.151
	S13U	393.738	259.760	111.767
	S13D	393.878	259.734	101.576
	S21U	432.229	267.438	111.589
	S21D	432.467	267.427	101.731

LIDAR MODELS FOR EPOCH 1 AT B1-CROSSGATE

At this site, one pair of virtual 3D point-cloud models was generated using static terrestrial LiDAR during Epoch 1 (summer 2023). The pair consisted of a TB model and a VA (Visual-Aligned) model. Since only one data acquisition epoch was conducted at this site, displacement analysis across time was not applicable; however, accuracy evaluation relative to RTS benchmark coordinates was still performed. For this bridge, the LiDAR models were based on 6 individual scans collected with a Leica C10 scanner. After noise removal eliminating pedestrian and vehicle interference, as well as any ambient scanning artifacts (e.g., solar beams), each scan was registered into a common system of reference using both TB and VA registration methods. This doble modeling approach enabled comparison of their respective spatial accuracies against RTS-derived measurements.

Each scan captured 6 spherical targets (one at each GCP). While all 6 targets were acquired in the field during scanning, only 4 targets were selected and used during the registration process in Cyclone Core software to establish the final coordinate transformations required by the georeferencing process. For the VA model, alignment relied on visual overlap and C2C matching. Each scan had substantial overlapping areas within its closest neighbors, and less superposition with distant neighbors, but still some overlapping with all 5 neighbors. This consistent overlap was crucial for ensuring the effectiveness of the VA approach. Both the TB and VA models were georeferenced to the local coordinate system defined by the closed traverse. The final models shared the same coordinate system as the GCPs, ensuring consistent alignment for comparison. The 3D coordinates of the 12 CPs were extracted from each of the two LiDAR models. These extracted sets are herein referred to as TBL1 and VAL1, respectively. Each set was then compared to the RTS1 coordinates measured in the field, enabling PD (position discrepancy) and DDs (distance discrepancy) analysis of the TB and VA models at this site.

Figure 69 and Figure 70 show the TB and VA LiDAR point-cloud models, respectively, of the MSE walls, at B1-Crossgate, for Epoch 1.

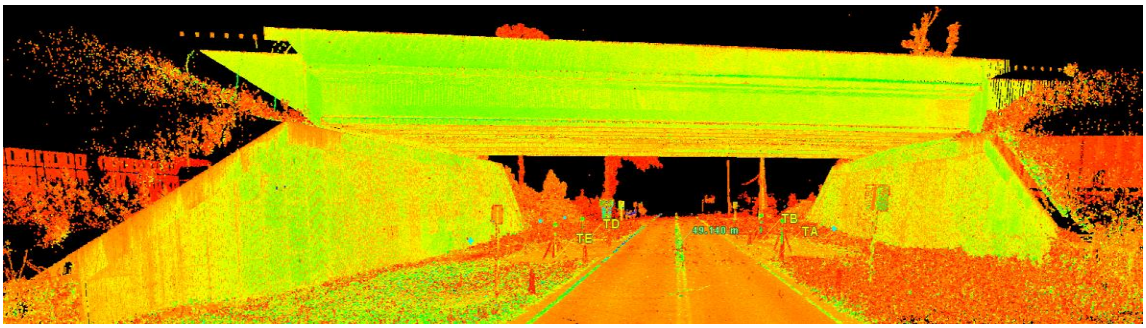

Figure 69. Photo. TB LiDAR model of MSE walls for Epoch 1, at B1-Crossgate

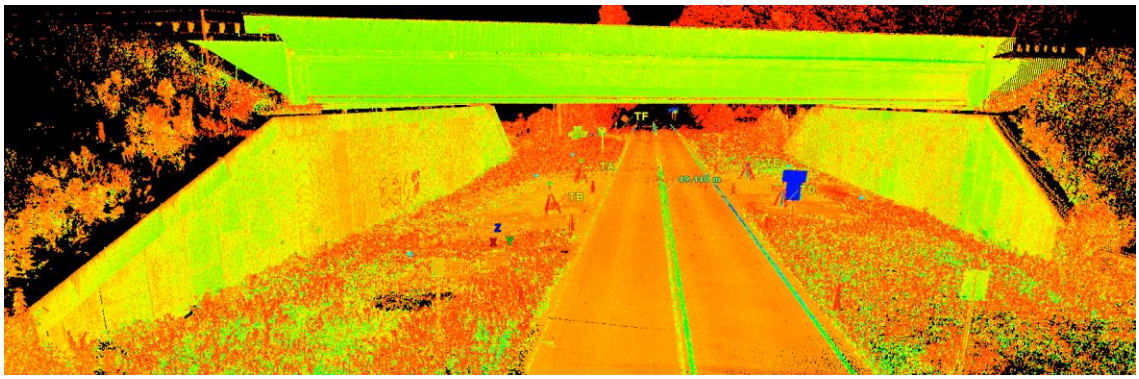

Figure 70. Photo. VA LiDAR model of MSE walls for Epoch 1 at B1-Crossgate

PD Analyses: [TBL1 vs RTS1], [VAL1 vs RTS1]

At B1-Crossgate, PD (position discrepancy) analyses were conducted to evaluate the spatial accuracy of LiDAR-derived checkpoint (CP) coordinates from Epoch 1. Two LiDAR models were analyzed, one registered using the TB method (TBL1) and the other using the VA method (VAL1). Both were compared against the field-measured coordinates obtained by using the accurate RTS instrument, which served as the reference dataset (RTS1). For each of the twelve CPs on the North and South MSE walls, a position vector was computed using both LiDAR and RTS data. The discrepancy vector for each checkpoint was calculated by subtracting RTS1 coordinates from the corresponding LiDAR model coordinates. The magnitudes of these vectors were then computed to quantify the PD values. Table 32 and Figure 71 present the summary statistics of the PDs for both TBL1 and VAL1 models. Although both models performed similarly with respect to RTS1 field measurements, the visual-alignment LiDAR model slightly outperformed the TB LiDAR model. These results suggest that both registration methods can produce similar accurate outcomes for documentation of wall displacements.

Table 32. Position discrepancies of 12 CPs comparing TB and VA LiDAR models (Epoch 1) against RTS field measurements (Epoch 1)

Epoch 1: LiDAR vs RTS1 (mm)							
LiDAR Values	Min	Max	Mean	Median	STD-S	STD-P	RMSV
[TBL1-RTS1]	3.1	12.6	7.6	6.9	2.6	2.5	8.0
[VAL1-RTS1]	3.1	14.5	6.3	5.4	3.7	3.6	7.2
Differences: { [TBL1-RTS1] – [VAL1-RTS1] } (mm)							
{ [TBL1-RTS1] – [VAL1-RTS1] }	0.06	-1.84	1.32	1.60	-1.11	-1.06	0.78

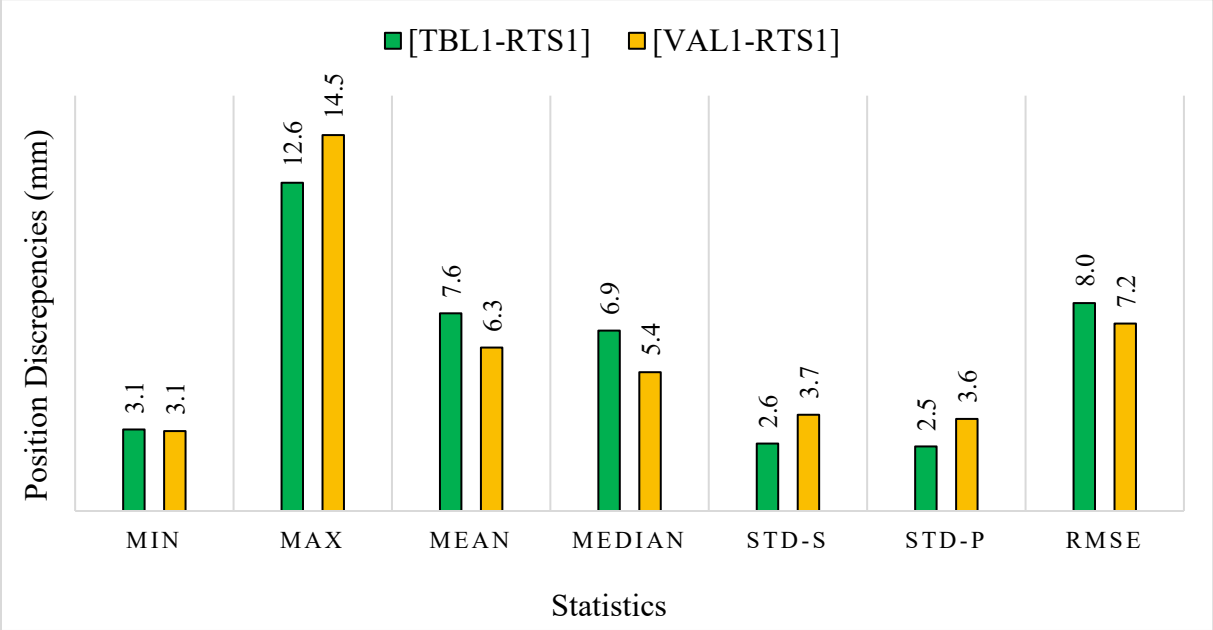

Figure 71. Chart. Position discrepancies of 12 CPs: TB and VA LiDAR models vs. RTS measurements at B1-Crossgate (Epoch 1)

If the discrepancies in positions follow a Gaussian distribution, 95% of them are expected to lie within the interval $\{\mu - 1.96\sigma, \mu + 1.96\sigma\}$, where μ represents the mean and σ the standard deviation of the population. For the models considered in Figure 71, those intervals are:

For [TBL1-RTS1]: $= \{7.6 - 1.96 \times 2.5, 7.6 + 1.96 \times 2.5\} = \{2.7 \text{ mm}, 12.5 \text{ mm}\}$

For [VAL1-RTS1]: $= \{6.3 - 1.96 \times 3.6, 6.3 + 1.96 \times 3.6\} = \{-0.8 \text{ mm}, 13.4 \text{ mm}\}$

After ordering the models based on the increasing magnitude of their maximum absolute displacement errors, the estimated maximum expected errors at a 95% confidence level are found to be 12.5 mm for TBL1 and 13.3 mm for VAL1. These values can be interpreted as indicative noise levels associated with each respective modeling technique, reflecting the extent of their positional uncertainty under typical field conditions.

DD Analysis: [TBL1 vs RTS1] and [VAL1 vs RTS1]

In addition to the PD evaluation, DD analyses were performed to quantify the accuracy of relative distances between CPs. A total of 66 non-repeated (unique) distances were computed among the 12 CPs marked on the MSE walls. These distances were extracted from two LiDAR models, one registered using the TB method (TBL1) and the other using the VA method (VAL1). Each were compared against field-measured RTS1 values.

For any pair of CPs, *P* and *Q*, their respective coordinates are (x_p, y_p, z_p) and (x_q, y_q, z_q). The distance *PQ* between them is calculated by using the three-dimensional Euclidean formula in equation 19:

$$PQ = \sqrt{(x_p - x_q)^2 + (y_p - y_q)^2 + (z_p - z_q)^2} \qquad (19)$$

Initially, these distances were computed using RTS-derived coordinates, resulting in benchmark values denoted as PQ_{RTS}. Subsequently, the same distances were calculated using coordinates

extracted from a point-cloud model, yielding corresponding values PQ_{Mod}. The discrepancy between each pair was then evaluated with equation 20:

$$\text{DD}= DD = PQ_{Mod} - PQ_{RTS} \qquad (20)$$

Note that DDs can be either positive or negative, reflecting slight overestimations or underestimations by the model. With 12 CPs placed on the walls, a total of 66 non-repeated (unique) pairwise distances were computed among them. Accordingly, for each model, 66 DDs were quantified relative to the benchmark RTS measurements. Since the number of distances is relatively high (66), the mean values help indicate systematic shifts while the standard deviations reflect the dispersion of those discrepancies, and the RMSV indicates a measure of the discrepancy magnitude.

Table 33 summarizes the statistical outcomes of these comparisons, for Epoch 1, suggesting that the visual-alignment registration achieved slightly better relative accuracy, between CPs, at this site. The difference row in Table 33 further highlights that VAL1 consistently outperformed TBL1 across all metrics for relative accuracy in distances. These results reinforce the notion that although TB registration is often more rigorous,VA—when applied with properly overlapping scans—can yield comparable or even superior internal distance consistency in LiDAR models. Figure 72 illustrates the statistics shown in Table 33.

Table 33. DDs of 12 CPs comparing TB and VA LiDAR models (Epoch 1) against RTS field measurements (Epoch 1)

Epoch 1: LiDAR vs RTS1 (mm)							
LiDAR Values	Min	Max	Mean	Median	STD-S	STD-P	RMSV
[TBL1-RTS1]	-10.7	9.1	-1.5	-1.0	4.7	4.7	4.9
[VAL1-RTS1]	-8.0	8.0	-0.7	-0.5	3.3	3.3	3.3
Differences: {[TBL1-RTS1] – [VAL1-RTS1]} (mm)							
{[TBL1-RTS1] – [VAL1-RTS1]}	-2.66	1.01	-0.78	-0.56	1.42	1.41	1.56

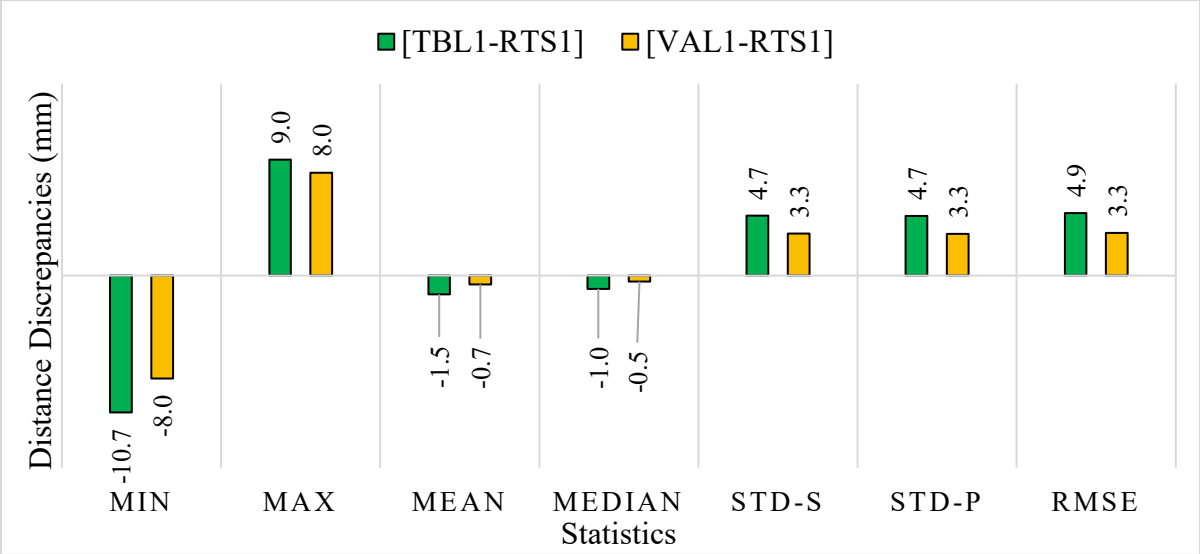

Figure 72. Chart. Sixty-six DDs: LiDAR TB and VA models vs. RTS measurements at B1-Crossgate, (Epoch 1)

Assuming the displacement errors follow a Gaussian distribution, approximately 95% of the errors are expected to lie within the interval $\mu \pm 1.96\sigma$, where μ is the mean value and σ is the standard deviation of the population. For the models shown in Figure 71, the 95% confidence intervals are:

For [TBL1-RTS1]: = {-1.5 - 1.96×4.7, -1.5 + 1.96×4.7} = {-10.7 mm, 7.7 mm}

For [VAL1-RTS1]: = {-0.7 - 1.96×3.3, -0.7 + 1.96×3.3} = {-7.2 mm, 5.8 mm}

When ordering these models based on the increasing magnitude of their maximum expected displacement error (at 95% confidence), the results suggest VAL1 has a lower uncertainty range than TBL1. Specifically, the estimated noise levels represented by the upper bounds of the confidence interval are approximately 10.7 mm for TBL1 and 7.2 mm for VAL1. These values may serve as practical indicators of the inherent uncertainty or noise associated with each modeling technique. Figure 73 illustrates the actual discrepancies in 66 non-repeated distances among all 12 CPs. The scatter plot shows similar variation in both methods. TBL1 shows a wider range of discrepancies, particularly below the zero line, with several values approaching or exceeding –10 mm, suggesting a tendency to underestimate distances, especially in the 20–40-meter range. In contrast, VAL1 displays more centralized clustering near the zero-discrepancy line, indicating better overall consistency. Nevertheless, both variations are relatively small.

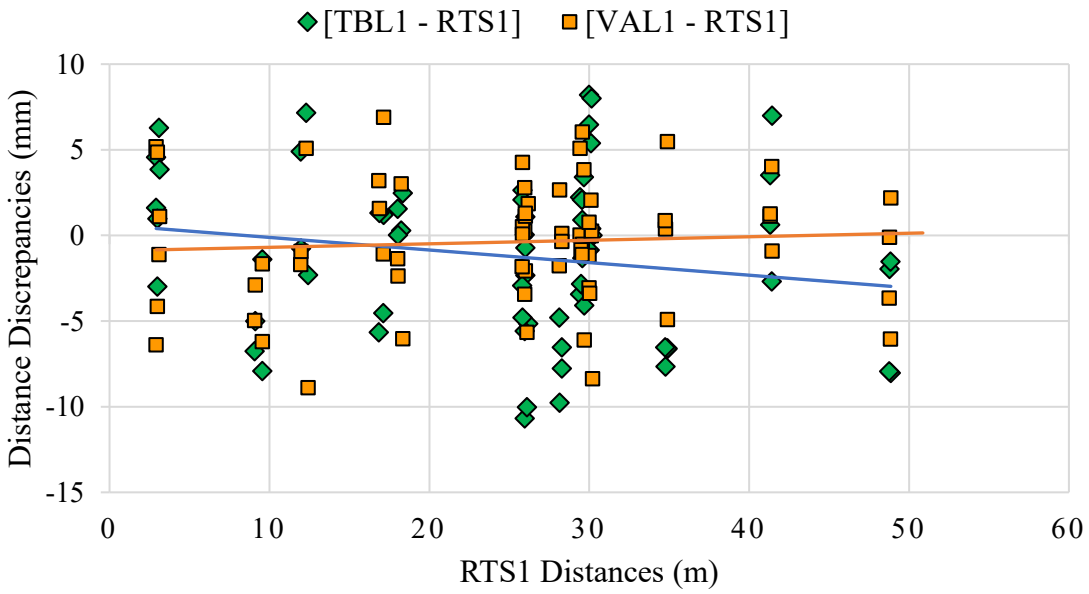

Figure 73. Graph. Sixty-six DDs between TB & VA LiDAR models versus RTS measurements (in Epoch 1).

The regression lines offer additional insight, TBL1 shows a slight negative slope, implying a mild distance-dependent bias, where larger distances correlate with increasing underestimation. Conversely, the VAL1 trend line is nearly flat, reinforcing its stability across all ranges. At the B1-Crossgate site, the visual-aligned registration method (VAL1) outperformed the TB method (TBL1) in terms of distance accuracy and consistency. While both approaches produced acceptable results, VAL1 demonstrated reduced variation and less systematic bias, making it better suited for applications like precision displacement monitoring where inter-point geometric fidelity is critical. However, the accuracy of visual-alignment LiDAR requires well overlapped scans to minimize stitching errors during the registration process.

PHOTOGRAMMETRY MODELS FOR EPOCH 1 AT B1-CROSSGATE

At B1-Crossgate, UAV-based photogrammetry was performed during Epoch 1 using a DJI Matrice 30 (M30) drone. This drone utilized its integrated RTK system, but no external GNSS base station or RTK rover was deployed for this site. A total of 246 nadir and oblique exterior images, along with 67 interior shots (under the bridge), were captured to ensure full coverage of both North and South MSE walls. These images were collected during optimal lighting and weather conditions to minimize shadows and surface noise. Out of the 6 GCPs) established with RTS instrument, 4 were selected for use in this photogrammetry workflow: A, B, D, and E. Large 2’×2’, black-and-white markers were placed at the locations of those 4 GCPs to improve visual recognition during photogrammetric processing. Additionally, to enhance vertical accuracy and scaling, two EACPs were designated on each MSE wall. These EACPs were used only during postprocessing to help the software, DroneDeploy, correctly interpret and align the wall surfaces in 3D space.

After image acquisition, all photos were uploaded to the DroneDeploy cloud platform, which automatically performed image alignment, sparse point generation, and preliminary model construction. Once GCPs were detected, DroneDeploy prompted the user via email to review and manually adjust their positions. After confirmation, processing resumed to generate a dense 3D mesh and high-resolution point cloud, with a notification sent upon completion. To ensure spatial consistency with LiDAR and RTS datasets, a CSV file containing the GCP local coordinates was uploaded, transforming the model from global to local coordinates. The same 12 checkpoints (six per wall) used in the LiDAR analysis were identified in the DroneDeploy point cloud, and pinpoints were placed at each CP center to extract their coordinates. These values, designated as DS1, were then compared to RTS-derived coordinates (RTS1) to calculate both PD and DD, enabling a direct assessment of the model's relative spatial accuracy against field benchmarks. Figure 74 presents the final DroneDeploy virtual 3D model for the MSE walls at B1-Crossgate.

Figure 74. Photo. DroneDeploy's 3D photogrammetry model of Bridge B1-Crossgate

CPs Local Coordinate from DroneDeploy Model

After completing the UAV-based photogrammetry workflow in DroneDeploy and aligning the model to the local coordinate system, the spatial coordinates of the 12 CPs (six on each MSE wall) were extracted. Each CP was visually identified in the 3D model, and its center was manually marked to record the Easting, Northing, and Elevation values. Figure 75 illustrates an example of how CP coordinates were extracted directly from the 3D point cloud environment within the DroneDeploy platform.

Table 34 presents the complete set of local coordinates for all 12 CPs, extracted from the DroneDeploy model. These values were later used for accuracy assessments through PD and DDs analyses by comparing them against RTS-derived benchmark coordinates.

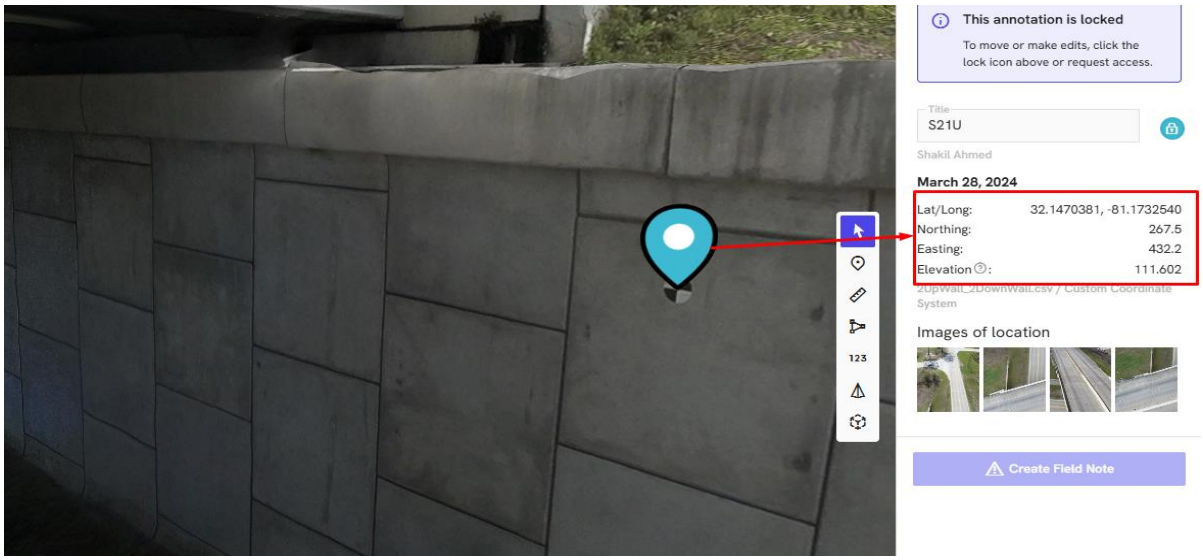

Figure 75. Photo. Extracting local coordinates of a checkpoint from photogrammetry model of bridge B1-Crossgate

Table 34. Local coordinates (DS1) of CPs extracted from the 3D photogrammetry model generated in DroneDeploy

Wall	CPs	Easting (ft)	Northing (ft)	Elevation (ft)
		Y	X	Y
North	N1U	485.600	192.100	112.650
	N1D	485.600	192.000	102.970
	N7U	456.200	186.100	112.670
	N7D	456.300	186.100	103.030
	N18U	401.900	175.500	112.550
	N18D	401.900	175.500	102.180
South	S1U	335.800	248.200	111.970
	S1D	335.800	248.200	102.050
	S13U	393.700	259.800	111.790
	S13D	393.900	259.800	101.520
	S21U	432.300	267.400	111.600
	S21D	432.500	267.500	101.700

PD Analysis: [DS1 vs RTS1]

At the B1-Crossgate site, PD analysis was performed to evaluate the relative spatial accuracy of the 3D photogrammetry model generated using DroneDeploy with respect to field measurements completed with the accurate benchmarking RTS instrument. Both the photogrammetry model (DS1) and the benchmark reference data (RTS1) were acquired during Epoch 1. No second epoch photogrammetry was conducted at this site. The coordinates of 12 CPs were extracted from the georeferenced DS1 model. For each checkpoint, a discrepancy vector was computed by subtracting the RTS1 coordinates from the DS1 coordinates, and the magnitude of each vector was calculated to determine the position discrepancy.

Figure 76 summarizes the statistical results. These findings indicate moderate to high variability in the spatial accuracy of the DroneDeploy model, even when elevated GCPs were used. The results suggest that while the model provides sufficient detail for general monitoring, its precision falls short of RTS benchmarks and TB LiDAR registration. Nonetheless, for single-epoch documentation or non-critical inspection, the DS1 model offers a practical balance between ease of data collection and spatial resolution.

Assuming the referred displacement errors follow a Gaussian distribution, 95% of those errors will be in the interval $\{\mu - 1.96\ \sigma, \mu + 1.96\ \sigma\}$, where μ is the mean value and σ is the standard deviation of the population. For the model considered in Figure 76, that interval is:

$$\text{For [DS1-RTS1]:} \quad = \{26.6 - 1.96 \times 10.4,\ 26.6 + 1.96 \times 10.4\} \quad = \{6.2 \text{ mm},\ 47.0 \text{ mm}\}$$

The magnitude of their maximum expected displacement error (at 95% confidence) is 47 mm. This value may serve as a practical indicator of the inherent uncertainty or noise associated with this modeling technique.

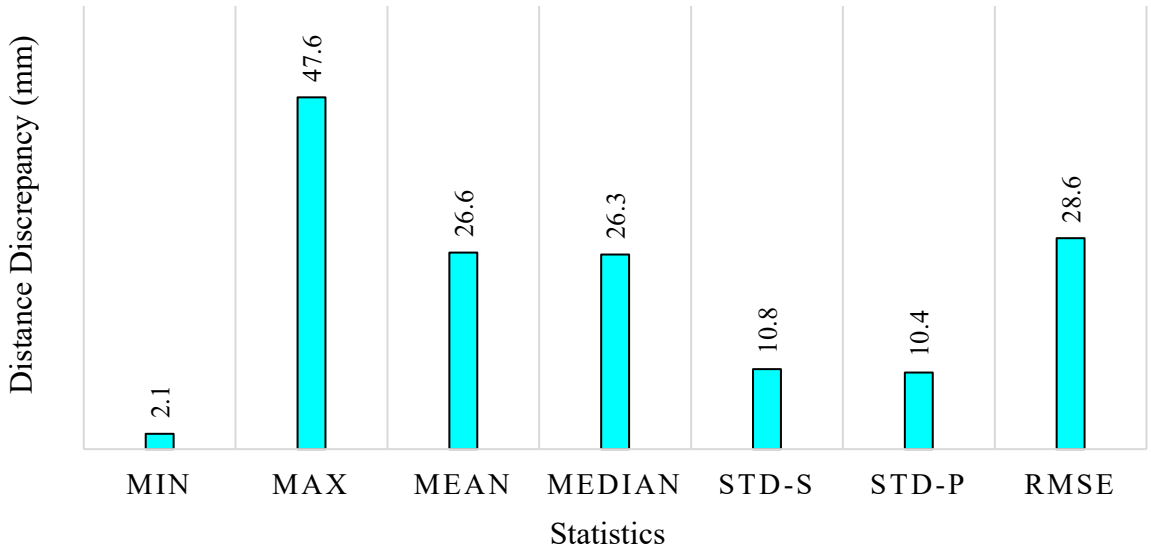

Figure 76. Chart. Position discrepancies of 12 CPs: Drone Deploy (DS1) models vs. RTS measurements at Crossgate, (Epoch 1)

DD Analysis: [DS1 vs RTS1]

In addition to PD evaluation, a DD analysis was carried out to assess the internal geometric accuracy of the photogrammetry model generated by DroneDeploy for Epoch 1. This analysis compares 66 non-repeated distances, among all 12 CPs, extracted from the photogrammetry model (DS1), against the same distances measured in the field with the benchmarking RTS instrument (RTS1). These values indicate how well the internal spacing between points is preserved in the DroneDeploy model with respect to RTS measurements. Positive values indicate overestimation, while negative values show underestimation.

Table 35 summarizes the statistical results of this comparison. These metrics indicate some internal inconsistency in the DS1 model. Figure 77 plots all 66 DDs against RTS-measured distances (RTS1), shows that the DroneDeploy model demonstrates greater scatter than the results obtained with both LiDAR models (compare Figures C7 and C11). Additionally, Figure C11 shows a distance-dependent bias, particularly underestimating longer spans. Factors contributing to this low

geometric fidelity could be the use of not fully optimized EACPs and only using the in-built RTK from the drone without GNSS base station correction. Overall, while the DS1 model provides useful data for visual inspection and surface modeling, its internal distance consistency is inferior to that of the LiDAR models, suggesting caution when relying on this type of photogrammetry modeling for high-precision displacement measurement or structural diagnostics.

Table 35. DDs of 12 CPs comparing Photogrammetry models (Epoch 1) against RTS field measurements (Epoch 1)

Epoch 1: Photogrammetry vs RTS1 (mm)							
Photogrammetry Values	**Min**	**Max**	**Mean**	**Median**	**STD-S**	**STD-P**	**RMSV**
[DS1-RTS1] (mm)	-66.0	47.1	5.6	10.2	22.7	22.6	23.2

Assuming the referred displacement errors follow a Gaussian distribution, 95% of those errors will be in the interval $\{\mu - 1.96\ \sigma, \mu + 1.96\ \sigma\}$, where μ is the mean value and σ is the standard deviation of the population. For the model considered in Figure 76, that interval is:

$$\text{For [DS1-RTS1]:} \quad = \{5.6 - 1.96 \times 22.6,\ 5.6 + 1.96 \times 22.6\} \quad = \{-38.7 \text{ mm},\ 49.9 \text{ mm}\}$$

The magnitude of their maximum expected displacement error (at 95% confidence) is 49.9 mm. This value may serve as a practical indicator of the inherent uncertainty or noise associated with this modeling technique.

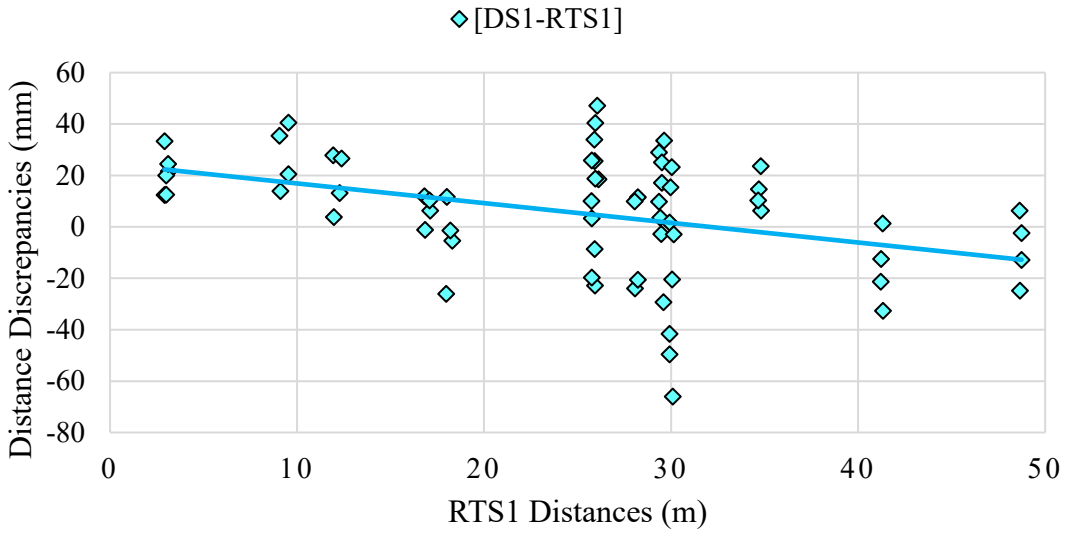

Figure 77. Graph. DDs of 12 CPs:
DroneDeploy (DS1) models vs. RTS measurements (Epoch 1) at B1-Crossgate

CHAPTER 8. RESULTS AT BRIDGE B2-OLD RIVER

DESCRIPTION OF THE WORK AT B2-OLD RIVER

This bridge, at the intersection of I-16 and Old River Road, has two MSE walls, one at each abutment. At this site, virtual 3D models of the MSE walls were generated at two different times, separated by one year, in fall 2023 and fall 2024. In this Chapter, those two times are referred to as Epoch 1 (fall 2023) and Epoch 2 (fall 2024). This dual time modeling was performed as an attempt to capture potential wall displacements occurring during that one-year period. At each epoch, two types of LiDAR modeling techniques were investigated to assess their relative accuracy with respect to field measurements completed with the accurate, one-second, benchmarking RTS instrument. Each LiDAR method used a different approach to stitch (register into the same coordinate system) individual scans. They are the TB LiDAR and the Visual-Alignment (VA) LiDAR schemes. Independent measurements were completed at each epoch. The point positions captured with the RTS instrument are referred to as RTS1 and RTS2 for Epochs 1 and 2, respectively. Similarly, measurements extracted from the finalized and georeferenced TB LiDAR models are designated as TBL1, completed in Epoch 1, and as Target-Based LiDAR at Epoch 2 (TBL2), completed in Epoch 2. Likewise, measurements extracted from the finalized and georeferenced VA LiDAR models are referred to as VAL1 and Visual-Alignment LiDAR at Epoch 2 (VAL2), for Epochs 1 and 2, respectively.

This bridge is not new, it was built 5 years ago, in 2020. During the duration of this study, fall 2023-fall 2024, its MSE walls did not show signs of deterioration, including settlements or other

types of displacements. The measurements and 3D virtual point-cloud models generated in this project, during Epochs 1 and 2, showed very small positional discrepancies between and among them. Most likely, those marginal discrepancies are due to the level of noise associated with the employed measuring and modeling techniques, and do not represent actual displacements of the MSE walls between the two epochs. Therefore, the models generated at those two times were employed to estimate the referred level of noise between two independent measurements or two different models of the same static, unchanged structures.

The referred noise is due to several factors, including various small random and potentially systematic errors, occurring in the field, while acquiring data, and in a laboratory setting, when postprocessing it. Examples of random errors in the field are: (i) slightly off centering of instruments on the GCPs, (ii) small imperfections in the verticalization of the instruments, (iii) small aiming imprecisions at involved reference points, including CPs, (iv) varying environmental conditions, etc. An example of a field systematic error are slim miscalibrations of instruments due to their normal use. Examples of random errors in postprocessing include the incorporation of minor errors when extracting point positions (coordinates) from point clouds. Due to the discontinuous nature of those clouds, those coordinates may not represent the exact positions of the intended points, but those of close neighbors. The denser the clouds, the smaller these coordinate-extraction errors are. Other postprocessing random errors may occur when using the modeling methods and their programmed algorithms to stitch (register) different scans together, using targets or VAs, or when georeferencing fully stitched models using the determined coordinates of GCPs. The above-mentioned errors are not exhaustive. Additional ones could contribute to the noise associated with the employed different measuring and modeling techniques.

The following sections describe the work, measurements, and models completed for this bridge.

LOCAL SYSTEM OF REFERENCE AT B3-OLD RIVER

In Epoch 1, a selected local system of reference was established by using 6 GCPs. They constituted the vertices of a 6-sided closed traverse. Figure 78 presents an aerial view (not at scale) of this bridge with the approximate location of the established polygonal traverse and its 6 vertices, the 6 GCPs. Figure 79 shows a plan view of the same closed traverse, indicating the relative horizontal location of all GCPs, in feet. In this selected system of reference, the North direction approximates North, but it is not the actual true North. Nevertheless, the selected local reference North is shown upward.

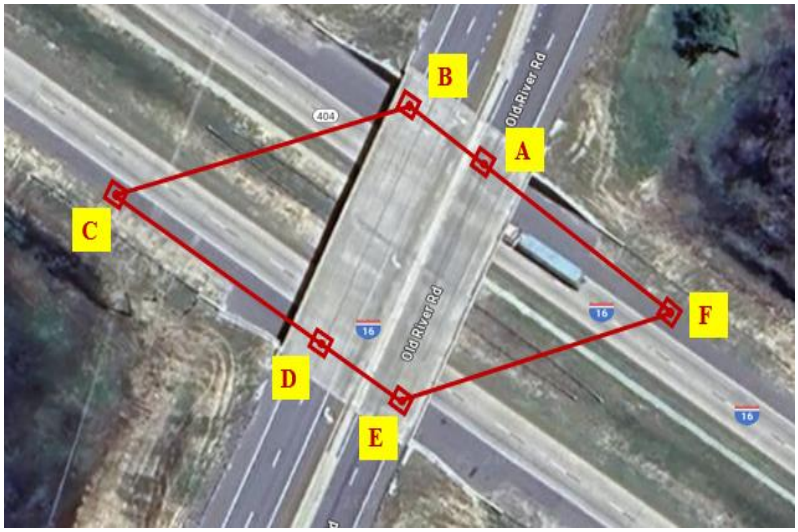

Figure 78. Photo. Aerial view of 6-sided closed traverse near B2-Old River

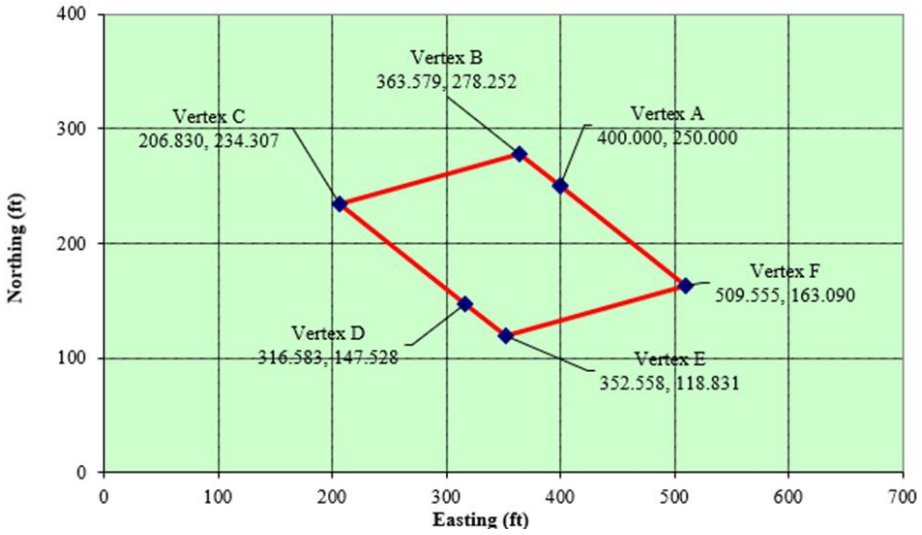

Figure 79. Graph. Horizontal coordinates of 6-sided closed traverse near B2-Old River

Table 36 presents a summary of the characteristics of the resulting traverse calculations, in Epoch1, for B2-Old River, including their errors of closure and attained longitudinal precision.
Table 37 shows the resulting spatial coordinates (X, Y, Z) of all 6 GCPs.

Table 36. Characteristics of 6-sided, closed traverse near B2-Old River

Traverse at Bridge	Perimeter	Total Horizontal Angular Error of Closure	Attained Longitudinal Precision	Elevation Error of Closure
	ft ; [m]	seconds	Ratio	ft ; [mm]
Old River	697.780 ; [212.683]	-14.5	1/26,324	-0.026 ; [-7.9]

Table 37. Local spatial coordinates of GCPs near B2-Old River

GCPs	Easting (ft)	Northing (ft)	Elevation (ft)
	X	Y	Z
A	400.000	250.000	100.000
B	363.579	278.252	100.088
C	206.830	234.307	100.063
D	316.583	147.528	100.022
E	352.558	118.831	99.946
F	509.555	163.090	98.941

CPS AT B2-OLD RIVER

At this bridge site, a total of 12 CPs were painted on the MSE walls to monitor their potential displacement over time. Six of them were placed on one MSE wall and six on the other MSE wall, across highway I-16. Each CP consists of a 6-inch-diameter circle with black-and-white quadrants, as seen in Figure 80. Three pairs of CPs were painted on each MSE wall. Each pair consisted of one CP near the top of the wall and one CP near the bottom of the wall. One pair was near the beginning of the wall, another pair near the center of the wall, and a third pair near the end of the wall.

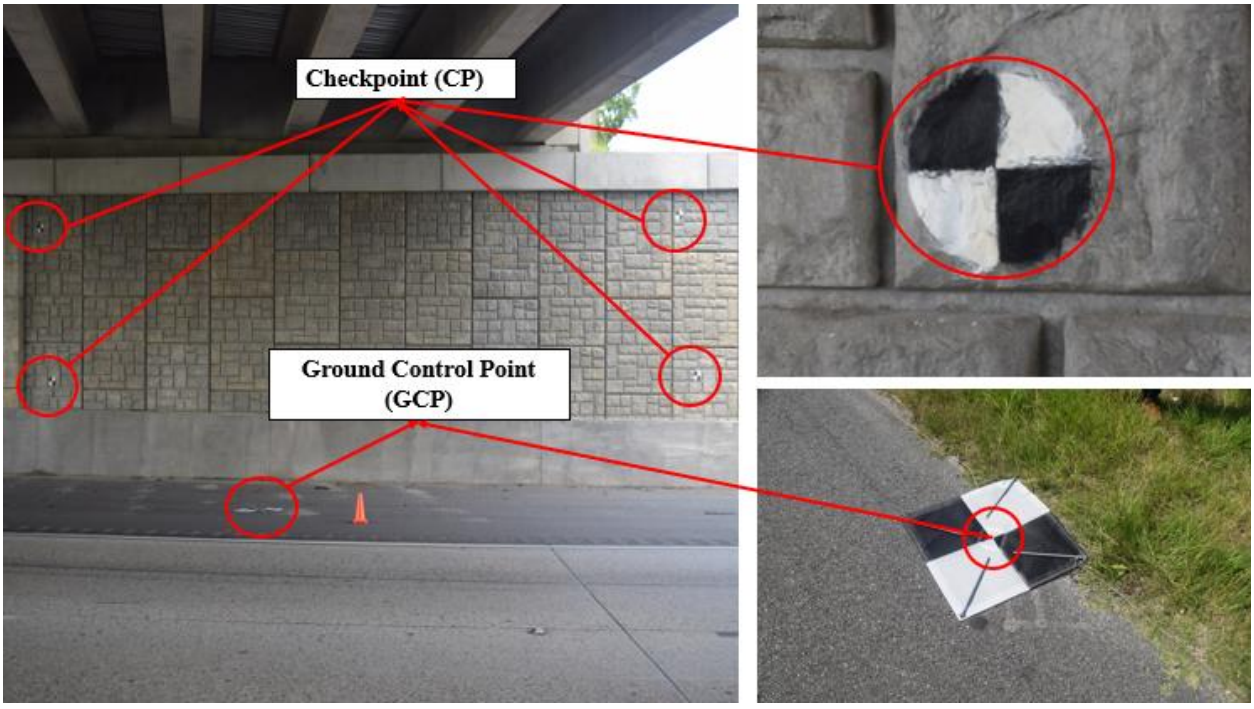

Figure 80. Photo. Sample GCP and CPs on an MSE wall in B2-Old River

In Epoch 1, after the 12 GCPs were painted, their spatial coordinates were determined in the field via the accurate RTS instrument. For that purpose, the RTS device was stationed on a nearby GCP and used another GCP as backsight. This was done twice to detect and avoid errors. That is, in

Epoch 1, the coordinates of each CP were calculated twice, each time from a different GCP. The resulting two sets of coordinates, for each CP, were averaged to reach the calculated coordinates of that CP, in Epoch 1. This was completed for each of the 12 CPs. For quick reference, the values of those average field coordinates are herein referred to as RTS1 values. Similarly, the same process and averaging was performed in Epoch 2, resulting in RTS2 values. These two sets (RTS1 and RTS2) of field coordinates for the 12 CPs are presented in Table 38. They were obtained with the accurate RTS instrument to compare them and potentially capture wall displacements that occurred between Epochs 1 and 2.

Table 38. Coordinates of 12 CPs near B2-Old River

CPs	Easting (ft)		Northing (ft)		Elevation (ft)	
	X		Y		Y	
	RTS1	RTS2	RTS1	RTS2	RTS1	RTS2
1. NWU	353.384	353.358	309.356	309.369	113.221	113.210
2. NWD	353.898	353.873	309.006	309.021	104.536	104.533
3. NMU	394.614	394.607	276.860	276.859	112.978	112.985
4. NMD	395.416	395.409	276.251	276.255	104.561	104.565
5. NEU	433.612	433.593	246.236	246.262	113.627	113.620
6. NED	434.736	434.715	245.415	245.440	105.149	105.139
7. SWU	285.117	285.114	150.184	150.174	112.881	112.878
8. SWD	286.024	286.008	149.430	149.434	105.076	105.077
9. SMU	323.324	323.315	119.997	120.003	113.491	113.481
10. SMD	322.926	322.927	120.278	120.273	105.018	105.017
11. SEU	364.106	364.086	87.839	87.838	112.702	112.698
12. SED	364.574	364.554	87.489	87.496	104.166	104.167

LIDAR MODELS FOR EPOCHS 1 AND 2 AT B2-OLD RIVER

In B2-Old River, 2 pairs of virtual 3D point-cloud models were generated using static terrestrial LiDAR. One pair consisted of TB and VA models generated in Epoch 1 (fall 2023) and the other

pair were TB and VA models produced in Epoch 2 (fall 2024). Those 2 pairs were generated one year apart to potentially capture wall displacements that may have occurred during that period. Note that to capture wall displacements, occurring between two different time epochs, they are to be larger than the measuring noise associated with the employed LiDAR modeling approaches. Therefore, in this study, several measurements were repeated to estimate that noise.

In this bridge, each LiDAR model was formed by 6 scans. After undesired noise was removed from each scan, they were registered into a common system of reference, following two different approaches, TB and VA, as described earlier in this report. These two registration techniques were employed to study their relative accuracy with respect to measurements, completed in the field, via an accurate RTS instrument.

Each scan captured 6 common targets (one at each GCPs). Those targets assisted in the stitching of all 6 scans when using the TB approach. Additionally, each scan overlapped with all remaining 5 scans. This overlapping was more pronounced between close neighboring scans than between more separated scans. Nevertheless, even the two most separate scans presented some overlapping. That is, each of the 6 scans shared overlapping areas with the remaining 5 scans. This is mentioned because overlapping is a necessary condition to improve the accuracy of the VA registration approach.

For each Epoch, the resulting 2 full LiDAR models, TB and VA, were georeferenced using the coordinates of the GCPs. That is, the system of reference of the final georeferenced models coincides with the system of reference used for the GCPs (traverse vertices). For illustrative

purposes, Figure 81 and Figure 82 show the TB georeferenced point clouds for Epochs 1 and 2, respectively. After georeferencing all 4 LiDAR models, the coordinates of the 12 CPs were extracted from each of them. For quick reference, the coordinates of the CPs from Epoch 1, extracted from the TB and VA LiDAR models, are herein referred to as LT1 and VAL1, respectively. Similarly, those from Epoch 2 are referred to as LT2 and VAL2. Each set was compared against the coordinates of the same CPs, determined in the field, with the accurate RTS instrument. This allowed the analysis of PD and DD for all 4 models.

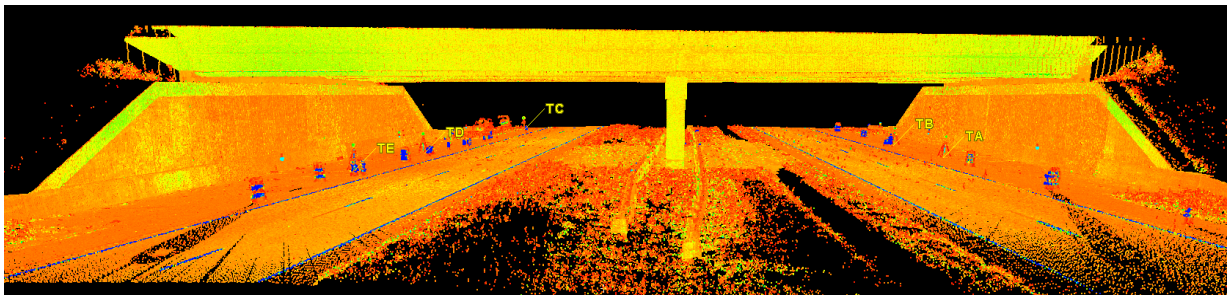

Figure 81. Photo.TB LiDAR point cloud of Epoch 1 for MSE walls at B2-Old River

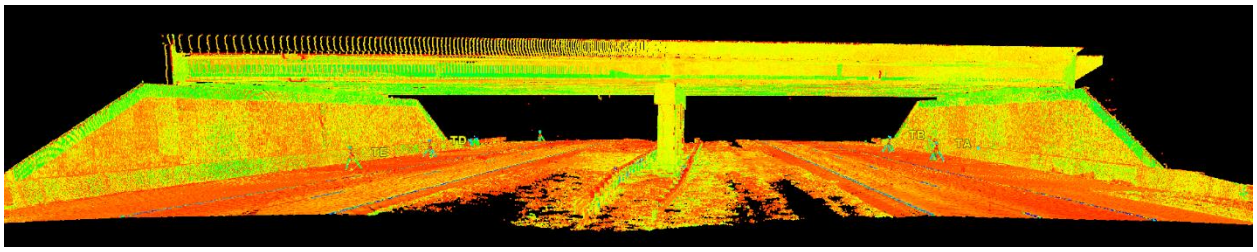

Figure 82. Photo. TB LiDAR point cloud of Epoch 2 for MSE walls at B2-Old River

PD Analyses: [LT1 vs RTS1], [VAL1 vs RTS1], [LT2 vs RTS1], and [VAL2 vs RTS1]

In each Epoch, 1 and 2, the coordinates of all 12 CPs points were extracted from the georeferenced TB and VA full LiDAR models. This resulted in the following 4 sets of 12 values each: TBL1,

VAL1, TBL2, and VAL2. Additionally, the coordinates of the 12 CPs were determined via field measurements performed with the accurate, benchmarking, RTS instrument, in Epoch 1. Those are the RTS1 values. The relative position discrepancies of the CPs in each LiDAR model, with respect to their respective field positions determined with the RTS device, were calculated as indicated in the following paragraph.

Since the position coordinates (x, y, z) for each CP can be considered as a position vector, the PDs were calculated in a vectorial sense. For example, considering the TB LiDAR model of Epoch 1, the 12 position vectors (coordinates) of the 12 CPs were determined twice. One time in the field, via the benchmarking RTS instrument (the RTS1 set), and a second time by extracting them from the georeferenced full TB LiDAR model of Epoch 1 (the LT1 set). The RTS1 set was subtracted, point by point, and coordinated by coordinate, from the LT1 set. For each CP, this difference resulted in a discrepancy vector. Then, the magnitudes of those 12 discrepancy vectors were calculated. Those magnitudes are referred to as position discrepancies (PDs). Note that the above-defined PDs are positive numbers. That is, their average values will not be zero, but a positive number. Their mean values will only be zero when all sample PDs are zero. Their statistics, for the 12 CPs, were calculated. Summarizing, the PDs considered in the example used in the previous explanation resulted from the LT1 vs RTS1 comparison. A similar PD analysis was performed for the VA LiDAR model of Epoch 1 (VAL1 vs RTS1), for the TB LiDAR of Epoch 2 (TB2 vs RTS1), and for the VA LiDAR model of Epoch 2 (VAL2 vs TRS1). In all cases, the positions extracted from the TB and VA LiDAR models, from Epochs 1 and 2, were compared against the positions determined by field measurements completed with the RTS instrument, in Epoch 1.

Table 39 shows the statistics of the PDs for all 12 CPs, attained in the TB and VA LiDAR models, during Epochs 1 and 2, with respect to field measurements obtained with the accurate RTS instrument, in Epoch 1. In that table, it is observed that The PDs are similar for the TB and VA LiDAR models in both epochs. However, the statistics for Epoch 2 show values closer to RTS1 than those of Epoch 1. Also, a reduction in discrepancies is observed from Epoch 1 to 2, with the VA LiDAR models showing a slightly more notable reduction than the TB models. This indicates that there may not have been measurable wall displacements between Epochs 1 and 2, via the employed LiDAR approaches. Additionally, the overall relative positional accuracy, with respect to the RTS device used in Epoch 1, improved in Epoch 2. Perhaps, this is since two different laser scanners were employed in each Epoch (the older C10 scanner in Epoch 1 and the newer P50 scanner in Epoch 2), and the involved operators had already acquired more scanning experience in Epoch 2. Nonetheless, it is likely that the observed positional differences between Epochs 2 and 1 do not correspond to actual wall displacements but are part of the noise associated with measuring and modeling techniques.

Overall, the above comparisons indicate that, in this bridge, both registration approaches, TB and VA, presents similar relative accuracies with respect to field measurements completed with an accurate robotic total-station instrument. That is, both approaches can be used for LiDAR modeling of this bridge with similar accuracy.

Table 39. PD of 12 CPs. TB and VA, from Epochs 1 & 2, versus measurements completed in the field with RTS instrument in Epoch 1

Epoch 1: LiDAR vs RTS1 (mm)							
LiDAR Values	Min	Max	Mean	Median	STD-S	STD-P	RMSV
[TBL1-RTS1]	2.61	13.15	6.51	5.26	3.30	3.15	**7.24**
[VAL1-RTS1]	1.02	14.10	6.31	4.56	4.26	4.08	**7.51**
Epoch 2: LiDAR vs RTS1 (mm)							
[TBL2-RTS1]	3.04	7.49	4.91	4.58	1.62	1.55	**5.15**
[VAL2-RTS1]	1.76	6.55	4.57	4.61	1.56	1.49	**4.81**
Differences: [Epoch 2 – Epoch 1] (mm)							
[TBL2-TBL1]	0.43	-5.66	-1.61	-0.68	-1.67	-1.60	**-2.09**
[VAL2-VAL1]	0.74	-7.55	-1.74	0.05	-2.70	-2.58	**-2.70**

PD Analyses [RTS2 vs RTS1], [LT2 vs TBL1], and [VAL2 vs VAL1], at B2-Old River

Since the previous analysis used as reference the coordinates of the CPs determined in the field with the RTS instrument in Epoch 1 (RTS1 values), and it indicates that there were no measurable wall displacements between Epochs 1 and 2, additional PD analyses were completed. This time, the field coordinates were calculated again in Epoch 2 (RTS2) and, for each measurement/modeling technique, the coordinates acquired in Epoch 2 were directly subtracted from the coordinates acquired in Epoch 1, as follows: [RTS2 - RTS1], [LT2 - TBL1], and [VAL2 - VAL1]. That is, this time the discrepancies were defined between epochs, not with respect to RTS1 values. These new 3 types of PDs were determined for each CP and are shown in Table 40 and Figure 83, where each CPs is identified by a three-character name, according to the following convention: (i) The first letter is either N or S to identify the North or South MSE wall in this bridge. (ii) The second letter is either W, or M, or E identify the West, Middle or East portion of the MSE wall where the CP is located. (iii) The third letter is either U or D to identify the Up or Down location of the CP.

If there were no wall displacements between Epochs 1 and 2, and the performed measurements/ modeling were perfect, those PDs should be zero. However, they are not. This is because even if no wall displacements occurred, our employed processes incorporate some level of error. We refer to that error as noise. If wall displacements are not larger than that noise, they cannot be captured by the employed techniques.

Table 40 and Figure 83 show that the maximum PD values are 10.5 mm for [RTS2-RTS1], 11.7 mm for [TBL2-TBL1], and 14.3 mm (0.047 ft) for [VAL2-VAL1]. For each technique, the discrepancies between Epochs 1 and 2 are rather small. Again, assuming that there was no wall displacements between those two epochs, the indicated maximum values can be considered as a coarse approximation to the noise level associated with the employed measuring/modeling techniques.

Table 40. Position discrepancies of 12 CPs, [Epoch 2 - Epoch 1].

Checkpoint (CP)		[RTS2-RTS1]		[TBL2-TBL1]		[VAL2-VAL1]	
		ft	mm	ft	mm	ft	mm
North MSE Wall	NWU	0.031	9.5	0.016	4.8	0.043	13.3
	NWD	0.029	8.9	0.033	10.0	0.015	4.5
	NMU	0.010	2.9	0.019	5.7	0.013	3.9
	NMD	0.009	2.7	0.018	5.6	0.018	5.6
	NEU	0.033	10.1	0.039	11.7	0.047	14.3
	NED	0.035	10.5	0.016	4.9	0.046	14.1
South MSE Wall	SWU	0.011	3.3	0.021	6.3	0.010	3.1
	SWD	0.016	5.0	0.023	6.9	0.027	8.1
	SMU	0.015	4.4	0.027	8.1	0.028	8.4
	SMD	0.006	1.7	0.026	7.9	0.022	6.8
	SEU	0.020	6.2	0.002	0.7	0.013	3.9
	SED	0.022	6.6	0.017	5.3	0.007	2.2
12 CPs STATISTICS							
Function		**[RTS2-RTS1]**		**[TBL2-TBL1]**		**[VAL2-VAL1]**	
		ft	**mm**	**ft**	**mm**	**ft**	**mm**
Min =		0.006	1.7	0.002	0.7	0.007	2.2
Max =		0.035	10.5	0.039	11.7	0.047	14.3
μ = Mean =		0.020	6.0	0.021	6.5	0.024	7.4
Median =		0.018	5.6	0.020	6.0	0.020	6.2
STD-S =		0.010	3.1	0.009	2.8	0.014	4.4
σ = STD-P =		0.010	3.0	0.009	2.7	0.014	4.2
RMSV =		0.022	6.7	0.023	7.0	0.028	8.5

In statistics, it is well known that the standard deviation (STD) is a measure of the dispersion of a dataset around its mean value. RMSV is a measure of the magnitude of a set of numbers. For a gaussian (normal) distribution, approximately 95% of the data falls within 1.96 standard deviations of the mean value. Therefore, if PDs follow a gaussian distribution, 95% of all PDs will be in the following intervals $\{\mu - 1.96\ \sigma, \mu + 1.96\ \sigma\}$:

For [RTS2-RTS1]: = {6.0 - 1.96 * 3.0, 6.0 + 1.96 * 3.0} = {0.1 mm, 11.9 mm}

For [TBL2-TBL1]: = {6.5 - 1.96 * 2.7, 6.5 + 1.96 * 2.7} = {1.2 mm, 11.8 mm}

For [VAL2-VAL1]: = {7.4 - 1.96 * 4.2, 7.4 + 1.96 * 4.2} = {-0.9 mm, 15.6 mm}

If no wall displacements occurred between Epochs 1 and 2, as inferred from the previous analysis, the maximum values in those intervals could be considered as an additional measure of the level of noise attained in the corresponding measuring/modeling techniques. The [RTS2 - RTS1] PDs ranged from 1.7 mm (0.006 ft) to 10.5 mm (0.035 ft) and presented a RMSV of 6.7 mm (0.022 ft). The PDs of the LiDAR models presented a similar range of values and dispersion as those measured with the RTS instrument, with slightly larger RMSVs, 7.0 mm (0.023 ft) for [LT2 - TBL1] and 8.5 mm (0.028 ft) for [VAL2 - VAL1]. Since RMSVs are a measure of the magnitude of a set of numbers, they can also be considered estimates of the level of noise associated with the corresponding measuring/modeling techniques.

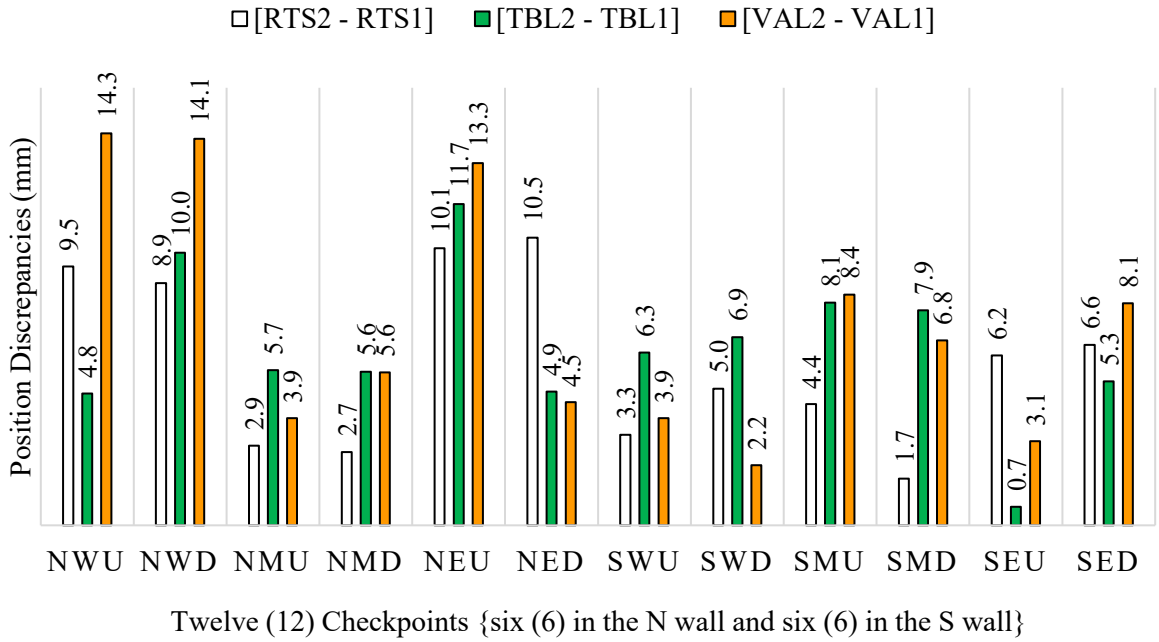

Figure 83. Chart. Position discrepancies of 12 CPs, [Epoch 2 – Epoch 1]

Figure 84 presents the same PD data as Figure 83 but grouped into 4 interquartile ranges: 0%-25%, >25%-50%, >50%-75%, and >75%-100%. The y-axis represents the magnitude of discrepancies. The colored rectangles include the central half of the data, in the 2nd and 3rd quartile (i.e., cenrtral 50% of the samples), highlighting the concentration of discrepancies around the median. This comparative interquartile graph assists in visualizing the distribution and variability of the PDs between Epochs 1 and 2, [Epoch 2 – Epoch 1].

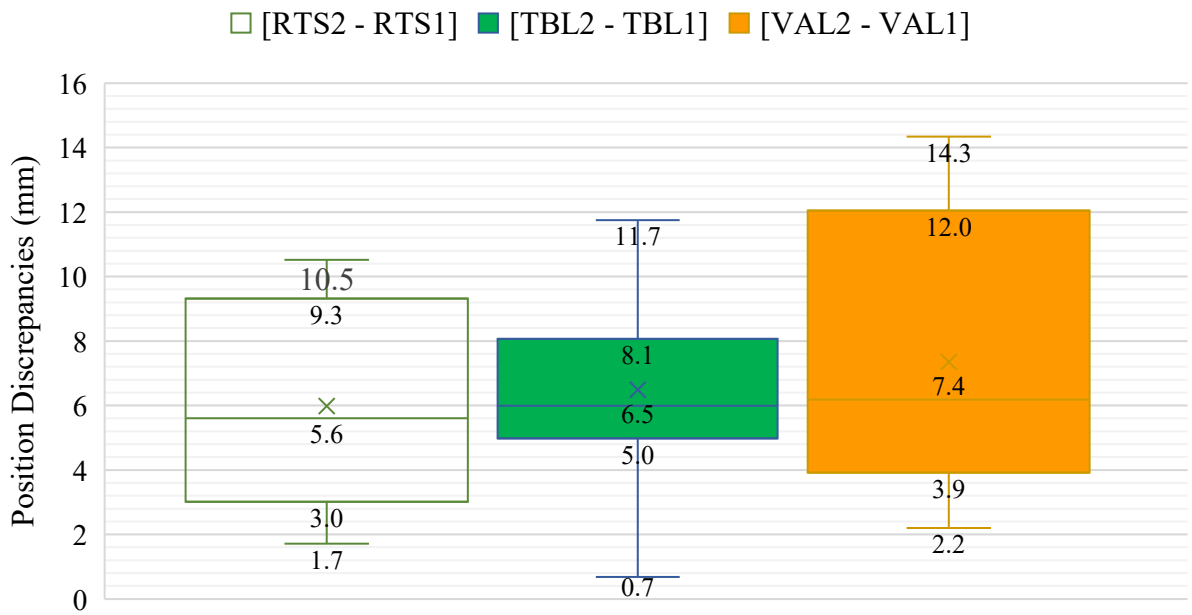

Figure 84. Chart. Position discrepancies of 12 CPs, [Epoch 2 – Epoch 1]. Interquartile ranges.

Figure 84 indicates that the RTS measurements, [RTS2-RTS1], showed the lowest PD, with a PD median value of 5.6 mm, within the shortest total range, (10.5 – 1.7 = 8.8 mm), but with half of the central data dispersed in a relatively wide interval (9.3 – 3.0 = 6.0 mm). The TB LiDAR measurements, [TBL2-TBL1], show a similar but slightly higher median value of 6.5 mm, within a larger total range (11.7 – 0.7 = 11.0 mm), but with half of the total data dispersed in the narrowest

interval (8.1 – 5.0 = 3.1 mm). Finally, the VA LiDAR measurements, [VAL2-VAL1], presented the largest median value of 7.4 mm, within the largest total range
(14.3 – 2.2 = 12.1 mm), and the largest dispersion of the central 50% of the data (12.0 – 3.9 = 8.1 mm). Consequently, from the interquartile analysis, it can be inferred that RTS and TB LiDAR performed better than VA LiDAR. Since RTS showed a smaller total dispersion range, but a larger dispersion of the central portion of the data, than TB LiDAR, from this analysis, it is difficult to indicate which of them is the best performer. Overall, the above results indicate that RTS and TB LiDAR performed very well. Both are the most consistent methods providing the smallest PDs, with relatively low dispersions, and highest reliability when compared to VA LiDAR. This underscores the suitability of TB LiDAR for applications requiring global accurate, precise and consistent positional data.

Figure 85 shows a visual comparison of the PD statistics included in Table B2-04 for [Epoch 2 – Epoch 1]. Again, as suggested in the previous section, it is considered that there were no measurable wall displacements between Epochs 1 and 2. That is, it is assumed that the measured/modeled MSE walls maintained their same geometric configurations in both Epochs, 1 and 2. Therefore, a pair of two different measurements with the same technique, at different times, is considered a simple estimate of the noise associated with the measuring/modeling methods involved. Thus, it is observed that measurements completed with the RTS instrument present the lowest discrepancies, between Epochs 1 and 2, when compared against the TB and VA LiDAR modeling techniques. Measurements with the RTS device show a maximum PD of 10.5 mm, mean value of 6.0 mm, and RMSV of 6.7 mm, indicating more consistent and smaller errors. In contrast, TB LiDAR and VA LiDAR show higher discrepancies, with VA LiDAR exhibiting the largest ones

(maximum = 14.3 mm, mean value = 7.4 mm, and RMSV = 8.5 mm). TB LiDAR presents slightly lower values (maximum = 11.7 mm, mean = 6.5 mm, and RMSV = 7.0 mm) than RTS. Additionally, VA LiDAR has the highest standard deviations (STD-P = 4.2 mm) and RMSVs, indicating greater variability in the position measurements. Therefore, as originally assumed in this study, the accurate benchmarking RTS instrument achieves slightly more precise measurements of point positions compared to both LiDAR approaches, especially more precise than VA LiDAR, which showed slightly higher discrepancies.

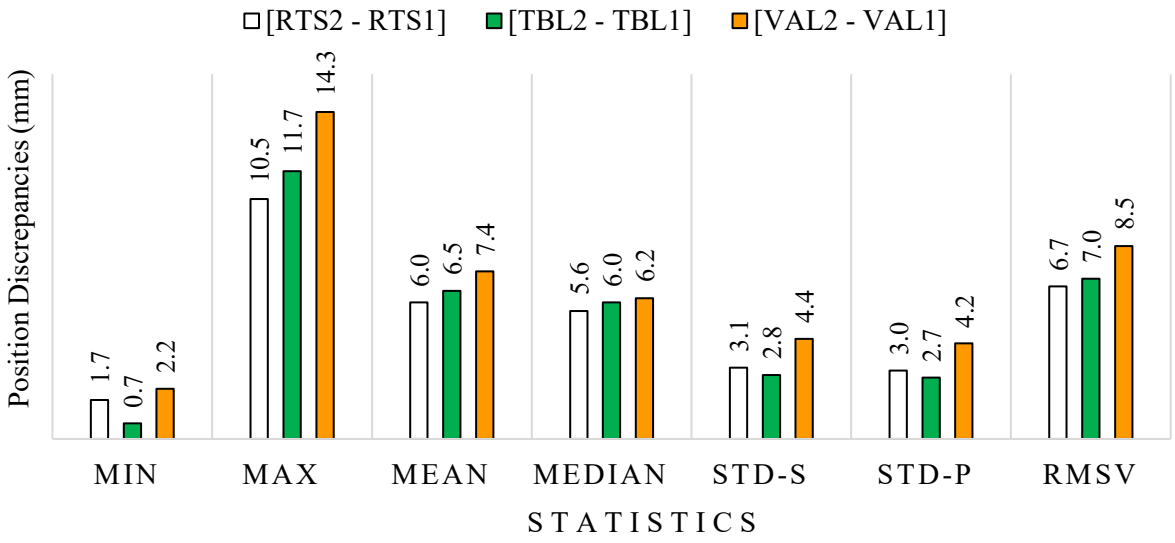

Figure 85. Chart. Statistical Analysis of 12 PDs between Epoch 1 and 2, [Epoch 2 – Epoch 1]

DD Analyses, [RTS2 vs RTS1], [TBL2 vsRTS1] and [TVL2 vs RTS1} at B2-Old River

In addition to position discrepancies, DD analyses were also performed. They considered all 66 non-repeated distances, among the 12 CPs painted on the MSE walls of this bridge. The distances extracted from the TB and VA LiDAR point-cloud models, in Epochs 1 and 2, were compared against the same distances calculated with the coordinates determined in the field with the RTS

instrument, in Epoch 1. For example, a given distance $Dist_{pq}$, between CPs *P* and *Q*, was calculated as

$$Dist_{pq} = \sqrt{(x_p - x_q)^2 + (y_p - y_q)^2 + (z_p - z_q)^2},$$

where (x_p, y_p, z_p) and (x_q, y_q, z_q) are the spatial coordinates of points *P* and *Q*, respectively, in the selected geo-reference system for this bridge. The DDs were calculated by subtracting comparable distances. It should be noted that this generated positive and negative DDs. If the positive and negative values were equally distributed, their mean values will approach zero when considering numerous samples (or will be close to zero for a reduced number of samples). Additionally, when the mean values approach zero, the RMSVs approach the standard deviation.

Figure 86 shows DDs results associated with the TB LiDAR models. It considers two sets of DDs in 66 non-repeated distances among all 12 CPs, one set for Epoch 1 and another set for Epoch 2. For each Epoch, the DDs were calculated by subtracting the distances measured in the field with the RTS instrument in Epoch 1 (RTS1 values) from the same distances extracted from the TB LiDAR models in Epoch 1 (TBL1 values) and from Epoch 2 (TBL2 values). That is, Figure 86 shows the DDs calculated as [TBL1-RTS1] and as [TBL2-RTS1]. The x-axis represents the RTS1 distances, while the y-axis represents the DDs extracted (calculated) from both TB LiDAR models, in Epochs 1 [TBL1-RTS1] and 2 [TBL2-RTS1]. This allows for a direct visual comparison of the DDs attained at each epoch, by the TB LiDAR models, with respect to the RTS1 values. This graph includes trend lines followed by the DDs of each set as measured distances increase. Additionally,

it is observed that the DDs from Epoch 2 are smaller (in magnitude) and less dispersed than those from Epoch 1.

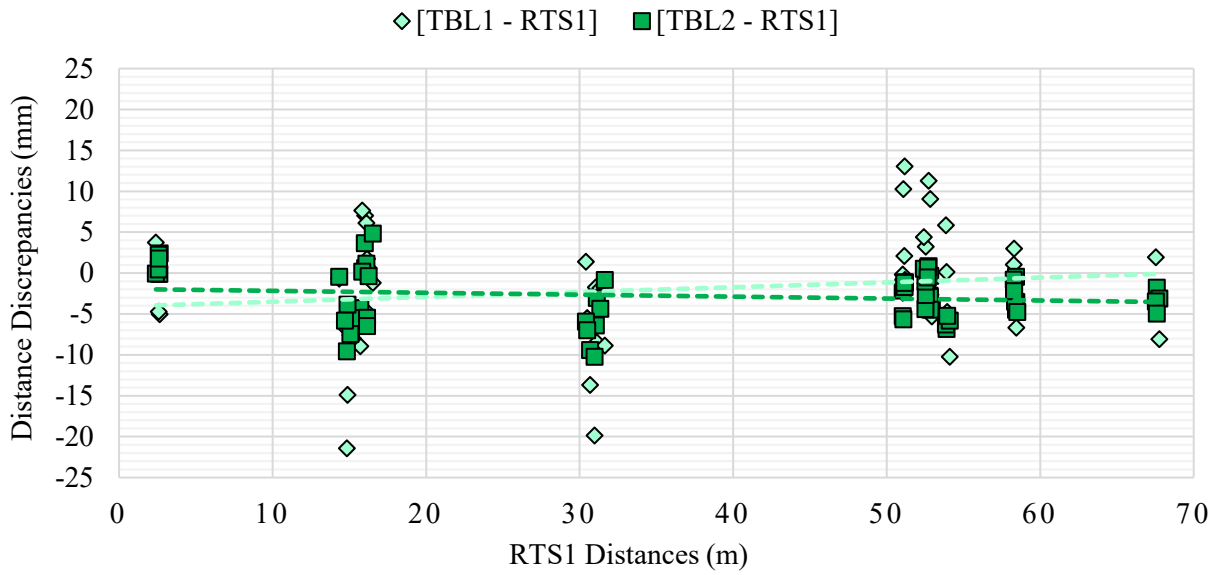

Figure 86. Graph. Sixty-six DDs between TB LiDAR models (in Epochs 1 and 2) versus RTS measurements (in Epoch 1).

The statistics of the DDs, calculated as [TBL1-RTS1] and as [TBL2-RTS1], are shown in Table 41. This table also includes the statistics for the two VA LiDAR models, in Epoch 1 [VAL1-RTS1], and in Epoch 2, [VAL2-RTS1].

Table 41 presents the statistics of 66 DDs generated by the same technique at two different Epochs, 1 and 2. It is observed that, in both Epochs, the RMSVs of the DDs, between each LiDAR model and the RTS1 distances, is low. The RMSVs of Epoch 2 are even smaller than Epoch 1. This further implies that, most likely, there were no measurable wall displacements in this bridge, between Epochs 1 and 2, via the employed LiDAR modeling approaches.

Table 41. Statistics of DDs among 12 CPs. TB and VA, from Epochs 1 & 2, versus RTS instrument in Epoch 1

Epoch 1: LiDAR vs RTS1 (mm)							
Type	Min	Max	Mean	Median	STD - S	STD - P	RMSV
[TBL11 - RTS1]	-21.44	13.03	-1.85	-1.24	6.44	6.39	**6.66**
[VAL1 - RTS1]	-12.49	16.43	4.27	3.66	6.48	6.43	**7.72**
Epoch 2: LiDAR vs RTS1 (mm)							
Type	Min	Max	Mean	Median	STD - S	STD - P	RMSV
[TVL2 - RTS1]	-10.24	4.82	-2.83	-2.84	3.20	3.18	**4.26**
[VAL2 - RTS1]	-6.81	8.24	0.66	0.56	2.98	2.96	**3.03**
Differences: [Epoch 2 – Epoch 1] (mm)							
Type	Min	Max	Mean	Median	STD - S	STD - P	RMSV
[LT2 - TBL1]	11.19	-8.20	-0.98	-1.59	-3.24	-3.22	**-2.40**
[VAL2 - VAL1]	5.67	-8.18	-3.61	-3.10	-3.51	-3.48	**-4.70**

Figure 87 presents similar results as those shown in Figure 86 but for the VA LiDAR models from Epochs 1 and 2. Again, in this case, distances measured in the field, with the RTS instrument in Epoch 1 (RTS1 values), were subtracted from the same distances extracted from the VA LiDAR model generated in Epoch 1 (VAL1 values), and from the VA LiDAR model produced in Epoch 2 (VAL2 values). That is, Figure 87 shows the DDs calculated as [VAL1-RTS1] and as [VAL2-RTS1]. The x-axis represents the RTS1 distances, while the y-axis represents the DDs extracted (calculated) from both VA LiDAR models, in Epochs 1 [VAL1 - RTS1] and 2 [VAL2 – RTS1]. As was the case in Figure 86, Figure 87 also shows that DDs in Epoch 1 are higher and less dispersed than those in Epoch 2. Again, this is an indication that no wall displacements, between Epochs 1 and 2, were measurable by the VA LiDAR approach.

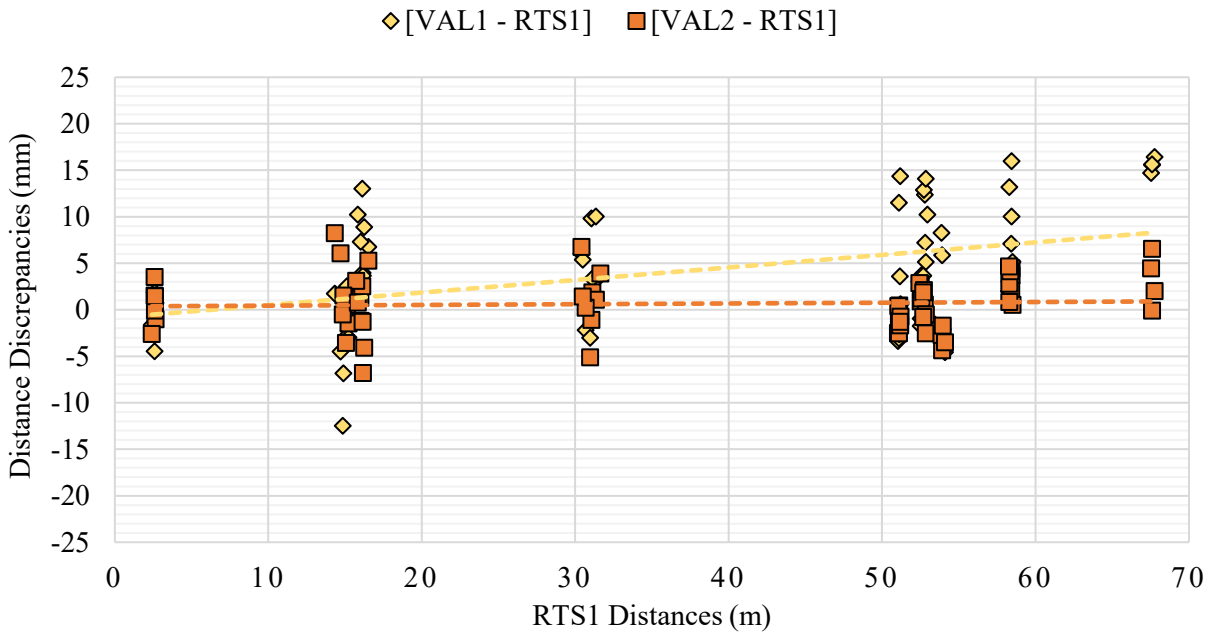

Figure 87. Graph. Sixty-six DDs between VA LiDAR models (in Epochs 1 & 2) vs RTS measurements (in Epoch 1)

As was the case in the above PD analyses, the DDs were also calculated between the two considered epochs. That is, for each measuring technique, RTS, TB LiDAR, and VA LiDAR, new sets of DDs were calculated as [Distances in Epoch 2 – Distances in Epoch 1].

Figure 88 shows DDs between Epochs 1 and 2, over all 66 non-repeated distances among the 12 CPs, for the RTS, TB LiDAR, and VA LiDAR techniques. That is, its x-axis represents 66 non-repeated distances, measured with the RTS instrument in Epoch 1 (i.e., RTS1 values). The DDs, shown in the y-axis of this figure, were calculated as [RTS2-RTS1], [TBL2-TBL1], and [VAL2-VAL1]. In this comparison, it is observed that the RTS measurements presented less dispersed and smaller DDs than both LiDAR approaches. Additionally, the VA LiDAR technique showed slightly larger DDs magnitudes and somewhat more dispersion than TB LiDAR. For VA LiDAR, the

maximum amplitudes of those discrepancies are negative side, reaching 8.2 mm for RTS, 14.7 mm for TB LiDAR, and 16.0 mm. The maximum positive DDs are smaller, 7.7 mm, 11.9 mm, and 12.0 mm, respectively, indicating a slight negative bias.

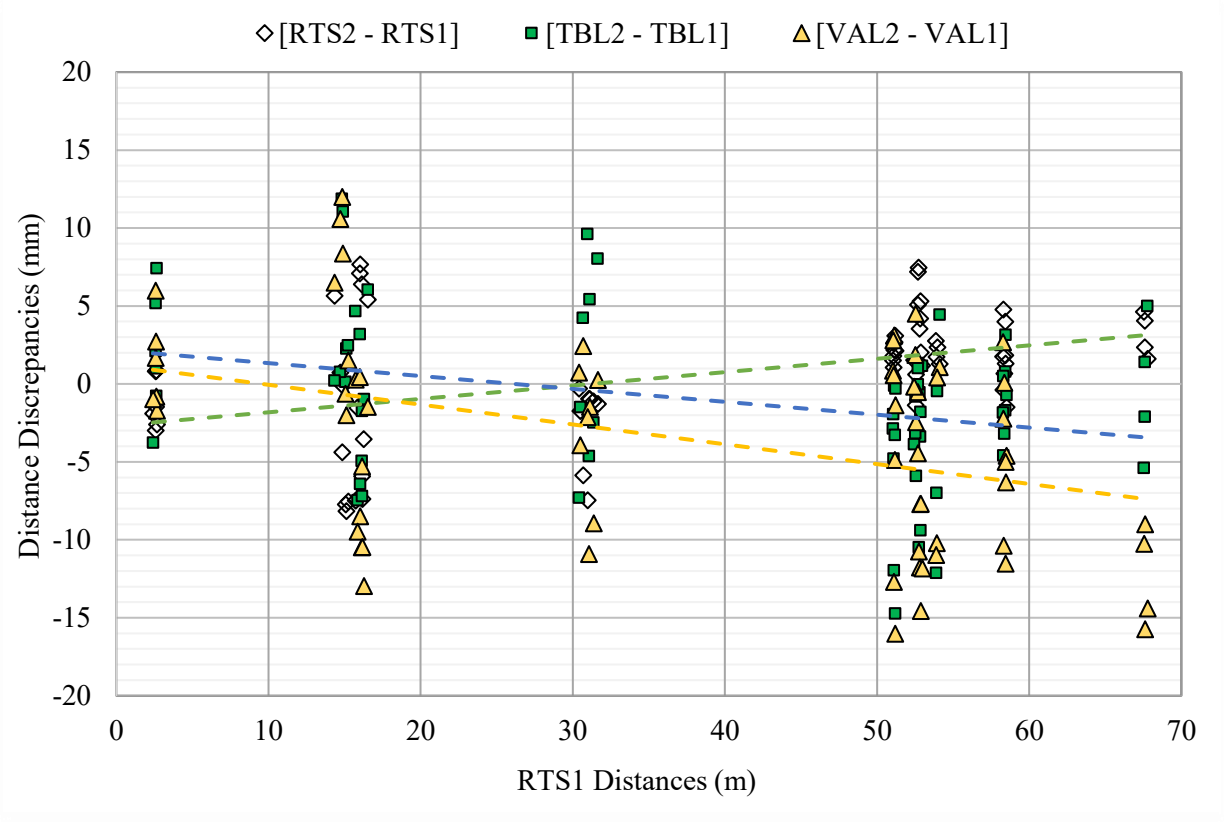

Figure 88. Graph. Discrepancies in 66 non-repeated distances among 12 CPs, between Epochs 1 and 2, at B2-Old River

Figure 89 shows the statistics of DDs between Epochs 1 and 2. In this case, Epoch 1 serves as reference. That is, for all 3 techniques, RTS, TB LiDAR and VA LiDAR, those discrepancies were calculated as [Epoch 2 – Epoch 1]. The maximum magnitude of the DDs occurred on the negative side, presenting the following values: 8.2 mm for RTS, 14.7 mm for TB LiDAR, and 16.0 mm for VA LiDAR. Again, assuming that there were no measurable wall displacements between Epochs 1 and 2, these maximum magnitudes serve as a coarse approximation to the noise level, associated

with these measuring/modeling techniques, when acquiring distances. For these positive/negative DDs, with mean values close to zero, a good estimate of their dispersion is given by the standard deviations of their population (STD-Ps), which are very close to their respective RMSVs. Those STD-Ps are 3.9 mm for RTS, 5.3 mm for TB LiDAR and 6.5 mm for VA LiDAR. If DDs follow a Gaussian distribution, 95% of their population will have a magnitude less than 1.96*STD-P. Therefore, when measuring distances, the estimated noise level, in 95% of the measurements, is 7.6 mm for RTS, 10.4 mm for TB LiDAR, and 12.7 mm for VA LiDAR.

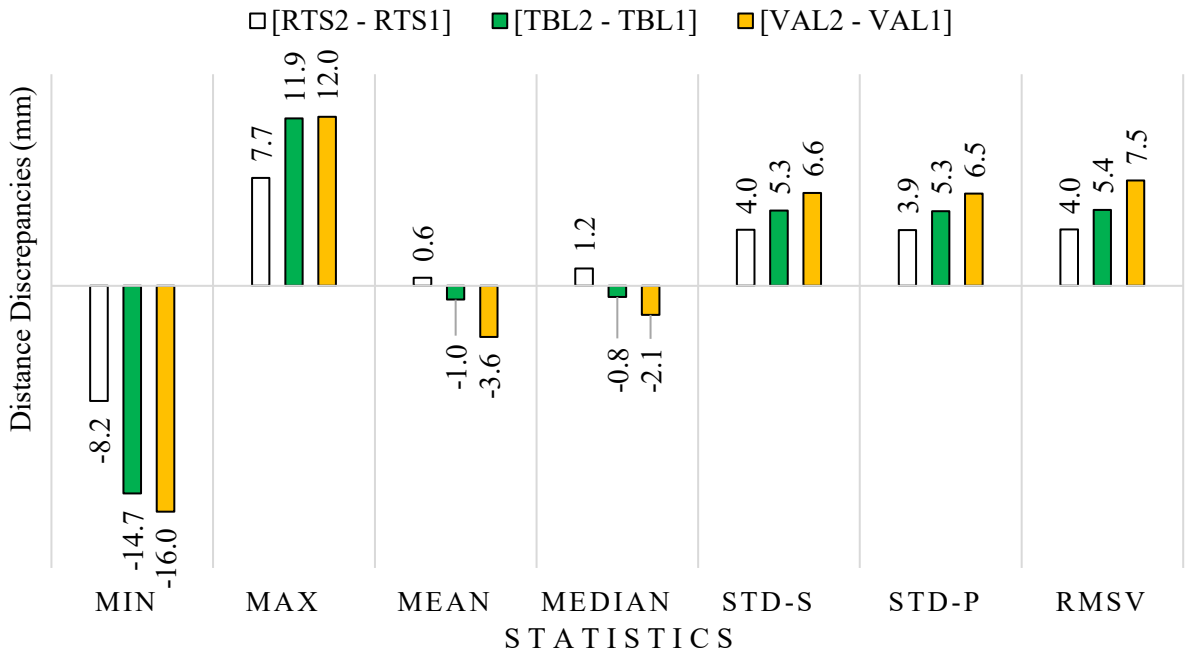

Figure 89. Graph. Statistics of discrepancies in 66 non-repeated distances among 12 CPs, between Epochs 1 and 2, at B2-Old River

These results show that while the RTS dataset exhibits relatively stable and smaller discrepancies, the LiDAR datasets do not deviate too much from the RTS measurements. Additionally, both TB and VA LiDAR models present almost the same level of DDs, with TB LiDAR showing slightly lower DDs than VA LiDAR.

CC COMPARISONS AT B2-OLD RIVER

Previous PD and DDs analyses considered the positions of only 12 points and 66 non-repeated distances among them. That is, only 6 representative points on each MSE wall were analyzed. This is considered a relatively low number of points to monitor the whole façade surface of each wall. Therefore, it was decided to expand these comparative analyses to include most, or all, spatial information contained in the point clouds modeling those wall façades at different times. For this purpose, the open-source CC software was selected and employed to test its ability to identify and quantify structural displacements and deformations over time. By comparing two point-cloud models from different epochs, this software presents potential to provide a comprehensive, accurate assessment of wall displacements between epochs (i.e., PDs), surpassing the capabilities of traditional visual inspections or point-based measurements. When CC compares two clouds of points, one of them must be designated as “reference” and the other as “compared”. The actual comparison is completed by selecting one of three possible approaches or algorithms. One of them is the comparison consisting in determining “absolute” distances between corresponding points in two comparable clouds. Each “absolute” distance is the length, or magnitude, of a virtual straight-line segment separating a point in the “reference” cloud from its nearest point in the “compared” cloud. However, that nearest point may not provide the actual distance from the reference surface to the compared surface. This often results in longer distances than actual distances. Since these distances are always positive, CC refers to them as “absolute”. Each of them can be considered the PD between two corresponding points. However, those two points may not be their actual corresponding points. Alternatively, CC can also compare “signed” distances, which provides information about the direction of those distances, inside or outside the referenced cloud. For signed distances, CC uses the Cloud-to-Mesh (C2M) approach and the Multiscale Model to Model Cloud

Comparison (M3C2). The latter approach computes distances between point clouds by projecting points onto a local neighborhood in the reference cloud, considering the directions normal to the surface, and then calculating the distance along that projection. Additionally, the M3C2 method considers multiple scales when calculating distances, allowing it to discern changes at different levels of detail. This is particularly useful when dealing with complex surfaces or when there is a need to account for both fine-scale roughness and larger-scale changes. This approach is more robust to noise and outliers compared to the simpler C2C method. In this study, the C2C and M3C2 are considered and compared. Both are considered useful to compare point positions and to identify position discrepancies between two comparable point clouds.

In this bridge, two georeferenced full LiDAR models were considered with the CC software. Both models used the same system of reference, originally established via a closed traverse, and the same spatial units. They were the TB LiDAR model, completed in Epoch 1 (TBL1), and the TB LiDAR model, completed in Epoch 2 (TBL2).

Each of the two MSE walls in this bridge, the North (N) wall and the South (S) wall, were individually extracted (segmented) from the referred two full georeferenced models. For the N wall, its corresponding two extracted and exported point clouds are indicated as North wall Target Based LiDAR (N-TBL1), from Epoch 1, and North wall Target Based LiDAR (N-TBL2), from Epoch 2. Similarly, for the S wall, its corresponding two extracted point clouds are referred to as South wall Target Based LiDAR – Epoch 1 (S-TBL1), and South wall Target Based LiDAR – Epoch 2 (S-TBL2). Each of them was exported from Leica's Cyclone Core software, as a "*.las*" file, to the CC software. CC requires that comparable point clouds share the same system of reference and use

the same spatial units (i.e., m or ft). After a pair of comparable point-cloud models was imported into the CC software, one of them was designated as "reference" and the other as "compared" to proceed with its comparison.

C2C "absolute" distance comparison between TB LiDAR Point Clouds [TBL2 vs TBL1]

The C2C comparison was implemented, via the CC software, to estimate "absolute" distances (PDs), occurring between Epochs 1 and 2, between two comparable models. Appendix C8 presents a brief protocol describing the parameters, settings, and necessary steps to use the C2C approach in the CC software.

The TB LiDAR models from Epochs 1 and 2 were compared. This was done separately for the N wall and for the S wall. That is, the TB LiDAR models for the N wall, N-TBL1 (designated as reference) and N-TBL2 (designated as compared) were compared against themselves. Similarly, the VA LiDAR models for the S wall, South wall Visual-Alignment LiDAR – Epoch 1 (S-VAL1) (reference) and South wall Visual-Alignment LiDAR – Epoch 2 (S-VAL2) (compared) were compared against themselves. These comparisons are based on a straightforward superposition scheme, where both comparable models use the same system of reference and spatial units. After running CC, the attained results (PDs) are discussed in the following paragraphs.

Part A of Figure 90 shows the two compared (superposed) point-cloud models for the N wall, N-TBL2 vs N-TBL1. Part B of that same Figure 90 shows the two compared (superposed) models for the S wall, S-TBL2 vs S-TBL1. In this figure, the color scale represents the "absolute" distances

(PDs), in meters, between corresponding points in both compared clouds. In both cases, the reddish area represents larger distances than the blueish area.

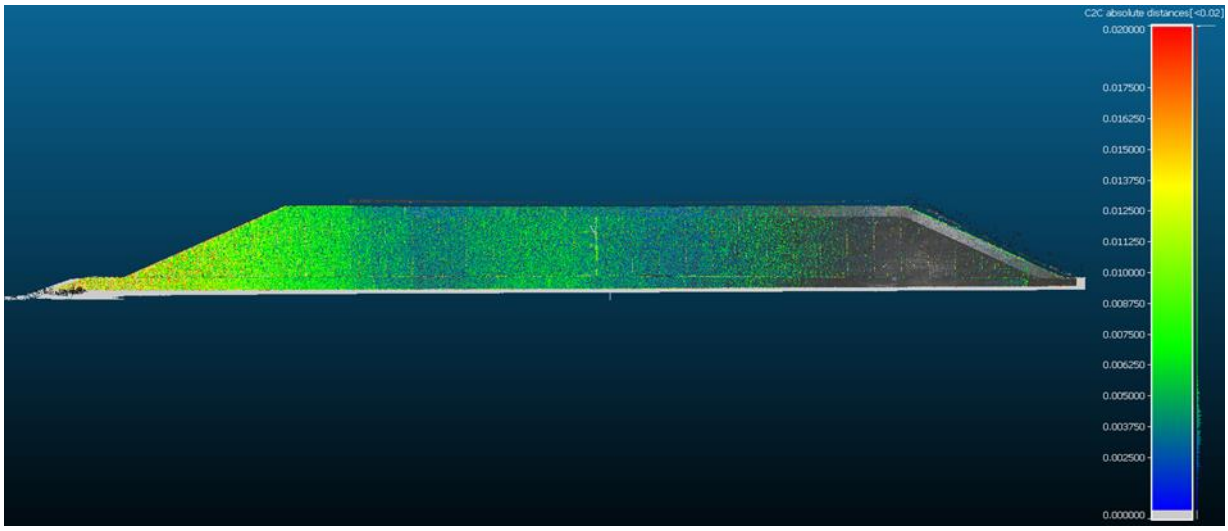

A. North wall, TB LiDAR models, [N-TBL2 vs N-TBL1]

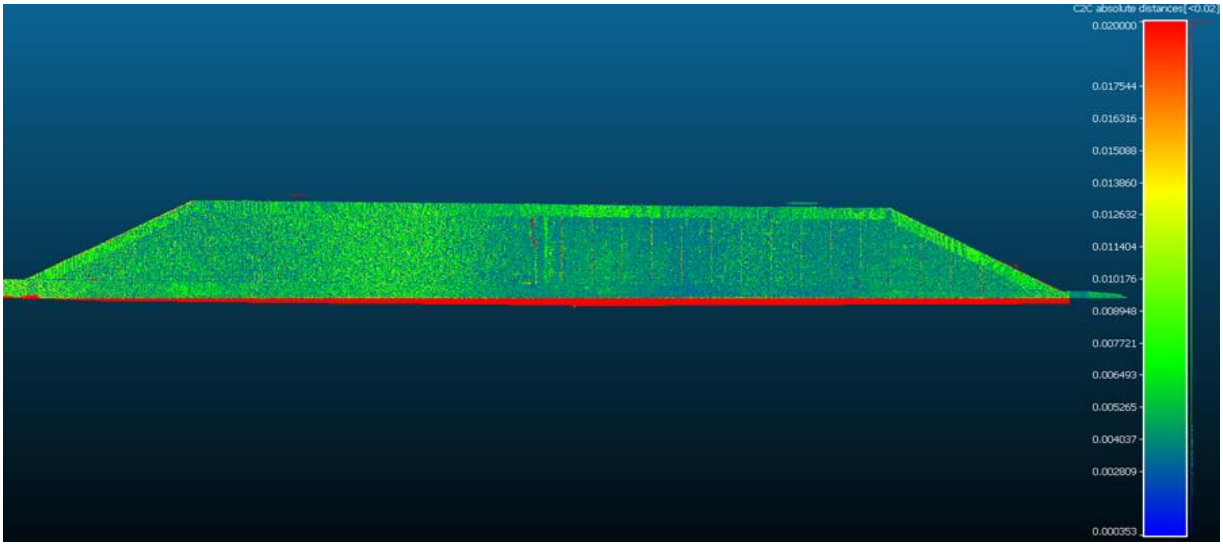

B. South wall, TB LiDAR models, [S-TBL2 vs S-TBL1]

Figure 90. Photo. C2C "absolute" distance comparison, Epoch 2 vs Epoch 1

Figure 91 shows a C2C histogram, or frequency distribution, of "absolute" distances (PDs) between two comparable point clouds of the N wall. In this case, two TB LiDAR models of the N wall have

been compared: N-TBL1 (at Epoch 1), serving as the reference cloud, and N-TBL2 (at Epoch 2), selected as the compared cloud. After trial and error, it was observed that the largest amplitude of the determined PDs was approximately 20 mm. In this figure, the x-axis represents the PDs between the compared point clouds, divided into 120 intervals (or classes). Each interval represents a small range (20 mm / 120 = $0.1\overline{6}$ mm) of PD values. The y-axis represents the "count", i.e., the number of PDs with magnitudes included within each interval. Often this count is referred to as the frequency of occurrences of events in the same interval, or also frequency count.

For the N wall, as observed in Figure 91, ~14.11 million points were compared between Epochs 1 and 2, and most of their resulting "absolute" distances (PDs) are less than 10 mm. Note that there is a large quantity of PDs in the last interval, between $18.\overline{3}$ and 20 mm (see red bar on the right-hand side of the graph). The count in that last interval considers erroneously calculated PDs. This is because the two compared clouds did not encompass the same exact area. When they were extracted from their respective full point-cloud models, some small portions were included in one of them, but not in the other. Therefore, when PDs are determined for each point, if a compared point does not have its corresponding companion point in the other cloud, the algorithm will still search for the closest alternative companion point in the missing portion, and may finally find one farer apart, in a noncorresponding but existing area, calculating erroneous PDs in those zones. The red portion thus serves as a visual indicator of non-relevant comparisons, emphasizing that meaningful distance measurements are confined to the wall area where point pairs overlap in both epochs. Therefore, that red last interval has been discarded in this analysis. Additionally, it is observed that the maximum count is approximately 670×10^3 and it occurs in the 20^{th} interval, where

the magnitudes of the PDs are between 3.1$\overline{6}$ mm and 3.3$\overline{3}$ mm. That is, most of the PDs in that highly populated interval are relatively small.

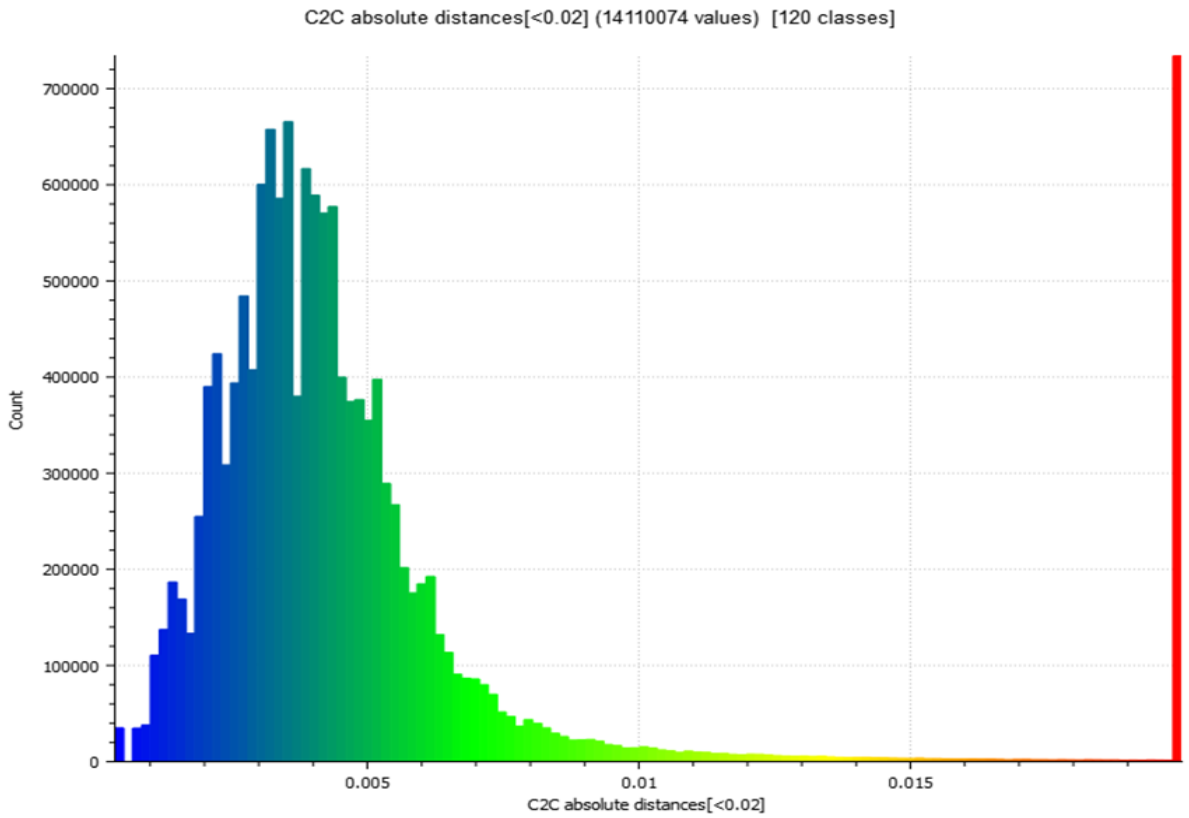

Figure 91. Graph. N wall histogram of C2C "absolute" distances (m), [N-TBL1 vs N-TBL2]

Similarly, Figure 92 indicates that ~13.47 million points were compared in the S wall, between the S-TBL1 and S-TBL2 point clouds, from Epoch 1 and 2, respectively. Again, most of the resulting "absolute" distances (PDs) are less than 10 mm. Also, as previously indicated, the last interval (red bar on the right-hand side) contains erroneous data, and is discarded in this analysis. The maximum count is approximately 580×10^3 and it occurs in the 18th interval, where the magnitudes of the PDs are between 2.8$\overline{3}$ mm and 3.0 mm. That is, the PDs in the most populated interval are relatively small.

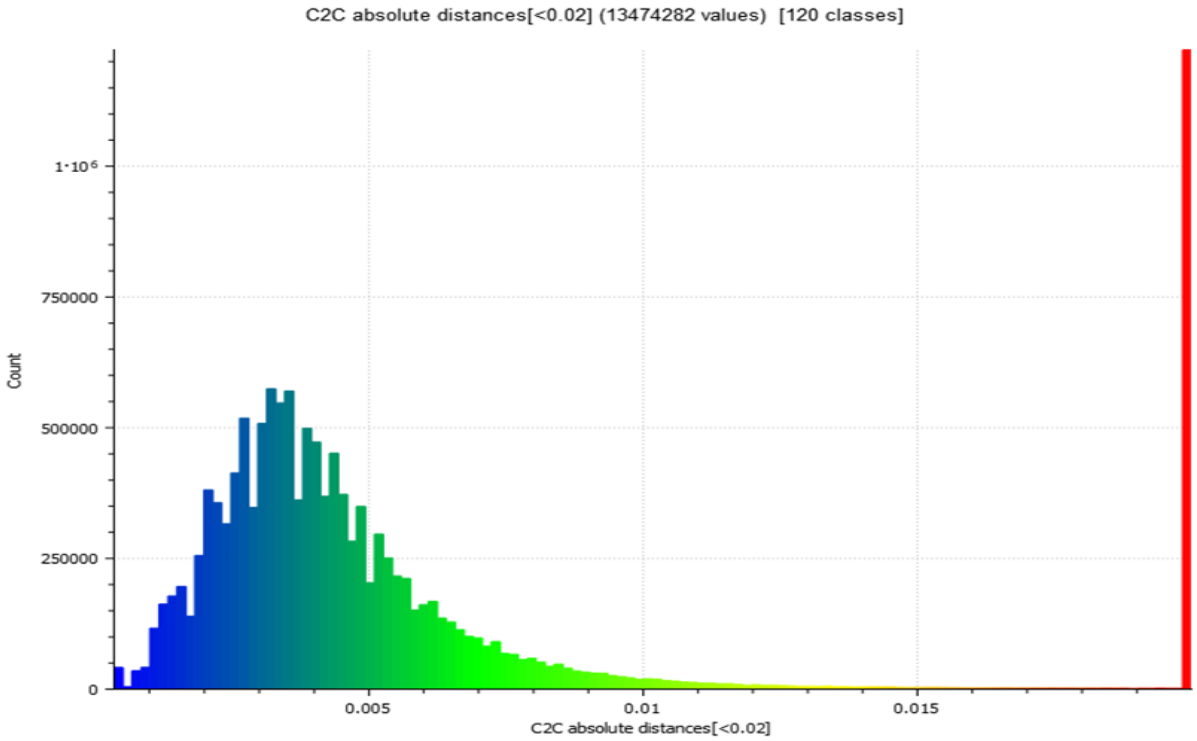

Figure 92. Graph. S wall histogram of C2C "absolute" distances (m), [S-TBL1 vs S-TBL2], (m)

Analysis of C2C CDFs at B2-Old River

Figure 93 illustrates the C2C cumulative distribution functions corresponding to the two histograms (frequency distributions) presented in Figure 91 and Figure 92. They correspond to "absolute" distances, which may also be referred to as point-position discrepancies (PDs), determined for each wall (N or S) when their TB LiDAR models, for Epochs 1 and 2, were compared. The x-axis represents the "absolute" distance (PDs), in meters, ranging from 0 to 0.020 m (20 mm). The y-axis represents the probability that a PD takes on a value less than or equal to a given value x. In other words, for a given PD value, on the x-axis, the y-axis value indicates the proportion or percentage of observations in the dataset that are below that value. In this regard, the

data indicates that each wall (N or S) achieves, approximately, a 98% probability that their PDs, between Epochs 1 and 2, be less or equal than 10 mm.

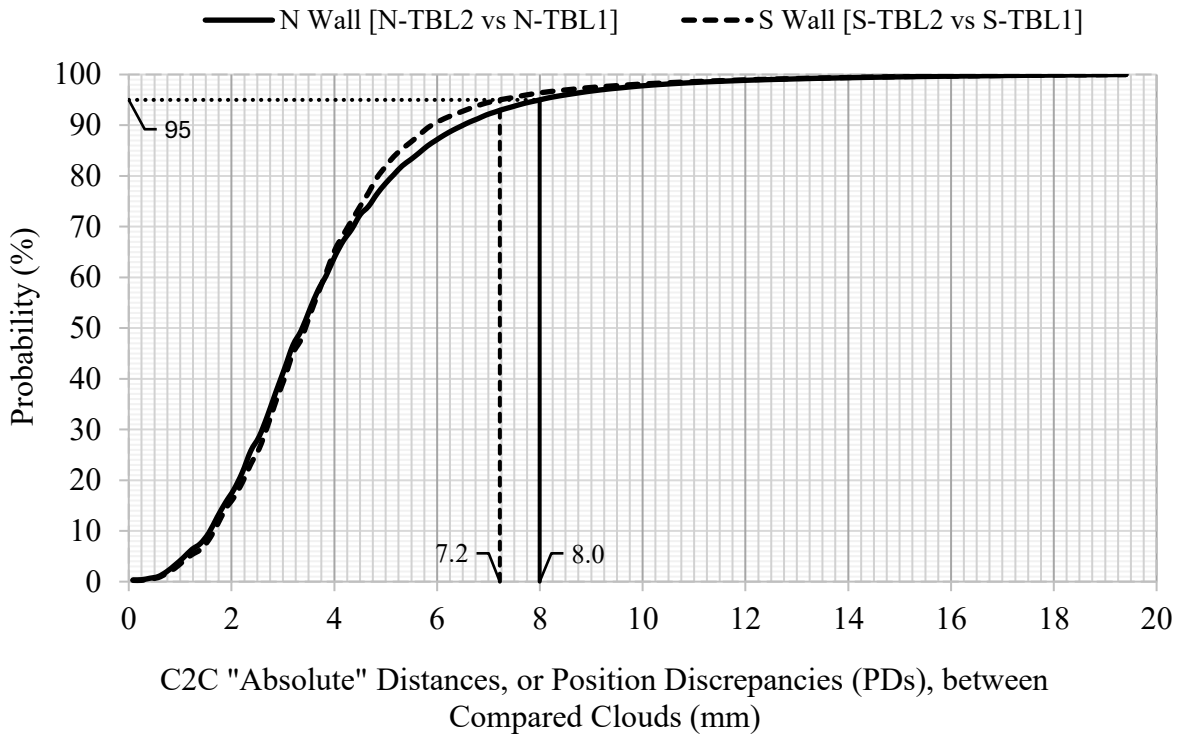

Figure 93. Graph. Cumulative distribution function of C2C "absolute" distances between Epochs 1 and 2 at Old River

Also, it is observed that there is a 95% probability that, for the S wall, the PDs, between Epochs 1 and 2, be ≤ 7.2 mm, and for the N wall be ≤ 8.0 mm. This suggests that most of the "absolute" distances (PDs) between clouds modeled at Epochs 1 and 2, are small, and most likely below the level of noise associated with the employed TB LiDAR modeling technique. That noise, for TB LiDAR in this bridge, was previously estimated for both walls as 11.9 mm, in a coarse sense (maximum value of 12 measured CPs; see Figure 85), and as 13.7 mm when considering a 95% probability derived from only 12 observations (1.96*RMSV = 1.96 * 7 mm = 13.7 mm; see Figure 85). The 12 referred observations were completed when comparing the positions of 12 CPs in two

TB LiDAR point clouds, generated in Epochs 1 and 2, via Microsoft's Excel spreadsheet. This further reaffirms the previous indication that, in this bridge, there were no measurable wall displacements between Epochs 1 (fall 2023) and 2 (fall 2024), when using the TB LiDAR modeling approach.

M3C2 comparisons between TB LiDAR in Epochs 1 and 2 at Old River

The elaborated M3C2 algorithm, employed by the CC software, is described by Lague et al. (2013). For each wall, N and S, the M3C2 method was applied to further examine positional differences between Epochs 1 and 2 and obtain an additional estimate of the noise level associated with the TB LiDAR modeling technique. For this, while using the CC software, the surface corresponding to Epoch 1 was set as the "reference" point cloud, and the surface from Epoch 2 was designated as the "compared" point cloud. Then, the M3C2 algorithm computed required directions normal to the "reference" surface and compared the relative distances between the clouds from Epochs 1 and 2. This resulted in calculated "signed" distance values, where positive quantities represent outward deviations and negative distances indicate inward shifts relative to the "reference" surface. The "signed" distance values are visualized using a color scale, where red shows positive distances (positive position discrepancies, +PDs), and blue represents negative distances (negative position discrepancies, -PDs). Areas with no significant discrepancies are marked with a neutral color green. In this analysis, the full color scale covered a range of 40 mm (±20 mm), allowing a smooth gradient transition across the spectrum of "signed" positional discrepancies between the two Epochs, 1 and 2, for each wall, N and S. Figure 94 and Figure 95 show those outward and inward distances for the N and S walls, respectively, between Epochs 1 and 2. Regions with positive values

indicate outward bulging or displacement of one cloud with respect to the other, whereas negative values suggest contraction or inward shift. The presence of points with zero, or close-to-zero, values indicate stable areas with no detectable changes.

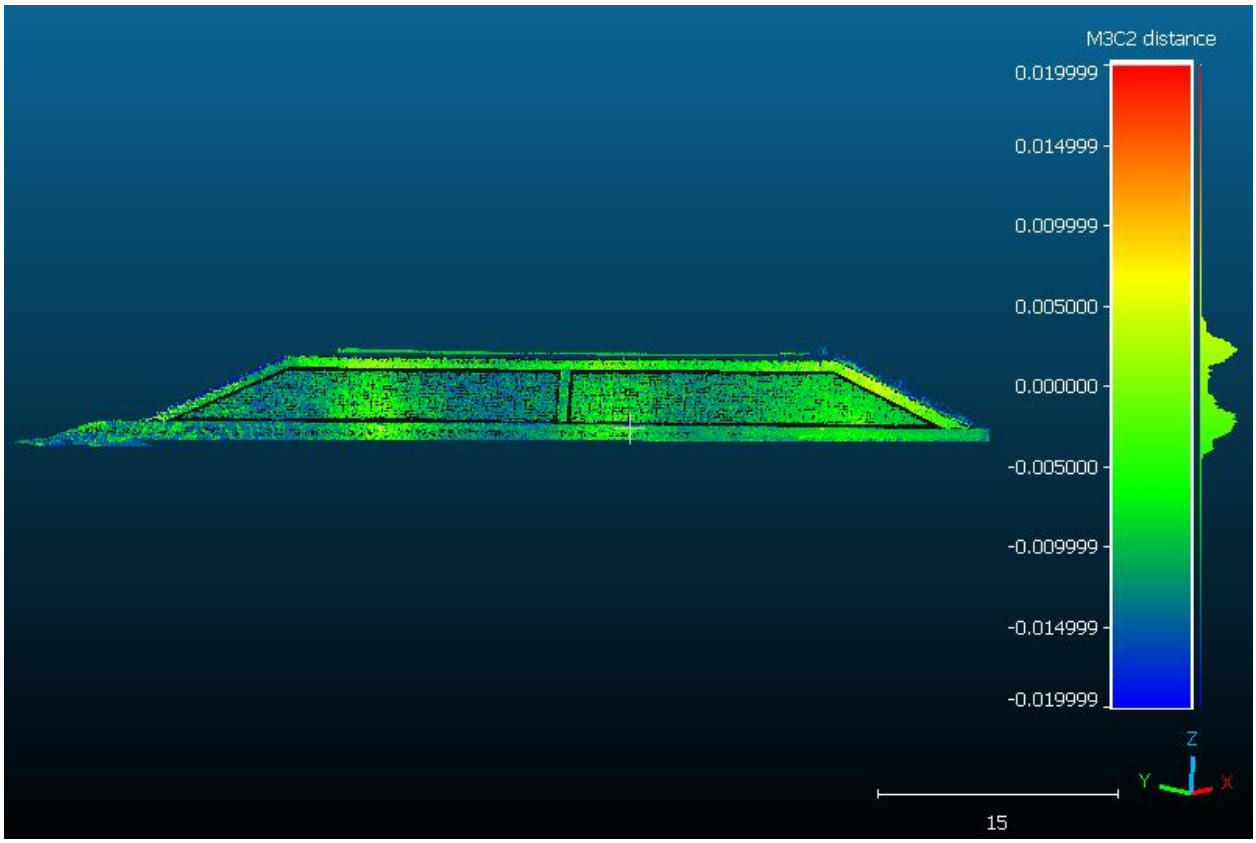

Figure 94. Photo. M3C2 “signed” distances in the N wall, between Epochs 1 and 2 (m)

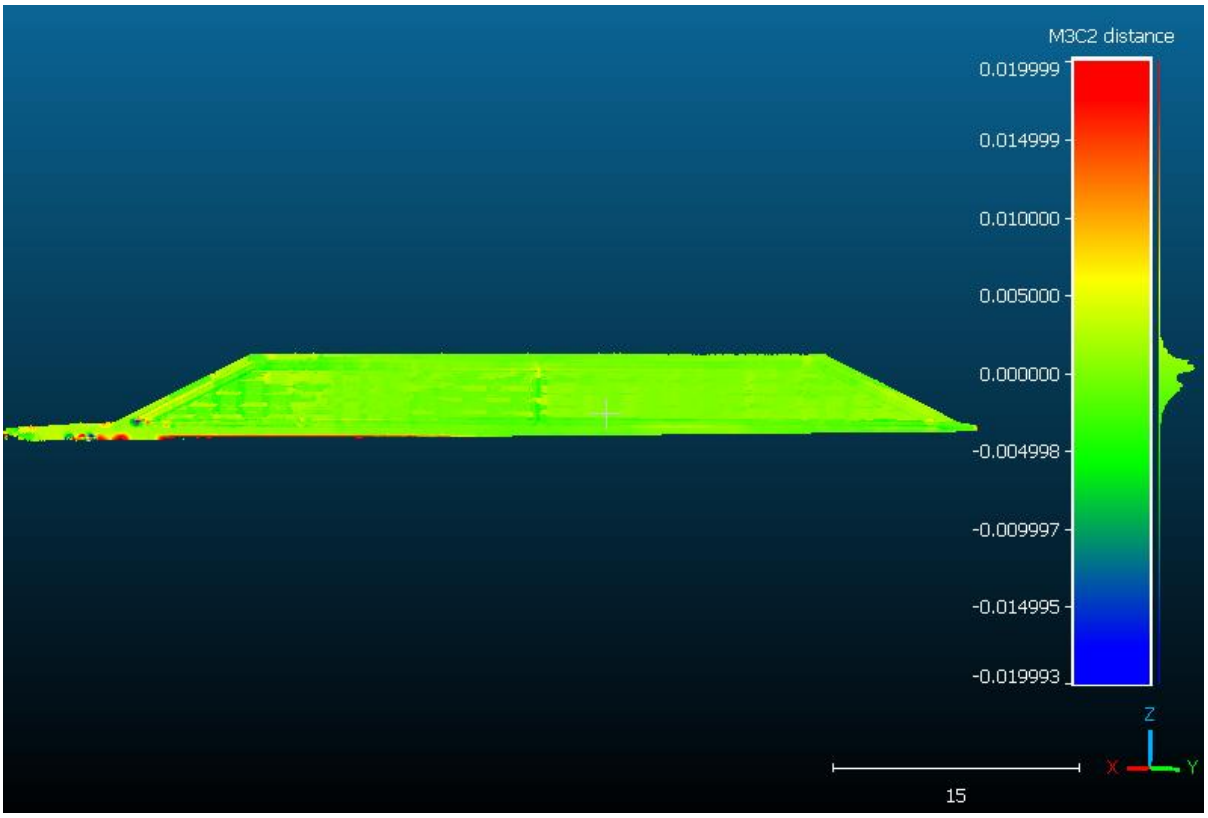

Figure 95. Photo. M3C2 "signed" distances in the S wall, between Epochs 1 and 2 (m)

Histogram graphs present the distribution of the M3C2 "signed" distance values, between Epochs 1 and 2, for each wall, N or S. The first histogram, shown in Figure 96, represents the N wall, with ~5,25 million data points compared, while the second one, in Figure 97, corresponds to the S wall, with ~4,57 million points. This contrasts with the histograms obtained with the C2C "absolute" distance approach, where the number of compared points in the N and S walls were ~14.11 and ~13.47 million, respectively. The number of compared points in the M3C2 is considerably less because its algorithm discard points with no comparable counterpart within the comparison cylinder assigned to each point.

In both M3C2 histograms, the horizontal axis, M3C2 “signed” distances, represents inward and outward positional discrepancies (±PDs) relative to the “reference” surface at Epoch 1. The ±PDs range was selected from -0.020 m to +0.020 m (-20 mm to +20 mm), and it was divided into 240 intervals (classes). This corresponds to the 0-20 mm range used in the previous C2C “absolute” distance (PDs) analyses, where 120 intervals were considered, as presented in Figure 91 and Figure 92. The new 240 classes group the “signed” distances values, providing a detailed view of “signed” position discrepancies (±PDs) of the full façade surface of each wall, N and S. Again, the vertical axis shows the frequency (Count) of ±PDs values within each interval.

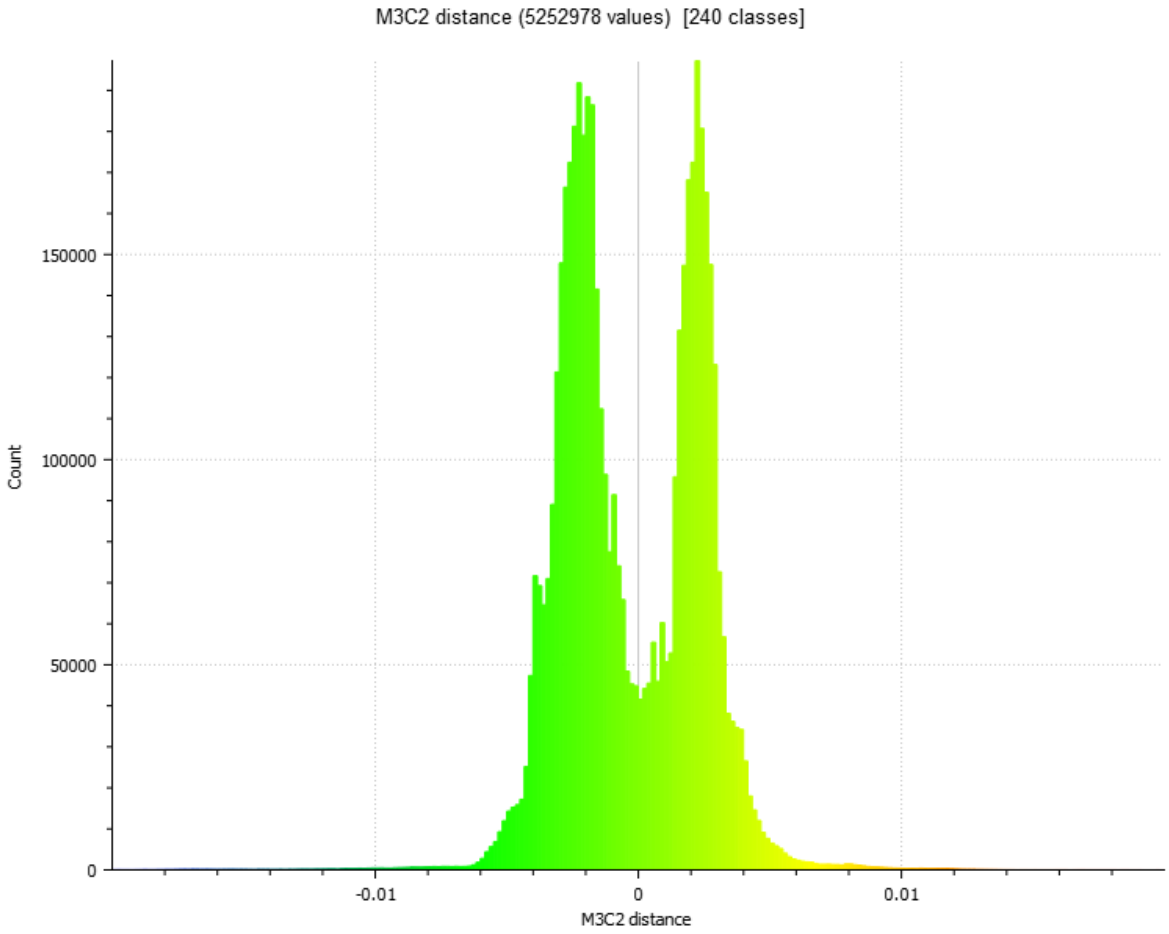

Figure 96. Graph. North wall histogram of M3C2 “signed” distances (m), between Epochs 1 & 2

A prominent feature in the histograms of both walls is their quasi-symmetrical distribution with respect to zero M3C2 distance. In both cases, the distributions are bimodal ones. That is, they present two distinct peaks or modes. Bimodal histograms deviate from a normal distribution, which would have only one peak (mode). The two modes indicate that there are two groups, or ranges, of M3C2 "signed" distances, each having one of the two highest counts or frequencies. For the North wall, one of the two most frequent M3C2 "signed" distances is close to -2.3 mm while the other is close to +2.2 mm. Similarly, for the South wall, one mode shows M3C2 "signed" distances close to -0.9 mm and the other close to +0.4 mm. That is, both walls present modes with small, "signed" position discrepancies, with the N wall showing slightly higher discrepancies. Additionally, the count of ±PDs between the modes, and closer to zero, are not negligible, showing substantial frequency. Therefore, for each wall (N or S), their "signed" point-position discrepancies, between Epochs 1 and 2, present two small positive and negative frequent values, with numerous points showing zero or close to zero discrepancies. That is, most areas of both walls experienced negligible displacement between Epochs 1 and 2. Additionally, the histogram of the North wall shows slightly wider tails, extending beyond ±0.01 m compared to the South wall, suggesting greater variability in its positional discrepancies between Epochs 1 and 2. Additionally, the higher total point count at the N wall, ~5.25 million, vs ~4.57 million at the S wall, could indicate either more comprehensive scanning coverage of the N wall, at both epochs, or genuinely more complex discrepancy behavior at that wall. The tighter distribution of the S wall implies more uniform discrepancies between Epochs 1 and 2.

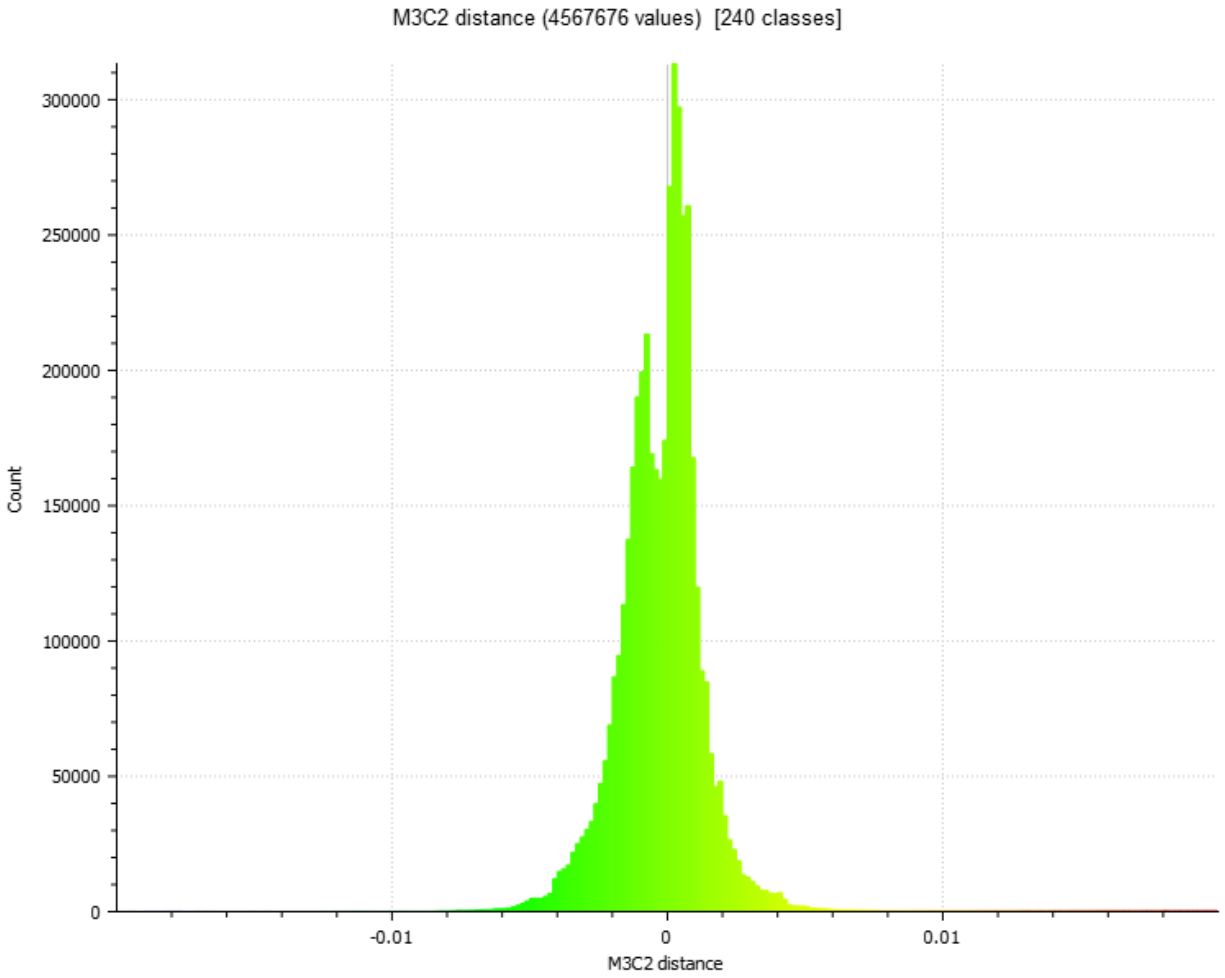

Figure 97. Graph. South wall histogram of M3C2 "signed" distances (m), between Epochs 1 & 2

Analysis of M3C2 CDF

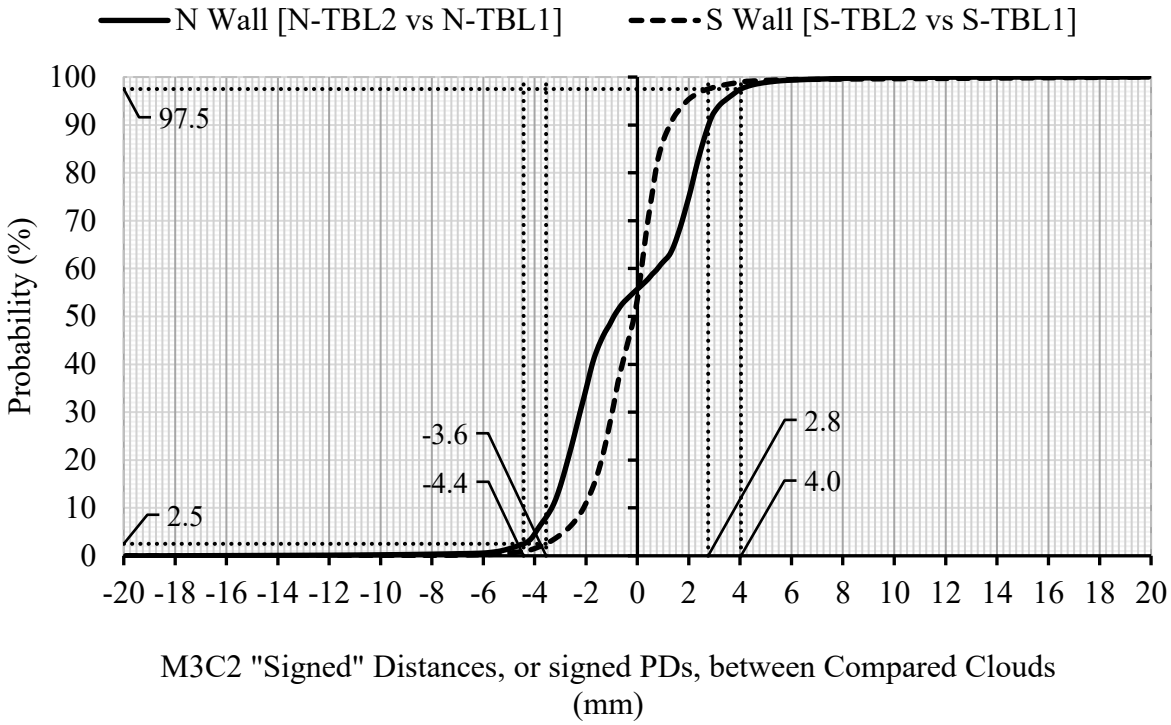

Figure 98. Graph. Cumulative distribution function of M3C2 "signed" distances, between Epochs 1 and 2 at Old River

For both walls, North (solid line) and South (traced line), Figure 98 shows the CDF of M3C2 "signed" distances (or ±PDs), between the TB LiDAR models for Epochs 1 and 2. Each CDF curve, in that figure, assists in visualizing the probability that M3C2 "signed" distances (or ±PDs), between the TB LiDAR models completed in Epochs 1 and 2, be at a certain range, for one of the two MSE walls (N or S) at this bridge. The x-axis represents the "signed" distances (±PDs) measured by the elaborated M3C2 algorithm. The y-axis indicates, again, the probability that ±PDs take on a value less than or equal to a given value x.

Since in the previous analysis of C2C “absolute” distances (PDs), the discrepancy range was selected between 0 and 20 mm, now for proper comparison, in the analysis of M3C2 “signed” distances (±PDs), the range was also selected from -20 mm to +20 mm. Additionally, since in the C2C “absolute” distance analysis, the maximum magnitude of discrepancies with a 95% probability of occurrence was determined, now in the M3C2 “signed” distance analysis, that 95% probability has to be considered between the 2.5% and 97.5% levels. Accordingly, for the N wall, Figure 98 indicates a 95% probability that all ±PDs are in the [-4.4 mm, +4.0 mm] interval. Similarly, for the S wall, 95% probability corresponds to the [-3.6 mm, +2.8 mm] interval. Those ranges are translated into “absolute” magnitudes of position discrepancies, resulting in the following two statements: (i) For the N wall, there is a 95% probability that the magnitude of all position discrepancies, between Epochs 1 and 2, be equal or less than 4.4 mm. Similarly, for the S wall, that amplitude is equal or less than 3.6 mm. These smaller amplitudes contrast with the values obtained in the previous C2C “absolute” distance analysis, 7.2 mm and 8.0 mm, respectively (see Figure 93). The resulting smaller M3C2 discrepancies highlight the ability of the M3C2 algorithm to detect and measure smaller, normal-to-surface deviations.

The previous low-magnitude results indicate that most of the computed “signed” and “absolute” distances (±PDs and PDs), between the TB LiDAR clouds modeled at Epochs 1 and 2, are small, and most likely below the level of noise associated with the employed TB LiDAR technique. This further implies that, most likely, there were no measurable wall displacements between Epochs 1 and 2 and the attained different magnitudes of discrepancies should be considered intrinsic noise associated with the implemented TB LiDAR technique.

ESTIMATION OF NOISE ASSOCIATED WITH RTS, AND TB & VA LIDAR TECHNIQUES AT B2-OLD RIVER

While analyzing the MSE walls at this bridge, in Epochs 1 and 2, several estimates of the underlaying noise, associated with the employed measuring/modeling techniques, have been determined from position and DDs. For that purpose, most of the collected data has been considered. These discrepancies are presented in Table 42, which also shows the estimated noise for RTS measurements and for the TB LiDAR & VA LiDAR modeling techniques.

Table 42. Estimated noise level associated with different measuring/modeling techniques

	Type of Noise Estimator for position (PDs) and DDs between two measuring/modeling techniques	Figure #	**RTS** [RTS2-RTS1] (mm)	**TB-LiDAR** [TBL2-TBL1] (mm)	**VA-LiDAR** [VAL2-VAL1] (mm)
From Position Discrepancy	12 CPs (2 walls), Coarse Estimate = Abs Max PD	Figure 85	10.5	11.7	14.3
	12 CPs (2 walls), 95% Prob. = Max $\|\mu+1.96*\sigma\|$	Figure 85	**11.9**	11.8	15.6
	12 CPs (2 walls), RMSV (measure of discrep. magnitude)	Figure 85	6.7	7.0	8.5
	C2C "absolute" dist., 95% Prob. = Abs Max of 2 walls	Figure 93	–	8.0	–
	M3C2 "signed" dist., 95% Prob. = Abs Max of 2 walls	Figure 98	–	4.4	–
	A. *Averaged PD Values* =		9.7	8.6	12.8
From Distance Discrepancy	66 non-repeated distances (among 12 CPs), Coarse Estimate = Abs Max	Figure 89	8.2	14.7	16.0
	66 non-repeated distances (among 12 CPs), 95% Prob. = $\mu+1.96*\sigma$	Figure 89	11.5	**15.7**	**19.3**
	66 non-repeated distances (among12 CPs), RMSV (measure of discrepancy magnitude)	Figure 89	4.0	5.4	7.5
	B. *Averaged DDs Values* =	–	7.9	11.9	14.3
COMBINED ESTIMATES					
Potential Noise Levels	(i) Average of **A** & **B**	–	8.8	10.3	13.5
	(ii) Moderately Conservative Estimate: Max of **A** & **B**	–	9.7	11.9	14.3
	(iii) Conservative Estimate: Max of all	–	11.9	15.7	19.3
ESTIMATED NOISE LEVEL					
	Moderately Conservative Estimate: Max of **A** & **B**	–	**9.7**	**11.9**	**14.3**

To effectively use most of the collected data, Table 42 presents noise estimates derived from PD and DD analysis.

Regarding distance measurements, it is known that expected distances calculated with erroneous coordinates will generally be greater than the true distance due to the concept of Jensen's Inequality (Schenewerk & Marshall, 2010). This is in general true unless very specific and unlikely conditions of error distribution and consistency are met. However, quantifying the exact overestimation in distances due to Jensen's inequality is not straightforward. The magnitude of overestimation depends on several factors: (i) The level of noise in the collected point position data, i.e., greater noise will lead to a larger overestimation. (ii) The characteristics of the specific measuring device and measuring conditions, i.e., different devices and environmental factors, can affect the accuracy of the coordinate readings. (iii) The intrinsic noise added by the data postprocessing required by the employed modeling techniques. In essence, while Jensen's inequality explains the reason for the overestimation, there's no single, fixed percentage or amount that applies universally. It is an effect that arises from the combination of noisy data, errors in the registration processes leading to the generation of final georeferenced 3D models, and the mathematical properties of distance calculations. Its accurate estimation requires a relatively large number of observations and substantial data collection, beyond the scope of this project. Accordingly, since measured distances are overestimated, DDs among measurements were considered here as adequate (perhaps high) estimates for the noise associated with the employed measuring/modeling approaches. Therefore, they have been included, with equal weight, in this noise-determination analysis.

From the measurements performed at B2-Old River site, the estimated noise levels, following a moderately conservative approach, are as follows:

For RTS measurements:	9.7 mm
For TB B LiDAR modeling:	11.9 mm
For Visual-Alignment LiDAR modeling:	14.3 mm

CHAPTER 9. RESULTS AT BRIDGE B3-SANDERSVILLE

DESCRIPTION OF THE WORK AT B3-SANDERSVILLE

At this bridge, during summer 2024, one (1) set of benchmark measurements was completed to attain reference coordinates for all CPs considered. This was performed with an accurate, one-second device, the RTS instrument. Here, the corresponding measurements (point positions and distances among points) are referred to as RTS values. Additionally, four (4) virtual, 3D LiDAR models were generated with Leica's Cyclone Core software, and one (1) close-range (C-R) photogrammetry model was produced with Agisoft Metashape software with pictures taken with a hand-held, DSLR camera. Furthermore, another C-R photogrammetry model was attempted in spring 2025, with pictures taken from an UAV, or drone. The corresponding measurements, completed in the field, or extracted from the finalized georeferenced models, are named and briefly described as follows:

(1) RTS: Field measurements with accurate, benchmarking, one-second RTS instrument.

(2) FTL: TB LiDAR model with target positions acquired in the field.

(3) STL: TB LiDAR model with target positions acquired via software.

(4) LVL: Visual-aligned LiDAR model with scans registered in a sequential loop.

(5) RVL: Visual-aligned LiDAR model with scans registered in a random fashion.

(6) MHP: C-R Photogrammetry model via Metashape with pictures from a hand-held camera

(7) MDP: C-R Photogrammetry model via Metashape with pictures from a drone camera

In this bridge, two TB LiDAR modeling techniques, each with a different registration workflow, were compared. The Field TB terrestrial LiDAR (FTL**)** scheme used 6 targets that were physically placed on poles verticalized at 6 of the 7 GCPs employed at this bridge. GCP X1 was too far and not included in the scanning process. Those 6 targets were acquired, one by one, at high resolution, by each scan, on-site, prior to completing each full 360° scan. This necessitated added field time, easily triplicating the amount of scanning-related time. After setting up and acquiring the white spherical targets (each 6- or 9-inch in diameter) on the 6 involved GCPs, the entire area was scanned. This involved a total of 8 scanning stations (scans) and was completed with the Leica P50 scanner. Figure 99 shows all 8 scanning stations as small red circles. They were designated as ST1, ST2, ST3, ST4, ST5, ST6, ST7 and ST8. Additionally, the same figure shows the location of all employed targets: TA (almost fully covered by ST2), TB, TC, TD, TE, and TF. The field-collected targets were employed to stitch the 8 scans via a swift TB registration process, characterized by its fast-processing time. That is, the required postprocessing time was minimum. Then, the coordinates of 6 GCPs were employed to georeferenced the previously generated full model. This method attained a truthful and reliable final registration, using targets at the accurately established GCPs.

In comparison, the STL (Software Target LiDAR) technique relied on extracting targets directly from the scan data using Leica's Cyclone Core software. In this case, the original field-acquired targets were removed to enable software-only target detection and acquisition workflow. This technique is fast in the field because it does not require individual acquisition of each target at high resolution. It just needs regular scanning of the targets, like any other object in the scanning range of the instrument, at the selected scanning resolution, without the need to increase that resolution. Yet, the STL technique presents slower postprocessing time because it requires user intervention to

acquire each needed target via software. Nevertheless, the postprocessing time required by STL is still substantially less than the required by visual-aligned (VA) LiDAR registration approaches.

In this project, 2 different types of VA LiDAR models were generated; each used a different VA registration approach to stitch the 8 scans completed at this bridge. The first approach, called Loop Visual-Alignment LiDAR (LVL), consisted in sequentially aligning adjacent, close neighboring, scans to follow a continuous loop (preferably a closed loop) of consecutive scans, with optimum point overlap between each pair of neighboring registered scans, minimizing error propagation. The employed 8 individual scans were all relatively close to each other, and each contained larger or smaller overlapping areas with the other 7 scans. The high overlapping mentioned, in all 8 involved scans, assisted in obtaining a relatively accurate LVL model. Figure 99 shows the relative location of all 8 scans. That figure also shows a green line with a length of 27.234 m that can be used as a reference to estimate the distance between scanning stations.

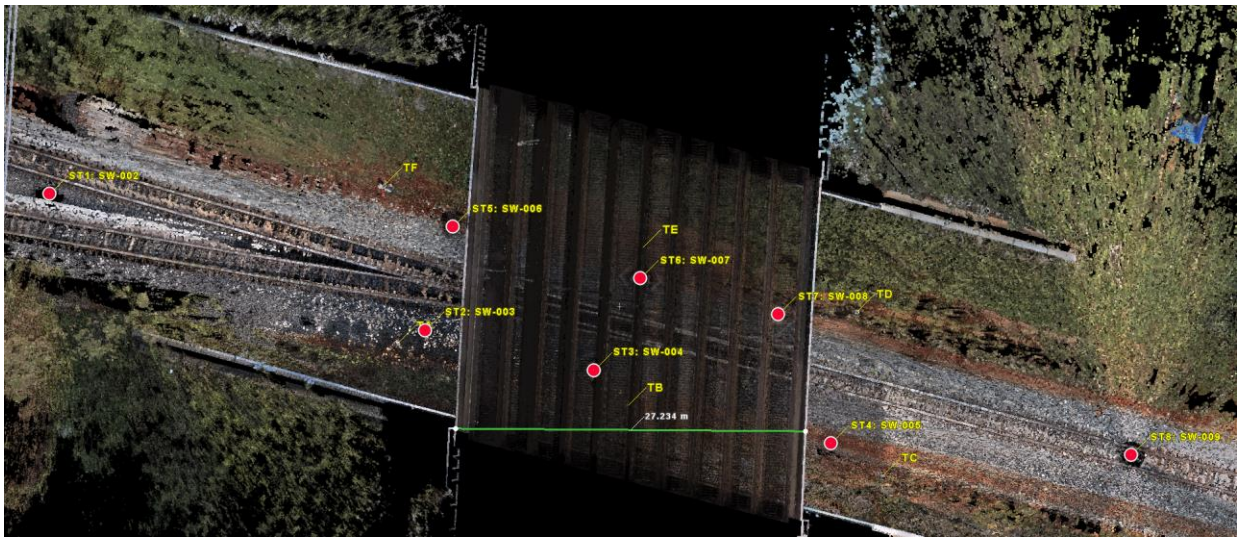

Figure 99. Photo. Eight scanning stations (scans) completed at B3-Sandersville

The registration process to generate the LVL model started with the stitching of two close-neighbor scans (ST1 & ST2) into a single group. Then, a third scan (ST3) was stitched (registered) to one of the scans (ST2) in that first group to form a group of 3 scans. Successively, in the same manner, consecutive registrations of additional scans were completed to add one scan, at a time, to the growing, already registered (stitched), group. Table 43 presents the successive pairs of scans that were stitched together via this visual-alignment approach, LVL. Additionally, that table shows the RMSV attained while registering each pair of scans, and the number of overlapping, or quasi-overlapping points considered in that process.

Table 43. Characteristics of the visual-alignment registration process associated with the LVL technique at B3-Sandersville

Registration Sequence	Registered Scanning Stations (Scans)	LVL	
		RMSV* (mm)	Overlapping Point Count ($\times 10^3$)
1st pair	ST1 & ST2	16.6	672
2nd pair	ST2 & ST3	11.0	1,588
3rd pair	ST3 & ST4	11.9	1,428
4th pair	ST4 & ST7	10.9	1.384
5th pair	ST4 & ST8	16.1	705
6th pair	ST8 & ST7	15.4	621
7th pair	ST7 & ST6	13.5	1,769
8th pair	ST6 & ST5	13.0	1,602

*RMSV: RMSV in the alignment of coincident (or quasi-coincident) points.
MAE of this valid registration = 1 mm (for Enabled Constraints) and 0mm (for Disabled Constraints)

The second analyzed VA LiDAR approach, the RVL (Random Visual-Alignment LiDAR) technique, did not consider the amount of overlapping when sequentially registering 2 scans, out of the original 8 scans. In this case, the registration order is considered random. This assisted in investigating how low overlapping, or alignment disorder, affects the accuracy of the resulting models.

Additionally, a C-R photogrammetry technique, MHP (Metashape Handheld Pictures), was investigated in this bridge. It used highly overlapped pictures of the MSE walls taken with a handheld DSLR camera. For this, the photographer attempted to take most of the images pointing along a direction approximately perpendicular to the walls, from different positions, separated by only one step. Radial pictures from the same point were avoided. Some photos were taken from a low elevation (~1m) and others from a higher elevation (~2m or ~3m). The distance from the camera to the walls varied from approximately 4 m to 10 m. The overlap attained in two consecutive pictures was substantial (close or more than 80%). Those images were processed via the Agisoft Metashape software. Furthermore, we may want to mention here the photogrammetry model with pictures taken by the drone.

Each modeling technique was compared against measurements completed in the field with the accurate, benchmarking RTS instrument. This was done to assess the resulting relative accuracy of each modeling technique with respect to RTS measurements. For proper comparison purposes, all models were georeference in the same selected local system of reference. That is, all field measurements and model-extracted coordinates were in the selected local system of reference, which was adopted via the mentioned polygonal, closed traverse.

Figure 100 illustrates one of the georeferenced LiDAR models produced with Leica's Cyclone Core software. Figure 101 shows one of the georeferenced photogrammetry models generated via the Agisoft Metashape software.

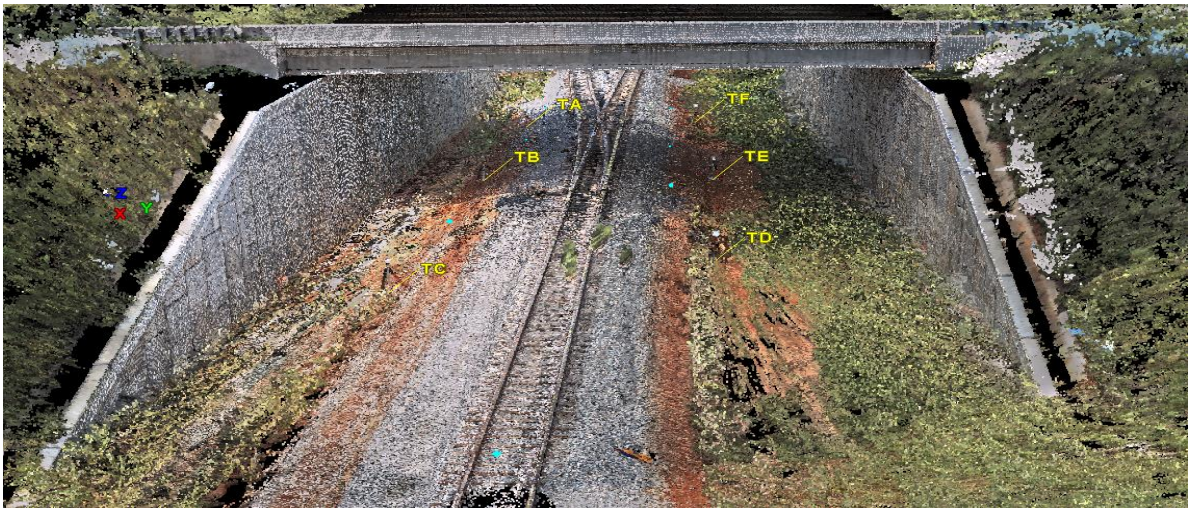

Figure 100. Photo. One of the LiDAR-based models of B3-Sandersville

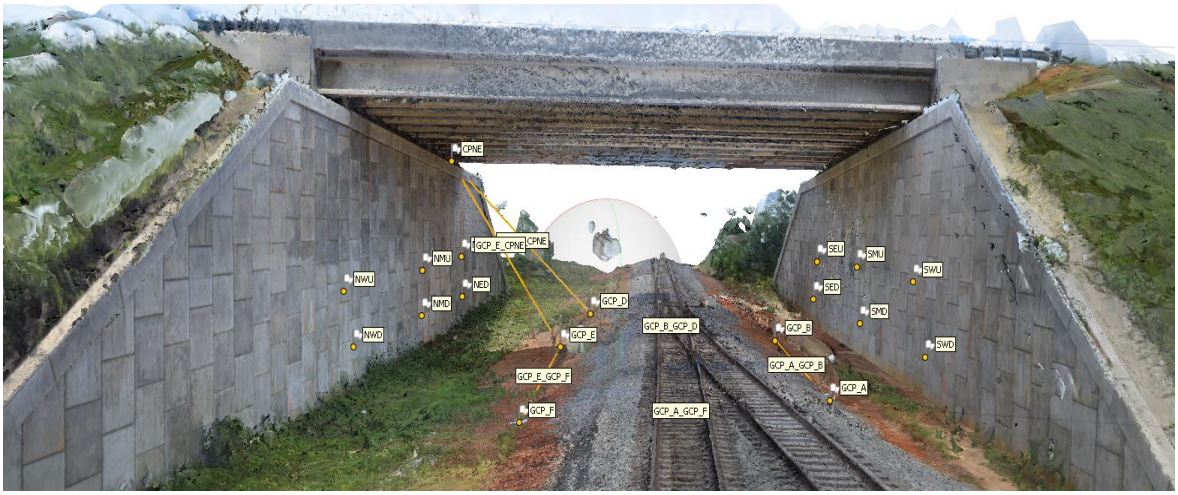

Figure 101. Photo. One of the C-R photogrammetry models of B3-Sandersville

LOCAL SYSTEM OF REFERENCE AT B3-SANDERSVILLE

At this bridge site, a 7-sided, polygonal, closed traverse was implemented and properly balanced to establish a selected accurate system of reference. For this purpose, the precise, one-second RTS instrument was employed. The traverse consisted of 7 vertices, labeled A, B, C, X1, D, E and F. During traverse calculations, each internal horizontal angle was balanced twice, one time locally (at

each vertex with respect to its corresponding external angle), and one time globally (considering the closure of the sum of all internal angles). Longitudinal horizontal errors were adjusted using the Compass (Bowditch) rule. Each vertical angle was also measured twice, and both values were averaged.. Appendix A shows the horizontal traverse and elevation calculations, respectively, for this bridge. Figure 102 presents an aerial view (not at scale) of this bridge with the approximate location of the established polygonal traverse and its 7 vertices, the 7 GCPs. Figure 103 illustrates the relative horizontal position of those vertices and their resulting horizontal local coordinates (X=Easting, Y=Northing), in feet, in the selected local system of reference. In this system, the North direction approximates North, but it is not the actual true North. Nevertheless, the selected reference North is shown upward.

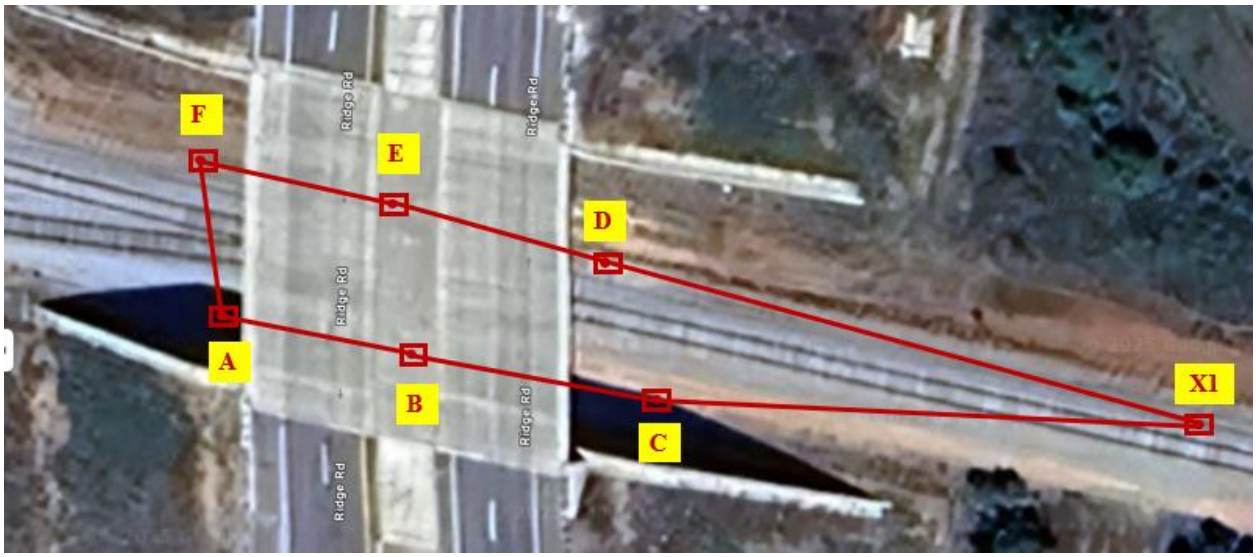

Figure 102. Photo. Aerial view of 7-sided closed traverse near B3-Sandersville

Table 44 presents a summary of the characteristics of the resulting traverse calculations, completed in summer 2024, including their errors of closure and attained longitudinal precision. That

precision, 1: 221,872, is well in excess to the one indicated by GDOT Survey Manual, 1:20,000 (GDOT, 2022). Table 45 shows the resulting spatial coordinates (X, Y, Z) of all 7 GCPs.

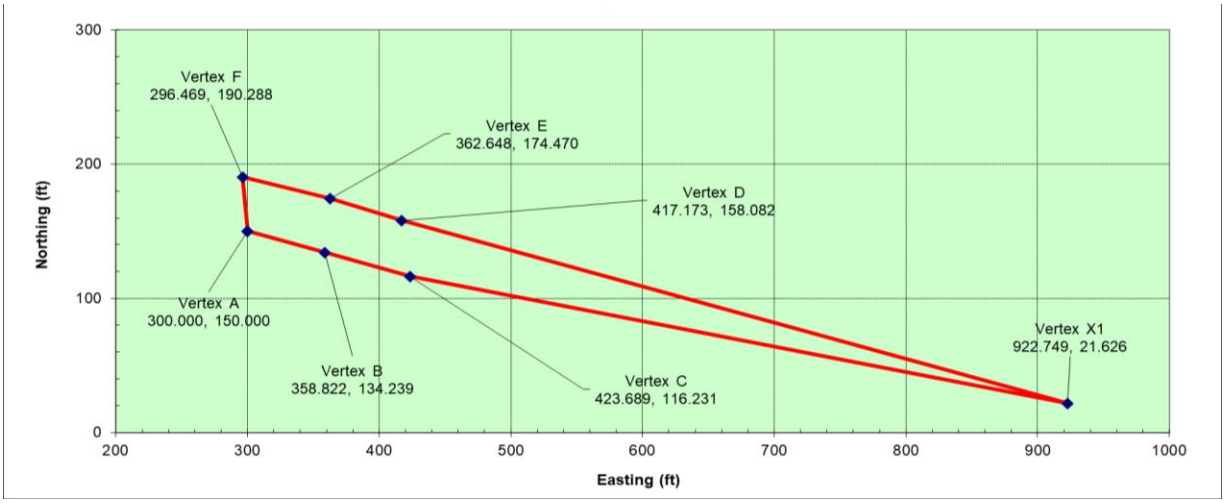

Figure 103. Graph. Horizontal coordinates of 7-sided closed traverse near B3-Sandersville

Table 44. Characteristics of 7-sided, closed traverse near B3-Sandersville

Traverse at Bridge	Perimeter	Total Horizontal Angular Error of Closure	Attained Longitudinal Precision	Elevation Error of Closure
	ft ; [m]	seconds	Ratio	ft ; [mm]
Sandersville	1,325.252 ; [403.937]	14.50	1 / 221,872	-0.007; [-2.3]

Table 45. Local spatial coordinates of seven GCPs near B3-Sandersville

GCPs	Easting (ft)	Northing (ft)	Elevation (ft)
	X	Y	Z
A	300.00	150.000	100.00
B	358.822	134.239	100.600
C	423.689	116.231	101.222
X1	922.749	21.626	108.833
D	417.173	158.082	100.318
E	362.648	174.470	99.280
F	296.469	190.288	98.916

CHECKPOINTS AT B3-SANDERSVILLE

Twelve (12) CPs were marked on the façades of the MSE walls, at the abutments of this bridge. Six CPs were painted on each of the two walls. As illustrated in Figure 104, the CPs were 6-inch diameter, black & white circles. Three pairs of CPs were positioned on each wall. Each pair consisted of an upper and a lower CP. One pair was near the beginning of the wall, another near its middle region, and the remaining pair near the end of the wall. Then accurate one-second RTS instrument was employed to measure angles and distances needed to determine the coordinates of all 12 CPs from the already established GCPs. These measurements were repeated twice to identify potential mistakes. Then, both measurements were averaged to reach the final adopted coordinate values for each CP. Their 3D coordinates were in the selected local coordinate system (same system used in the corresponding traverse) to assess position and DDs between the different measuring/modeling techniques employed in this analysis.

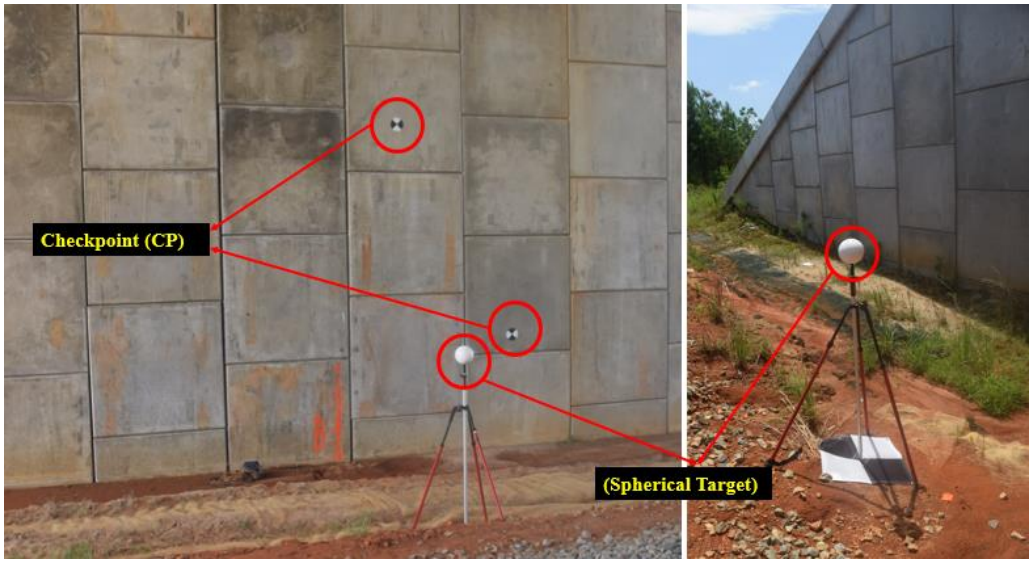

Figure 104. Photo. Black-&-white CPs on MSE wall and white spherical targets on GCPs

For quick reference, those averaged field coordinates are herein referred to as RTS values and are presented in Table 46.

Table 46. RTS Coordinates of 12 CPs near B3-Sandersville

#	CP Names	Easting (ft)	Northing (ft)	Elevation (ft)
		X	Y	Z
1	NWU	323.800	211.209	110.229
2	NWD	327.576	210.095	103.230
3	NMU	368.690	199.226	110.935
4	NMD	367.700	199.381	103.838
5	NEU	404.725	189.828	112.115
6	NED	405.528	189.500	104.441
7	SEU	395.388	110.079	112.503
8	SED	398.524	109.349	104.832
9	SMU	352.230	121.398	113.051
10	SMD	347.483	122.757	104.475
11	SWU	313.179	131.718	112.663
12	SWD	305.530	133.763	104.200

POSITION DISCREPANCIES (PDS) ANALYSES AT BE-SANDERSVILLE

[MHP vs RTS], [STL vs RTS], [FTL vs RTS], [LVL vs RTS], and [RVL vs RTS]

For each of the 12 CPs, five position discrepancies were determined. Each of them corresponded to the discrepancy between the positions extracted from one of the five completed virtual, 3D point-cloud models (MHP, or STL, or FTL, or LVL, or RVL values) and the corresponding position measured in the field with the accurate, robotic, total-station instrument (RTS values). These PDs are positive values. Each represents the magnitude of the difference vector obtained by subtracting the RTS position vector (coordinates), of a given CP, from the corresponding position vector (coordinates) extracted from each of the five point-cloud models. Therefore, for each CP, the following five PDs were calculated [MHP-RTS], [STL-RTS], [FTL-RTS], [LVL-RTS], and [RVL-

RTS]. Figure 105 depicts those PDs for all 12 CPs. They ranged from 1.7 mm to 30.5 mm, showing the relative accuracy of each method with respect to the benchmarking RTS instrument.

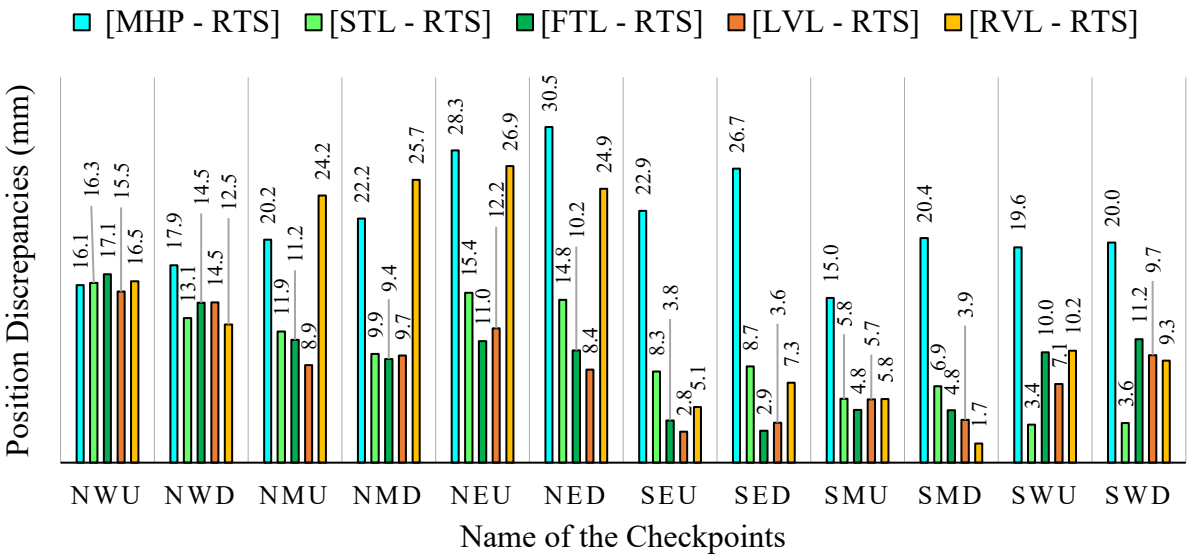

Figure 105. Chart. Position discrepancies for each of the 12 CPs at B3-Sandersville

The TB LiDAR method, FTL, and the closed-loop, visual-aligned (VA) LiDAR approach, LVL, often show discrepancies near the lower end of the range, reflecting their superior alignment with RTS data. The STL technique, using targets acquired via software, presents slightly larger discrepancies than the previous two mentioned approaches. The RVL technique, using random registration of the scans presents larger discrepancies. Finally, the MHP photogrammetric technique, using pictures acquired with a hand-held DSLR camera, showed the largest discrepancies.

Figure 106 presents the same PD data as Figure 105, now organized into four interquartile ranges: 0%-25%, >25%-50%, >50%-75%, and >75%-100%. The y-axis quantifies the magnitude of PDs,

while the colored rectangles highlight central data within the second and third quartiles (comprising 50% of the samples), emphasizing the concentration of PDs near the median. This graph provides insight into the distribution and variability of PDs attained by each modeling technique with respect to field measurements completed with the accurate RTS instrument.

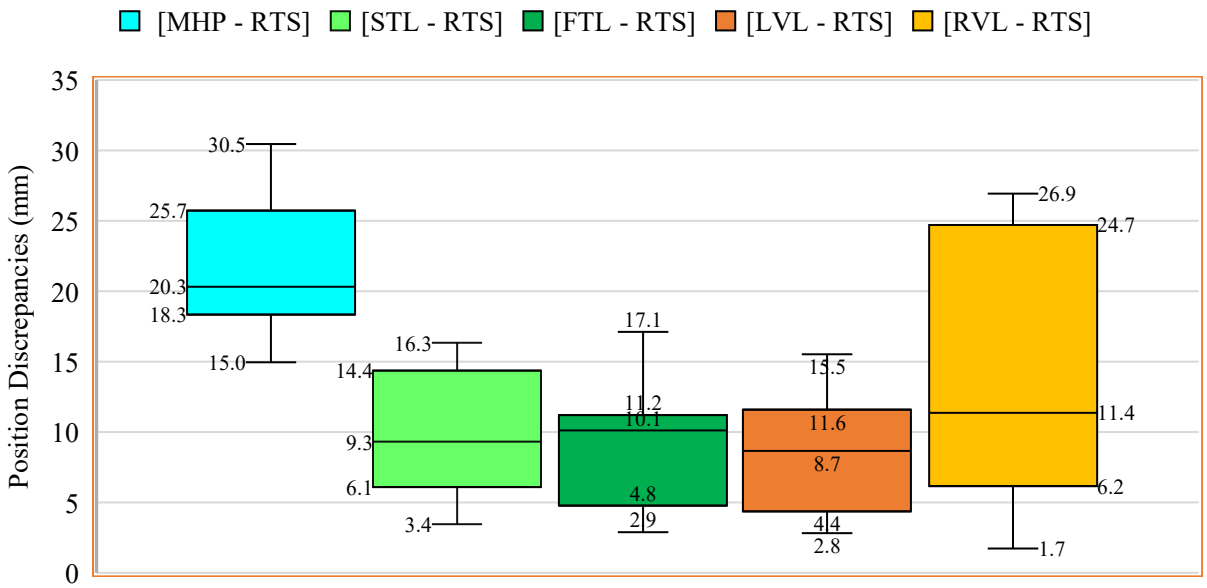

Figure 106. Chart. Interquartile ranges of position discrepancies of 12 CPs, between 3D Models and RTS. B3-Sandersville

According to Figure 106, the comparative interquartile graph reveals that the FTL vs RTS and the LVL vs RTS comparisons showed the most effective performance with respect to the benchmarking RTS measurements, with a median PD of approximately 10.1 mm, and 8.7 mm, respectively. Additionally, FTL and LVL presented the lowest dispersions out of the central 50% of the samples (11.2 – 4.8 = 6.4 mm), and (11.6 – 4.4 = 7.2 mm), respectively. This indicates that both techniques, FTL and LVL align closely with the RTS measurements, showcasing reliability and precision. At the same time, the STL technique, with targets acquired via software, also presents a low median, 9.3 mm, but a slightly higher dispersion (14.4 - 6.1 = 8.3 mm) out of the central half of the samples,

making it the third modeling performer with respect to the RTS instrument. On the other hand, the MHP and RVL techniques showed the largest discrepancies with respect to RTS. The MHP approach presented the highest median value, 20.3 mm, with relatively low dispersion (25.7 – 18.3 = 7.4 mm) out of the central half of the samples. The RVL median was 11.4 mm, which is not too high compared with the others, but it showed the largest dispersion (24.7 – 6.2 = 18.5 mm) out of the central 50% of the samples. Overall, the interquartile analysis indicates that FTL and LVL performed very well with respect to RTS. Both are the most consistent methods providing the smallest PDs, with respect to RTS measurements, with low dispersions, and highest reliability. This underscores their suitability for applications requiring global (full wall) accurate, precise and consistent positional data.

Additionally, a statistical analysis was completed considering the 12 PDs attained between each modeling technique (MHP, STL, FTL, LVL, & RVL) and the RTS benchmarking measurements, for all 12 CPs.

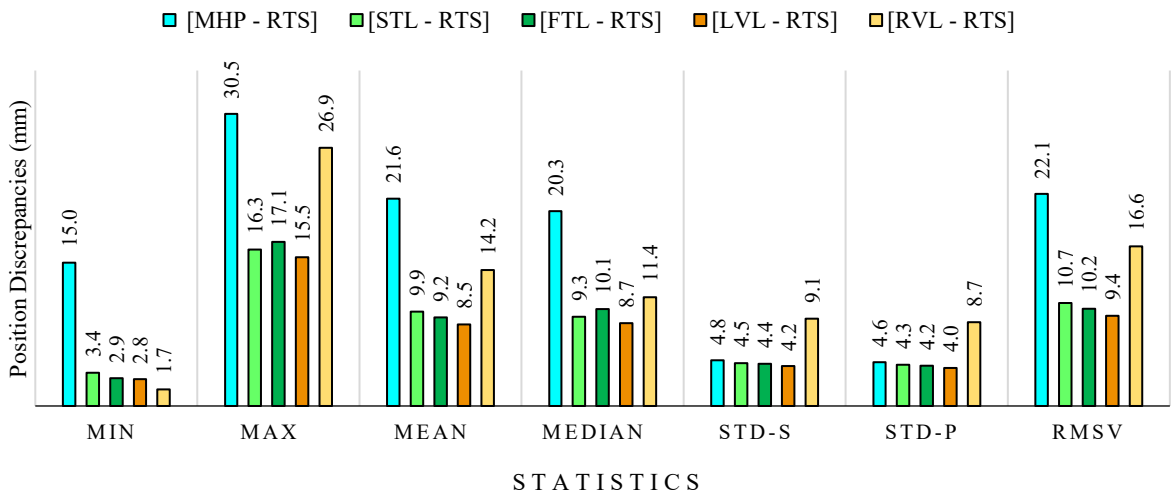

Figure 107. Chart. Statistics of position discrepancies for 12 CPs at B3-Sandersville

Figure 107 presents those statistics, where it is observed that the PDs ranged from 1.7 mm to 30.5 mm, with lower values indicating closer proximity to RTS measurements. The minimum (MIN) PDs ranged from 1.73 mm to 15.0 mm, with 4 of them below 3.4 mm, showcasing instances of exceptional relative accuracy with respect to RTS. By contrast, the maximum (MAX) PD values ranged from 15.5 mm to 30.5 mm. The standard deviation values of the population (STD-P) ranged from 4.0 mm to 8.7 mm, with lower values reflecting less dispersion (among the 12 CPs considered), and more consistent performance, with respect to the benchmarking RTS measurements.

Since the calculated PDs are positive magnitude values, independently if the measured positions are beyond or before (on one or the other side of) the actual point positions, their mean (μ) values are not zero and their RMSVs are different from the standard deviations of their populations (σ = STD-P). This can be observed in Figure 107. Additionally, if the PDs are Gaussian distributed, 95% of them will be within the following interval $\{\mu 1.96*\sigma, \mu+1.96*\sigma\}$. For each of the 5 comparisons presented in Figure 107, those intervals are:

For [MHP-RTS]: = {21.6 1.96 * 4.6, 21.6 + 1.96 * 4.6} = {12.6 mm, 30.6 mm}

For [STL-RTS]: = {9.9 1.96 * 4.3, 9.9 + 1.96 * 4.3} = { 1.4 mm, 18.3 mm}

For [FTL-RTS]: = {9.2 1.96 * 4.2, 9.2 + 1.96 * 4.2} = { 1.0 mm, 17.4 mm}

For [LVL-RTS]: = {8.5 1.96 * 4.0, 8.5 + 1.96 * 4.0} = { 0.7 mm, 16.3 mm}

For [RVL-RTS]: = {14.2 1.96 * 8.7, 14.2 + 1.96 * 8.7} = {-2.9 mm, 31.3 mm}

These above metrics, and all statistics presented in Figure 107, highlight the variability and reliability of the evaluated different methods, with respect to measurements completed in the field with the benchmarking RTS instrument. In this regard, the LVL technique presented the lowest RMSV value (9.4 mm), and consistently demonstrated the best performance. The FTL approach presented a similar very good performance (RMSV = 10.2 mm), close to the level attained by the LVL technique. However, it requires extended field work to acquire spherical targets, at high resolution, in the field. Even though, typically, the FTL scheme is the most reliable and accurate method, the LVL approach slightly outperforms it due to the extensive overlapping of the 8 scans employed in this bridge. The LVL requires less work in the field, but more time dedication during postprocessing. Additionally, it is observed that the performance of the STL technique, with a RMSV of 10.7 mm, is at a slightly lower level than LVL and FTL, but still good, indicating that acquiring spherical targets from scans, via software (without physically acquiring them at high resolution in the field) reduces field time and still produces practically good results. Conversely, the MHP (RMSV = 22.1 mm) and RVL (RMSV = 16.6 mm) techniques present the largest deviations from the RTS measurements. In particular, the RVL scheme generated less accurate results because the most adjacent scans (those with more overlapping) were not necessarily selected during the successive alignment (stitching or registration) of pairs of scans. Conversely, by carefully selecting and connecting highly overlapped adjacent scans, during a closed-loop alignment of all 8 of them, the LVL technique showed superior performance with minimal error, resulting in the most reliable and precise approach of the 5 methods compared in this bridge.

DD ANALYSES AT B3-SANDERSVILLE, [MHP VS RTS]

[STL vs RTS], [FTL vs RTS], [LVL vs RTS], and [RVL vs RTS] at B3-Sandersville

Figure 108 presents DD analysis of all possible 66 non-repeated distances among the 12 CPs employed in this bridge. In this case, five distinct modeling techniques have been considered, MHP, STL, FTL, LVL, and RVL. Each has been compared against the same 66 distances determined in the field by the benchmarking RTS instrument. This figure also includes the linear trends associated with each technique for its set of 66 distances. As shown, most DD are cluttered near the zero level with [RVL – RTS] showing more dispersion and the largest DD magnitudes. Conversely, [FTL – RTS] presents DD magnitudes equal or less than 7.1 mm, which is the smallest maximum amplitude of all compared methods.

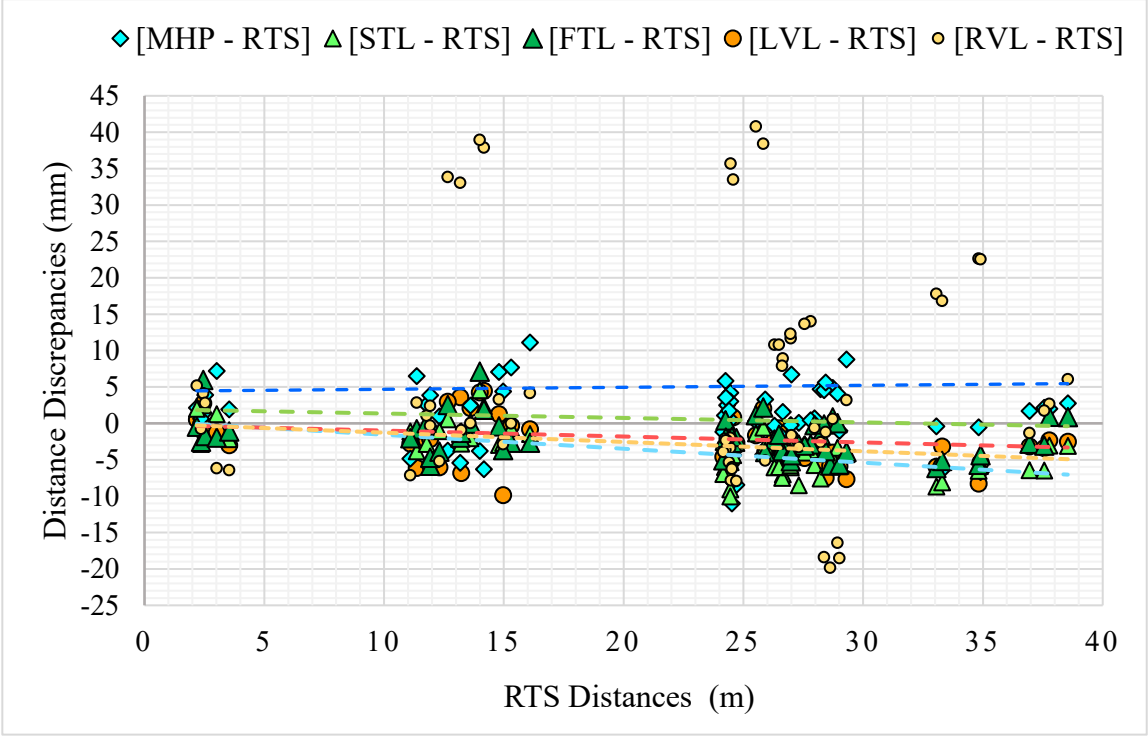

Figure 108. Graph. Sixty-six DDs among 12 CPs at B3-Sandersville

In general, 4 of the 5 techniques (excluding RVL) show relatively low DD, with the FTL and LVL methods being closer to the measurements attained with the benchmarking RTS device. Additionally, the photogrammetry approach, MHP, is clearly more accurate than RVL, but it shows slightly higher DD than FTL, LVL and STL, with respect to RTS.

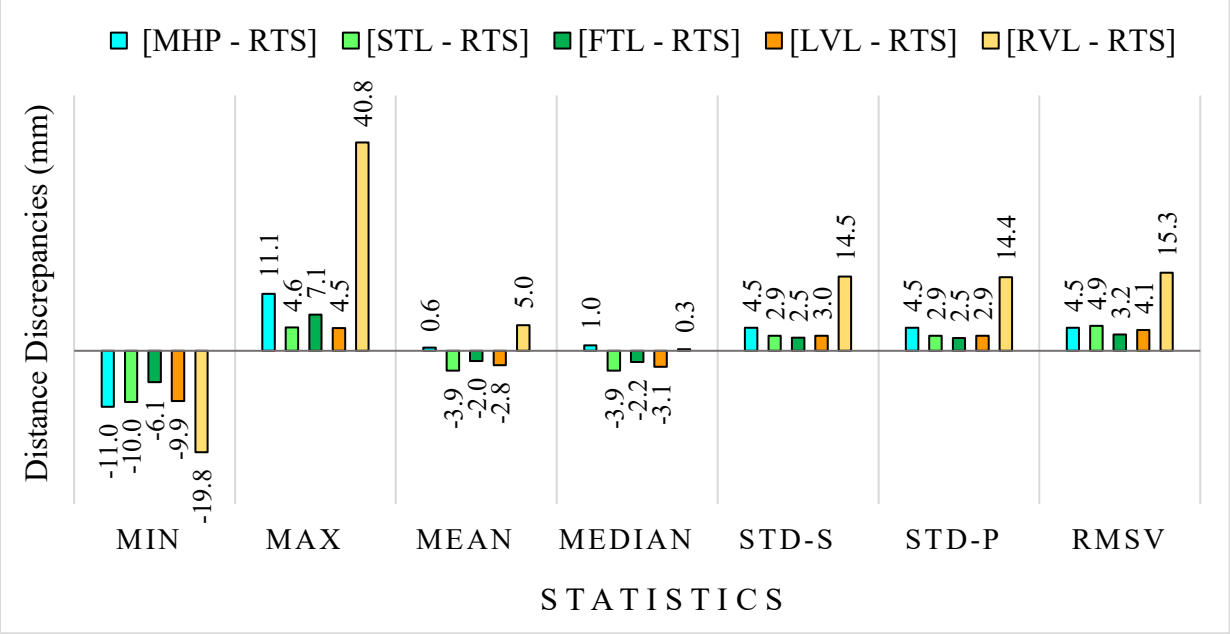

Figure 109. Chart. Statistics of 66 DDs among all 12 CPs, at B3-Sandersville

Figure 109 presents the statistics of all 66 DDs attained by each of the employed modeling techniques with respect to the 66 corresponding distances measured with the RTS instrument. It shows the following DDs metrics: minimum values (MIN), maximum values (MAX), mean values (MEAN), median values (MEDIAN), standard deviation of the samples (STD-S), standard deviation of the population (STD-P), and RMSV. They assist in evaluating the variability, dispersion, precision, and magnitude of the corresponding DDs, with respect to measurements

completed with the RTS instrument. In all cases, the DDs mean values are approximately zero, and the RMSVs approximate those of the standard deviations. The analysis of RMSV and STDs assists in identifying the methods exhibiting the best performance when compared against the accurate RTS instrument. In this instance, the FTL technique (with RMSV=3.2 mm & STD-P=2.5 mm) and the LVL approach (with RMSV=4.1 mm & STD-P=2.9 mm) showed the smallest DDs magnitudes and dispersions, with FTL demonstrating a slightly better performance than LVL. A similar excellent performance, but at a marginally lower accuracy level, was also attained by STL (RMSV= 4.9 mm & STD-P= 2.9 mm). The fourth best performance was accomplished by the photogrammetry MHP approach, with RMSV= 4.5 mm & STD-P= 4.5 mm. Nevertheless, the magnitude and dispersion of the photo-based DDs are only slightly over those of the best 3 performers.

Overall, the distance measuring analyses performed at this bridge indicate that FTL (which is a TB LiDAR technique) is the best-performing modeling method, offering the most accurate and consistent results. At almost the same level of accuracy, the LVL method (which is a VA LiDAR technique) also presented excellent distance measuring abilities. It requires less time for data acquisition in the field, but more postprocessing time for full model generation than FTL. Nonetheless, LVL necessitates highly overlapped scans to attain a level of accuracy like that of FTL, which provides an optimal balance of accuracy and practicality, with robust alignment to GCPs, and minimal error propagation.

METASHAPE PROCESSED DRONE PICTURE MODEL (MDP) WITH UVA IMAGES

Figure 110 presents the positional discrepancies of the UAV-based MDP relative to RTS benchmark data, with DSLR-based Metashape (MHP) and FTL models included for comparison. The MDP model showed a mean discrepancy of 22.29 mm and an RMSV of 24.40 mm, indicating moderate spatial accuracy. While these values are higher than those of the FTL model (mean 9.25 mm, RMSV 10.16 mm) and the MHP model (mean 21.64 mm, RMSV 22.12 mm), the results are still within a reasonable range for UAV-based photogrammetry, especially considering the practical advantages of broader coverage and accessibility. However, the maximum error of 41.47 mm and higher standard deviations (STD-S 10.36 mm) suggest greater variability and less consistency compared to the other methods. Overall, while MDP offers acceptable accuracy for general structural monitoring tasks, it may be less suitable for high-precision applications unless supported by improved flight planning, denser ground control, and tighter quality control.

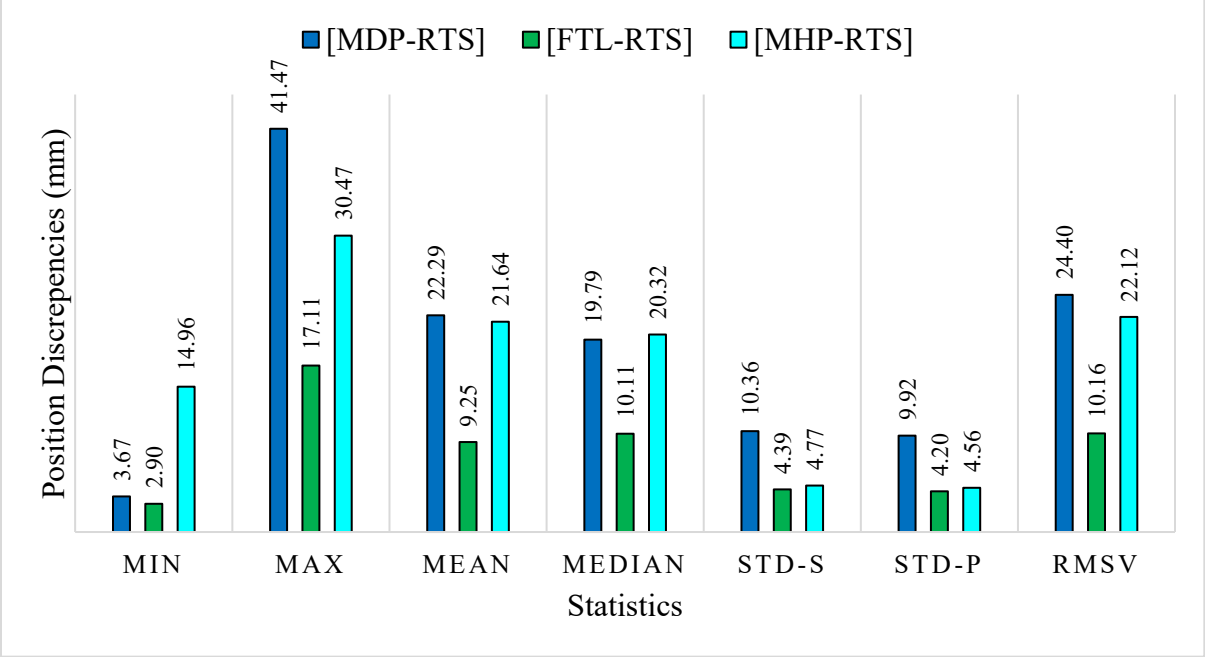

Figure 110. Chart. Statistics of position discrepancies for 12 CPs at B3-Sandersville

Figure 111 illustrates the DDs between the RTS benchmark data and three modeling approaches: MDP, DSLR-based Metashape (MHP), and Field TB terrestrial LiDAR (FTL). The MDP-RTS model shows the highest variability in distance errors, with a maximum discrepancy of +35.46 mm and a minimum of -45.62 mm, indicating substantial over and underestimation in some measurements. The mean value of -10.34 mm and median of -8.86 mm suggest a consistent underestimation of distances compared to RTS. In contrast, FTL-RTS (mean: -1.90 mm, RMSV: 3.21 mm) and MHP-RTS (mean: +0.61 mm, RMSV: 4.54 mm) demonstrate much tighter error distributions. The standard deviation for MDP (STD-S: 19.12 mm) is significantly larger than that of FTL (2.55 mm) and MHP (4.53 mm), reflecting less consistency and higher noise in the UAV-based results. The RMSV of 21.61 mm for MDP further confirms its lower reliability for precise distance estimation.

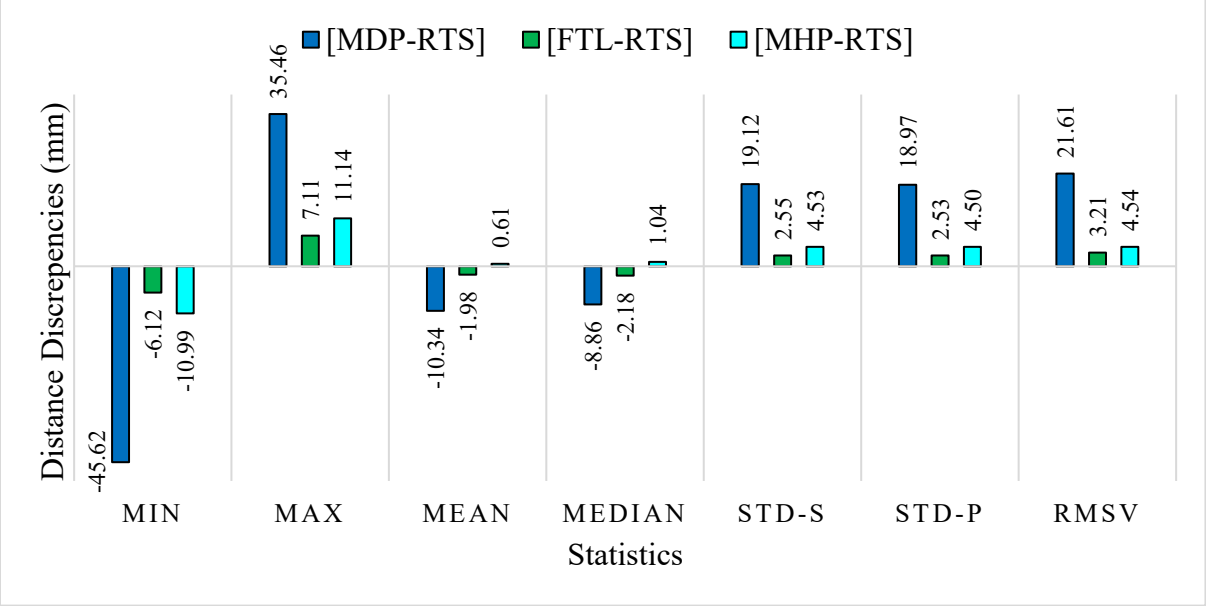

Figure 111. Chart. Statistics of 66 DDs among all 12 CPs, at B3-Sandersville

CC COMPARISONS AT B3-SANDERSVILLE

The CC software enables precise, quantitative evaluation of surface discrepancies by comparing two point-cloud models of the same surface over time. In this regard, it is highly effective to compare models of the same retaining (MSE or modular) wall, at different times, to capture displacements or deformations that occurred during those two times. This analysis assists in detecting even minor displacements or structural shifts, providing early warning signs of potential settlements, wall movements, or construction deficiencies. By delivering exact measurements of surface changes, CC can be employed to confirm that a retaining wall aligns with design specifications and to monitor its long-term geometry, stability and safety. In this bridge, two different comparison procedures were employed to capture surface discrepancies in point clouds generated, at the same time, by two different modeling techniques, LiDAR and CRP. One of the comparison procedures is the C2C "absolute" distance method, and the other is the M3C2 "signed" distance approach. They are further described in the next subsections.

C2C "absolute" distance comparison between LiDAR and photogrammetry models [FTL vs MHP]

The C2C "absolute" distance approach determines the magnitude of the distances exiting between points in the "reference" point cloud and their closest points in the "compared" point cloud. Those distances are always positive and can be considered PDs. Figure 112 shows the two individual models that are being compared and the combined model. Subfigure A shows the "reference" LiDAR model, FTL, while subfigure B shows the "compared" photogrammetry model, MHP. Subfigure C presents both models uploaded into the same space. Since both models were

georeferenced in the same system of coordinates, they should occupy the same space. Since each modeling technique carries its own noise, they present positional discrepancies. Even though the initial model contained both walls, N and S, each wall segmented from the full model and compared individually to assess their geometric discrepancies, as shown in Figures 34 (a) and Figure 34 (b) Discrepancies observed among the models highlight the importance of selecting an appropriate data acquisition method based on project requirements, with the combined model presenting a robust solution for comprehensive 3D documentation.

A. FTL model, (LiDAR model serving as the “reference” point cloud)

B. MHP model (Photogrammetry model serving as the “compared” point cloud)

C. Combined model, containing both comparable models

Figure 112. Photo. Point-cloud models of the walls at B3-Sandersvillefor Analysis via CC

Figure 113 illustrates the C2C “absolute” distances existing between points in the FTL and MHP models of the N wall. Likewise, Figure 114 shows C2C “absolute” distances between the FTL and

MHP models of the S wall. In both cases, those distances are represented by a scalar field, ranging from 0 to 0.15 m (150 mm), and visualized by a color scale. Unlike the analysis performed for B2-Old River, involving geometric discrepancies generated while using twice the same modeling TB LiDAR technique, the study in B3-Sandersville consists of comparing two different modeling approaches, FTL and MHP, completed at the same time. While the FTL technique is a TB LiDAR method using field-acquired targets, MHP is a CRP modeling approach using the Agisoft Metashape software with pictures taken by a hand-held DSLR camera. Namely, the current study focused on comparing the MHP model to the FTL one. The resulting C2C deviation map reveals localized discrepancies, with green/yellow regions indicating larger deviations, potentially due to photogrammetry's sensitivity to texture or occlusions, and blue areas representing closer alignment.

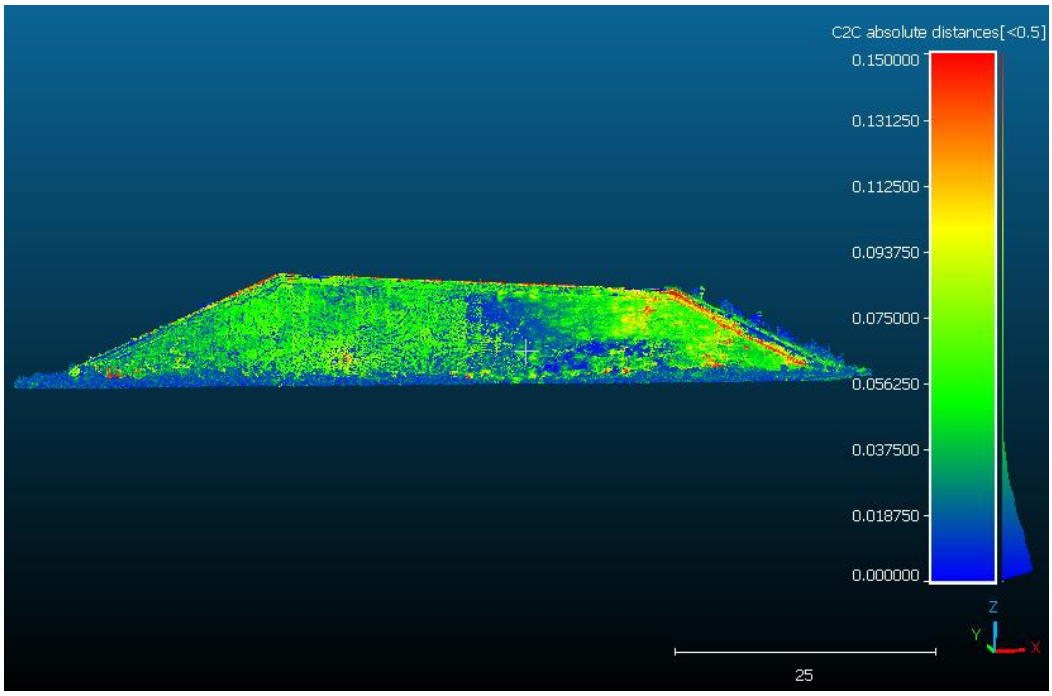

Figure 113. Photo. N Wall, scalar field of C2C "absolute" distances (m)

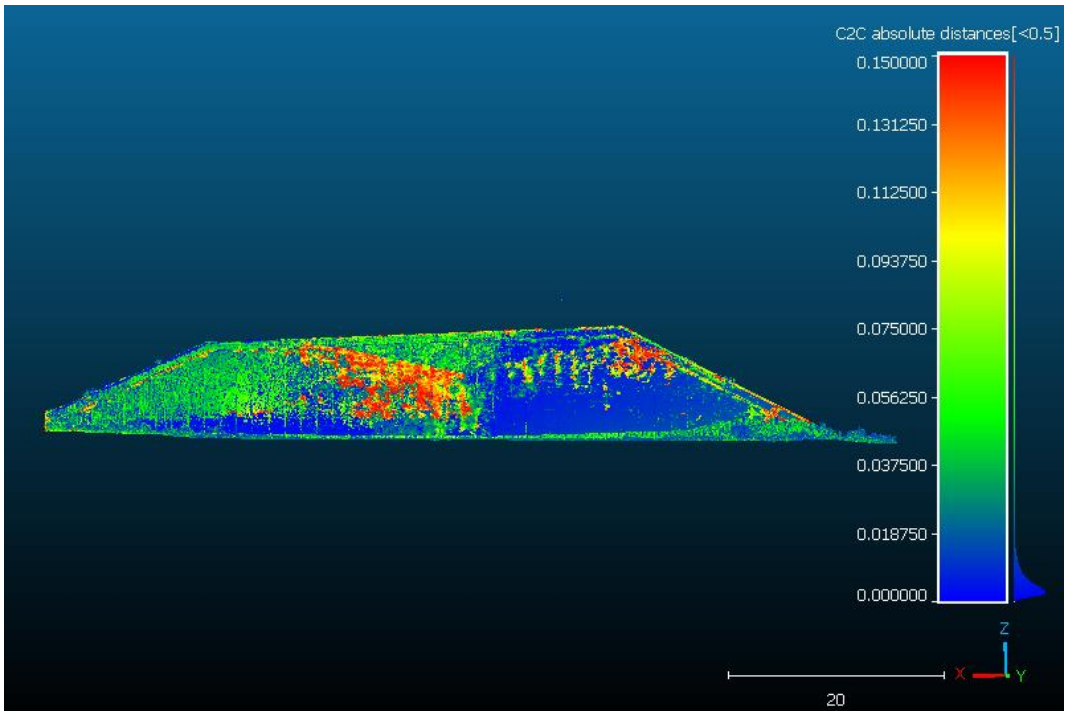

Figure 114. Photo. S Wall, scalar field of C2C "absolute" distances (m

Figure 115 displays a histogram for the North (N) MSE wall, showing the distribution of ~10.993 million C2C "absolute" distances (or position discrepancies, PDs), between the 3D point-cloud models generated by the FTL and the MHP approaches. Those clouds are referred to as North wall – Fixed-Target LiDAR (N-FTL) and Metashape Handheld Photogrammetry (N-MHP). This histogram focuses on PD values less than 0.15 m. Its x-axis represents "absolute" distances, from 0 to 0.15 m, divided into 120 classes, or intervals. That is, each interval has a width of 1.25 mm. The y-axis indicates the count, or frequency, of PDs with values within each interval. The maximum count, ~660×10^3, is at the 4^{th} interval, with a PD of ~4.4 mm, representing ~6.0% of the total number of calculated "absolute" distances, between the N-FTL and N-MHP clouds. At a PD = 25 mm, the count is ~250×10^3 (~2.3%), and it keeps decreasing after that. For example, at PD = 50 mm, the count is ~21×10^3 (~0.2%). The sharp drop in counts, from 4.4 mm to ~45 mm, implies that positional discrepancies larger than 45 mm are rare between those two models of the same N wall.

Nevertheless, noticeable discrepancies exist between the 3D point clouds generated via the FTL and the MHP approaches. Additionally, in the previous statistical analysis of 12 CPs and 66 distances among them, it was observed that the FTL technique presented larger relative accuracies than the MHP approach, with respect to measurements completed with the accurate benchmarking RTS instrument.

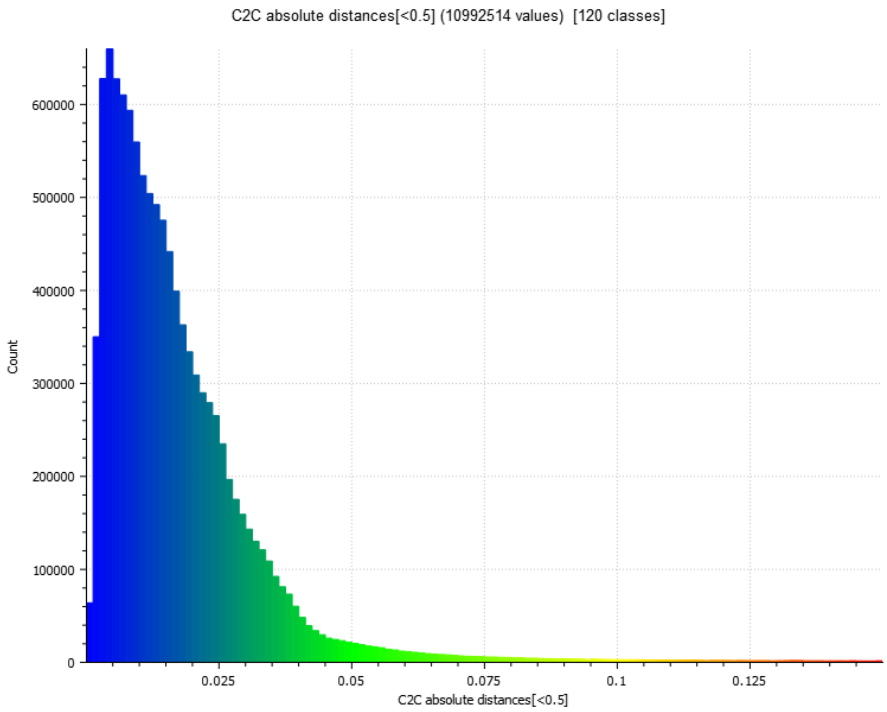

Figure 115. Graph. N wall histogram of C2C "absolute" distance (m), between LiDAR and Photogrammetry, [N-FTL vs N-MHP]

Similarly, Figure 116 presents the histogram corresponding to the South (S) MSE wall. It analyzes the distribution of C2C "absolute" distances, or PDs, below 0.15 m, across 9.938 million PDs, between the 3D point-cloud models generated by the FTL and MHP techniques. Those clouds are referred to as South wall – Fixed-Target LiDAR (S-FTL) and South wall – Metashape Handheld Photogrammetry (S-MHP), respectively. The histogram reveals a striking concentration of minimal positional discrepancies between both models of the S wall. Frequency counts soar to 1.8 million

(~18.1% of the total distances) for near-zero distances (~3.1 mm) and taper sharply from 3.1 mm to ~20 mm. This highlights how profoundly small deviations dominate this dataset. While maintaining the same 120-class interval structure and 0-0.15 m range as Figure 115, the higher frequencies of this visualization dramatically suggest that most of the calculated positional discrepancies, between the S-FTL and S-MHP point-cloud models, exhibited small magnitudes.

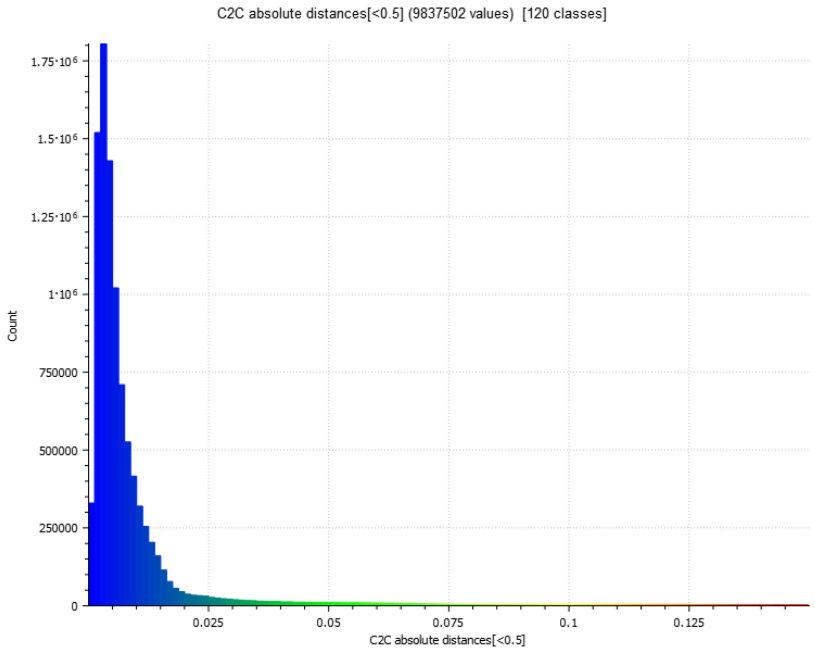

Figure 116. Graph. S wall histogram of C2C "absolute" distance (m), between LiDAR and Photogrammetry, [S-FTL vs S-MHP]

Analysis of C2C CDFs at B3-Sandersville

The C2C cumulative distribution function plots show the probability that the C2C "absolute" distances, between the FTL and MHP models of each wall, N or S, be at or below a given level. Namely, for each wall, they reveal positional discrepancy magnitudes between the two considered modeling techniques, FTL and MHP.

As seen in Figure 117, each wall exhibits similar but different CDF curves. Both show an initial steep rise, but with two different slopes, of cumulative PDs at small magnitude values, indicating that a considerable amount of wall surface points has a relatively low level of discrepancy when modeled by the FTL and MHP techniques. For example, for the S wall, Figure 117 shows that there is approximately an 80% probability that positional discrepancies, between its S-FTL and South wall North-side Handheld Photogrammetry (S-NHP) point-cloud models, be 10 mm or less. However, for the N wall, it shows that there is only a 40% probability that their wall surface points present discrepancies equal or less than 10 mm, between the N-FTL and North wall – N-MHP models. That is, the FTL and MHP approaches produce substantially closer models to each other for the S wall than for the N wall. Since the FTL technique is more accurate than the MHP method, the above-mentioned different PDs, observed when comparing the models of the S and N walls, indicate larger variability when using the MHP modeling method for different walls.

As it was the case in the analyses performed for B2-Old River, the commonly referred 95% probability level was also considered in the MSE walls of B3-Sandersville. In this regard, Figure 117 indicates that, for the S wall, there is a 95% probability that all its PDs, between the S-FTL and S-MHP models, be ≤ 39.3mm. Similarly, for the N wall, there is 95% probability that all its PDs, between the N-FTL and N-MHP models, be ≤ 42.2 mm.

The CDF plots effectively highlight the relative PDs between the FTL and MHP modeling techniques. Since FTL is more accurate than MPH, the previously mentioned two large peak discrepancies (39.3 and 42.2 mm) for both walls, at 95% probability, indicate that the photogrammetry-based MPH approach is less suitable to capture small wall displacements than the

LiDAR-based FTL technique. Beyond 95% coverage, both curves remain close to each other, with a decreasing number of points presenting larger PD values.

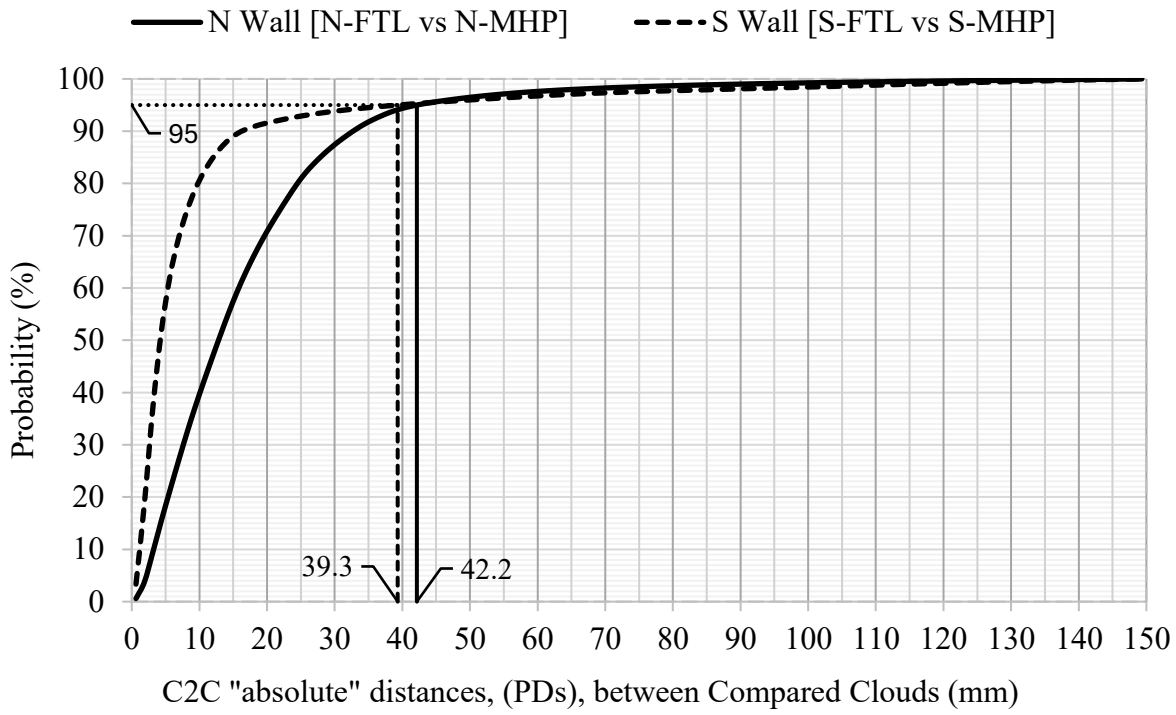

Figure 117. Graph. Cumulative distribution function of C2C "absolute" distances at Sandersville

M3C2 "signed" distance comparison between LiDAR and photogrammetry models [FTL vs MHP]

This section presents spatial discrepancies between two different point-cloud models of the MSE walls at B3-Sandersville. These discrepancies were determined by using the "signed" M3C2 distance ("signed" positional discrepancy, ±PD) metric.

Figure 118 presents result for the North (N) MSE wall and Figure 119 for the South (S) MSE wall. Each assesses the spatial deviation between a LiDAR-based, “reference” point-cloud model, FTL, with targets acquired in the field, and a photogrammetry-based, “compared”, point-cloud model, MHP, generated via Metashape, with pictures from a hand-held camera. In Figure 118 the models compared have been designated as N-FTL and N-MHP. Similarly, in Figure 119 the models compared are referred to as S-FTL and S-MHP. In both instances, a 3D color-coded visualization is displayed and the deviation ranged from -0.15 m to +0.15 m. This range was selected to capture all significant discrepancies. The color scale uses gradient from blue, for negative distances (where the photogrammetry wall surface lies on one side the LiDAR surface) to red and yellow for positive distances (where the photogrammetry model lies on the other side).

For the N wall, Figure 118 shows a prevalence of blue tones with some small green areas across the full surface. This indicates that the N-MHP model predominantly lies on one side of the N-FTL. Conversely, for the S wall, Figure 119 shows negative and positive colors across its full surface, indicating that the S-MHP model lies at both sides of the S-FTL model.

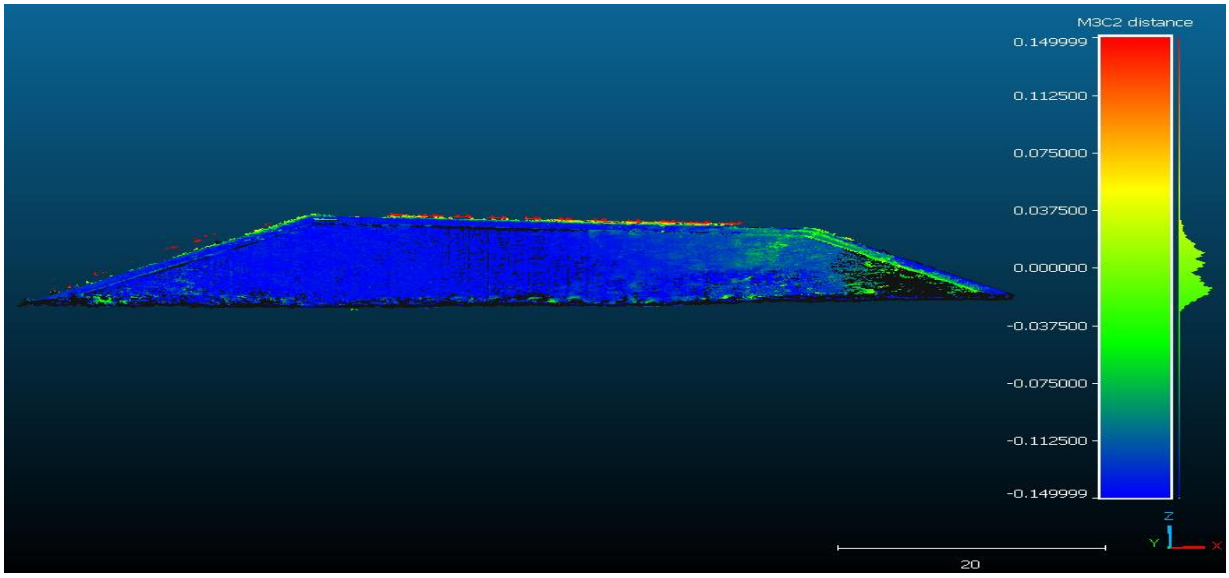

Figure 118. Photo. North Wall, scalar field of M3C2 “signed” distances (m)

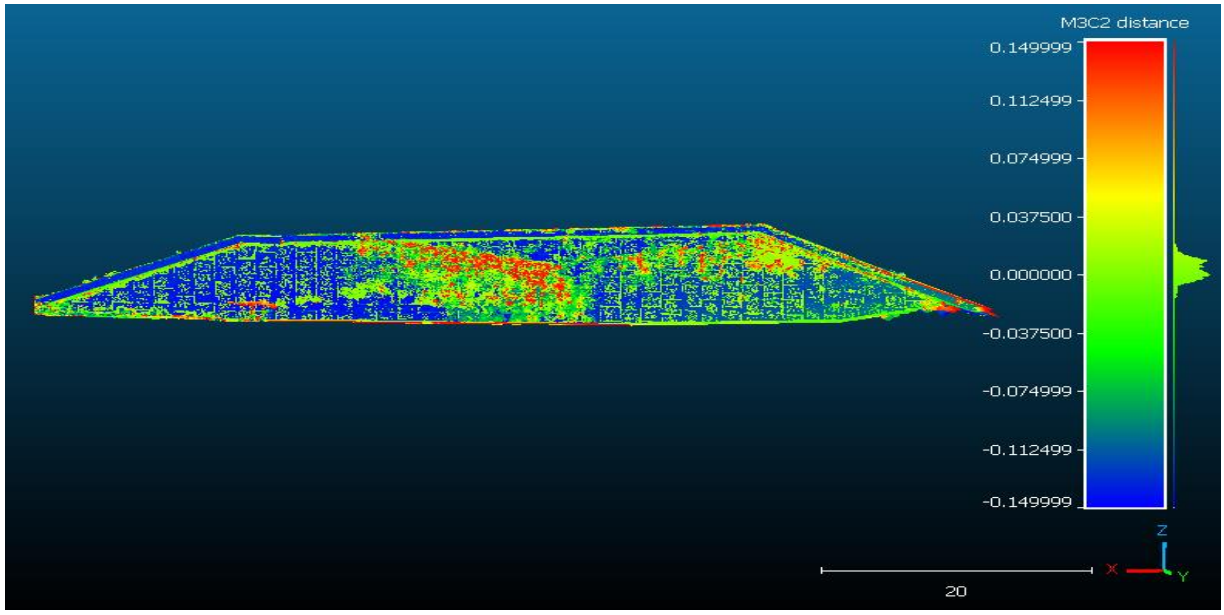

Figure 119. Photo. South Wall, scalar field of C2C “absolute” distances (m)

Figure 120 and Figure 121 present histograms displaying the distribution of M3C2 “signed” distances, between the FTL and MHP models, for the N and S walls, respectively. They range from -0.15 m to +0.15 m, and use a total of 240 intervals, each with a width of 1.25 mm.

As seen in Figure 120, the histogram of the N wall is based on approximately 18.976 million surface points. It shows a peak at -13.1 mm (with a count of ~726×10^3), and a left-skewed distribution, confirming a negative bias where the photogrammetry-based model, MHP, tends to fall on the negative side of the LiDAR-based, FTL, surface. The majority of values are tightly clustered within -0.03 m to +0.03 m, reflecting a strong alignment within a ±30mm discrepancy range.

Figure 121 presents the histograpm for the S wall. It includes over 28.653 million points, and reveals a quasi symmetric distribution, narrower than the one attained at the N wall. Nonetheless, the histogram for the S wall presents a slight positive bias, but it is still centered near zero with its tails showing not significant discrepancies beyond ±0.10 m. It presents two contiguous intervals with the highest counts, one at -0.6 mm, with a large count of ~$1{,}951\times10^3$, and the other at +0.6mm, with a similar large count of ~$1{,}963\times10^3$. This quasi symmetry indicates no significant dominant directional bias.

Together, these histograms indicate that the positional discrepancies between the FTL and MHP modeling techniques are considerable and substantially larger in the N wall than in the S wall. The following subsection analyzes the respective cummulative distribution functions and presents numeric measures supporting the previous statements.

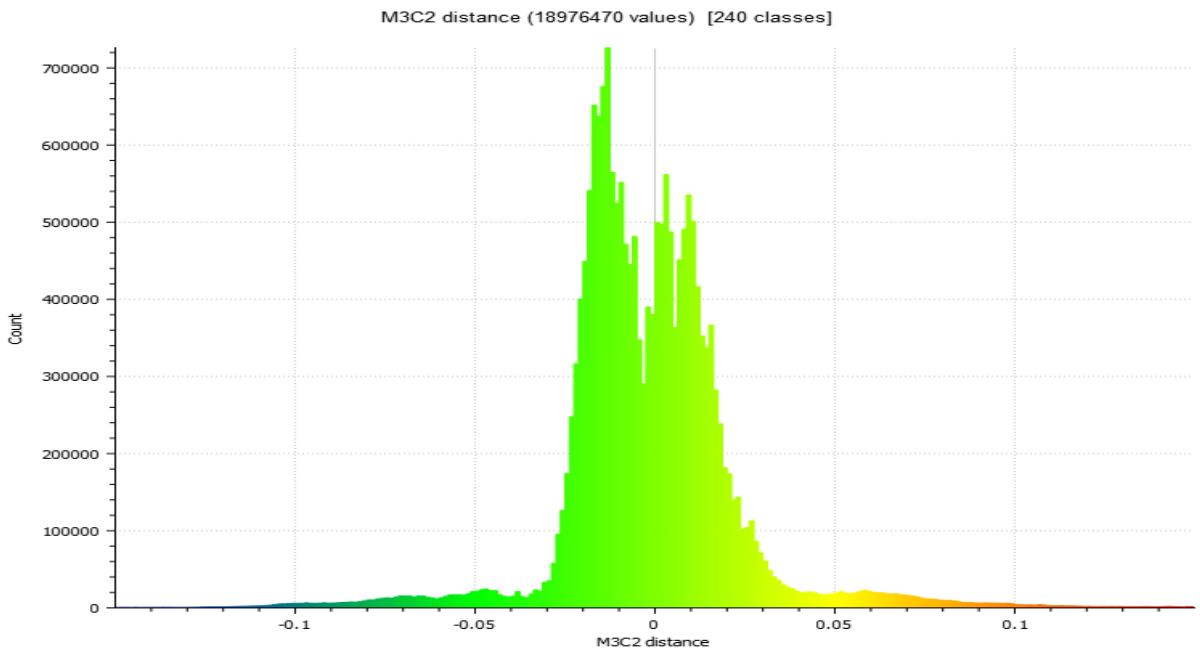

Figure 120. Graph. N wall histogram of M3C2 "signed" distances (m), between LiDAR and Photogrammetry, [N-FTL vs N-MHP]

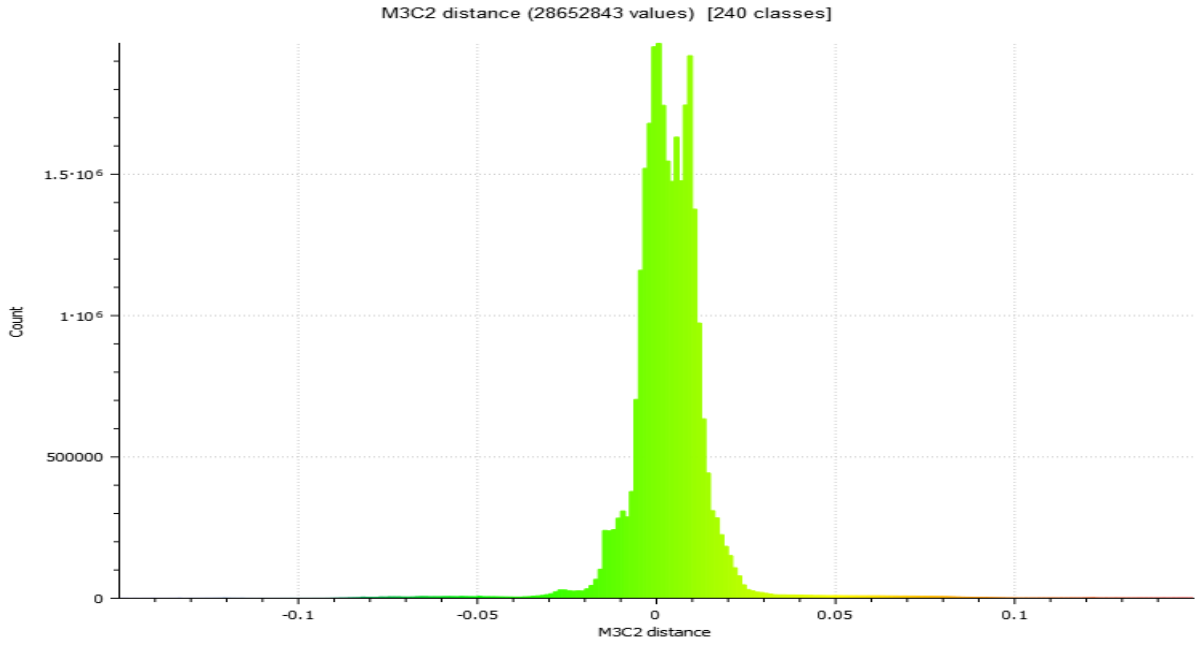

Figure 121. Graph. S wall histogram of M3C2 "signed" distances (m), between LiDAR and Photogrammetry, [S-FTL vs S-MHP]

Analysis of M3C2 CDFs at B3-Sandersville

For both North (solid line) and South (traced line) walls, Figure 122 shows the CDF of M3C2 "signed" distances (or ±PDs), between the point-cloud models generated by the LiDAR-based FTL technique and the photogrammetric-based MHP approach. Each CDF curve in that figure assists in visualizing the probability that M3C2 "signed" distances (or ±PDs), between the FTL and MHP models, be at a certain range, for one of the two MSE walls (N or S) at this bridge. The x-axis represents the "signed" distances measured by the elaborated M3C2 algorithm, and the y-axis indicates the probability that "signed" PDs take on a value less than or equal to a given value x. This statistical representation allows for a clear comparison of the agreement level between the two modeling techniques. A steeper CDF curve indicates smaller dispersion and stronger alignment between LiDAR and photogrammetric measurements.

Since in the previous analysis of C2C "absolute" distances (PDs), the discrepancy range was selected between 0 and 150 mm, now for proper comparison, in the analysis of M3C2 "signed" distances (±PDs), the range was also selected from -150 mm to +150 mm. Additionally, since in the C2C "absolute" analysis, the maximum magnitude of discrepancies with a 95% probability of occurrence was determined, now in the M3C2 "signed" analysis, that 95% probability has to be considered between the 2.5% and 97.5% levels. Accordingly, for the N wall, Figure 122 indicates a 95% probability that all ±PDs are in the [-53.9 mm, +57.8 mm] interval. Similarly, for the S wall that 95% probability corresponds to the [-15.7 mm, +22.3 mm] interval. After translating those ranges to maximum "absolute" magnitudes, the following two statements result: (i) For the N wall, there is a 95% probability that the magnitudes of all position discrepancies, between the FTL and

MHP models, be equal or less than 57.8 mm. Similarly, for the S wall, that amplitude is equal or less than 22.3 mm.

The above values contrast with those obtained in the previous C2C “absolute” distance analysis, 42.2 mm and 39.2 mm, respectively (see Figure 117). The differences presented by the C2C and M3C2 schemes are due to the distinct algorithms employed by each of them. In general, the M3C2 algorithm can detect and measure smaller, normal-to-surface deviations, and it is designed to be more resilient to noise in the point clouds. It uses a local neighborhood approach and normal estimation to filter out some of the noise effects and better identify the underlying discrepancies.

As observed in previous analyses, the FTL method is more accurate than the MHP approach. This is confirmed by the M3C2 scheme which indicated 95% probability of attaining positional discrepancies magnitudes equal or less than 57.8 mm for the N wall, and equal or less than 22.3 mm, for the S wall, between the FTL and MHP modeling techniques.

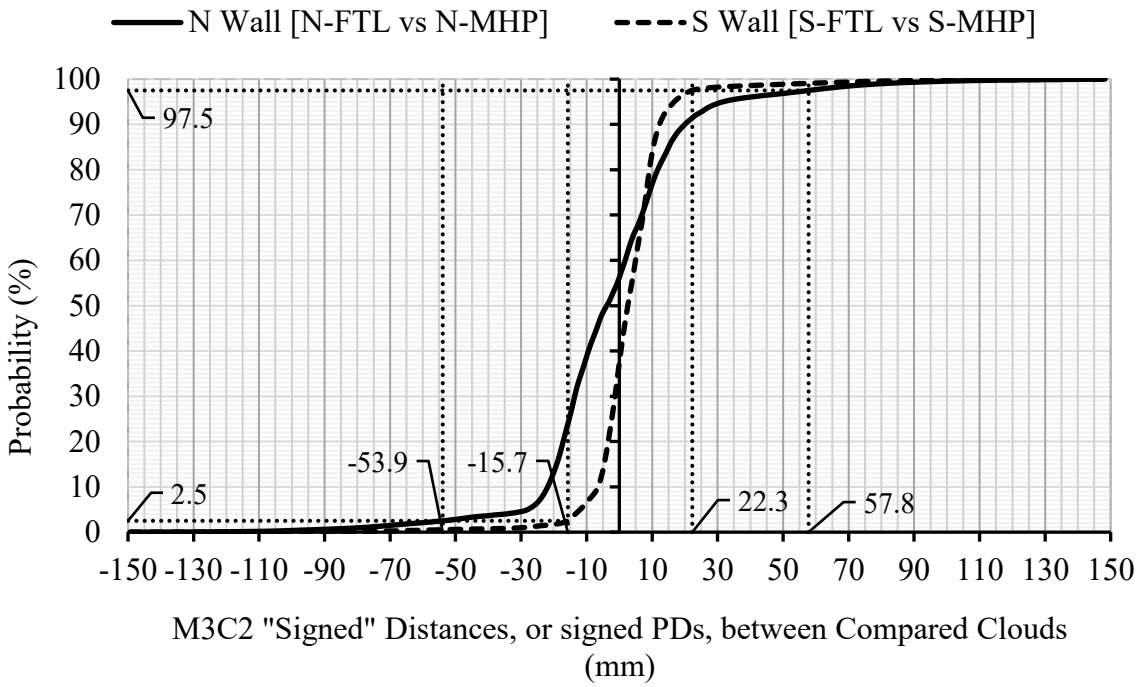

Figure 122. Graph. Cumulative distribution function of M3C2 “signed” distances, between the FTL and MHP techniques.

CHAPTER 10. RESUTLS AT BRIDGE B4-KING GEORGE

Bridge B4 – King George is equipped with two MSE walls, one at each abutment. The research conducted at this site focused on generating high-fidelity 3D virtual models to assess their effectiveness in capturing the spatial configuration of the MSE walls with precision. Unlike the CW or Bridge B2 – Old River, this location was surveyed only during a single data acquisition period, Epoch 1, conducted during the Summer 2024 academic term. As such, temporal displacement tracking was not feasible. Instead, the emphasis was placed on evaluating the relative accuracy and geometric consistency of the generated models by comparing them with high-precision field measurements obtained using a RTS. Two primary modeling techniques were employed during this field campaign: (i) static terrestrial LiDAR and (ii) CRP using a handheld DSLR camera. For LiDAR scanning, a total of 16 scans were performed using Leica's ScanStation P50. Spherical targets were mounted on six GCPs, and both TB and Visual-Alignment (VA) registration techniques were used in Cyclone Core to align the individual scans into unified models. These were then georeferenced into a local coordinate system established via a precisely measured closed traverse, using the Leica TCRP 1201+ RTS. The resulting LiDAR datasets were designated TBL1 and VAL1 (visual alignment), both representing Epoch 1. RTS-derived checkpoint coordinates were labeled RTS1 and served as the benchmark reference for all model discrepancy analyses.

Photogrammetry was also conducted at this site using a Nikon D5300 DSLR camera. A total of 2,449 images were captured and processed using Agisoft Metashape. The photogrammetry model was created following established best practices: high image overlap (>80%), consistent focal length, and a structured coverage of the full wall surfaces. Unlike other sites, UAVs were not used

at this location due to insufficient clearance beneath the overpass to ensure safe flight operations. The photogrammetric point cloud was subsequently georeferenced to the same local coordinate system established for the RTS and LiDAR datasets, ensuring comparability across platforms. This dataset was designated as MS1. A total of 16 CPs (8 per MSE wall) were installed and measured using the RTS and extracted from the georeferenced point clouds of each model. These CPs formed the basis for conducting PD and DD analyses. A total of 120 unique pairwise distances between CPs were evaluated in the DDs analysis.

Since only one epoch of data was collected at this site, all observed discrepancies between RTS1 and the virtual models (TBL1, VAL1, and MS1) were interpreted as indicative of modeling accuracy, rather than structural deformation. These discrepancies could result from field-related uncertainties (such as leveling errors, imperfect instrument alignment, or environmental conditions) or postprocessing limitations (such as scan stitching accuracy, GCP detection quality, or photogrammetric image matching variability). The following sections provide detailed descriptions of the survey configuration, processing workflows, and results of the PD and DDs analyses for Bridge B4-King George.

LOCAL SYSTEM OF REFERENCE AT B4 – KING GEORGE

At this bridge site, a 6-sided polygonal closed traverse was established and rigorously balanced to serve as a local system of reference for all subsequent measurements and 3D modeling tasks. The precise, one-second RTS instrument (Leica TCRP 1201+) was employed to complete the traverse, which consisted of six vertices labeled A, B, C, D, E, and F. Each internal horizontal angle was measured twice and balanced both locally—against the corresponding external angle—and globally,

ensuring that the sum of all interior angles matched the theoretical closure for a hexagon. To reduce longitudinal error, horizontal distances were adjusted using the Compass (Bowditch) rule. In addition to horizontal and angular measurements, the Topcon AT-B2 auto level instrument was used to determine the relative elevations of the GCPs. This leveling process established vertical relationships between all traverse stations. Each vertical angle was measured twice, and the averaged values were used to compute elevations. The total vertical error of closure was then distributed proportionally among the vertices, based on the relative horizontal distances between consecutive points and the total perimeter of the traverse.

Appendix A presents the traverse and elevation calculation details for this bridge. Figure 123 shows an aerial view (not to scale) of Bridge B4 – King George, illustrating the approximate location of the six traverse vertices (the GCPs). Figure 124 displays the relative horizontal positions of those GCPs and their corresponding local coordinates (Easting and Northing) in feet. As with other bridge sites, the local North direction approximates true North but is not exactly aligned; nonetheless, the reference North is shown in the upward direction of the figures.

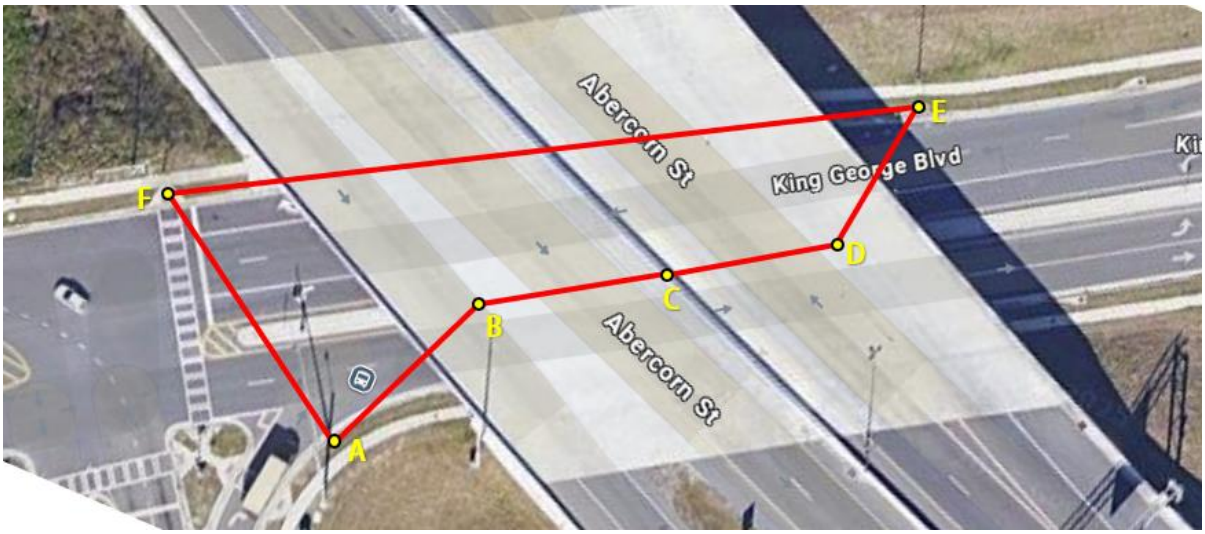

Figure 123. Photo. Aerial view of 7-sided closed traverse near B4-King George

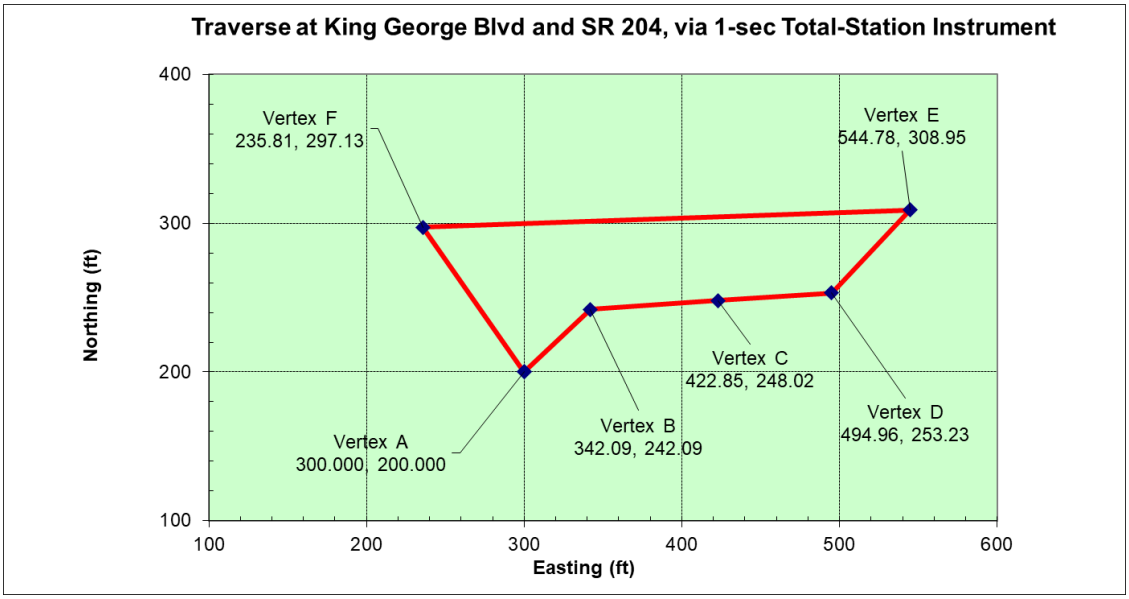

Figure 124. Graph. Horizontal coordinates of 7-sided closed traverse near B4–King George

Table 47 presents a summary of the characteristics of the resulting traverse calculations, completed in summer 2024, including their errors of closure and attained longitudinal precision. That precision, 1: 31,601, is well in excess to the one indicated by GDOT Survey Manual, 1:20,000 (GDOT, 2022). Table 48 shows the resulting local spatial coordinates (X, Y, Z) of all 6 GCPs.

Table 47. Characteristics of 6-sided, closed traverse at B4– King George

Traverse at Bridge	Perimeter	Total Horizontal Angular Error of Closure	Attained Longitudinal Precision	Elevation Error of Closure
	ft ; [m]	seconds	Ratio	ft ; [mm]
King George	713.17; 217.37	+1.5	1/31601	0.023; 7.01

Table 48. Local spatial coordinates of six GCPs at B4– King George

GCPs	Easting (ft)	Northing (ft)	Elevation (ft)
	X	Y	Z
A	300.00	200.00	100.00
B	342.09	242.09	100.25
C	422.85	248.02	98.19
D	494.96	253.23	96.59
E	544.78	308.95	95.16
F	235.81	297.13	101.04

CHECKPOINTS AT B4 – KING GEORGE

A total of 16 CPs were established eight on each of the two MSE walls (Northwest and Southeast) to support displacement detection and model validation. Each CP was marked using a black-and-white circular sticker, 6 inches in diameter. The CPs were arranged in vertical pairs, with each pair consisting of one checkpoint near the upper portion of the wall and another at the lower portion. These pairs were spatially distributed from the start to the end of the wall to ensure even coverage and accurate representation of any movement across the structure. On the Northwest wall, the CPs were labeled: NW1U, NW1D, NW2U, NW2D, NW3U, NW3D, NW4U, NW4D, and on the Southeast wall, the CPs were labeled: SE5U, SE5D, SE6U, SE7U, SE8U, SE8D. Here, the suffix “U” denotes the upper CP and “D” denotes the lower CP in each vertical pair. Figure 125 illustrates a sample of the CPs and GCPs as marked on the MSE walls at Bridge 3 – King George Blvd.

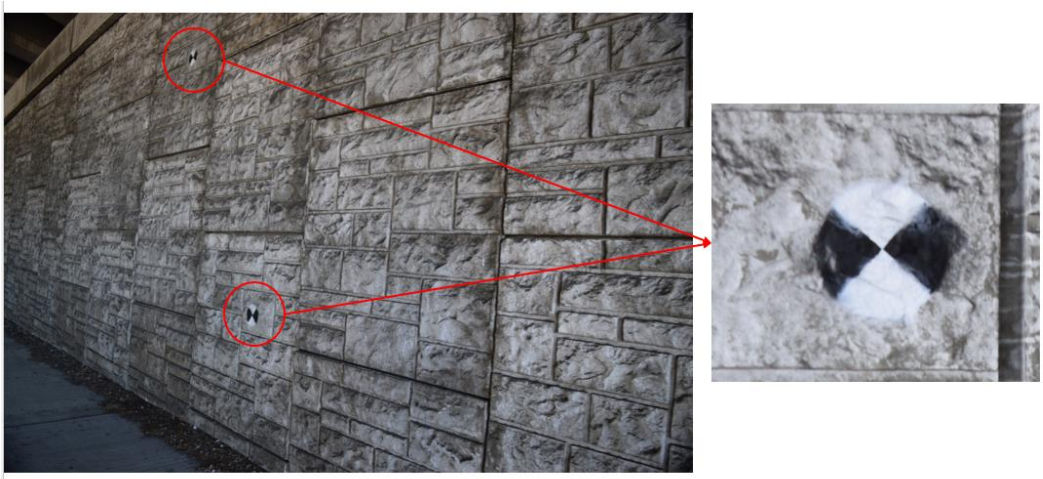

Figure 125. Photo. Painted CPs on MSE wall at B4 – King George

During the summer of 2024 (Epoch 1), these 16 CPs were surveyed using the Leica TCRP 1201+RTS. For each CP, observations were taken from two different GCPs (used alternately as station and backsight), and the resulting local coordinates were averaged to ensure precision and reliability. These are referred to as the RTS1 values, which serve as the benchmark dataset for evaluating the spatial accuracy of 3D models created via LiDAR and photogrammetry. Since this site was only assessed in a single epoch, no RTS2 dataset was generated, and no temporal displacement analysis was conducted. Table 49 below summarizes the RTS-derived local coordinates for the 16 CPs across both walls.

Table 49. RTS Coordinates of 16 CPs at B4– King George

Wall	Check Points	Easting (ft)	Northing (ft)	Elevation (ft)
		Y	X	Z
Northwest	**NW1 U**	303.013	308.986	110.835
	NW1 D	299.451	308.757	103.288
	NW2 U	339.635	311.678	109.668
	NW2 D	338.659	311.547	101.937
	NW3 U	382.080	314.817	109.488
	NW3 D	377.302	314.413	102.008
	NW4 U	424.115	317.856	108.394
	NW4 D	426.790	317.916	99.660
Southeast	**SE5 U**	506.829	207.472	105.945
	SE5 D	504.668	207.397	100.345
	SE6 U	464.814	204.380	105.721
	SE6 D	465.708	204.548	100.189
	SE7 U	422.827	201.298	107.583
	SE7 D	421.540	201.365	100.736
	SE8 U	384.951	198.421	109.653
	SE8 D	380.147	198.335	102.124

LIDAR MODELS FOR EPOCH 1 AT B4 – KING GEORGE

At B3-King George site, a pair of 3D point cloud models were created during Epoch 1 (Summer 2024) using static. One model was processed using TB registration, and the other using Visual-Aligned (VA) registration. These models were used to document the geometry of the MSE walls and to evaluate spatial accuracy against benchmark coordinates acquired from RTS measurements. Since only a single data acquisition epoch was conducted at this site, inter-epoch displacement analysis was not applicable; however, accuracy evaluation was still conducted using RTS1 field data. Data collection was performed using a Leica P50 laser scanner at six scanning stations. During fieldwork, a total of six spherical targets a mix of 9-inch and 6-inch white spheres were mounted on vertical poles and placed precisely at each of the six GCPs. These targets were all captured in every scan. For the TB model, registration in Cyclone Core software utilizes all six

targets for alignment, ensuring high accuracy through a least-squares-based target matching process. For the VA model, visual and geometric alignment between overlapping scan areas was used instead, applying a C2C matching strategy without relying on targets.

Both registration workflows resulted in a full 3D model georeferenced to the local coordinate system established from the closed traverse of RTS measurements. This alignment ensured that the coordinate frames of both TB and VA models were consistent with RTS-derived spatial data. From each point cloud, the coordinates of 16 CPs, eight placed on the Northwest wall and eight on the Southeast wall were extracted. The datasets from the TB and VA models are referred to as TBL1 and VAL1, respectively. These were compared to the RTS1 benchmark coordinates through PD and DD analyses, quantifying the performance of each registration method in reproducing known control geometry. Figure 126 and Figure 127 display the TB and VA LiDAR point cloud models generated for Epoch 1 at Bridge 3 – King George Blvd.

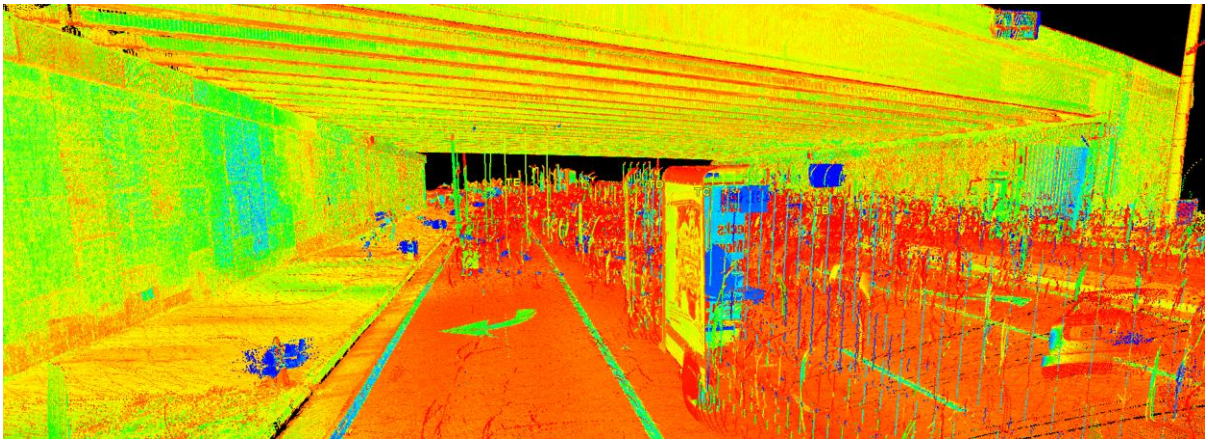

Figure 126. Photo. TB LiDAR point cloud of Epoch 1 for MSE walls at B4 – King George

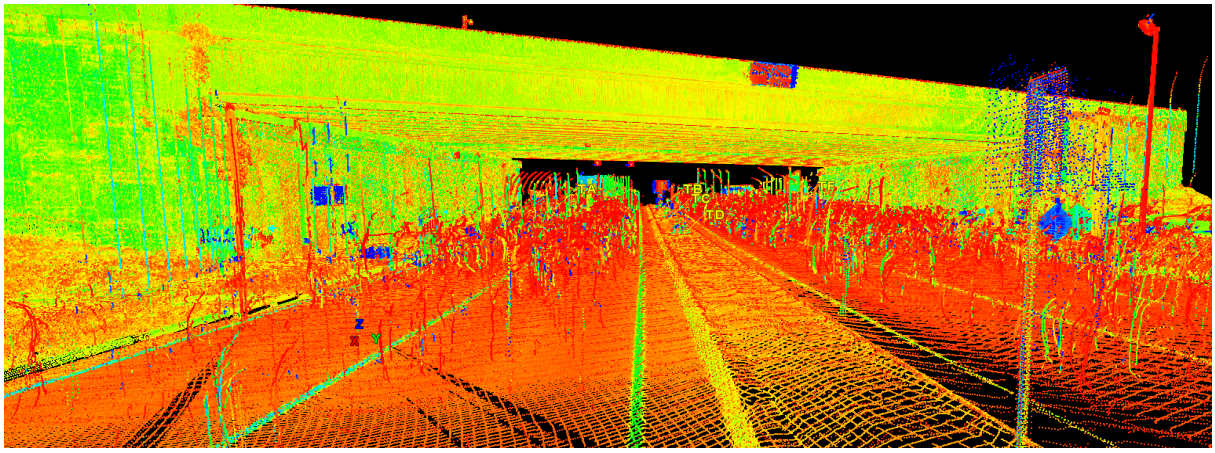

Figure 127. Photo. VA LiDAR point cloud of Epoch 1 for MSE walls at B4 – King George

PD Analyses: [TBL1 VS RTS1], [VAL1 VS RTS1]

At King George, a thorough evaluation of PD was carried out to assess the spatial precision of LiDAR-derived checkpoint coordinates from Epoch 1. This analysis involved two distinct LiDAR models: one registered via the TB approach (TBL1) and the other using the VA method (VAL1). Both models were benchmarked against field-measured coordinates acquired with the Leica TCRP 1201 plus RTS, designated as the reference dataset (RTS1). For each of the twelve CPs situated on the north and south MSE walls, a position vector was determined using both the LiDAR and RTS data. The discrepancy vector for each checkpoint was then derived by subtracting the RTS1 coordinates from the respective LiDAR model coordinates. The magnitudes of these vectors were subsequently computed to quantify the PD values. A comprehensive summary of the PD statistics for both the TBL1 and VAL1 models is presented in Table 50 and Figure 128. For the TBL1 model, the observed minimum discrepancy was 1.74 millimeters, while the maximum reached

8.17 millimeters. The mean discrepancy for TBL1 was calculated at 4.73 millimeters, with a RMSV of 5.29 millimeters. In contrast, the VAL1 model exhibited a mean discrepancy of 5.88 millimeters and an RMSV of 6.18 millimeters, with its discrepancies ranging from a minimum of 3.37 millimeters to a maximum of 9.69 millimeters. The mean difference of 1.16 mm and RMSV difference 0.90 mm suggest moderate advantage of TB registration in achieving tighter spatial alignment with RTS benchmarks. While both registration methods yielded comparable performance, the TBL1 model demonstrated slightly superior overall accuracy, as evidenced by its marginally lower mean and RMSV values. These findings suggest that both registration techniques can produce acceptable outcomes for structural documentation. Nevertheless, the TB method exhibits a slight edge in accuracy across all CPs, which could prove advantageous in scenarios demanding high repeatability or were critical monitoring decisions hinge on consistent precision.

Table 50. Position discrepancies of 16 CPs comparing TB and VA LiDAR models (Epoch 1) against RTS field measurements (Epoch 1)

Epoch 1: LiDAR vs RTS1 (mm)							
LiDAR Values	Min	Max	Mean	Median	STD-S	STD-P	RMSV
[TBL1-RTS1]	1.74	8.17	4.73	4.62	2.02	1.96	5.29
[VAL1-RTS1]	3.37	9.69	5.88	5.68	1.97	1.90	6.18
Differences: {[TBL1-RTS1] – [VAL1-RTS1]} (mm)							
{[TBL1-RTS1] – [VAL1-RTS1]}	1.63	1.52	1.16	1.06	0.06	0.06	0.90

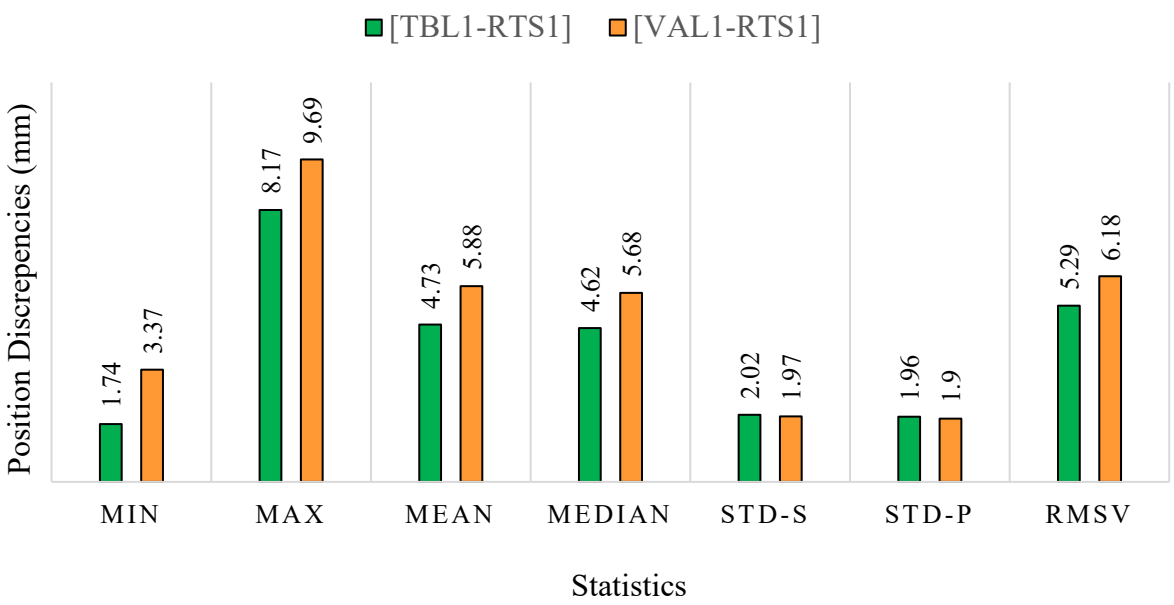

Figure 128. Chart. Position discrepancies of 16 CPs: TB and VA LiDAR models vs. RTS measurements (Epoch 1) at B4-King George

Assuming the displacement errors follow a Gaussian distribution, approximately 95% of the errors are expected to lie within the interval $\mu \pm 1.96\sigma$, where μ is the mean and σ is the standard deviation. For the models shown in Figure 114 & 120 the 95% confidence intervals are:

For [TBL1-RTS1]: = {4.74 - 1.96×1.96, 4.74 + 1.96×1.96} = {0.90 mm, 8.58 mm}

For [VAL1-RTS1]: = {5.88 - 1.96×1.90, 5.88 + 1.96×1.90} = {2.16 mm, 9.60 mm}

For [ML1-RTS1]: = {18.2 - 1.96×4.30, 18.2 + 1.96×4.30} = {9.77 mm, 26.63 mm}

By comparing the models based on the upper bound of their 95% confidence intervals, representing the maximum expected error TBL1 demonstrates a slightly lower noise level (8.58 mm) than VAL1 (9.60 mm). But the ML1 models showed a greater noise level of 26.63 mm. These upper limits

provide practical estimates of the positional uncertainty inherent in each modeling approach and can aid in selecting the most suitable technique for applications that demand high measurement precision.

DD Analyses: [TBL1 VS RTS1], [VAL1 VS RTS1]

In addition to the PD evaluation, DD analyses were performed to quantify the accuracy of relative distances between CPs. A total of 120 non-repeated (unique) distances were computed among the 16 CPs marked on the MSE walls. These distances were extracted from two LiDAR models, one registered using the TB method (TBL1) and the other using the VA method (VAL1). Each were compared against field-measured RTS1 values.

For any pair of CPs, *P* and *Q*, their respective coordinates are (x_p, y_p, z_p) and (x_q, y_q, z_q). The distance *PQ* between them is calculated by using the three-dimensional Euclidean formula:

$$PQ = \sqrt{(x_p - x_q)^2 + (y_p - y_q)^2 + (z_p - z_q)^2}$$

Initially, these distances were computed using RTS-derived coordinates, resulting in benchmark values denoted as PQ_{RTS}. Subsequently, the same distances were calculated using coordinates extracted from a point-cloud model, yielding corresponding values PQ_{Mod}. The discrepancy between each pair was then evaluated as:

$$\text{DD= } DD = PQ_{Mod} - PQ_{RTS}$$

Note that DDs can be either positive or negative, reflecting slight overestimations or underestimations by the model. With 16 CPs placed on the walls, a total of 120 non-repeated (unique) pairwise distances were computed among them. Accordingly, for each model, 120 DDs were quantified relative to the benchmark RTS measurements. Since the number of distances is relatively high (120), the mean values help indicate systematic shifts while the standard deviations reflect the dispersion of those discrepancies, and the RMSV indicates a measure of the discrepancy magnitude.

Table 51 and Figure 129 summarizes the statistical outcomes of the PD analysis conducted at B4 – King George for Epoch 1. The comparison between the TBL1 (TB LiDAR) model and RTS1 revealed a mean PD of -1.10 mm, with a maximum deviation of 8.18 mm and an RMSV of 3.76 mm. The VAL1 (Visual-Aligned LiDAR) model showed a slightly improved mean discrepancy of 0.90 mm, a maximum of 9.56 mm, and an RMSV of 3.82 mm. While both models exhibited similar statistical patterns, the VAL1 model demonstrated marginally better median accuracy (–1.68 mm vs –2.14 mm) and slightly lower standard deviations in both spatial (STD-S = 3.74 mm) and projected (STD-P = 3.71 mm) metrics, compared to TBL1 (STD-S = 3.62 mm, STD-P = 3.59 mm). The difference row in Table 51 representing the metric-wise subtraction of VAL1 values from TBL1 shows minor differences across all categories, with the largest delta being –1.38 mm in the maximum discrepancy. At the King George site, both TB and visual-aligned registrations produced comparably accurate LiDAR models relative to the RTS benchmark. Although the TBL1 model displayed slightly more consistent performance in terms of RMSV, the VAL1 model achieved better alignment in mean and median discrepancy values. These

results suggest that VA, when executed with sufficient scan overlap and careful registration, can rival traditional TB approaches in accuracy and reliability for structural monitoring of MSE walls.

Table 51. DDs of 16 CPs comparing TB and VA LiDAR models (Epoch 1) against RTS field measurements (Epoch 1)

Epoch 1: LiDAR vs RTS1 (mm)							
LiDAR Values	Min	Max	Mean	Median	STD-S	STD-P	RMSV
[TBL1-RTS1]	-6.49	8.18	-1.10	-2.14	3.62	3.59	3.76
[VAL1-RTS1]	-6.80	9.56	-0.90	-1.68	3.74	3.71	3.82
Differences: {[TBL1-RTS1] – [VAL1-RTS1]} (mm)							
{[TBL1-RTS1] – [VAL1-RTS1]}	0.31	-1.38	-0.2	-0.46	-0.12	-0.12	-0.06

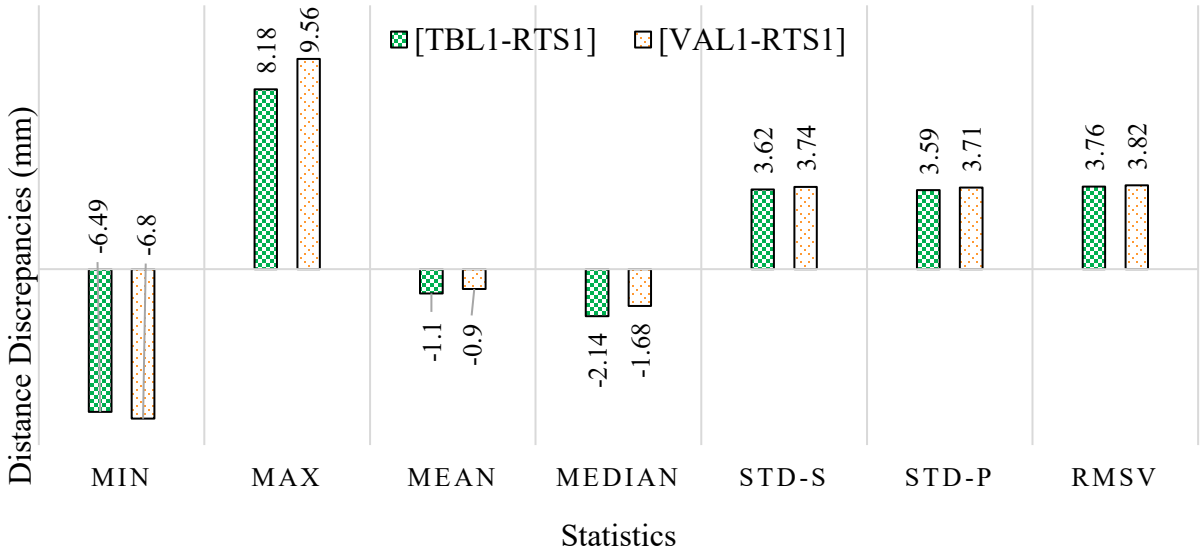

Figure 129. Chart. DDs of 16 CPs: LiDAR TB and VA models vs. RTS measurements (Epoch 1) at B4 - King George.

Assuming the displacement errors follow a Gaussian distribution, approximately 95% of the errors are expected to lie within the interval $\mu \pm 1.96\sigma$, where μ is the mean and σ is the standard deviation. For the models shown in Figure 128 and 121, the 95% confidence intervals are:

For [TBL1-RTS1]: = {-1.1 - 1.96×3.59, -1.1 + 1.96×3.59} = {-8.14 mm, 5.94 mm}

For [VAL1-RTS1]: = {-0.9 - 1.96×3.71, -0.9 + 1.96×3.71} = {-8.17 mm, 6.37 mm}

For [ML1-RTS1]: = {1.0 - 1.96×6.10, 1.0 + 1.96×6.10} = {-10.95 mm, 12.96 mm}

When ranking the models based on the magnitude of their upper bound (i.e., maximum expected error at 95% confidence), TBL1 exhibits a slightly lower noise level of 8.14 mm, compared to 8.17 mm for VAL1. On the other hand, ML1 shows a higher noise level of 12.96 mm compared to the LiDAR models. These values serve as useful estimates of the positional uncertainty or noise associated with each modeling technique and can inform the selection of appropriate methods for precision-critical applications.

Figure 130 illustrates the DDs between the 16 RTS1 CPs and the corresponding distances derived from the TBL1 and VAL1 (visual-aligned) LiDAR models at B4 – King George during Epoch 1. A total of 120 distance measurements is plotted against their respective RTS1 distances. The discrepancies for both methods generally cluster near the zero line, indicating acceptable alignment with the RTS benchmark. However, TBL1 (orange squares) exhibits slightly tighter grouping around zero, particularly in the mid- to far-range distances (30–70 m), suggesting more consistent geometric performance across varying distances. In contrast, VAL1 (blue diamonds) displays slightly more scatter and a few noticeable outliers in the closer range (0–20 m), indicating less stability in those regions. Both models show a mild negative trend, as depicted by their respective regression lines, implying a small distance-dependent bias where discrepancies slightly increase (negatively) with greater RTS1 distances. Notably, TBL1's trend line is flatter, reinforcing its more uniform performance across the distance spectrum. While both registration techniques demonstrate

strong alignment with RTS measurements, the TB registration (TBL1) performs marginally better in maintaining internal distance consistency across varying measurement ranges. This is especially relevant in applications such as long-term displacement monitoring, where geometric fidelity over longer spans is critical.

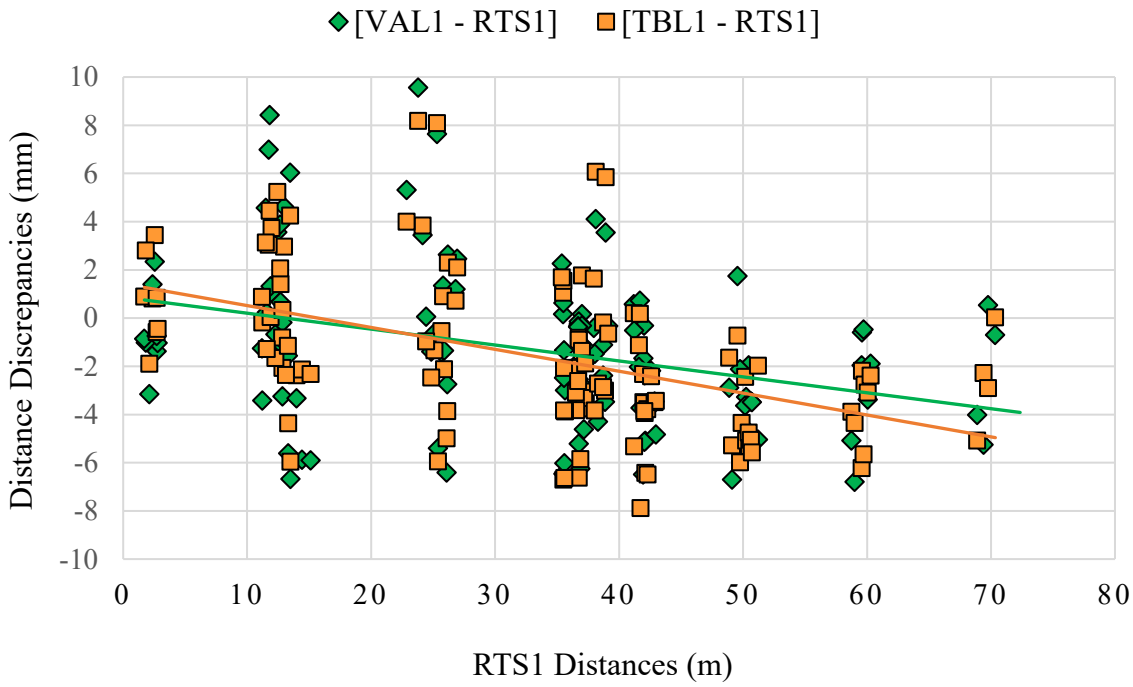

Figure 130. Graph. Sixty-six DDs between TB & VA LiDAR models vs RTS1

PHOTOGRAMMETRY MODEL FOR EPOCH 1 AT B4 – KING GEORGE

At King George, CRP was performed during the summer of 2024 (Epoch 1) using a Nikon D5300 DSLR camera. A total of 2,449 high-resolution images were captured from varying angles and distances to ensure full coverage of both the Northwest and Southeast MSE walls. The imaging campaign was conducted under consistent lighting to minimize surface glare and maximize visual clarity of features.

All six GCPs, established via a Leica TCRP 1201+ RTS and leveled with a Topcon AT-B2 auto level, were used to georeferenced the photogrammetry model. The images were processed in Agisoft Metashape, beginning with photo alignment through the software's structure-from-motion algorithm. This model is called ML1. Common features across overlapping images were identified and matched to generate a sparse point cloud. This was followed by dense point cloud generation, mesh creation, and texture mapping. To ensure spatial consistency with other datasets, the model was scaled and georeferenced using the local coordinates of the six GCPs. Sixteen circular black-and-white checkpoint stickers (8 per wall) were applied to the MSE walls prior to imaging. In the final 3D model, these CPs were manually identified, and pinpoints were placed at their centers to extract local coordinates. These photogrammetry-derived checkpoint coordinates were then compared to the field-measured RTS values (RTS1) to evaluate spatial accuracy. The analysis involved calculating PD and DD metrics for each checkpoint. The comparison results provided insight into the reliability of DSLR-based photogrammetry for structural monitoring. Figure 131 shows the resulting Metashape 3D point cloud for B4 – King George Blvd.

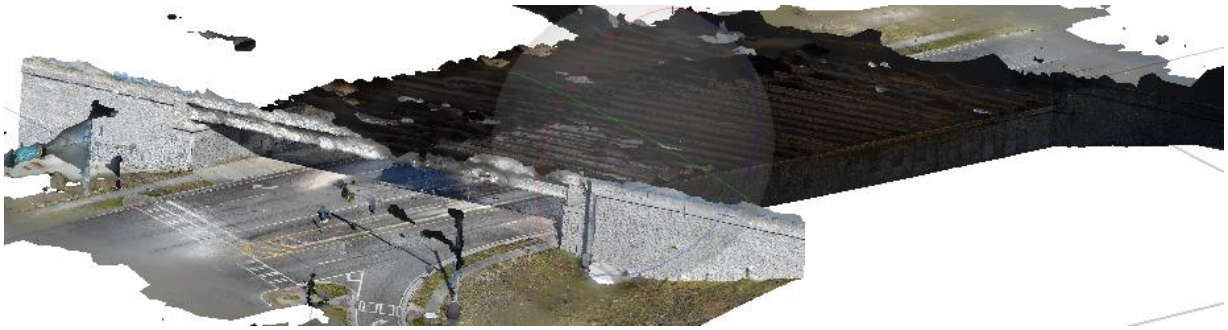

Figure 131. Photo. Agisoft's Metashape 3D photogrammetry model of B4 – King George

Checkpoint Local Coordinates from Metashape Model

After processing the CRP images in Agisoft Metashape and georeferencing the model using the local coordinate system established by the RTS-derived GCPs, the spatial coordinates of sixteen CPs (eight on each MSE wall) were extracted. Each checkpoint, identified by a circular black-and-white target applied during field preparation, was manually located in the 3D model. A pinpoint was placed at the center of each marker to obtain its Easting, Northing, and Elevation values. Figure 132 illustrates an example of the coordinate extraction process within the Metashape environment. Table 52 summarizes the full set of local coordinates for all sixteen CPs. These values served as the photogrammetry-derived dataset for comparison against RTS1 benchmark coordinates, enabling PD and DD evaluations to assess the spatial accuracy of the Metashape model.

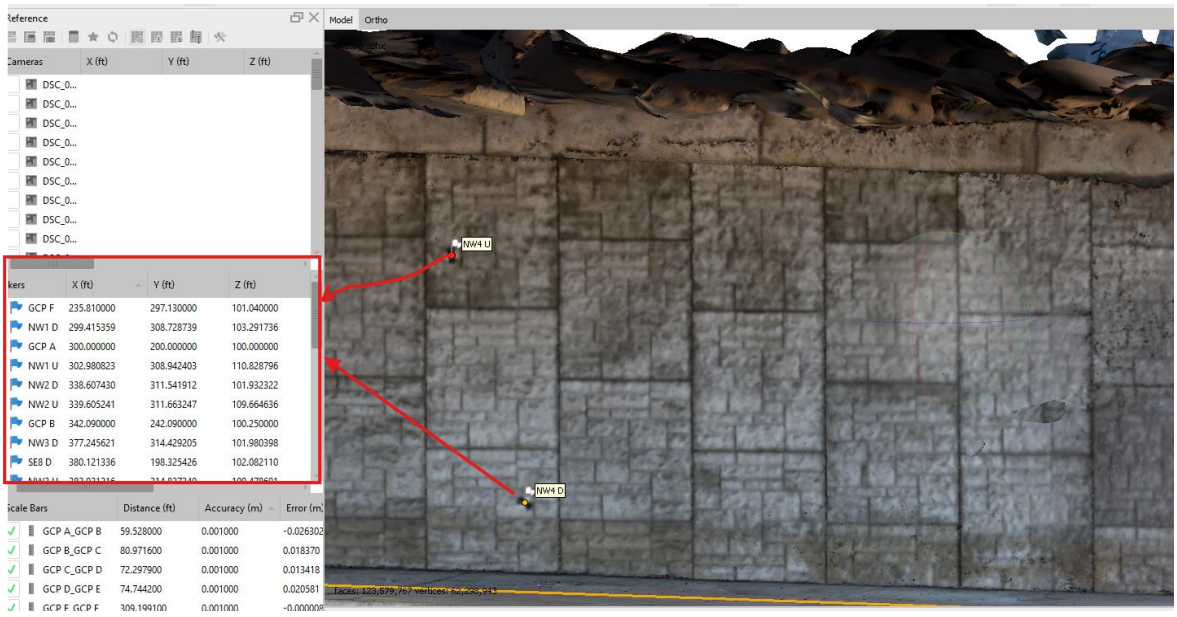

Figure 132. Photo. Extracting local coordinates of a checkpoint from the 3D photogrammetry model of B4 – King George

Table 52. Local coordinates of CPs from model generated in Metashape

Wall	CPs	Easting (ft) X	Northing (ft) Y	Elevation (ft) Z
NORTHWEST	**NW1 U**	302.981	308.942	110.829
	NW1 D	299.415	308.729	103.292
	NW2 U	339.605	311.663	109.665
	NW2 D	338.607	311.542	101.932
	NW3 U	382.021	314.827	109.479
	NW3 D	377.246	314.429	101.980
	NW4 U	424.059	317.859	108.374
	NW4 D	426.737	317.928	99.664
SOUTHEAST	**SE5 U**	506.813	207.466	105.871
	SE5 D	504.643	207.392	100.272
	SE6 U	464.779	204.365	105.667
	SE6 D	465.670	204.547	100.125
	SE7 U	422.783	201.281	107.529
	SE7 D	421.500	201.368	100.702
	SE8 U	384.896	198.426	109.580
	SE8 D	380.121	198.325	102.082

PD Analyses: [ML1 vs RTS1]

At King George, a PD analysis was carried out to assess the spatial accuracy of the 3D photogrammetry model generated in Agisoft Metashape (ML1). Both the photogrammetry data and the reference dataset from the Leica TCRP 1201+ RTS1 were collected during a single epoch in Summer 2024. A total of sixteen CPs—eight on the northwest wall and eight on the southeast wall were analyzed. Coordinates were extracted from the georeferenced MS1 model, and for each checkpoint, a discrepancy vector was calculated by subtracting RTS1 coordinates from ML1 coordinates. The magnitudes of these vectors represent the PD values. The statistical summary of the PDs is shown in Figure 133. The minimum and maximum discrepancies were 9.97 mm and 27.75 mm, respectively. The mean PD was 18.19 mm, and the median was 18.25 mm. The standard

deviations for the sample (STD-S) and population (STD-P) were 4.41 mm and 4.27 mm, respectively. The RMSV was calculated as 19.15 mm. These results indicate moderate positional accuracy for the Metashape model. While it does not match the precision of RTS or TB LiDAR approaches, the photogrammetry model remains effective for documentation, general inspections, and non-critical monitoring applications.

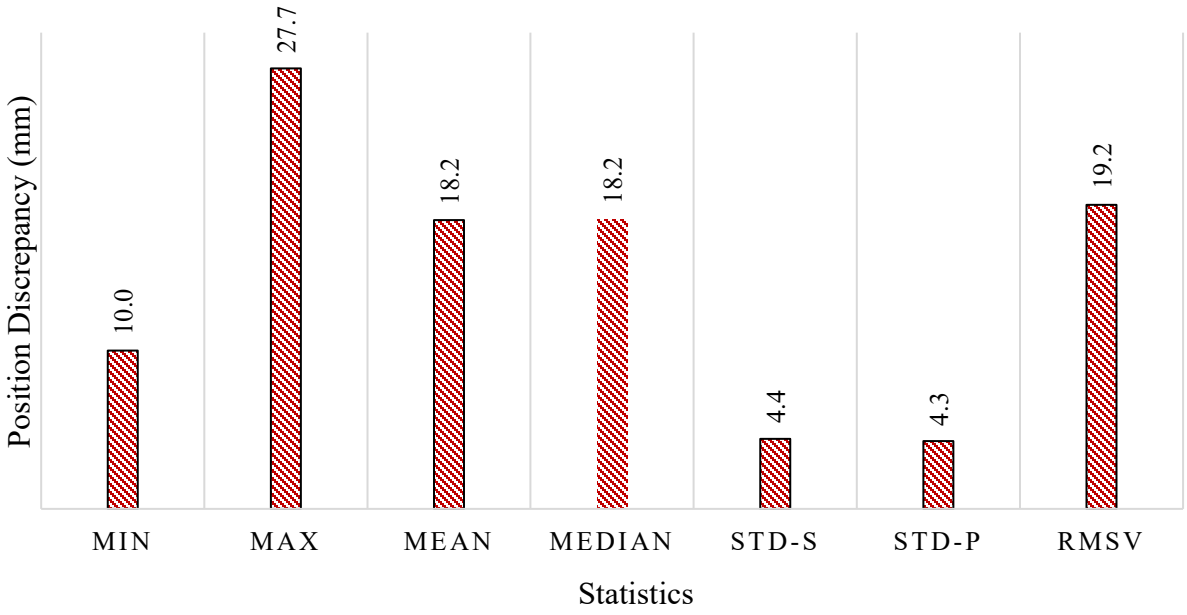

Figure 133. Chart. Position discrepancies of 16 CPs: Metashape (ML1) Model vs. RTS measurements (Epoch 1) at King George

DD Analysis: [Ml1 vs RTS1]

To complement the PD assessment, a DD analysis was conducted to evaluate the internal geometric fidelity of the ML1 produced using Agisoft Metashape at B4 – King George Blvd. This analysis involved calculating all 120 non-repeated pairwise distances between the 16 CPs distributed across the two MSE walls. The distances derived from the ML1 model were then compared to those obtained from the RTS1 during the same epoch. By analyzing the differences between these paired

distances, the study assessed how accurately the photogrammetry model preserved the spatial relationships among CPs. This evaluation is particularly relevant for understanding the model's reliability in structural monitoring applications where relative measurements are critical. For any pair of CPs *i* and *j*, the spatial distance $Dist_{ij}$ was calculated using the Euclidean formula in equation 21:

$$Dist_{ij} = \sqrt{(x_i - x_j)^2 + (y_i - y_j)^2 + (z_i - z_j)^2} \qquad (21)$$

Where (x_i, y_i, z_i) and $(x_j, y_j, z_j)$are the local coordinates of the CPs derived from each respective dataset (ML1 and RTS1). The resulting distances from the ML1 model were then subtracted from the corresponding RTS1 distances to calculate the DDs. These values indicate how well the internal spacing between points is preserved in the Metashape model. Positive values suggest overestimation, while negative values suggest underestimation.

Table 53 and Figure 134 presents the statistical summary of DD analysis between the photogrammetry model (MS1) generated via Agisoft Metashape and the RTS1 benchmark distances for the 66 non-repeated checkpoint pairs at B4 – King George Blvd. The minimum discrepancy was –15.82 mm, and the maximum was 13.76 mm, reflecting moderate spread in relative distance accuracy. The mean and median discrepancies were –0.60 mm and –0.99 mm, respectively, suggesting a slight tendency for underestimation. Standard deviations were approximately 6.29 mm, and RMSV was 6.28 mm. These values indicate relatively consistent internal geometry, with low noise and minor bias. Compared to UAV-based photogrammetry, this DSLR-based model using

Metashape demonstrates better internal fidelity, making it more suitable for detecting subtle structural displacements when high-precision GNSS is not available.

Table 53. DDs of 16 CPs comparing Photogrammetry models (Epoch 1) against RTS field measurements (Epoch 1)

Epoch 1: Photogrammetry vs RTS1 (mm)							
Photogrammetry Values	Min	Max	Mean	Median	STD-S	STD-P	RMSV
[ML1-RTS1] (mm)	-15.82	13.76	0.98	0.77	6.13	6.10	6.18

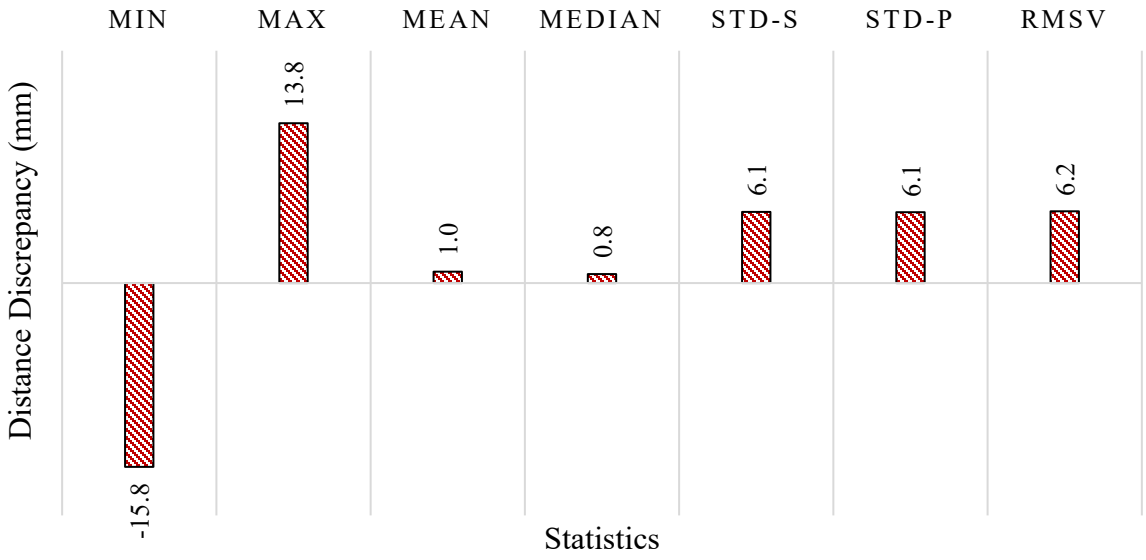

Figure 134. Chart. DDs of 16 CPs: Metashape (ML1) models vs. RTS measurements (Epoch 1) at King George

Figure 135 displays the DDs between checkpoint pairs derived from the ML1 and the RTS1 field measurements at Bridge 3 – King George Blvd. Each blue diamond represents a discrepancy between a checkpoint pair, plotted against the corresponding RTS-measured distance. The

distribution of points appears relatively symmetrical around the zero line, with most discrepancies falling to within 10 mm. The slight upward slope in the trendline suggests a mild distance-dependent overestimation in the ML1 model for longer spans. However, the spread is relatively constrained compared to UAV-based models, indicating that DSLR-based Metashape photogrammetry maintains better internal geometric consistency. While a few outliers exceed ±15 mm, the overall scatter pattern confirms that the model can be considered reliable for moderate-precision applications such as deformation screening and qualitative inspection.

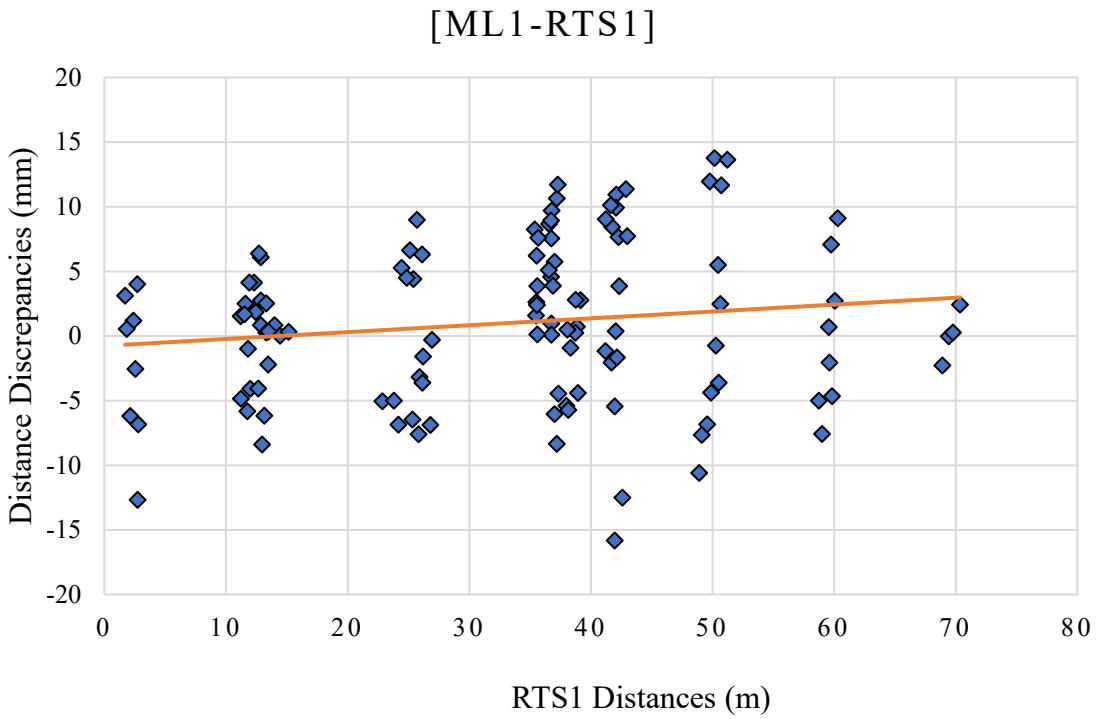

Figure 135. Graph. DDs of 16 CPs: Metashape (ML1) models vs. RTS measurements (Epoch 1) at King George

REFERENCES

Admassu, K. A., Lynch, J., Athanasopoulos-Zekkos, A., Zekkos, D., & Benhamida, B. (2024). "Risk-based asset management framework for highway retaining wall systems using wireless structural health monitoring data." *Advances in Structural Engineering*, 27(16), 2929-2949.

Adamson, D. (2020). "Construction and post-construction deformation analysis of an MSE wall using terrestrial laser scanning and finite element modelling." In Geo-Congress 2020 (pp. 767-777). Reston, VA: American Society of Civil Engineers.

Aldosari, M. D. A. (2019). "Mobile LiDAR for Monitoring MSE Walls with Smooth and Textured Precast Concrete Panels." Doctoral dissertation, Purdue University.

Al-Rawabdeh, A., Aldosari, M., Bullock, D., & Habib, A. (2020). "Mobile LiDAR for scalable monitoring of MSE walls with smooth panels." *Applied Sciences*, 10(13), 4480.

Algadhi, A., Psimoulis, P., Grizi, A., & Neves, L. (2023). "Assessment of accuracy and performance of terrestrial laser scanner in monitoring of retaining walls." In 5th Joint International Symposium on Deformation Monitoring (JISDM 2022) (pp. 467-473). Editorial Universitat Politècnica de València.

Alimohammadi, H., & Memon, A. A. (2023). "A Case Study of MSE Retaining Wall Failure in the State of Tennessee"; Recommendations for Future Design and Constructions.

Allen, T. M., & Bathurst, R. J. (2019). "Geosynthetic reinforcement stiffness characterization for MSE wall design." *Geosynthetics International*, 26(6), 592-610.

Aljagoub, D., & Cheng, C. (2025). "Delamination detection in concrete decks using numerical simulation and UAV-based IRwith deep learning." *Automation in Construction*.

Athanasopoulos-Zekkos, A., Lynch, J., Zekkos, D., Grizi, A., Admassu, K., Benhamida, B., … & Mikolajczyk, M. (2020). "Asset management for retaining walls (No. SPR-1676)". Michigan. Dept. of Transportation. Research Administration.

Bao, S., Fang, X., Bu, H., Yu, X., & Cai, Z. (2025). "Monitoring of the Deformation of Deep Foundation Pit Using 3D Laser Scanning." *Buildings*, 15(8), 1290.

Bathurst, R. J. (2019). "Developments in MSE wall research and design." Paper presented at the International Congress and Exhibition" Sustainable Civil Infrastructures".

Bell, J. R., & Steward, J. E. (1977). "Construction and observation of fabric retained soil walls." In Proceedings of the International Conference on the Use of Fabrics in Geotechnics (Vol. 1, pp. 23-128).

Brutus, O., & Tauber, G. (2009). “Guide to asset management of earth retaining structures.” Washington, DC, USA: US Department of Transportation, Federal Highway Administration, Office of Asset Management. https://onlinepubs.trb.org/onlinepubs/nchrp/docs/nchrp20-07(259)_fr.pdf

Butler, C. J., Gabr, M. A., Rasdorf, W., Findley, D. J., Chang, J. C., & Hammit, B. E. (2016). “Retaining wall field condition inspection, rating analysis, and condition assessment.” *Journal of Performance of Constructed Facilities*, 30(3), 04015039.

Catelan, F. T., Bossi, G., Schenato, L., Tondo, M., Critelli, V., Mulas, M., ... & Marcato, G. (2025). “Long-term monitoring of active large-scale landslides for non-structural risk mitigation-integrated sensors and web-based platform.” *Journal of Mountain Science*, 22(1), 1-15.

Chen, J., & Zhao, G. (2013). “Infrared thermographic inspection technique for concrete retaining wall.” *Journal of Civil Engineering and Management*, 18(6), 1521–1528.

Cheng, Y., Huang, L., & Pan, X. (2019). “Predictive maintenance strategies for MSE walls using thermal imaging*.” Journal of Infrastructure Inspection*, 22(4), 305–315.

Chew, Y. L. M. (1998). “Building facades: a guide to common defects in tropical climates.” *World Scientific.*

Cho, N., Kim, H., & Cha, W. (2016). “Non-destructive detection of underground cavities using thermal images.” *Electronic Journal of Geotechnical Engineering*, 21(16), 5465–5476.

Christopher, B. R., Gill, S., Giroud, J. P., Juran, I., Mitchell, J. K., Schlosser, F., & Dunnicliff, J. (1990). “Reinforced soil structures. Volume I. Design and construction guidelines (No. FHWA-RD-89-043).” Federal Highway Administration.

Congress, S. S. C. (2018). “Novel infrastructure monitoring using multifaceted unmanned aerial vehicle systems-close range photogrammetry (UAV-CRP) data analysis.” Doctoral thesis, ThUniversity of Texas at Arlington.

Cosser, E., Roberts, G. W., Meng, X., & Dodson, A. H. (2003). “Measuring the dynamic deformation of bridges using a total station.” In Proceedings of the 11th FIG Symposium on Deformation Measurements, Santorini, Greece (Vol. 25).

Colorado Department of Transportation. (2016). “Retaining and noise wall inspection and asset management manual.” Denver, CO: Colorado Department of Transportation.

Debees, M., & Catbas, F. N. (2025). “Rapid Evaluation and Decision-Making for Concrete Bridges.” Transportation Research Record: *Journal of the Transportation Research Board*.

Donahue, S. J. (2010). “Performance and Cost Effectiveness of Modular Block Retaining Walls.” Master Thesis, Pennsylvania State University.

Dos Santos, R. C., Larocca, A. P. C., de Araújo Neto, J. O., Barbosa, A. C. B., & Oliveira, J. V. M. (2019). “Detection of a curved bridge deck vibration using RTSs for structural health monitoring.” *Journal of Civil Structural Health Monitoring*, 9(1), 63-76.

Ehrhart, M., & Lienhart, W. (2015). “Monitoring of civil engineering structures using a state-of-the-art image assisted total station.” *Journal of Applied Geodesy*, 9(3), 174-182.

Ekinci, A., Muturi, T., & Ferreira, P. M. V. (2021). “Aerial CRP to quantify deformations of the pile retaining walls.” *Journal of the Indian Society of Remote Sensing*, 49(5), 1051-1066.

Federal Highway Administration. (2011). “Bridge Inspection Reference Manual.” U.S. Department of Transportation.

Federal Highway Administration. (2009). “Design and construction of mechanically stabilized earth walls and reinforced soil slopes—Volume II (FHWA-NHI-10-025).” U.S. Department of Transportation. https://www.fhwa.dot.gov/engineering/geotech/pubs/10025/

Federal Highway Administration. (2019). “Applications for Unmanned Aircraft Systems in Highway Infrastructure Inspection. FHWA-HIF-19-026.” U.S. Department of Transportation.

Fisher, A. (2021). “MSE Wall Design Submittal for SR-307 Over I-16 Walls Nos. 1 & 2.” The Reinforced Earth Company.

Fordham, F. (2019). “MSE Wall Design Submittal for Walls No. 1 & 2.” The Reinforced Earth Company.

Fuqua, D. (2016). “MSE Structure Shop Drawings.” Tensar.

GDOT. (2022). “GDOT Automated Survey Manual. GDOT.” https://www.dot.ga.gov/PartnerSmart/DesignManuals/SurveyManual/SurveyManual.pdf

Gerber, T. M. (2012). “Assessing the long-term performance of MSE walls (Vol. 437).” Transportation Research Board.

Gong, C. (1991). “Earth retaining structures.” *Substructure Design*, 283

Habib, A. F., Ghanma, M. S., & Tait, M. (2004). “Integration of LIDAR and photogrammetry for close range applications*.” International Archives of Photogrammetry, Remote Sensing and Spatial Information Sciences*, 35(B5), 1045-1050.

Hain, A., & Zaghi, A. E. (2020). “Applicability of photogrammetry for inspection and monitoring of dry-stone masonry retaining walls.” *Transportation Research Record*, 2674(9), 287-297.

Hansberger, J. (2019). “Old River Road (CR 310) & I-16 Wall 4 CIP Headwall.” The Reinforced Earth Company.

Holtz, R. D. (2017). "46th Terzaghi lecture: geosynthetic reinforced soil: from the experimental to the familiar." *Journal of Geotechnical and Geoenvironmental Engineering*, 143(9), 03117001.

Hossain, M. M. (2025). "Comparative Analysis of LiDAR and CRP Techniques for Inspection of MSE Walls in Two Georgia Bridges."

Kaartinen, S. (2022)." Organisaatiotekijöiden merkitys työntekijän tavoitteisiin sitoutumisessa." Mater thesis, LTU University.

Lague, D., Brodu, N., & Leroux, J. (2013). "Accurate 3D comparison of complex topography with terrestrial laser scanner: Application to the Rangitikei canyon (NZ*)." ISPRS Journal of Photogrammetry and Remote Sensing*, 82, 10–26. https://doi.org/10.1016/j.isprsjprs.2013.04.009

Lawal, C. (2025). "An IRAssessment For Monitoring Aging MSE Walls. M.Sc." Thesis Dissertation in Geogia Southern University.

Lee, N. (2025). "Drone-Based Bridge Health Monitoring and Inspection." Thesis Dissertation, Aalto University.

Leica. (2006). "Leica Geosystems AG-Leica TPS1200+ series: Technical data." https://www.leica-geosystems.com

Leica. (2011). "Leica ScanStation C10: The All-in-One Laser Scanner for Any Application (Document No. 776632enUS-VIIL11-RDV)." Heerbrugg, Switzerland. https://secure.fltgeosystems.com/uploads/tips/documents/170-1407352313.pdf?srsltid=AfmBOoqfA12gyhmkuyUfYbGj25JM4a_c0ZlLK8i11UayQa9oMgb51X-3

Leica. (2017). "Leica ScanStation P50 Product Specifications (Document No. 869145en-12.20)." Heerbrugg, Switzerland. https://leica-geosystems.com/en-us/products/laser-scanners/scanners/leica-scanstation-p50

Maldonado, G. O., Maghiar, M. M., Nam, S., Hossain, M. M., & Ahmed, S. (2025). "Discrepancies of LiDAR registrations to capture potential displacements of MSE walls." *Geomechanics and Engineering*, 42(1), 43–55. https://doi.org/10.12989/gae.2025.42.1.043

Man, J. (2024). "Addressing New York's Scaffolding Issue through an Arbitration Framework." *Cardozo J. Conflict Resol*., 26, 325.

Marendić, A., Paar, R., & Damjanović, D. (2017). "Measurement of bridge dynamic displacements and natural frequencies by RTS." *Građevinar*, 69(04.), 281-294.

Mitchell, J. K. (1990). "North American practice in reinforced soil systems." Paper presented at the Proc. American Society of Civil Engineers (ASCE) Conf. on the Design and Performance of Earth Retaining Structures.

NCHRP. (2006). NCHRP Report 567: “Geotechnical Asset Management for Transportation Infrastructure.” Transportation Research Board.

NCHRP. (2009). “Design of Roadside Barrier Systems Placed on MSE Retaining Walls. Transportation Research Board.” https://apps.trb.org/cmsfeed/TRBNetProjectDisplay.asp?ProjectID=693&utm_source=chatgpt.com

NCHRP. (2011). “NCHRP Synthesis 20-05/Topic 42-09 Cost Effective and Sustainable Road Slope Stabilization and Erosion Control.” Transportation Research Board. https://westerntransportationinstitute.org/wp-content/uploads/2018/04/4W3431_NCHRP-Synthesis-42-09_Final.pdf

NCDOT. (2012). “North Carolina Department of Transportation- Standard specifications for roads and structures.” https://connect.ncdot.gov/resources/Specifications/2012StandSpecsMan/PDF/2012%20Standard%20Specifications%20Manual%20with%20ASTM.pdf

NCDOT. (2014). “North Carolina Department of Transportation – Earth Retaining Structures Asset Management Plan.” NCDOT Geotechnical Engineering Unit.

Newhart, K. B. (2020). “Data-Driven Process Monitoring and Control in Municipal Wastewater Treatment.” Colorado School of Mines.

NYC Department of Buildings. (2014). “New York City Department of Buildings construction codes.” NYC.gov. Retrieved July 13, 2025, from https://www.nyc.gov/site/buildings/codes/2014-construction-codes.page

Oats, R. C., Escobar-Wolf, R., & Oommen, T. (2017). “A novel application of photogrammetry for retaining wall assessment.” *Infrastructures*, 2(3), 10.

Omidi, Z. (2024). “Enhancing concrete infrastructure integrity: integrating active thermography and GPR for delamination detection.”

Oskouie, P., Becerik-Gerber, B., & Soibelman, L. (2016). “Automated measurement of highway retaining wall displacements using terrestrial laser scanners.” *Automation in Construction*, 65, 86-101.

Pan, P., Zhang, R., Zhang, Y., & Li, H. (2023). “Detecting Internal Defects in FRP-Reinforced Concrete Structures through the Integration of IRand Deep Learning.” *Materials*, 16(17), 3350.

Park, H., Cha, B., Cho, S., Kim, D., Choi, J. H., Pyo, B. G., & Rhee, B. (2016). “A study on the estimation of plastic deformation of metal insert parts in multi-cavity injection molding by injection-structural coupled analysis*.” The International Journal of Advanced Manufacturing Technology*, 83(9), 2057-2069.

Pehlivan, H. (2021). “The Analysis Methodology of RTS Data for Determination of Structural Displacements.” *Advanced Geomatics*, 1(1), 1-7.

Pennsylvania Department of Transportation. (2024). “Bridge safety inspection manual.” Harrisburg, PA: Pennsylvania Department of Transportation.

Raeburn, C. L., Monkul, M. M., & Pyles, M. R. (2008). “Evaluation of corrosion of metallic reinforcements and connections in MSE retaining walls (No. FHWA-OR-RD-08-10).” Oregon. Dept. of Transportation. Research Unit.

Rasdorf, W., Hummer, J. E., Zhang, G., & Frey, D. (2015). “Retaining wall inventory and assessment system (FHWA/NC/2013-15).” North Carolina Department of Transportation.

Rocha, J. A., & Póvoas, Y. V. (2017). “Iras a non-destructive test for the inspection of reinforced concrete bridges: A review of the state of the art.” *Revista Alconpat*, 7(3), 200-214.

Schenewerk, M. S., & Marshall, J. A. (2010). “Practical aspects of geodetic positioning.” National Geodetic Survey.

Sharma, S., Ibrahim, A., Lu, Y., Mahar, J., & Mashal, M. (2019). “Development of an inventory and inspection database framework for asset management of MSE walls (Rep. No. RP 270; FHWA ID).” Idaho Transportation Department.

Sirca Jr, G. F., & Adeli, H. (2018). “IRfor detecting defects in concrete structures.” *Journal of Civil Engineering and Management*, 24(7), 508-515.

Teng, J., Shi, Y., Wang, H., & Wu, J. (2022). “Review on the research and applications of TLS in ground surface and constructions deformation monitoring*.” Sensors*, 22(23), 9179.

Tensar. (2024.). “Geogrid Construction & Civil Engineering Resources.” Accessed November 5, 2024, from https://www.tensarcorp.com/resources

Teshev, I., Bespayev, A., Tamov, M., Zhambakina, Z., Altigenov, U., Zhussupov, T., & Tolegenova, A. (2025). “Stress State of Modular Blocks with Large Door Openings.” *Buildings*, 15(8), 1253.

Tsz Wai, C., Wai Yi, P., Ibrahim Olanrewaju, O., Abdelmageed, S., Hussein, M., Tariq, S., & Zayed, T. (2023). “A critical analysis of benefits and challenges of implementing modular integrated construction.” *International Journal of Construction Management*, 23(4), 656-668.

Vaidis, M., Giguère, P., Pomerleau, F., & Kubelka, V. (2021, May). “Accurate outdoor ground truth based on total stations.” In 2021 18th Conference on Robots and Vision (CRV) (pp. 1-8). IEEE.

Vidal, H. (1969). “The principle of reinforced earth.” *Highway research record*, (282).

WISCONSIN DOT. (2024). Wisconsin Department of Transportation. (2024). “Structure Inspection Field Manual.”

https://wisconsindot.gov/dtsdManuals/strct/inspection/2024%20WisDOT%20Field%20Manual%20-%20Final%202024-02-27.pdf

Wondolowski, M., Hain, A., & Motaref, S. (2024). “Experimental evaluation of 3d imaging technologies for structural assessment of masonry retaining walls.” *Results in Engineering*, 21, 101901.

Wu, C., Yuan, Y., Tang, Y., & Tian, B. (2021). “Terrestrial laser scanning TLS in the architecture, engineering and construction (AEC) industry.” *Sensors*, 22(1), 265.

Wu, J., Armaghani, J., Stewart, J., & Graves, D. (2019). “Rating and inventory of TDOT retaining walls (No. RES2016-27).” Tennessee Department of Transportation.

Zschiesche, K. (2021). “Image assisted with total stations for SHM review.” *Geomatics*, 2(1), 1-16.

Zou, L., & Liu, A. (2025). “Intelligent Detection Algorithm for Concrete Bridge Defects Based on SATH–YOLO Model.” *Sensors*, 25(5), 1449.